Atoms in a Propagating-Wave Cavity for Squeezed Mach-Zehnder Atom Interferometry

by

Sebastian Wald

November, 2025

A thesis submitted to the
Graduate School
of the
Institute of Science and Technology Austria
in partial fulfillment of the requirements
for the degree of
Doctor of Philosophy

Committee in charge:

Scott Waitukaitis, Chair
Onur Hosten
Mikhail Lemeshko
Morgan Mitchell

The thesis of Sebastian Wald, titled *Atoms in a Propagating-Wave Cavity for Squeezed Mach-Zehnder Atom Interferometry*, is approved by:

Supervisor: Onur Hosten, ISTA, Klosterneuburg, Austria

Signature: _____

Committee Member: Mikhail Lemeshko, ISTA, Klosterneuburg, Austria

Signature: _____

Committee Member: Morgan Mitchell, ICFO, Barcelona, Spain

Signature: _____

Defense Chair: Scott Waitukaitis, ISTA, Klosterneuburg, Austria

Signature: _____

Signed page is on file

ISTA Thesis, ISSN: 2663-337X

ISBN: 978-3-99078-075-6

I hereby declare that this thesis is my own work and that it does not contain other people's work without this being so stated; this thesis does not contain my previous work without this being stated, and the bibliography contains all the literature that I used in writing the dissertation.

In this thesis, ChatGPT assisted in refining writing style. Limitations in AI interpretations were mitigated by cross-checking and validating AI recommendations by the author to the best of their capacity.

I accept full responsibility for the content and factual accuracy of this work, including the data and their analysis and presentation, and the text and citation of other work.

I declare that this is a true copy of my thesis, including any final revisions, as approved by my thesis committee, and that this thesis has not been submitted for a higher degree to any other university or institution.

I certify that any republication of materials presented in this thesis has been approved by the relevant publishers and co-authors.

Signature: _____

Sebastian Wald
November, 2025

Signed page is on file

Abstract

Atom interferometers measure the relative phase shifts between coherent matter-wave paths that arise from interactions with external fields or inertial forces. Due to their exceptional phase sensitivity, atom interferometers became an essential tool for precision measurements and fundamental physics experiments, finding applications in geodesy, gravimetry, and inertial navigation. However, their measurement precision is limited by quantum projection noise, which arises from the Heisenberg uncertainty principle, preventing the measurement of atomic states with absolute precision. The generation of entanglement between the atoms offers a path to surpass this so-called standard quantum limit, thereby enhancing the interferometer's phase sensitivity beyond classical measurement bounds.

This thesis reports on the development of an atom interferometer experiment designed to realize cavity-mediated, squeezed Mach-Zehnder-type interferometry with ultra-cold ^{87}Rb atoms. The experiment combines cavity-aided spin-squeezing with cavity-mediated Mach-Zehnder interferometry to demonstrate entanglement-enhanced phase sensitivity. The experiment is centered on a triangular optical cavity that mediates all relevant atom-light interactions. The cavity provides optical trapping, spin-squeezing, and Raman beam-splitter operations, enabling to perform interferometry on a continuously trapped atomic ensemble.

The thesis elaborates on the fundamental theoretical framework, the cavity design, and the full optical setup, including the detailed configuration of the developed laser stabilization methods. Experimentally, continuous loading methods were explored, resulting in an accumulation of up to 4×10^6 atoms in the dipole trap within a cycle time of $500\,\mathrm{ms}$. The AC Stark shift compensation method developed for continuous loading was further applied for *in-trap* cooling to $10\,\mu\mathrm{K}$, and optical pumping for efficient atomic state preparation. Coherent state control was verified via observation of microwave-driven Rabi oscillations, and used to characterize atom-cavity coupling.

These presented results establish the experimental groundwork for the future development of cavity-mediated, entanglement-enhanced Mach-Zehnder-type atom interferometry.

Acknowledgements

A PhD is not just an opportunity to pursue your research interests, it is also a journey of personal growth, guided by the people around you. Now, at the end of my PhD and close to the conclusion of my time at ISTA, it is a moment to look back and sincerely appreciate all those without whom this journey would not have been possible.

First of all, I want to thank my supervisor, Onur. Thank you for affiliating me, for the trust I've felt, your constant approachability, and the calm and thoughtful guidance whenever I needed advice. You are an inspiration, not only for your knowledge but also for the way you treat and mentor your students. It has been a great pleasure to learn from you, and I hope I have been able to adopt some of your skills and make them my own.

Fritz, I honestly don't know how to express just how thankful I am to you. You are one of the people who truly changed the course of my life. If you hadn't told me about Onur's research and shared your experience in the group as a postdoc at your home party, I might never have applied. Your patience with me and your eagerness to teach me your skills in optics were invaluable when I arrived in the group. Our gatherings after busy lab weeks during the pandemic kept me sane and helped me cope with this situation. I am just thankful for your camaraderie and friendship.

Vyacheslav, we can be proud of the experiment we built together. Starting this project from scratch was a demanding task, but we succeeded! We share many great memories, from dressing up to prepare the vacuum chamber to our first observation of the MOT and more. The experimental control system you created is such an intuitive beauty! Thank you for being my lab buddy over the main part of my PhD. I wish you and your family all the best and a bright future in Amsterdam.

Edward, you are a monster, a monster in the lab! I've enjoyed every moment working with you, and the progress we've made over the last two years is incredible. None of this would have been possible without your dedication and cheerful nature. I owe you drinks for life for all your support during my thesis writing, whether it was discussing results or proofreading my manuscript. I have no doubt that the experiment is in excellent hands, and I'm excited to see all that you will achieve next.

Andrea, even though you just joined a couple of months ago, your input was immediately felt! Thank you for your dedication and proofreading my thesis. I think you will be a great team with Ed, and you will be capable of achieving our goal to demonstrate an entangled Mach-Zehnder.

Sofia, Umang, Alexei, Theo, Marta (special thanks for proofreading the theory section), and Gabi, thank you for your camaraderie and friendship. I have always felt comfortable around you, and I enjoyed every day we shared in the office and lab. There is just one thing I still

don't understand: Why do you sometimes want to go to lunch with 'friends', and what are those? ;)

My experience at ISTA was unique. Starting the PhD with a cohort made up of people from all around the world and working in such an international environment has been a mesmerizing experience. I am sure most of these friendships that were created here will endure time and I will keep you all close to my heart.

Hier ist auch Platz für euch, Mama und Papa. Ich bin euch so unglaublich dankbar für eure bedingungslose Unterstützung. Ohne euch wäre das alles nicht möglich gewesen, schon das Studium nicht und schon gar nicht dieser PhD. Euer Vertrauen gibt mir unendlich viel Kraft und lässt mich zu einem Menschen werden, den ich mir selbst nicht hätte vorstellen können. Auch ein Dank an dich, Magdalena, mein Schwesterherz. Du bist so eine coole Socke und ich bin so stolz auf dich. Danke für deine und Bastis Essenslieferungen und deine Anrufe, speziell in den letzten anstrengenden Monaten.

Mein Dank gilt auch dir, Saskia, meiner Partnerin. Ohne dich hätte ich die letzten Monate nicht geschafft. Du bist unglaublich, gibst mir gleichzeitig so viel Halt, Motivation und neue Ziele. California, here I come! Ich freue mich wahnsinnig auf unsere Zukunft!

Ein weiterer großer Dank geht an meine Freunde, die mich konstant in meinem Leben begleiten und mir Halt geben. Seien es meine Steyrer, mit denen ich seit der Schulzeit Schabanack treibe, oder meine Wiener Physiker:innen, die mein Leben so bereichern. Ein spezielles Shout-out natürlich auch an meine (früheren) Mitbewohner Max, Michi, Franzi und Gabi. Ihr glaubt vielleicht gar nicht, wie wichtig es mir war, nach einem langen Tag im Labor euch zu sehen, auch wenn's nur 5 Minuten waren.

Last but not least, I would like to thank ISTA for providing the funding that made this research possible.

About the Author

Sebastian Wald completed his undergraduate studies at the Vienna University of Technology, where he obtained his MSc in Technical Physics in 2017. His Master's thesis, "Probing solid-state electron spin-phonon interaction at the quantum limit," was conducted under the supervision of Prof. Jörg Schmiedmayer.

After a short period in industry, he joined ISTA in September 2019 as a PhD student, affiliating with Onur Hosten to develop an entanglement-enhanced Mach-Zehnder-type atom interferometer. During his PhD, Sebastian designed and realized the optical cavity at the core of the experiment and developed stabilization techniques for lasers, modulators, and optical cavities. Furthermore, he implemented atomic cooling and trapping schemes, forming the foundation for ongoing efforts to realize cavity-mediated, entanglement-enhanced atom interferometry.

His work led to publications in Optics Letters and Applied Optics, and he presented at conferences, including the APS March meeting and the Terrestrial Very-Long-Baseline Atom Interferometry workshops. Beyond his research, Sebastian has been active in outreach and scientific community building, participating in public talks and serving as a student representative for the Vienna Center for Quantum Science and Technology (VCQ).

List of Collaborators and Publications

Sebastian Wald, Fritz Diorico, and Onur Hosten. Analog stabilization of an electro-optic i/q modulator with an auxiliary modulation tone. *Applied Optics*, 62:1–7, 1 2023

Umang Mishra, Vyacheslav Li, Sebastian Wald, Sofia Agafonova, Fritz Diorico, and Onur Hosten. Monitoring and active stabilization of laser injection locking using beam ellipticity. *Optics Letters*, 48:3973–3976, 8 2023

Edward Gheorghita, Sebastian Wald, Andrea Pupic, and Onur Hosten. Continuous accumulation of cold rubidium atoms in an optical cavity. *arXiv:TBD*, 2025

Table of Contents

Abstract vii

Acknowledgements viii

About the Author x

List of Collaborators and Publications xi

Table of Contents xiii

List of Figures xvi

List of Tables xviii

Acronyms xix

1 Introduction 1
- 1.1 Atom Interferometry with Entangled States . . . 1
- 1.2 Structure of this Thesis . . . 3

2 Entanglement-Enhanced Atom-Interferometry 5
- 2.1 Mach-Zehnder-Type Atom Interferometer . . . 5
- 2.2 Quantum Projection Noise . . . 9
  - 2.2.1 Collective Treatment of an Atomic Ensemble . . . 9
  - 2.2.2 Coherent Spin States & the Standard Quantum Limit . . . 10
  - 2.2.3 Spin-Squeezed States . . . 11
- 2.3 Atoms in a Propagating-Wave Cavity . . . 14
  - 2.3.1 The Propagating-Wave Cavity . . . 14
  - 2.3.2 Tavis-Cummings Model . . . 20
  - 2.3.3 The Dispersive Hamiltonian . . . 20
  - 2.3.4 Cavity-Mediated Squeezing . . . 23
- 2.4 The Optical Dipole Trap . . . 30
  - 2.4.1 The Dipole Potential . . . 30
  - 2.4.2 AC Stark Shift of the $5P_{3/2}$ Level . . . 31
  - 2.4.3 AC Stark Shift Compensation . . . 33
- 2.5 Cavity-Mediated Raman-Beam Splitter . . . 35
  - 2.5.1 Raman Transitions in ^{87}Rb . . . 35
  - 2.5.2 Three-Level Atom Interaction with Classical Fields . . . 36
  - 2.5.3 Adiabatic Elimination of the Excited State . . . 39
  - 2.5.4 Dressed Hamiltonian . . . 40

2.5.5 Raman-π-Pulses . . . 41
2.5.6 Outlook to an Adiabatic Raman Passage . . . 42

3 The Experimental Setup 43
3.1 The Vacuum Chamber . . . 43
3.2 The Science Cavity . . . 46
3.2.1 Cavity Length Calculation . . . 46
3.2.2 Stability and Mode Waists . . . 47
3.2.3 Science Cavity Assembly . . . 48
3.2.4 The Optical Cavity Coupling Setup . . . 49
3.2.5 Cavity Length Adjustment . . . 50
3.2.6 Linewidth Measurements . . . 50
3.2.7 Atom-Cavity Coupling Parameters . . . 53
3.2.8 Back-Scatter Characterization . . . 53
3.3 Optical Setup . . . 55
3.3.1 Modulation Transfer Spectroscopy . . . 58
3.3.2 Offset Lock for $1560\,\mathrm{nm}$-Laser . . . 60
3.3.3 Squash-Lock of Science Cavity . . . 61
3.3.4 Side-of-the-Fringe Lock of the $1527\,\mathrm{nm}$-Laser . . . 67
3.3.5 Bias-Feedback for Electro-Optic I/Q Modulators . . . 69
3.4 Imaging System . . . 75
3.4.1 Atom Number Measurements . . . 77
3.4.2 Temperature Measurement . . . 77
3.5 Microwave Setup . . . 78
3.6 Homodyne Detection Setup . . . 80
3.7 Quantrol - Experimental Control System . . . 82

4 Experimental Results 85
4.1 MOT & Molasses Cooling . . . 85
4.1.1 3D-MOT Cooling . . . 88
4.1.2 FD-MOT Sequence . . . 90
4.1.3 Molasses Sequence . . . 91
4.2 Dipole Trap Experiments . . . 94
4.2.1 Trap Activation Induced Parasitic Cavity Mode . . . 94
4.2.2 Steady-State Accumulation of Atoms in an Optical Cavity . . . 95
4.2.3 Molasses Cooling in Light Shift Compensated Dipole Trap . . . 98
4.2.4 An Alternative Loading Scheme . . . 99
4.3 Atomic-State Preparation . . . 100
4.3.1 Optical Pumping . . . 100
4.3.2 Microwave-Driven Rabi Oscillation . . . 103
4.4 Atom-Cavity Coupling . . . 105

5 Conclusion & Future Prospects 109
5.1 Conclusion . . . 109
5.2 Short Term Prospects . . . 110
5.3 Long Term Prospect . . . 110

Bibliography 113

A Feedback Theory **123**

B Hyperfine structure of the ^{87}Rb D_1 and D_2 lines **125**

C Specification of Birefringent Mirror Coating **127**

D MOT Optical Power Distribution Setup **131**

List of Figures

2.1 Space-time diagram of a Mach-Zehnder-type atom interferometer 6
2.2 Coherent Spin State 11
2.3 Spin Squeezed State 12
2.4 Transverse mode spectrum of a propagating-wave cavity with unilateral triangular geometry 17
2.5 Diagram of a triangular cavity 18
2.6 Transmission and reflection of an ideal and lossy cavity 19
2.7 Dispersively coupled three-level system and resulting cavity resonance shift . . 22
2.8 SSS generated by OAT interaction 24
2.9 OAT mechanism 25
2.10 SSS generated by QND measurement 27
2.11 Level structure relevant or dipole trap and spacial profile of AC Stark shift across the cavity mode 32
2.12 Λ-level system interacting with the Raman beam pair 36
2.13 State-dependent momentum kick 38
2.14 MZI sequence 41

3.1 3D-CAD model of the vacuum chamber 44
3.2 Images of the science cavity and mirror holder assembly 48
3.3 Schematic diagram of the optical setup coupling to the science cavity 49
3.4 Cavity transmission of Raman tones after length adjustment 51
3.5 Linewidth measurement of the s-polarized $1560\,\mathrm{nm}$-mode 51
3.6 Linewidth measurement of the s-polarized $780\,\mathrm{nm}$-mode 52
3.7 Linewidth measurement of the p-polarized $780\,\mathrm{nm}$-mode 53
3.8 Linewidth measurement of the p-polarized $1527\,\mathrm{nm}$-mode 54
3.9 Schematic diagram of the grand optical setup 56
3.10 Optical and electronic configuration of the MTS setup 58
3.11 MTS signal and level scheme of the ^{85}Rb D_2 line 59
3.12 Offset lock feedback circuit for the $1560\,\mathrm{nm}$ laser 61
3.13 Squash lock - conceptual illustration 62
3.14 Mode matching simulation for squash lock 63
3.15 Control circuit for the linear stage 65
3.16 Feedback circuit diagram for cavity-laser 66
3.17 Circuit diagram of the third-order filter for ring piezo feedback 66
3.18 Diagram of the VCO feedback circuit 68
3.19 Diagram for the $1527\,\mathrm{nm}$ laser feedback circuit 68
3.20 Schematic of an electro-optic I/Q modulator 70
3.21 Schematic and measured frequency spectrum with frequencies Ω_{HF} (blue) and Ω_{LF} (red) 73
3.22 Schematic experimental setup for CS-SSB stabilization 74

3.23 Error signals over phase bias voltage scan . . . 75
3.24 CS-SSB modulation stability over time . . . 76
3.25 Fluorescence imaging setup . . . 77
3.26 Examples for fluorescence images . . . 78
3.27 Circuit diagram of the microwave generation chain . . . 79
3.28 Frequency response plot of the $\lambda/4$ antenna . . . 80
3.29 Homodyne detection setup . . . 81
3.30 Schematic diagram for the path length stabilization circuit . . . 82
3.31 Screenshot of the Quantrol - *Sequence* tab . . . 83
3.32 Screenshot of the Quantrol - *DDS* tab . . . 84

4.1 Schematic diagram of a MOT in 1D & hyperfine structure of the ^{87}Rb D_2 line 86
4.2 Image of the ^{87}Rb MOT prior to installation of the science cavity in the vacuum chamber. . . . 88
4.3 Atom number over MOT loading time . . . 90
4.4 TOF measurement of the atomic temperature following the FD-MOT sequence. 91
4.5 Schematic diagram of the Zeeman shift of the magnetic sublevels in the hyperfine ground states of ^{87}Rb . . . 92
4.6 MW spectroscopy of the ^{87}Rb ground state hyperfine transitions in presence of a $100\,\mathrm{mG}$ bias field . . . 93
4.7 TOF measurement of the atomic temperature following the molasses sequence. 93
4.8 Fluorescence image of an atomic ensemble in the dipole trap . . . 94
4.9 Cavity transmission profile during the dipole trap activation . . . 95
4.10 *In-situ* dipole potential tomography . . . 96
4.11 Number of accumulated atoms in the dipole trap as a function of compensation tone power. . . . 97
4.12 Temperature measurement of atoms in dipole trap . . . 99
4.13 Schematic diagram of the optical pumping scheme in ^{87}Rb . . . 101
4.14 MW spectroscopy of the atomic ensemble before and after optical pumping . . 102
4.15 Rabi oscillation measurement . . . 104
4.16 Rabi oscillation contrast measurement . . . 105
4.17 Dispersive shift of the cavity resonance during a Rabi-$\pi/2$ cycle . . . 106

5.1 Experimental sequence of squeezed Mach-Zehnder atom interferometer . . . 111

A.1 Block diagram of a generalized electronic feedback circuit. . . . 123

B.1 Hyperfine structure of the ^{87}Rb D_1 line . . . 125
B.2 Hyperfine structure of the ^{87}Rb D_2 line . . . 126

D.1 Optical power distribution for cooling, repump and push beams. . . . 131

List of Tables

3.1 Geometrical properties of the cavity 48
3.2 Linewidth and Finesse values 53

4.1 MOT: Cooling and repump tone parameters 89
4.2 FD-MOT: Cooling ramp parameters 90
4.3 Molasses: Ramp parameters for cooling beam 92
4.4 Parameters of the continuous loading sequence. 98
4.5 Parameters of the *in trap* molasses sequence. 99
4.6 Parameters of an alternative AC Stark-compensated trap loading scheme . . . 100
4.7 Parameters of the optical pumping sequence. 102

Acronyms

AC alternating current.

ADC analog-to-digital converter.

AOI angle of incidence.

AOM acousto-optic modulator.

ARTIQ Advanced Real-Time Infrastructure for Quantum physics.

CAM camera.

CL cylindrical lens.

CS-SSB carrier-suppressed single-sideband.

CSS coherent spin state.

DAC digital-to-analog converter.

DC direct current.

DDS direct digital synthesizer.

DFB distributed feedback.

ECDL external-cavity diode laser.

EDFA erbium-doped fiber amplifier.

EOM electro-optic modulator.

FD-MOT far-detuned magneto-optical trap.

FPGA field programmable gate arrays.

FPI Fabry–Pérot interferometer.

FSR free spectral range.

FWHM full width at half maximum.

GUI graphical user interface.

HF high frequency.

ISTA Institute of Science and Technology Austria.

LF low frequency.

LO local oscillator.

MOT magneto-optical trap.

MTS modulation transfer spectroscopy.

MW microwave.

MZI Mach-Zehnder interferometer.

NEG non-evaporative getter.

OAT one-axis twisting.

PBS polarizing beamsplitter.

PD photodiode.

PhD Doctor of Philosophy.

QND quantum non-demolition.

QPD quadrant photodetector.

RF radio frequency.

SB sideband.

SOF side-of-the-fringe.

SQL Standard quantum limit.

SSB single-sideband.

SSS spin squeezed state.

TG tracking generator.

TOF time-of-flight.

TTL transistor-transistor logic.

UHV ultra-high vacuum.

VCO voltage-controlled oscillator.

VCQ Vienna Center for Quantum Science and Technology.

CHAPTER 1

Introduction

1.1 Atom Interferometry with Entangled States

Interferometers are devices that measure the relative phase between two paths of a coherently split, wave-like object. From a historical perspective, interference experiments had a remarkable impact on the development of Modern Physics. Michelson and Morley disproved the ether theory using a rotating light interferometer [MM87], a discovery that ultimately led to the development of special relativity. Three decades later, Davisson and Germer [DG27] demonstrated single-electron interference, confirming the wave-like behavior of matter postulated by De Broglie [Bro25]. Since then, single particle interference has been demonstrated with neutrons [RTB74], atoms [SGOAD96], and even massive molecules [FGZ+19].

Atoms, with their well-defined properties, are an ideal meter for precision tests of fundamental interactions, and the realization of matter-wave interferometers using atomic ensembles opened a new regime of measurements. However, such measurements require precise control of the atomic state and sufficiently long coherence times, which can only be achieved with cold atomic samples. Advances in laser cooling and trapping [PPM85, CBAC86] during the 1980s enabled the preparation of cold atomic gases and Bose-Einstein condensates [DMA+95, AEM+95]. Today, these methods are standard tools in modern laboratories, allowing cold atom experiments to achieve exceptional precision and stability. For instance, precise control of the electronic degrees of freedom of trapped atoms has enabled the development of the most accurate optical atomic clocks [AKW+24, MCAD+25], as well as precision tests of relativity [BKA+22] and electromagnetic interactions [BBB+21].

Inertial effects can be explored with Mach-Zehnder-type atom interferometers. In such interferometers, sequences of optical Raman or Bragg pulses coherently split, redirect, and recombine the atomic wave function [KC92, MCL+08]. The light pulses impart a well-defined differential momentum to the atoms, creating two spatially separated trajectories that accumulate a relative phase proportional to external forces coupling to atomic inertia. This principle forms the basis for atom-interferometric accelerometers and gyroscopes that are used to measure gravitational acceleration [PCC01], rotations [DSK06], gravity gradients [MAMFF+02], and for inertial navigation [ddCCA+24]. Beyond applied sensing, atom interferometer experiments have been developed for fundamental tests of physics, including the equivalence principle [TMP+14], the gravitational constant [RSC+14], general relativity [HSA+13], and the gravitational Aharonov-Bohm effect [OAC+22].

The phase sensitivity of an atom interferometer is ultimately limited by the quantum nature of the atoms, which gives rise to quantum projection noise. For an unentangled input state, the minimum achievable phase uncertainty, known as the standard quantum limit, is given by $\Delta\theta_{SQL} = \frac{1}{\sqrt{N}}$, where N is the total number of atoms participating in the interferometer sequence. The theoretical limit in phase uncertainty, which is approachable by deploying entangled states, is defined by the Heisenberg limit, which is given by $\Delta\theta_{Heis} = \frac{1}{N}$. For atom interferometry, where experiments are typically operated with 10^4-10^8 atoms, the implementation of entanglement schemes offers a substantial metrological gain, a reduction in phase variance relative to the standard quantum limit. Consequently, the development of entanglement-enhanced interferometer is in focus of current research [SHH21].

Over the past decade and a half, entanglement generation protocols mediated by optical cavities have been successfully demonstrated. Collective spin-squeezed states, a subclass of entangled states [PSO+18], have been generated either via off resonant probing, which produces one-axis-twisting dynamics [SSLV10b], or through projective quantum non-demolition measurements [BCN+14]. A combination of these methods was applied to prepare a $18.5 \pm 0.3\ dB$ spin squeezed state as input for an atomic clock measurement that demonstrated noise suppression of $10.5 \pm 0.3\ dB$ [HEKK16]. Furthermore, it has been shown [HKEK16, LCS+23] that one-axis twisting operations can be applied to the end of an interferometer sequence to magnify the acquired phase.

However, all the demonstrations discussed above of entanglement-enhanced phase sensitivity were performed on the atomic internal states. The implementation of such entangled states in Mach-Zehnder-type atom interferometer, and thus creating delocalized entangled states remains challenging. Any local variation of the states' interaction with the environment leads to degrading of entanglement and the reduction of the metrologiacal gain. Two potential approaches have been explored. In the first, the internal collective atomic state is entangled prior to being mapped onto the interferometer paths via the beam-splitter operation. This approach was demonstrated in [CMHRK25], reporting a metrological gain of $1.7^{+0.3}_{-0.5}\ dB$, where atomic scattering within a Bose-Einstein condensate was tuned to generate spin squeezing before Raman pulses mediated the interferometer sequence. In the second approach, entanglement is generated directly between the momentum states of the interferometer. This method was demonstrated in [GLWT22, MWMRK22, LZK+24], where cavity-mediated two- and four-photon interactions induced one-axis twisting and two-axis counter-twisting dynamics between two momentum states.

This thesis reports on the development of an experiment that aims to demonstrate a Mach-Zehnder atom interferometer with significant entanglement-enhanced metrological gain. The experiment combines and expands the concept of the cavity-aided squeezing demonstrated in [HEKK16] with the cavity-mediated Mach-Zehnder atom interferometry reported in [JXH+18]. At the core of the apparatus is a triangular propagating-wave cavity, which serves as the central element governing all atom-light interactions.

The cavity serves several essential functions. A mode at $1560\,\mathrm{nm}$ generates the dipole trap potential with weak axial confinement, allowing the atomic ensemble to remain trapped throughout the interferometer sequence. A high-finesse cavity mode at $780\,\mathrm{nm}$ is tuned to dispersively couple the two ^{87}Rb hyperfine ground states to the first optical excited state, facilitating spin-squeezing via one-axis twisting and quantum non-demolition measurements. The cavity additionally supports Raman beam-splitter operations. A $780\,\mathrm{nm}$ mode with polarization perpendicular to the squeezing mode has a defined frequency offset to the later of $6.834\,\mathrm{GHz}$, the ^{87}Rb hyperfine ground state splitting. This configuration enables the coupling

of counter-propagating beams, allowing momentum transfer through Raman transitions. Finally, an auxiliary $1527\,\mathrm{nm}$ tone coupled to the cavity compensates the AC Stark shift induced by the main $1560\,\mathrm{nm}$ trap, allowing continuous loading, *in-trap* cooling, and optical pumping for efficient atomic state preparation.

1.2 Structure of this Thesis

The development of a cold atom experiment is typically a long-term endeavor, sometimes spanning over more than one generation of PhD and postdoctoral researchers. As part of the first generation of PhD students working on this experiment, a major part of my work has been devoted to the design, construction, and optimization of the experimental apparatus. Through this process, one inevitably develops an intuitive, almost 'gut-feeling'-like understanding of the system, where, for example, the ringing of the magnetic field stabilization is identified from the faint noise-pickup in your headphones.

This thesis is intended to transfer this deep knowledge of the experiment to future researchers who will continue its development. The scope of the thesis is twofold: First, it provides a comprehensive foundation for the theoretical concepts underlying the design of the experiment. Second, it describes the experimental setup in a manual-like detail. This includes all essential experimental parameters, ranging from the optical specification of the science cavity to feedback settings and sequences used for atom cooling, trapping, and state preparation.

The thesis is structured as follows. Chapter 2 introduces the theoretical background relevant for an entanglement-enhanced atom interferometer. It begins with the basic principles of a Mach–Zehnder-type atom interferometer and the concept of quantum projection noise. Subsequently, the formalism of collective spin states is introduced, leading to the description of spin squeezing as a route to surpass the standard quantum limit. The dispersive interaction between the atoms and the optical cavity is derived from the Tavis–Cummings model, forming the theoretical basis for the discussion of cavity-mediated spin squeezing. The chapter concludes with theoretical treatments of the optical dipole trap and the Raman beam splitter, both of which are essential for the cavity-mediated Mach-Zehnder atom interferometer.

Chapter 3 gives a detailed description of the experimental apparatus. It covers the design of the vacuum chamber and provides a detailed characterization of the science cavity, which mediates all atom–light interactions required for the squeezed Mach–Zehnder atom interferometer, including the dispersive coupling for spin-squeezing and state readout, the Raman beam splitter, and the AC Stark shift compensated dipole trap. In addition, the chapter describes the optical infrastructure, including frequency stabilization and control techniques, as well as the imaging and microwave systems. It further details the path-length stabilization of the homodyne detection setup and provides an introduction to the experimental control system.

Chapter 4 focuses on the experimental results and provides reference parameters for the state preparation in future squeezing and interferometry experiments. First, it details the realization and optimization of the magneto-optical trap and molasses cooling. Then, the implementation of a light-shift-compensated dipole trap is described, which enables the continuous loading of the dipole trap as well as *in-trap* molasses cooling and optical pumping. Furthermore, controlled state preparation is demonstrated with measurements of microwave-driven Rabi oscillations, and the atom-cavity coupling is characterized with measurements of the state-dependent dispersive shift of the cavity resonance.

At last, Chapter 5 concludes the thesis and gives a short- and long-term perspective on the development of the experiment.

CHAPTER 2

Entanglement-Enhanced Atom-Interferometry

The experiment developed in the course of this thesis aims to demonstrate entanglement-enhanced phase sensitivity in a Mach-Zehnder-type atom interferometer. The central element of the setup is a propagating wave cavity, which, aside from cooling of the atoms, mediates all light-matter interactions required to generate entanglement and to facilitate the Mach-Zehnder interferometer.

This chapter provides the theoretical framework for the main conceptual building blocks that underly the experiment. We begin with a description of the Mach-Zehnder atom interferometer, followed by a discussion of its phase resolution defined by quantum projection noise and a motivation for spin-squeezed states as a route to surpass the standard quantum limit. In Sec. 2.3, geometric and spectral properties of the optical cavity are derived, and the coherent interaction of an atomic ensemble with a cavity mode, as well as the mechanism for cavity-mediated spin squeezing, is described. The optical dipole trap potential, which is generated by the cavity and confines the ensemble of ^{87}Rb atoms during the experimental sequence, is introduced in Sec. 2.4. The weak confinement of the dipole trap along the cavity mode axis allows implementation of Raman transitions, which serve as the mirror and beam splitter operations of the interferometer. The theoretical background for Raman transitions is presented at the end of this chapter (Sec. 2.5).

2.1 Mach-Zehnder-Type Atom Interferometer

Interference is a fundamental phenomenon that arises from the superposition of wave-like objects that have a fixed phase relation to each other. The arising interference pattern, which can be observed either in the spatial or time domain, reflects the relative phase between these interfering objects. Atom interferometers exploit the interference of the atomic wave function with itself, where coherent, light-pulse-induced beam-splitting and recombination enable the precise measurement of differential phase shifts accumulated along the distinct interferometer trajectories [CSP09]. The observed relative phase shifts originate from the interaction of the atoms with external fields or forces encountered along the interferometer paths. In contrast to optical interferometers, such matter-wave interferometers have a unique feature: the momentum of the interfering particles couples to inertial forces such as acceleration and rotation, thereby imparting a high sensitivity to such effects.

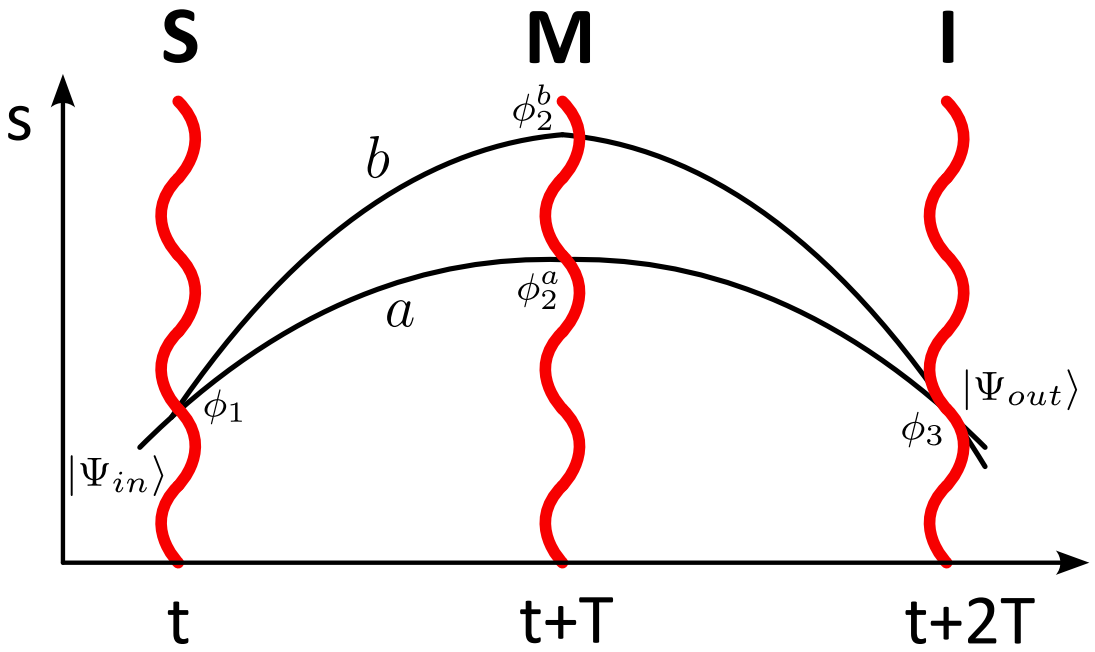

Figure 2.1: Typical space-time diagram of a Mach-Zehnder-type interferometer implemented in an atomic fountain experiment. Red waves indicate the time of the beam splitter (S), mirror (M), and recombination (I) pulses. Each light pulse imprints a position dependent-phase $\phi_i^{a,b}$ as it intersects with the interferometer paths.

The type of an interferometer is defined by the geometry of its arms. A Mach-Zehnder-type atom interferometer is characterized by two spatially separated arms that are coherently split and recombined by beam splitter and mirror pulses. Fig. 2.1 illustrates the typical space-time diagram of a Mach-Zehnder-type interferometer implemented in an atomic fountain experiment [PCC01]. An ensemble of atoms is launched upwards and propagates, in the presence of gravity, along a parabolic trajectory. At the time t, the first light pulse sequence (S) coherently splits the atomic collective wave function ($|\Psi_{in}\rangle$) into two distinct paths, labeled a and b. This initial splitting creates a superposition state that can be expressed as

$$|\Psi\rangle = \frac{1}{\sqrt{2}}\Big(|a\rangle + |b\rangle\Big), \tag{2.1}$$

where $|a\rangle$, $|b\rangle$ denote the states associated with the corresponding interferometer paths. During the subsequent pulse separation time T, the atoms freely propagate with the momentum imparted by the beam splitter pulse. A mirror pulse sequence (M) then reverses the atomic momentum and closes the interferometer. When the atomic wave function spatially overlaps again at the time $2T$, the final pulse (I) interferes the arms of the interferometer with a beam splitter operation. The resulting output state can be written as

$$|\Psi_{\text{out}}\rangle = e^{i\theta/2}\left(\cos\left(\frac{\theta}{2}\right)|a\rangle - i\sin\left(\frac{\theta}{2}\right)|b\rangle\right). \tag{2.2}$$

Subsequent measurement of the population difference between the output ports or, depending on the detection scheme, between two internal states provides direct experimental access to the interferometer phase. The probabilities of detecting an atom in either one of the output

ports $P_i = |\langle\Psi_i|\Psi_{out}\rangle|^2$, are given by

$$P_a = \cos^2\left(\frac{\theta}{2}\right), \tag{2.3}$$

$$P_b = \sin^2\left(\frac{\theta}{2}\right). \tag{2.4}$$

Following the derivations presented in [KC92, SCT94, PCC01], the differential phase shift θ for the MZI can be expressed as the sum of two contributions. One arises from the atom's free evolution and the other from the interaction with the applied laser pulses,

$$\theta = \theta_p + \theta_l. \tag{2.5}$$

The first phase term θ_p originates from the classical action along each interferometer path and is defined by

$$S^i = \int_0^{2T} dt\, \mathcal{L}[z_i(t), \dot{z}_i(t), t], \tag{2.6}$$

where $\mathcal{L}[z_i(t), \dot{z}_i(t), t]$ is the Lagrangian and $z_i(t)$ is the trajectory of the atoms along the path $i = a, b$. The differential phase between the two interferometer paths is then given by

$$\theta_p = \frac{S^b - S^a}{\hbar}. \tag{2.7}$$

Considering the free evolution of the atoms in the presence of a uniform acceleration, $\vec{a}$, along the path separation axis, the Lagrangian becomes $\mathcal{L} = \frac{1}{2}m\dot{z}^2 - maz$, and the path contribution vanishes, $\theta_p = 0$ [PCC01].

Note that in the presented experiment, the MZI will be realized within a weak harmonic potential generated by an optical dipole trap (Sec. 2.4). In the absence of any external acceleration, the system's Lagrangian becomes $\mathcal{L} = \frac{1}{2}m\dot{z}^2 - \frac{1}{2}\omega^2 z^2$. For pulse separation times much smaller than the trap frequency period, $T \ll \omega^{-1}$, the atomic motion can be approximated in first order as free evolution, and $\theta_p = 0$. However, a careful evaluation of the path term considering the experimental parameters should be addressed in future work.

The second contribution to θ originates from the interaction of the atoms with the laser pulses that govern the beam splitter and mirror sequences (Sec. 2.5.5). Each time the interferometer arms interact with a pulse, the pulse imprints a phase onto the atoms of the form:

$$\phi_i^{a,b} = k_{\text{eff}} z_i^{a,b}(t) - \omega_{\text{eff}} t_i, \tag{2.8}$$

where $\omega_{\text{eff}} = \omega_1 - \omega_2$ is the two-photon detuning of lasers that form the light pulses and $\vec{k}_{\text{eff}} = \vec{k}_1 - \vec{k}_2$ is the effective wave vector, which defines the momentum transfer imparted to the atoms by the light pulses. The relative light-induced phase shift in an interferometer then becomes the difference of the shifts accumulated along each path:

$$\theta_l = \sum_b \phi_j^b - \sum_a \phi_i^a = (\phi_2^b - \phi_1) - (\phi_3 - \phi_2^a). \tag{2.9}$$

In Fig. 2.1, the light-induced phase shifts at the relevant path-light crossings are indicated and correspond to the terms on the right of Eq. 2.9. The sensitivity of a MZI arises from the acceleration dependence of the trajectory $z(t)$ in Eq. 2.8. Any acceleration $\vec{a}$ with component

aligned with the path separation axis couples to the atom trajectory and thus to the light imprinted phase, resulting in the relative phase shift of

$$\theta_l = \vec{k}_{\text{eff}} \vec{a} T^2. \tag{2.10}$$

In conclusion, a Mach-Zehnder-type atom interferometer maps any acceleration along the path separation axis into a relative phase shift between its arms. Thereby, the effective momentum separation between the paths and the pulse separation time define the phase sensitivity of the interferometer. The momentum separation is set by the specific beam splitting method, and the pulse separation time is often limited by experimental parameters, like the free-fall time of the atoms. In the next section, we discuss how the atom number affects the sensitivity of a MZI and sets a fundamental limit.

2.2 Quantum Projection Noise

In this section, we discuss the phase resolution achievable with an atom interferometer. We begin by introducing the Dicke model, which provides a collective description of an atomic ensemble. Building on this framework, we then describe coherent spin states (CSS), whose intrinsic quantum projection noise sets the standard quantum limit (SQL) for phase resolution. To overcome this limitation, we introduce spin-squeezed states (SSS) with redistributed quantum projection noise and define the Wineland parameter as a measure for the metrological gain.

2.2.1 Collective Treatment of an Atomic Ensemble

For the theoretical description of an atomic ensemble, we apply the framework developed by Dicke in 1953 [DPA54]. He described spontaneous coherent radiation of an atomic/molecular gas as a collective effect originating from the coherent interaction of the atoms/molecules mediated by their coupling to a common electromagnetic field. Within this picture, an ensemble of N indistinguishable two-level systems is treated as a single quantum system described by the collective state $|\Psi\rangle$, which is an eigenstate of an angular momentum/spin-like operator $\hat{J}^2$ and a projection operator $\hat{J}_z$.

The collective pseudo-spin operator and its projections are defined as

$$\hat{J}^2 = \hat{J}_x^2 + \hat{J}_y^2 + \hat{J}_z^2, \tag{2.11}$$

$$\hat{J}_{x,y,z} = \frac{1}{2}\sum_{i=1}^{N} \sigma_{x,y,z}^i, \tag{2.12}$$

where $\sigma_{x,y,z}^i$ are the Pauli operators acting on the i-th atom. Furthermore, these collective projection operators fulfill the angular momentum commutation relations

$$[\hat{J}_i, \hat{J}_j] = i\varepsilon_{i,j,k}\hat{J}_k. \tag{2.13}$$

Using $\hat{J}_z$, we can define the Hamiltonian for the internal energy of the atomic ensemble as

$$\hat{H}_0 |\Psi\rangle = \hbar\omega_{ab}\hat{J}_z |\Psi\rangle, \tag{2.14}$$

$$\hat{J}_z |\Psi\rangle = m |\Psi\rangle, \tag{2.15}$$

where ω_{ab} is the atomic transition frequency, and $m = \frac{1}{2}(n_\uparrow - n_\downarrow)$ represents the inversion of the atomic population, with $n_\uparrow$ and $n_\downarrow$ denoting the populations of the excited state and the ground state, respectively.

As mentioned above, $|\Psi\rangle$ is an eigenstate of $\hat{J}^2$ with the eigenvalue

$$\hat{J}^2 |\Psi\rangle = J(J+1) |\Psi\rangle, \tag{2.16}$$

where J is the total pseudo-spin quantum number constrained by $|m| \leq J \leq \frac{1}{2}N$. At this stage, we can denote the collective state as a Dicke state $|\Psi\rangle = |J, m\rangle$.

The total pseudo-spin quantum number J is a measure of the atom's cooperativity and defines subspaces with distinct collective properties within the ensemble's Hilbert space. As an example, an ensemble in state $|\frac{N}{2}, \frac{N}{2}\rangle$, where all atoms are excited, exhibits super-radiant behavior. In contrast, the state $|0, 0\rangle$ does not show any cooperative behavior.

In analogy to the number states of the harmonic oscillator [SZ97], we can define the ladder operators

$$\hat{J}_{\pm} = \hat{J}_x \pm i\hat{J}_y, \tag{2.17}$$

to define Dicke states within the $J = \frac{N}{2}$ manifold in dependence on their ground state as

$$|\frac{N}{2}, m\rangle = \frac{1}{(m+\frac{N}{2})!}\binom{N}{m+\frac{N}{2}}^{\frac{1}{2}} \hat{J}_+^{m+\frac{N}{2}} \, |\frac{N}{2}, -\frac{N}{2}\rangle \, . \tag{2.18}$$

2.2.2 Coherent Spin States & the Standard Quantum Limit

An atom interferometer measures the phase accumulated during the time evolution of an atomic ensemble prepared in a superposition state. This can either be a superposition of internal states, as in atom clocks, or their external degrees of freedom, such as the spatial paths of a Mach-Zehnder interferometer. Dicke states, which are the eigenstates of $\hat{J}_z$ (Eq.2.15), have maximum uncertainty in the conjugate quadratures $\hat{J}_x$ and $\hat{J}_y$. Consequently, they do not have a defined phase and are, therefore, unsuitable to describe the interferometer.

Nevertheless, we can use the Dicke basis to construct coherent spin states (CSS), the product states where all N atoms are prepared in the same single-atom state. To make this connection, we introduce the Bloch sphere picture [FVH57]. The Bloch sphere is a geometric representation of a spin-$\frac{1}{2}$ system that we can generalize to depict the collective spin state of an atomic ensemble. The collective pseudo-spin system introduced in Sec.2.2.1 is mapped onto a sphere with radius $J = \frac{N}{2}$, where the expectation values of the collective spin operators define the a vector $\vec{J} = (\hat{J}_x, \, \hat{J}_y, \, \hat{J}_z)$. Alignment of the spin vector along the south- or north-pole corresponds to the atoms being polarized in either the ground or excited state, respectively.

Any CSS, denoted as $|\theta, \varphi\rangle$, can be obtained by rotating the Dicke ground state by an angle θ about the rotation axis $\hat{n} = (\sin\varphi, -\cos\varphi, 0)$. As a result, and following the derivation in [ACGT72], a CSS can be written in the Dicke basis as

$$|\theta, \varphi\rangle = \sum_{m=-J}^{J} \binom{2J}{J+m}^{1/2} \cos(\theta/2)^{J-m} (e^{-i\varphi}\sin(\theta/2))^{J+m} \, |\frac{N}{2}, m\rangle \, , \tag{2.19}$$

or as the displaced Dicke ground state

$$|\theta, \varphi\rangle = \left(\frac{1}{1+|\tau|^2}\right)^J e^{\tau J_+} \, |\frac{N}{2}, -\frac{N}{2}\rangle \, , \tag{2.20}$$

where

$$\tau = e^{-i\varphi}\tan(\theta/2). \tag{2.21}$$

In analogy to the coherent state of the harmonic oscillator, the CSS maintains its phase variance $\Delta\varphi$ under free time evolution [SZ97]. This makes it a suitable input state for an atom interferometer, where the central goal is the detection of a phase displacement. Furthermore, the CSS is the state of indistinguishable and uncorrelated atoms prepared in the identical single-particle state. As a result, the spin projection variances are equally distributed in the two orthogonal directions perpendicular to the mean spin, and they obey the Heisenberg uncertainty relation for the angular momentum projection operators given by

$$\langle \Delta J_i^2 \rangle \times \langle \Delta J_j^2 \rangle \geq \frac{1}{4} \langle J_k \rangle^2 \, . \tag{2.22}$$

To study the quantum projection noise, and hence the phase resolution of a CSS, we consider that the state is aligned along the J_x-axis, for which $|\langle J_x \rangle| = \frac{N}{2}$. According to Eq. 2.22, the uncertainties of the equally distributed orthogonal spin projections are

$$\Delta J_{CSS} = \Delta J_z = \Delta J_y = \frac{\sqrt{N}}{2}. \tag{2.23}$$

In Fig. 2.2, the Husimi-Kano Q representation [PSO+18] of a CSS with $N = 250$ atoms aligned along J_x is plotted on the Bloch sphere. The distribution illustrates the symmetric quantum projection noise. The intrinsic noise of the CSS imposes a fundamental limitation on

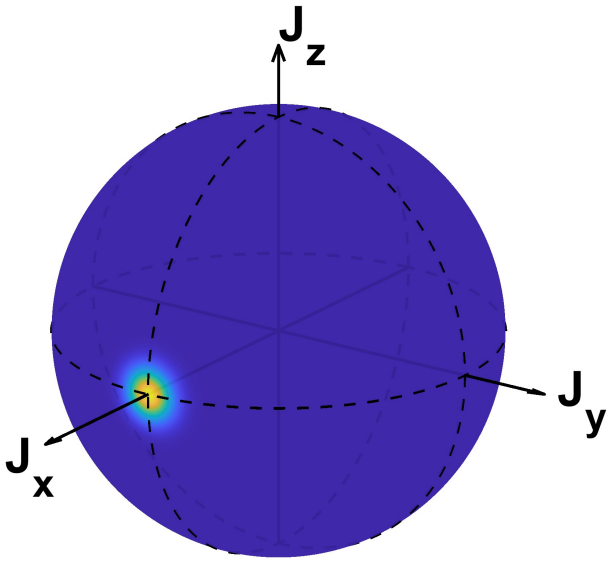

Figure 2.2: Q-representation of a CSS with $N = 250$ atoms aligned along J_x on the Bloch sphere. The distribution illustrates the equally distributed spin projection variances of the state.

the phase resolution of an atom interferometer, known as the standard quantum limit (SQL) [WBIH94], defined as

$$\Delta\varphi_{SQL} = \frac{\Delta J_\perp}{\langle \hat{J} \rangle} = \frac{1}{\sqrt{N}}, \tag{2.24}$$

where $\Delta J_\perp$ denotes the spin projection uncertainty along any direction perpendicular to the mean spin $\langle J \rangle$. For a CSS used as an input state for an atom interferometer, the SQL sets a fundamental limit for the interferometer's phase resolution. The enhancement of phase sensitivity by an order of magnitude requires increasing the atom number by two orders of magnitude.

2.2.3 Spin-Squeezed States

The SQL-limited phase resolution of an interferometer can be surpassed by using spin-squeezed states (SSS) as input. While still obeying to Heisenberg's uncertainty relations (Eq. 2.22), SSS exhibit unevenly redistributed variances for the spin projections perpendicular to the mean spin. Consequently, the spin component with reduced variance can be measured with precision beyond the SQL, whereas the conjugate quadrature exhibits increased variance. Since SSS are generated via correlations among the constituent particles, they are entangled states [PSO+18].

We can denote the squeezed (ΔJ_s) and anti-squeezed (ΔJ_a) uncertainties of a SSS in terms of CSS uncertainty (ΔJ_{CSS}, Eq. 2.23) as

$$\Delta J_s = \xi_s \Delta J_{\mathrm{CSS}}, \tag{2.25}$$
$$\Delta J_a = \xi_a \Delta J_{\mathrm{CSS}}, \tag{2.26}$$

where ξ_s and ξ_a are the squeezing and anti-squeezing parameters, which hold the uncertainty relation

$$\xi_s \times \xi_a \geq 1. \tag{2.27}$$

A measure for the metrological gain provided by a squeezed state is defined by the Wineland parameter [WBIH94]

$$\xi_W = (2J)^{\frac{1}{2}} \frac{\Delta J_\perp}{|\langle J \rangle|}, \tag{2.28}$$

where $|\langle J \rangle|$ is the absolute value of the mean spin. A parameter $\xi_W < 1$ indicates a reduced uncertainty compared to a CSS, and the factor $1/\xi_W^2$ quantifies the corresponding metrological enhancement.

When we consider that spin-squeezing interaction can induce decoherent processes, which leads to shrinking of the mean spin $|\langle J \rangle|$, where $|\langle J \rangle| \Big/ N/2 < 1$, and we assume a state polarized along the $\hat{J}_x$ direction, the Wineland parameter for the uncertainty ΔJ_z can be rewritten as

$$\xi_W = \frac{\Delta J_z}{\sqrt{N}/2} \frac{N/2}{|\langle J_x \rangle|}. \tag{2.29}$$

Here, the first factor accounts the noise reduction, and the second factor captures the loss of the mean spin due to decoherence.

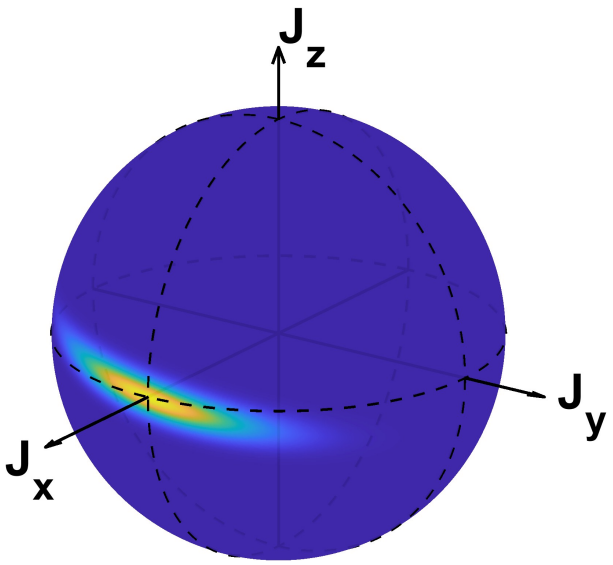

Figure 2.3: Q-representation of a SSS with N = 250 atoms and polarization along J_x on the Bloch sphere. The SSS was derived from one-axis twisting interaction with $\chi t = 0.02$

To illustrate a SSS, Fig. 2.3 shows the Q-representation of a SSS constituted by $N = 250$ atoms. The state is generated via one-axis twisting dynamics with $\chi t = 0.02$ (see Sec. 2.3.4). Compared to the CSS in Fig. 2.2, the redistribution of spin projection variances in the SSS

leads to a reduced uncertainty along one of the projections, thereby providing a metrological gain.

In this context of entanglement-enhanced phase sensitivity, we briefly introduce the Heisenberg limit, which sets the maximum attainable metrological gain. The minimum uncertainty for a spin projection operator orthogonal to the mean spin is $\Delta J_i = \frac{1}{2}$, leading to a phase sensitivity of

$$\Delta\varphi_{HL} = \frac{\Delta J_i}{|\langle J\rangle|} = \frac{1}{N}. \tag{2.30}$$

It should be noted that only maximally entangled states can reach the Heisenberg limit, which spin-squeezed states ultimately cannot achieve. A discussion of the entanglement classification is beyond the scope of this work, and the reader is referred to [PS09].

2.3 Atoms in a Propagating-Wave Cavity

2.3.1 The Propagating-Wave Cavity

In the following, we introduce the general geometric and spectral properties of triangular, propagating-wave resonators, with focus on a resonator with a plane-plane-convex mirror configuration. For a more general discussion of the properties of optical resonators and classical optics, we refer to [Nag14, ST91], the underlying textbooks for this introduction.

Geometrical Properties

For a description of the interaction between atoms and modes of an optical cavity, we first have to understand the geometric properties of these cavity modes. A cavity mode is a monochromatic electromagnetic wave that repeats itself after a round-trip upon reflection from the cavity mirrors. A realistic model for such a wave is the solution of the paraxial wave equation, the Gaussian beam [Nag14]. Assuming a propagation direction along the z-axis, we can formulate the expression for the Gaussian beam's electric field in dependence on the radial distance, r,

$$\vec{E}(r,z) = E_0\vec{p}\frac{\omega_0}{\omega(z)}\exp\Big(-\frac{r^2}{\omega^2(z)}\Big)\exp\Big(-i\Big(kz + k\frac{r^2}{2R(z)} - \phi_G\Big)\Big), \tag{2.31}$$

with a field amplitude E_0, a polarization vector $\vec{p}$ and a wave number $k = 2\pi n/\lambda$, where λ is the vacuum wavelength and n is the refractive index of the propagation medium. The real part in Eq. 2.31 describes the geometric effect on the field amplitude, a radial Gaussian dependence, and a longitudinal hyperbolic divergence. The beam is focused at $z = 0$, where the $1/e$-radius $\omega(z) = \omega_0$ is minimal, and has a radius of $\sqrt{2}\omega_0$ at the Rayleigh length, $z = z_R$. The relations between the radius, $\omega(z)$, the waist, ω_0, and $z = z_R$ are given in Eq. 2.32.

$$\omega(z) = \omega_0\sqrt{1 + \Big(\frac{z}{z_R}\Big)^2} \qquad z_R = \frac{n\pi\omega_0^2}{\lambda} \tag{2.32}$$

$$\phi_G = \tan^{-1}\frac{z}{z_R} \qquad R(z) = z + \frac{z_R^2}{z} \tag{2.33}$$

The imaginary part in Eq. 2.31 gives the phase of the beam, where the term dependent on k is interpreted as surfaces of constant phase with wavefront radius, $R(z)$. The Gouy phase, ϕ_G, has a purely geometric nature and depends solely on the ratio z/z_R. As one can derive from Eq. 2.33, the Gouy phase changes are most significant within one Rayleigh length distance to the beam waist.

To describe the propagation of the Gaussian beam through optical elements, like free-space and mirrors, we can define the complex beam parameter, q, which contains all Gaussian beam properties. The definition of q and its relation to the beam waist are given by Eq. 2.34.

$$\frac{1}{q} = \frac{1}{R} - i\frac{\lambda}{n\pi\omega^2} \qquad \xrightarrow{R\to\infty} \qquad \omega_0 = \sqrt{\frac{\lambda}{n\pi}Im(q)} \tag{2.34}$$

In paraxial ray optics, linear transformations of the ray vector - defined by the ray height y and slope y' - are used to describe its propagation through optical elements, which are represented

by $ABCD$ matrices. We can utilize the connection between the ray matrix formalism and the q-transformations, shown in Eq. 2.35, to derive the cavity mode parameters:

$$q_1 = \frac{Aq_0 + B}{Cq_0 + D} \longleftrightarrow \begin{pmatrix} y_1 \\ y_1' \end{pmatrix} = \begin{pmatrix} A & B \\ C & D \end{pmatrix} \begin{pmatrix} y_0 \\ y_0' \end{pmatrix}, \tag{2.35}$$

where indices $0, 1$ indicate the incident and transformed ray vector/q parameter.

Any optical cavity, regardless of its geometry or the number of its constituent optical elements, can be represented by a composite matrix M_C, obtained as the product of the individual $ABCD$ matrices characterizing each optical element within the cavity. The resonance condition, the requirement that the mode replicates itself after one cavity round trip, can be expressed using the q parameter formalism as follows:

$$q = \frac{Aq + B}{Cq + D}, \qquad M_C = \begin{pmatrix} A & B \\ C & D \end{pmatrix}, \tag{2.36}$$

$$\frac{1}{q} = \frac{D - A}{2B} \pm \frac{1}{2B}\sqrt{(A - D)^2 + 4BC}. \tag{2.37}$$

By solving Eq. 2.36 for $1/q$ and comparing the result, Eq. 2.37, with Eq. 2.34, we can associate the elements of the cavity's composite matrix M_C, with the characteristic parameters of the complex beam parameter. Furthermore, we can derive the stability criterion for the cavity geometry. The solution of Eq. 2.37 is only physical when the term within the square root is negative valued. With $\det M_C = 1$, we can define the stability criterion for an optical cavity:

$$|A + D| \leq 2. \tag{2.38}$$

In general, the composite matrix of a propagating-wave cavity in a triangular configuration is

$$M_C^{s,t} = \begin{pmatrix} 1 & 0 \\ -\frac{2}{R_1^{s,t}} & 1 \end{pmatrix} \begin{pmatrix} 1 & l_1 \\ 0 & 1 \end{pmatrix} \begin{pmatrix} 1 & 0 \\ -\frac{2}{R_2^{s,t}} & 1 \end{pmatrix} \begin{pmatrix} 1 & l_2 \\ 0 & 1 \end{pmatrix} \begin{pmatrix} 1 & 0 \\ -\frac{2}{R_3^{s,t}} & 1 \end{pmatrix} \begin{pmatrix} 1 & l_3 \\ 0 & 1 \end{pmatrix}, \tag{2.39}$$

the product of the six ABCD matrices describing the propagation of the cavity mode between the mirrors and the mirror reflections. R_i indicates the mirror's radius of curvature, and l_i indicates the distance between the mirrors. Reflections by a tilted and curved surface induce astigmatism. Consequently, the cavity is defined by two distinct matrices that describe the mode properties in the sagittal (s) and tangential (t) planes. The tangential plane is parallel to the plane of incidence, which contains the propagation axis and the surface normal. Its normal plane that contains the propagation axis is the sagittal plane. For a tilted mirror at angle (θ_{in}), the effective radii of curvature in the sagittal and tangential planes are given by

$$R^s = \frac{R_i}{\cos\theta_{\text{in}}} \quad \text{and} \quad R^t = R_i \cos\theta_{\text{in}}. \tag{2.40}$$

In the experiment, the cavity has an equilateral, equiangular (AOI $= 30°$), triangular geometry and will consist of two flat and one convex mirror. The ray matrices that describe the cavity modes in the sagittal and the tangential planes are the following:

$$M_C^s = \begin{pmatrix} 1 & L \\ 1 - \frac{2\cos(\pi/6)}{R} & -\frac{2\cos(\pi/6)}{R}L \end{pmatrix} \qquad M_C^t = \begin{pmatrix} 1 & L \\ 1 - \frac{2}{R\cos(\pi/6)} & -\frac{2}{R\cos(\pi/6)}L \end{pmatrix}. \tag{2.41}$$

To conclude the discussion of the geometrical properties of the propagating-wave cavity, we introduce Hermite-Gaussian modes. So far, we have not considered that the paraxial wave equation has solutions with a more complex radial profile compared to the Gaussian beam. A complete set of solutions in Cartesian coordinates, which are often observed in experiments, are Hermite-Gaussian modes. We can incorporate the previously discussed astigmatism of a cavity and formulate the expression for the Hermite-Gaussian beam:

$$E_{m,n}(x,y,z) = E_0\sqrt{\frac{\omega_{x0}\omega_{y0}}{\omega_x(z)\omega_y(z)}}H_m\Big(\frac{\sqrt{2}x}{\omega_x(z)}\Big)H_n\Big(\frac{\sqrt{2}y}{\omega_y(z)}\Big)\exp\Big(-\frac{x^2}{\omega_x^2(z)}-\frac{y^2}{\omega_y^2(z)}\Big) \times \exp\Big(-i\Big[kz+k\Big(\frac{x^2}{2R_x(z)}+\frac{y^2}{2R_y(z)}\Big)-\phi_G^{m,n}\Big]\Big). \tag{2.42}$$

The integer indices m and n denote the order of Hermite polynomials, $H_{m,n}$, which describe the beam profile in the sagittal (x) and tangential (y) planes, respectively. Note that the Gouy phase, $\phi_G^{m,n}$, becomes linearly dependent on the mode number (Eq. 2.43). As a result, the resonance condition for the cavity becomes dependent on the transverse mode order, leading to a non-degenerate eigenfrequency spectrum.

$$\phi_G^{m,n} = \Big(\frac{1}{2}+m\Big)\tan^{-1}\Big(\frac{z}{z_{xR}}\Big)+\Big(\frac{1}{2}+n\Big)\tan^{-1}\Big(\frac{z}{z_{yR}}\Big). \tag{2.43}$$

Eigenmode Spectrum

Above, we derived the geometrical properties of a cavity mode by applying the condition that the cavity field has to replicate itself after a round trip (Eq. 2.36). To derive the eigenfrequency spectrum of a propagating-wave cavity, we use the resonance condition for phase, that the round-trip phase has to be an integer multiple of 2π:

$$\delta_{RT} = 2\pi q = \frac{\omega}{c}L - \phi_G^{m,n} - \varphi_m - r\varphi_M^{s,p} - \varphi_h. \tag{2.44}$$

Here, q is the integer longitudinal mode number, and the first two terms on the left correspond to the phase term in Eq. 2.31, where ω is the resonance frequency, c is the speed of light, and L is the cavity length. The phase shift φ_m originates from the antisymmetry of odd-order sagittal Hermite-Gaussian modes upon reflection [CLM+16]. For an odd number of reflections, odd-numbered sagittal modes acquire a phase shift of $\varphi_m = \pi$. In addition, each of the reflections by the r-numbered cavity mirrors induces a phase shift of ideally $\varphi_M = \pi$. However, the birefringence of real mirrors leads to a polarization-dependent phase shift $\varphi_M^{s,p} \approx \pi$, where s and p are the two polarization modes of the cavity, and lifts the polarization degeneracy of the cavity mode spectrum. Furthermore, reflections cause a handedness flip of the polarization that can be described using the Jones Matrix formalism [PM15]. For an odd number of reflections, an additional relative phase, $\varphi_h = \pi$, is acquired between the polarization-eigenmodes of the cavity.

Assuming an equilateral, triangular cavity geometry (Eq. 2.41), we can solve Eq. 2.44 for the

resonant frequencies $\omega^{s,p}_{q,n,m}$, and get

$$\omega^{s,p}_{q,n,m} = \frac{c}{L}\Bigg[2\pi q + \left(m+\frac{1}{2}\right)\cos^{-1}\left(1-\frac{L}{R\cos(\pi/6)}\right) + \left(n+\frac{1}{2}\right)\cos^{-1}\left(1-\frac{L\cos(\pi/6)}{R}\right) + 3\varphi^{s,p}_{M} + \varphi_m + \varphi_h\Bigg]. \tag{2.45}$$

Note that the Gouy phase term is computed by solving Eq. 2.37 for the matrices in Eq. 2.41 and rewriting using the trigonometric relation, $\tan^{-1}(x) = \cos^{-1}(1/\sqrt{(1+x^2)})$. In addition to the resonance frequencies, we obtain the spectral separation of neighboring longitudinal modes, the free spectral range of the cavity:

$$\mathrm{FSR} = \frac{c}{L} \tag{2.46}$$

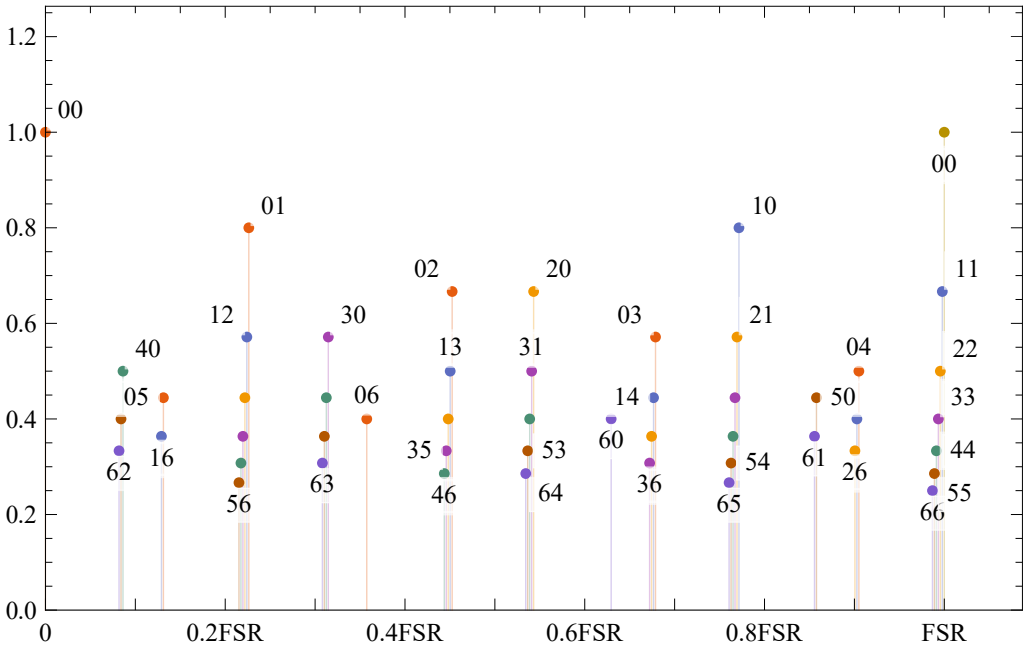

Figure 2.4: Transverse mode spectrum of a propagating-wave cavity with unilateral triangular geometry over a FSR. Indices (m, n) indicate the sagittal and tangential order of the plotted modes.

In Fig. 2.4, we plot the resonant frequencies (Eq. 2.44) for a fixed polarization up to a mode number $m = n = 6$ over a spectral span of one FSR. The cavity parameter used for the simulation corresponds to the configuration of our experimental setup ($L = 9.83\,\mathrm{cm}$, $R = 10\,\mathrm{cm}$). Bundles of modes, which are defined by $\delta_{mn} = m - n$, are symmetrically distributed around the 00-mode, which has the profile of the Gaussian beam. Even though the mode bundles appear nearly degenerate, this degeneracy is lifted by the mode-order-dependent Gouy phase.

Field & Intensity Relations

In the following, we derive expressions for the fields of a triangular, propagating-wave cavity. The schematic diagram (Fig. 2.5) shows the relations between the intra-cavity field E_C, the

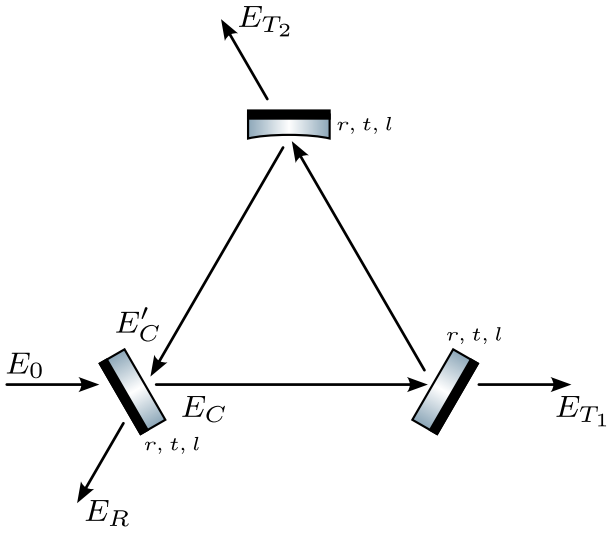

Figure 2.5: Diagram of a triangular cavity and its related fields

reflected field E_R, and the transmitted fields $E_{T_{1,2}}$ for an incident field E_0. We assume that the mirror properties are identical, where r and t are the real-valued reflection and transmission amplitudes, which satisfy $r^2 + t^2 = R + T = 1$ for ideal mirrors. To account for losses, we introduce a loss amplitude l and write the general relation $r^2 + t^2 + l^2 = 1$ The steady-state field amplitudes are then given by

$$E'_C = r^2 e^{-ikL} E_C, \tag{2.47}$$
$$E_C = t\, E_0 + r\, E'_C, \tag{2.48}$$
$$E_R = r\, E_0 - t\, E'_C, \tag{2.49}$$
$$E_{T_1} = t\, e^{ik\frac{L}{3}} E_C, \tag{2.50}$$
$$E_{T_2} = tr\, e^{ik\frac{2L}{3}} E_C, \tag{2.51}$$

where the intra-cavity field amplitudes E_C and E'_C are evaluated at the lower left mirror. We can solve for E_C using Eq. 2.47 and Eq. 2.48, assuming that the fields are close to resonance, where $k = \frac{1}{c}(\omega_0 + \delta\omega)$ and $\exp(-ikL) \approx (1 + i\frac{L}{c}\delta\omega)$, and get

$$E_C = \frac{t}{\frac{1}{2}(3t^2+3l^2)\left(1 - i\frac{1}{\frac{1}{2}(3t^2+3l^2)}\frac{L}{c}\delta\omega\right)} E_0 = \sqrt{\frac{c}{L}}\frac{2\sqrt{\kappa_m}}{\kappa}\frac{1}{1 - i\frac{\delta\omega}{\kappa/2}} E_0. \tag{2.52}$$

Note that for small amplitudes t and l, and integer exponents i, we can approximate $1 - r^i = \frac{i}{2}(t^2 + l^2)$ and we can assume near-unity reflection amplitude ($r \approx 1$). In addition, we define the photon decay rates through a mirror $\kappa_m = \frac{c}{L}t^2$ and all loss channels $\kappa_L = 3\frac{c}{L}l^2$. Their sum gives rise to the full linewidth of the cavity, $\kappa = 3\kappa_m + \kappa_L$.

To compute the remaining field amplitudes, we insert Eq. 2.52 into Eqn. 2.49-2.51, and get

the reflected and transmitted fields:

$$E_R = \left[1 - \frac{2\kappa_m}{\kappa}\frac{1}{1 - i\frac{\delta\omega}{\kappa/2}}\right]E_0 \tag{2.53}$$

$$E_{T_1} = \frac{2\kappa_m}{\kappa}\frac{e^{ik\frac{L}{3}}}{1 - i\frac{\delta\omega}{\kappa/2}}E_0 \tag{2.54}$$

$$E_{T_2} = \frac{2\kappa_m}{\kappa}\frac{e^{ik\frac{2L}{3}}}{1 - i\frac{\delta\omega}{\kappa/2}}E_0 \tag{2.55}$$

To conclude, we compute the quantities that can be observed in the experiment, namely the field intensities:

$$I_C = |E_C|^2 = \frac{c}{L}\frac{4\kappa_m}{\kappa^2}\frac{1}{1 + (\frac{\delta\omega}{\kappa/2})^2}E_0^2 = F\frac{4\kappa_m}{\kappa}\frac{1}{1 + (\frac{\delta\omega}{\kappa/2})^2}I_0 \tag{2.56}$$

$$I_R = |E_R|^2 = \left[1 - \frac{4\kappa_m}{\kappa}\frac{1}{1 + (\frac{\delta\omega}{\kappa/2})^2} + \left(\frac{2\kappa_m}{\kappa}\right)^2\frac{1}{1 + (\frac{\delta\omega}{\kappa/2})^2}\right]E_0^2 \tag{2.57}$$

$$I_{T_1} = I_{T_2} = |E_{T_1}|^2 = \left(\frac{2\kappa_m}{\kappa}\right)^2\frac{1}{1 + (\frac{\delta\omega}{\kappa/2})^2}E_0^2 \tag{2.58}$$

In the absence of any loss, where $\kappa_L = 0$ and $\kappa = 3\kappa_m$, the input power is conserved, $I_R + I_{T_1} + I_{T_2} = I_0$. Furthermore, we aim to derive expressions for the resonant, $\delta\omega = 0$, intra-cavity power in terms of the reflected and transmitted intensities. We define the cavity Finesse, $F = \frac{FSR}{\kappa}$, and substitute Eqn. 2.57, 2.58 into Eq. 2.56 to get

$$I_C = F\frac{4\kappa_m}{\kappa}I_0 = F\frac{\kappa}{\kappa_m}I_{T_1} = F\frac{\kappa}{\kappa - \kappa_m}(I_0 - I_R). \tag{2.59}$$

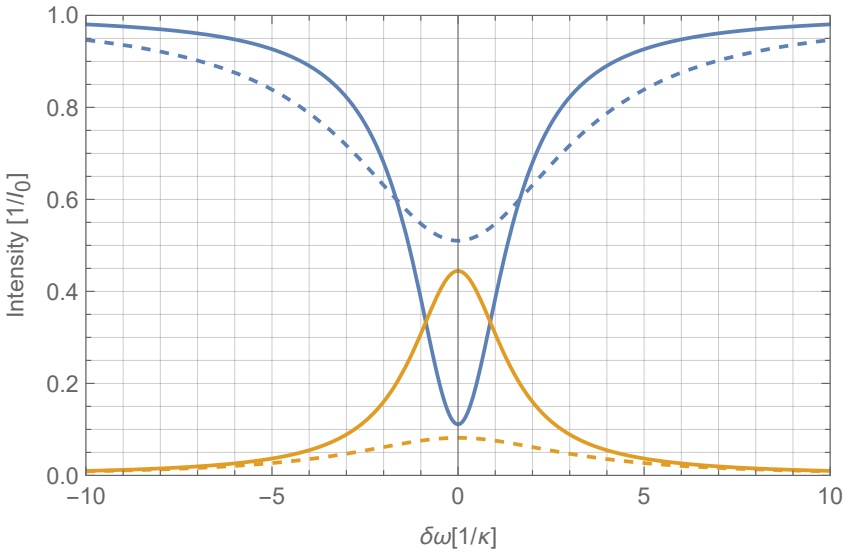

Figure 2.6: Transmission and reflection of an ideal and lossy cavity. The blue and orange plots show, respectively, the reflected and transmitted (T_1) intensities of an ideal triangular cavity. Dashed lines indicate the reflection and transmission of a lossy cavity with $\kappa_L = 4\kappa_m$.

Figure 2.6 shows the transmissions and reflections of an ideal cavity without losses ($\kappa_L = 0$) and a cavity with present losses ($\kappa_L = 4\kappa_m$). For an adequate determination of the intra-cavity power, the cavity loss rate has to be evaluated by measurements of the cavity transmission and reflection.

2.3.2 Tavis-Cummings Model

The interaction of an ensemble of two-level systems with a single-mode optical cavity is well described by the Tavis-Cummings Model [TC68, TC69]. It extends the collective-spin model introduced in Sec. 2.2.1 to describe the ensembles coupling to a quantized electromagnetic field mode in the rotating-wave approximation [JC63]. The Hamiltonian of the coupled atom-cavity system is given by

$$\hat{H}_{TC} = \hbar\omega_a \hat{J}_z + \hbar\omega_c \hat{a}^\dagger \hat{a} - \hbar g_0 (\hat{J}_- \hat{a}^\dagger + \hat{J}_+ \hat{a}). \tag{2.60}$$

The first term, identical to Eq.2.14, represents the internal energy of the ensemble of two-level systems with transition frequency ω_a. The second term describes the energy stored in the cavity with resonance frequency ω_c and photon number $\langle a^\dagger a \rangle$. The third term, the interaction term, captures the exchange of excitation between the ensemble and the cavity, with $\hat{J}_\pm$ the collective raising and lowering operators defined in Eq. 2.17, and $\hat{a}, \hat{a}^\dagger$ the annihilation and creation operators of the quantum harmonic oscillator depicting the cavity mode.

The coupling strength g_0, also known as single-photon Rabi frequency is defined by

$$g_0 = \frac{\mu_a}{\hbar}\sqrt{\frac{\hbar\omega_c}{2\epsilon_0 V_m}}, \tag{2.61}$$

where μ_a is the transition dipole matrix element, ω_c the angular resonance frequency of the cavity mode, ϵ_0 the vacuum permittivity and V_m the cavity mode volume, defined as

$$V_m = \frac{\int \epsilon_0 |E(r)|^2 dV}{\max(\epsilon_0 |E(r)|^2)}. \tag{2.62}$$

The cavity mode volume quantifies the spatial distribution of the electric field energy density, $\epsilon_0|E(r)|^2$, within the mode. A smaller mode volume corresponds to a more tightly confined electric field, which enhances the atom–cavity coupling strength but at the same time restricts the maximum size of the atomic ensemble that can be accommodated. Consequently, the choice of cavity geometry and mirror radii, which determine the mode volume, is a central aspect of the experimental design. Especially, homogeneous coupling of the atoms to the cavity is crucial for the intended spin-squeezing experiment [HEKK16]. The propagating wave character of the cavity employed in this experiment leads to a spatially uniform field amplitude in the vicinity of the mode waist, thereby ensuring homogeneous coupling of atoms to the cavity.

Another useful figure of merit in this context is the single-atom cooperativity, defined as

$$C = \frac{4g_0^2}{\kappa\Gamma}, \tag{2.63}$$

which compares g_0 to the dissipative coupling of the atoms to the environment, characterized by the cavity linewidth κ and the natural atomic linewidth Γ.

2.3.3 The Dispersive Hamiltonian

Next, we want to describe the dynamics of the coupled system for large atom-cavity detunings $\Delta = \omega_c - \omega_a$. In this dispersive regime, defined by

$$|\Delta| \gg \kappa, \Gamma, \sqrt{N} g_0, \tag{2.64}$$

and low intra-cavity photon number

$$\langle a^\dagger a\rangle \ll (\Delta/g_0)^2, \tag{2.65}$$

the excitation exchange between atoms and the cavity is suppressed, and the interaction term in Eq. 2.60, $\hat{H}_I = -\hbar g_0(\hat{J}_-\hat{a}^\dagger + \hat{J}_+\hat{a})$ can be perturbatively eliminated. To do so, we apply a time-independent unitary transformation of the form $\hat{U} = \exp(i\lambda\hat{S})$, where λ is a small perturbation and $\hat{S}$ is a Hermitian generator with only off-diagonal elements. The series expansion of the transformation can be written as

$$\hat{H}_{\text{disp}} = e^{i\lambda\hat{S}}\hat{H}_{TC}e^{-i\lambda\hat{S}} \tag{2.66}$$

$$= e^{i\lambda\hat{S}}\Big(\hat{H}_0 + \hat{H}_I\Big)e^{-i\lambda\hat{S}} \tag{2.67}$$

$$= \hat{H}_0 + \hat{H}_I + \lambda\Big([i\hat{S},\hat{H}_0] + [i\hat{S},\hat{H}_I]\Big) + \frac{\lambda^2}{2}\Big[i\hat{S},\Big([i\hat{S},\hat{H}_0] + [i\hat{S},\hat{H}_I]\Big)\Big] + \mathcal{O}(\lambda^3), \tag{2.68}$$

with the free Hamiltonian $\hat{H}_0 = \hbar\omega_a\hat{J}_z + \hbar\omega_c\hat{a}^\dagger\hat{a}$.

We choose an ansatz for $\lambda\hat{S}$ that eliminates the interaction term by fulfilling the relation

$$[i\lambda\hat{S},\hat{H}_0] = -\hat{H}_I, \tag{2.69}$$

and find the operator

$$e^{-i\lambda\hat{S}} = \exp\Big(\frac{g_0}{\Delta}(\hat{J}_+\hat{a} - \hat{J}_-\hat{a}^\dagger)\Big), \tag{2.70}$$

with $\lambda = g_0/\Delta$.

Keeping only terms of first order in $1/\Delta$, the dispersive Hamiltonian becomes

$$\hat{H}_{disp} = \hbar\omega_a\hat{J}_z + \hbar\frac{2g_0^2}{\Delta}\hat{J}_z\hat{a}^\dagger\hat{a} + \hbar\omega_c\hat{a}^\dagger\hat{a} + \frac{g_0^2}{\Delta}(\hat{\mathbf{J}}^2 - \hat{J}_z^2 + \hat{J}_z). \tag{2.71}$$

In analogy to the Tavis-Cumming model (Eq.2.60), the first and third terms describe the two-level pseudo-spin system and the cavity mode, respectively. The second term represents the dispersive interaction, which can be interpreted in two complementary ways. When grouped with the cavity term, it appears as a cavity resonance shift proportional to the atomic population $\hat{J}_z$. The collective atomic state modifies the effective optical refractive index, enabling the measurement of the atomic state by probing the cavity resonance. Alternatively, when grouped with the atomic term, the dispersive interaction appears as an AC-Stark shift of the atomic transition frequency induced by the number of intra-cavity photons $\hat{a}^\dagger\hat{a}$. In addition, the last term corresponds to a collective Lamb shift [HMY+24], the emission and reabsorption of virtual cavity photons by the collective state.

So far, we have discussed the dispersive interaction in the framework of a two-level atom coupled to a cavity mode. To describe the dynamics present in our experimental setup, we consider an ensemble of N atoms with a three-level structure consisting of two ground states $|\downarrow\rangle$ and $|\uparrow\rangle$, and an optically excited state $|e\rangle$. An optical cavity with frequency ω_c dispersively couples the two ground states to an excited state $|e\rangle$. We can treat the system as two separate two-level systems coupled to the same cavity mode that are connected by the total number of atoms $N = N_\downarrow + N_\uparrow$. For simplicity, we assume an equal coupling strength g_0 between each of the sub-systems and the cavity, and that the two ground states experience dispersive shifts

of equal magnitude but opposite sign, resulting in an absolute value of the cavity detuning $\Delta = \omega_{ab}/2$, where $\hbar\omega_{ab}$ is the energy splitting between the ground states. The three-level scheme and its coupling regime to the cavity mode is illustrated on the left of Fig.2.7.

When the population of the excited state $|e\rangle$ is negligible, the three-level system reduces to an effective two-level, pseudo-spin system and the collective Lamb shift term can be neglected since $\hat{\mathbf{J}}^2 \approx \hat{J}_z^2$ and $\frac{g_0^2}{\Delta} \ll \omega_{ab}$. With the elimination of $|e\rangle$, $\hat{J}_z$ can be redefined as the population inversion $\hat{J}_z = \frac{N_\uparrow - N_\downarrow}{2}$, and the effective dispersive Hamiltonian becomes

$$\hat{H}_{\text{eff}} = \hbar\omega_{ab}\hat{J}_z + \hbar\frac{2g_0^2}{\Delta}\hat{J}_z\hat{a}^\dagger\hat{a} + \hbar\omega_c\hat{a}^\dagger\hat{a}. \tag{2.72}$$

The right of Fig.2.7 illustrates the dispersive shift of the cavity resonance frequency. Depending on the polarization of the atomic population, the cavity resonance experiences a positive or negative shift. A homodyne detection of the cavity frequency enables the non-destructive measurement of the atomic population.

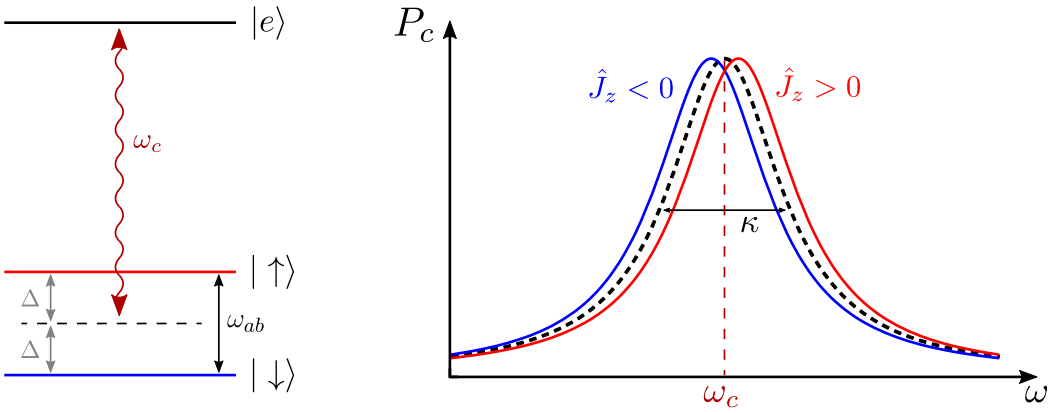

Figure 2.7: *Left:* Level scheme of the experimental setup. Two ground states $|\downarrow\rangle, |\uparrow\rangle$ are dispersively coupled to an excited state $|e\rangle$ via an optical cavity, with resonance frequency ω_c. The detuning between the cavity and the two atomic transitions is homogeneous $|\Delta = \omega_{ab}/2|$, but differs in sign. *Right:* Illustration of the dispersive cavity shift. The dashed black line illustrates the empty cavity with resonance frequency ω_c and linewidth κ. Dispersive coupling, depending on the polarization of the atomic population, causes positive ($\hat{J}_z > 0$) or negative ($\hat{J}_z < 0$) frequency shifts .

The described three-level system corresponds to the level structure of ^{87}Rb, the atomic species that will be employed in the experiment. ^{87}Rb possesses two hyperfine ground states $|5^2S_{1/2}, F = 1\rangle$ and $|5^2S_{1/2}, F = 2\rangle$, separated by $\omega_{ab} = 2\pi\times 6.834\,\text{GHz}$. The transition to the first optical excited state $5^2P_{3/2}$ corresponds to a wavelength of $780.241\,\text{nm}$ (D_2-line). The hyperfine structure of the excited state requires careful consideration when setting the cavity detuning, in order to ensure a homogeneous coupling of the ensemble. In particular, the detunings of all the hyperfine transitions and their relative transition strengths (Eq. 2.61) must be taken into account and fulfill the relation

$$\left|\sum_{F'=0,1,2}\frac{S_{1F'}}{\omega_c - \omega_{1F'}}\right| = \left|\sum_{F'=1,2,3}\frac{S_{2F'}}{\omega_c - \omega_{2F'}}\right|, \tag{2.73}$$

where $S_{FF'}$ are the relative hyperfine transition strengths [Ste10] and $\omega_{FF'}$ are the hyperfine transition frequencies.

2.3.4 Cavity-Mediated Squeezing

There are two methods to generate spin-squeezing governed by the dispersive interaction of the atomic ensemble with an optical cavity. Either the cavity is driven with a detuned tone (ω_{oat}) to drive one-axis twisting interaction, or the system is probed on resonance (ω_c) to project the atomic states onto a squeezed state. The latter method is a quantum non-demolition measurement, since the measured atomic population ($\hat{J}_z$) is a constant of motion. For this experiment, in analogy to [HEKK16, HKEK16], it is planned to combine both methods in order to enhance squeezing. Even though the demonstration of squeezed state preparation is beyond the scope of this thesis, the following discussion of cavity-mediated squeezing should motivate the chosen cavity parameters and should give a framework for the future implementation of squeezing in the experiment.

One-Axis Twisting Interaction

Kitagawa and Ueda showed in [KU93] that the unitary evolution of a CSS under nonlinear interaction can generate spin-squeezed states. The one-axis twisting (OAT) interaction is described by the unitary transformation in the form of

$$\hat{U}(t) = e^{-i\chi \hat{J}_z^2 t}, \tag{2.74}$$

which, in the Bloch sphere picture, corresponds to a rotation about the J_z-axis with a magnitude depending on the evolution time t, the interaction strength χ, and the J_z projection of the rotated state. For a CSS aligned along the J_x-axis, OAT leads to shearing of the spin distribution. The components in the northern hemisphere of the Bloch sphere experience a positive rotation, while components in the southern hemisphere experience a negative rotation, with the magnitude scaling with the displacement from the equator. Fig.2.8 illustrates an example for an SSS generated by OAT interaction. The effective shearing of the spin projection variances leads to their redistribution and alignment of the squeezed and anti-squeezed variances along an axis tilted by an angle δ with respect to the equatorial plane.

The exact derivation for the squeezed and anti-squeezed variances can be found in [KU93]. In the regime relevant to the experiment, where the collective spin is large, $J \gg 1$, the interaction is weak, $\chi t \ll 1$, and $|J\chi t| > 1$, the squeezed and anti-squeezed variances can be approximated as

$$\Delta J_s^2 = \frac{1}{8\chi^2 t^2}\frac{1}{J} + \frac{1}{3}\chi^4 t^4 J^3, \tag{2.75}$$

and

$$\Delta J_a^2 = 2J^3\chi^2 t^2. \tag{2.76}$$

Furthermore, the tilt angle is given by

$$\delta = \frac{1}{2}\arctan\left(\frac{1}{J\chi t}\right), \tag{2.77}$$

and the mean spin projection and its variance are

$$|\langle J_x \rangle| = J(1 - J\chi^2 t^2), \tag{2.78}$$

$$\Delta J_x^2 = 2J\chi^2 t^2. \tag{2.79}$$

Eq. 2.75 shows that the squeezed variance depends on two competing terms. The first term describes the shearing-induced reduction of the variance, while the second term accounts for

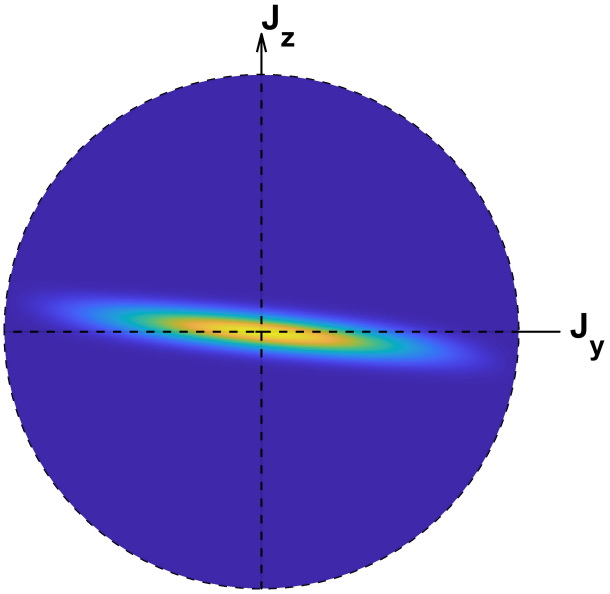

Figure 2.8: Front view of a SSS with N=250 atoms generated by OAT interaction with strength $\chi t = 0.02$. For this particular squeezing strength, the squeezed and anti-squeezed spin projection variances are oriented along an axis tilted by $\delta \approx 11^\circ$ with respect to the equatorial plane.

the Bloch sphere curvature, which becomes dominant at increasing interaction strength and duration. Since the Bloch sphere curvature scales inversely with the length of the collective spin J, the optimum product of the interaction strength and duration is $\chi t = \frac{3}{8} J^{-2/3}$, leading to the minimum variance achievable by OAT:

$$\min \Delta J_s^2 = \frac{1}{2}\left(\frac{J}{3}\right)^{\frac{1}{3}}. \tag{2.80}$$

Cavity-Mediated OAT

The dispersive interaction of an atomic ensemble with a cavity (introduced in Sec. 2.3.3) can be exploited to generate OAT dynamics. As demonstrated in [LSSV10, SSLV10b, SSLV10a, SSLV11], a SSS can be prepared via a cavity feedback mechanism induced by an off-resonant cavity probe with frequency (ω_{oat}).

The feedback mechanism can be described phenomenologically as follows. We consider the same coupling regime as in Sec. 2.3.3 with a CSS aligned along the J_x-axis. When the system is probed with an off-resonant cavity probe ($\delta_c = \omega_c - \omega_{\mathsf{oat}}$), fluctuations in the spin projection ΔJ_z induce fluctuations in the effective cavity resonance. These frequency shifts, in turn, are mapped into photon-number fluctuations that, as illustrated in Fig. 2.9, feed back into the dispersive interaction and lead to a J_z-dependent AC-Stark shift.

For a more quantitative description, we calculate the intra-cavity photon number as a function of J_z. Applying input-output theory [GC85, WM25], we write the Heisenberg-Langevin equation of motion for the cavity annihilation operator in the rotating frame of the driving field [SS11b, Eng16]:

$$\dot{a} = \left(-i(\delta_c + \Omega J_z) - \frac{\kappa}{2}\right) a + \beta(t), \tag{2.81}$$

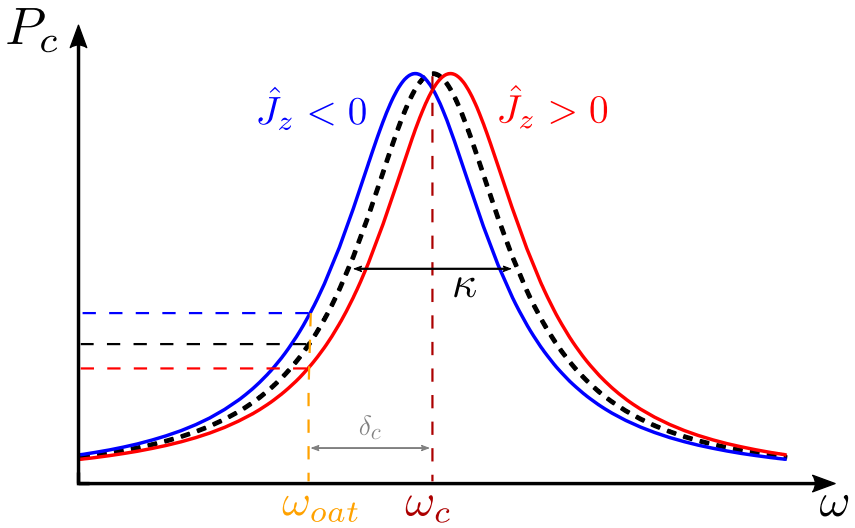

Figure 2.9: Illustration of the OAT mechanism in a dispersively coupled collective spin-cavity system. Fluctuations in J_z lead to resonance fluctuations, which in turn map into fluctuations of the intra-cavity photon number (P_c) through the off-resonant probe at frequency ω_{oat}.

where $\beta(t)$ is the amplitude of the driving field and $\Omega = \frac{2g_0^2}{\Delta}$ from Eq.2.72 is the cavity shift per spin flip. The solution for the steady state of Eq. 2.81 is given by

$$a(J_z, t) = \frac{\beta(t)}{i(\delta_c + \Omega J_z) + \frac{\kappa}{2}}. \tag{2.82}$$

In the regime of a slowly varying driving field [Eng16], and assuming that the spin-fluctuation induced cavity shift is small $\Omega\sqrt{J/2} \ll \kappa$, we can Taylor expand $a(J_z, t)$ around $J_z = 0$ and obtain

$$a(J_z, t) = \frac{\beta(t)}{i\delta_c + \kappa/2}\left(1 + \frac{\Omega}{i\delta_c + \kappa/2} J_z + \mathcal{O}(J_z^2)\right). \tag{2.83}$$

To first order of J_z, the intra-cavity photon number becomes

$$\hat{a}^\dagger \hat{a} = |\alpha(t)|^2 + |\alpha(t)|^2\left(\frac{2\delta_c \Omega}{\delta_c^2 + (\kappa/2)^2}\hat{J}_z + \mathcal{O}(\hat{J}_z^2)\right), \tag{2.84}$$

where $|\alpha(t)|^2 = \frac{|\beta(t)|^2}{\delta_c^2 + (\kappa/2)^2}$ is the steady-state intra-cavity photon number for the empty cavity. Substituting Eq. 2.84 into the interaction term of Eq. 2.72 and discarding the term linear in J_z, which corresponds to a linear rotation, we obtain the cavity-mediated OAT Hamiltonian

$$\hat{H}_{OAT} \approx \hbar \frac{2\delta_c \Omega^2 |\alpha(t)|^2}{\delta_c^2 + (\kappa/2)^2} \hat{J}_z^2. \tag{2.85}$$

By comparison with the squeezing operator in Eg. 2.74, we can identify the OAT interaction strength

$$\chi = \frac{2\delta_c \Omega^2 |\alpha(t)|^2}{\delta_c^2 + (\kappa/2)^2}. \tag{2.86}$$

Optimum OAT Interaction

The maximum achievable squeezing via cavity-mediated OAT interaction is fundamentally limited by two decoherence processes. The first arises from the photon shot noise in the

intra-cavity photon number $|\alpha(t)|^2$, induced by the coherent input and cavity losses. This noise leads to fluctuations in the light shift and consequently to uncertainty in the spin precession angle. The second decoherence process is Raman scattering, which induces spin-flips and thus causes a random walk in J_z. A detailed derivation of the decoherence processes induced reduction of squeezing is given in [SS11b]. The resulting normalized squeezed spin projection variance has the form

$$\frac{\Delta J_s^2}{\Delta J_{css}^2} \approx \frac{\kappa^2}{2J|\alpha|^2\Omega} + \frac{2|\alpha|^2\Omega}{\kappa\Delta} \tag{2.87}$$

$$\approx \frac{1}{2JCr} + \frac{4r}{3}, \tag{2.88}$$

where C is the single-atom cooperativity (Eq. 2.63) and the intra-cavity photon scattering probability is

$$r = \frac{\Gamma}{\kappa}\frac{g_0^2}{\Delta^2}|\alpha|^2 = \frac{\Gamma^2}{\Delta^2}\frac{C}{4}|\alpha|^2. \tag{2.89}$$

The optimum photon scattering probability for maximal squeezing becomes:

$$r_{opt} = \sqrt{\frac{3}{8JC}}. \tag{2.90}$$

Cavity-mediated OAT interaction is not limited to the dispersive atom-cavity coupling regime. In [BKPP+19, CGL+22, LCS+23], squeezing was demonstrated for a system where one of the ground states was resonantly coupled to a cavity. The OAT interaction was then generated by an off-resonant drive of the vacuum-Rabi-split cavity mode. Beyond the preparation of a squeezed state as input for an interferometer sequence, OAT-interaction can also be utilized at the end of the sequence to magnify the acquired relative phase of the state, as shown in [HKEK16, CPPA+22].

Quantum Non-Demolition Measurement (QND)

The second method to generate spin-squeezed states that we can implement in our experiment is a quantum non-demolition measurement of the atomic population $\hat{J}_z$. QND measurements are measurements of observables that obey the back action evading criterion [BVT80, AMW88], meaning that the observables commute with the system's time evolution. To give a more intuitive picture, a QND measurement projects the system onto an eigenstate of the observable, and determines the time evolution of the observable, while pushing the measurement back action onto the observable's conjugate.

For the dispersively coupled atomic ensemble of our experiment, the atomic population $\hat{J}_z$ is such a continuous QND observable, since it is a constant of motion ($\frac{d}{dt}\hat{J}_z = 0$). The interaction term in Eq. 2.72 couples $\hat{J}_z$ to the intra-cavity photon number, which is a measure that we can infer in experiment by a homodyne detection of the reflected or transmitted probe (Sec. 3.6). A weak input field probes the system resonantly at frequency ω_c. With an atom-induced cavity shift given by

$$\delta_a = \frac{2g_0^2}{\Delta}J_z, \tag{2.91}$$

we can calculate the phase shift of the reflected and transmitted light (Eq. 2.53 and Eq. 2.54) for small resonance shifts $\delta_a \ll \kappa$:

$$\tan\varphi_r = \frac{\Im(E_R)}{\Re(E_R)} \approx \frac{\frac{\delta_a}{\kappa/2}}{1-\frac{\kappa}{2\kappa_m}}, \tag{2.92}$$

$$\tan\varphi_t = \frac{\Im(E_T)}{\Re(E_T)} \approx \frac{\delta_a}{\kappa/2} - \sqrt{3}. \tag{2.93}$$

The constant term in Eq. 2.93 originates from the cavity geometry, the fixed phase relation of $2\pi/3$ between the input and output mirrors, and can be treated as a global phase. For small atom-induced cavity shifts, the relative phase shift of the transmitted light becomes

$$\varphi = \frac{\delta_a}{\kappa/2} = \frac{C\frac{\Gamma}{\Delta}}{1+C\frac{N}{4}\frac{\Gamma^2}{\Delta^2}} J_z. \tag{2.94}$$

Equation 2.94 shows that a measurement of the transmitted light phase determines J_z with a precision limited by the phase noise of the probe light. Simultaneously, the photon shot noise of the probe induces fluctuations in the intra-cavity photon number, which act back onto the system and increase the quantum noise of J_y, the conjugate of J_z. As a result, a QND measurement prepares a spin-squeezed state, with the degree of squeezing set by the noise of the cavity-resonance measurement and the reduced variance aligned along J_z. Fig. 2.10 illustrates an example of such an SSS prepared via a QND measurement. Cavity-mediated squeezing has been demonstrated with great success [SSLV10b, CBW+14, BCN+14], and, to date, the strongest squeezing reported [HEKK16] has been achieved using this method.

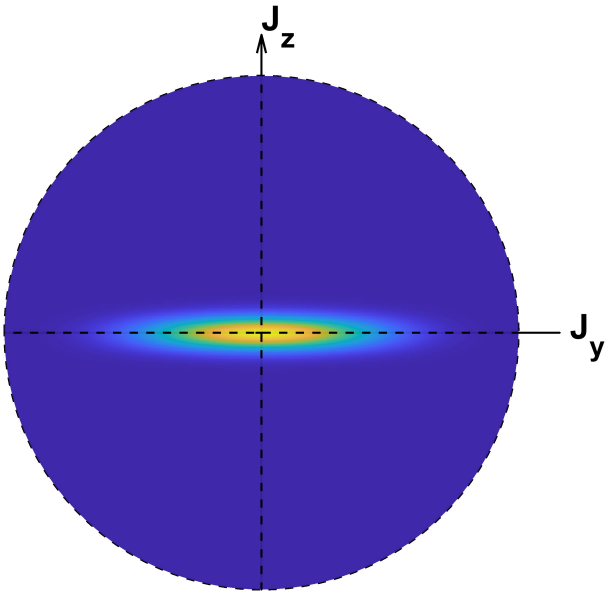

Figure 2.10: Front view of a SSS with N=250 atoms generated by QND measurement.

Optimum QND Measurement

In the following, we elaborate on the limitations of the attainable squeezing. In analogy to the OAT interaction, the optimum squeezing is a trade-off between the interaction strength and the measurement-induced decoherence processes [Eng16]. A stronger measurement is less affected by photon shot noise, but will induce more decoherent spin flips. To evaluate the

optimum measurement parameter, we first consider the atom-photon scattering. Even for a far-detuned system that is weakly driven by a low photon number $\bar{n}_c = \int dt \, \langle a^\dagger a \rangle$, the atoms are in a dressed state with a finite excited state population probability of $p_e = (g_0/\Delta)^2 \bar{n}_c$. Spontaneous decay of these excitations can lead to spin-flips and to information loss to the environment. For N atoms coupled to the cavity, the atom-photon scattering rate can be expressed as

$$\Gamma_s = \Gamma N \frac{g_0^2}{\Delta^2} \bar{n}_c, \tag{2.95}$$

and the atom-scattering broadened linewidth of the cavity becomes

$$\kappa = \kappa_0 (1 + N \frac{C}{4} \frac{\Gamma^2}{\Delta^2}). \tag{2.96}$$

In the subsequent derivation of the spin flip variance and measurement noise, we find it convenient to express the photon number in terms of the AC-Stark shift of the ground states, given by

$$\phi_{\mathsf{AC}} = \frac{2 g_0^2}{\Delta} \bar{n}_c. \tag{2.97}$$

According to [Ste10, CBW+14], the probability of a scattering event leading to a spin flip is $1/6$. These spin flips generate a random walk of J_z that gives rise to a variance that is proportional to the measurement-induced AC-Stark shift:

$$\delta^2_{\mathsf{flip}} = \frac{1}{6} N \frac{\Gamma}{2\Delta} \phi_{\mathsf{AC}}. \tag{2.98}$$

We continue to evaluate the noise induced by the measurement itself. In Eq. 2.94, we derived an expression for the phase shift that we measure to determine J_z. For a coherent probe, the phase noise of the measurement depends on the number of detected photons that carry information about the cavity phase shift. If we assume the detection of one of the two transmission channels, the number of detected photons is

$$n_d = \eta \kappa_m \bar{n}_c = \eta \epsilon \frac{2\Delta}{C\Gamma} \phi_{\mathsf{AC}}, \tag{2.99}$$

where $\epsilon = \frac{\kappa_m}{\kappa}$ is a measure for the cavity efficiency and η is the detection efficiency. The resulting phase noise of the measurement is given by

$$\Delta\varphi = \frac{1}{2\sqrt{n_d}}, \tag{2.100}$$

and the final uncertainty of the spin-projection measurement is

$$\Delta J_{z,\mathsf{meas}} = \frac{\Delta\varphi}{\varphi} J_z = \frac{1}{\sqrt{8\eta\epsilon C \frac{\Gamma}{\Delta}}} \left(1 + C \frac{N\Gamma^2}{4\Delta^2}\right) \frac{1}{\sqrt{\phi_{\mathsf{AC}}}}. \tag{2.101}$$

The resulting measurement variance is inversely proportional to the ac-Stark shift, and, if we consider the complete detection of all transmitted and reflected photons, the measurement variance is reduced by a factor of three:

$$\delta^2_{\mathsf{meas}} = \frac{\Delta J^2_{z,\mathsf{meas}}}{3} = \frac{1}{24\eta\epsilon C \frac{\Gamma}{\Delta}} \left(1 + C \frac{N\Gamma^2}{4\Delta^2}\right)^2 \frac{1}{\phi_{\mathsf{AC}}}. \tag{2.102}$$

To evaluate the optimum strength of the QND measurement to achieve maximum squeezing, we minimize the total measurement-induced noise ($\delta^2_{\text{tot}} = \delta^2_{\text{flip}} + \delta^2_{\text{meas}}$) with respect to ϕ_{AC}. The resulting optimum ac-Stark shift and measurement variance are

$$\phi_{\text{AC,opt}} = \frac{1 + C\frac{N\Gamma^2}{4\Delta^2}}{\frac{\Gamma}{\Delta}\sqrt{2NC\eta\epsilon}}, \tag{2.103}$$

$$\delta^2_{\text{opt}} = \sqrt{\frac{N}{72\eta\epsilon C}}\left(1 + C\frac{N\Gamma^2}{4\Delta^2}\right). \tag{2.104}$$

For a further, in-depth discussion on optimum squeezing for cavity-mediated QND measurements, we refer to [CBW+14].

2.4 The Optical Dipole Trap

Optical dipole traps are a well-established method for confining neutral atoms [GWO00]. When an atom interacts with far-detuned light, meaning that the light frequency is far from any allowed atomic transition, the light induces an electric dipole moment that interacts with the intensity profile of the light field. Depending on the sign of the detuning, whether the light field frequency is below or above the atomic transition, the induced dipole potential can be either attractive or repulsive.

In this experiment, the attractive dipole trap potential to confine an ensemble of ^{87}Rb atoms is created by a cavity mode (Sec. 2.3.1) at a wavelength of $1560\,\mathrm{nm}$. Besides the availability of commercial narrow-linewidth lasers at this wavelength, the main cause for the chosen wavelength is that the optical tones required for squeezing (Sec. 2.3.4) and for driving the Raman beam splitter (Sec. 2.5.1) address the ^{87}Rb D_2 line at $780\,\mathrm{nm}$. These tones are derived from the frequency doubling of the $1560\,\mathrm{nm}$ dipole trap laser, ensuring that all optical tones addressing the cavity remain intrinsically phase coherent and are simultaneously stabilized to the cavity resonance through a single $1560\,\mathrm{nm}$ laser-cavity lock (Sec. 3.3.3).

Due to the propagating-wave nature of the cavity mode, the resulting trap potential resembles the potential of a simple focused Gaussian beam, where the optical power, and hence the trap depth, is enhanced by the cavity build-up. This trap profile results in weak confinement along the cavity axis, a distinct feature of this experiment compared to similar experiments that deploy cavity-mediated dipole traps [BCV$^+$08, NKP$^+$18, XJP$^+$19], which enables the atoms to remain trapped during the complete Mach-Zehnder interferometer sequence.

In the following, the theoretical description of optical dipole traps is given. We will discuss the AC Stark shift of the first optical excited state ($5P_{3/2}$) that hinders direct loading of the atoms from the magneto-optical trap (MOT) into the dipole trap and the compensation of this shift via an auxiliary trap potential, which enables efficient loading of the dipole trap.

2.4.1 The Dipole Potential

The dipole interaction governed AC Stark shift [AS68, Sch72] experienced by an atomic state in an external light field with frequency ω_L is given by

$$\Delta E(r) = -\frac{1}{2}\alpha(\omega_L)E_{\mathrm{rms}}(r)^2 = -\frac{1}{2\epsilon_0 c}\alpha(\omega_L)I(r), \tag{2.105}$$

where $\alpha(\omega_L)$ is the scalar polarizability, $E_{rms}(r)$ is the spatially dependent rms value of the electric field [Ber11]. By substituting $E^2_{\mathrm{rms}} = \frac{I(r)}{\epsilon_0 c}$, the energy shift can be directly expressed in terms of the light intensity. This relation will be used throughout the manuscript. In Eq. 2.105, the tensor AC polarizability [Ste10] does not show up since this term vanishes for the $5S_{1/2}$ ground state.

According to [ASC07], the scalar polarizability of a monovalent atom in a state i is given by the sum

$$\alpha_0^i(\omega_L) = \frac{2}{3(2J_i+1)}\sum_k \frac{\mu_{ik}\omega_{ik}}{\omega_{ik}^2 - \omega_L^2}. \tag{2.106}$$

For the rubidium $5S_{1/2}$ ground state, the total angular momentum is $J = 1/2$, and the sum is taken over all dipole-allowed transitions to states k, characterized by the transition wavelength ω_{ik} and the reduced electric dipole matrix element μ_{ik}. A collection of relevant properties for the transitions in ^{87}Rb, including wavelengths and scalar polarizabilities, can be found in

[SS11a]. To calculate the scalar polarizability of the $5S_{1/2}$ ground state for a light field at $1560\,\mathrm{nm}$, only the transitions to the $5P_{1/2}$ transition (D_1 line) and $5P_{3/2}$ transition (D_2 line) [Ste10] are relevant. Using the corresponding transition wavelengths, linewidths, and dipole matrix elements, we obtain a scalar polarizability of

$$\alpha_0^{5S_{1/2}} = 6.804 \times 10^{-39} \frac{Jm^2}{W}. \tag{2.107}$$

The intensity profile of the fundamental cavity mode (Eq. 2.42) has the form

$$I(z,r) = \frac{2P_0}{\pi\omega_0^2\Big(1+(z/z_R)^2\Big)} \exp\left(-2\frac{r^2}{\omega_0^2\Big(1+(z/z_R)^2\Big)}\right), \tag{2.108}$$

where z_R is the Rayleigh length, as defined in Eq. 2.32. Since $\alpha_0^{5S_{1/2}}$ is positive, the potential is red-detuned with respect to the D_1 and D_2 line, the cavity mode creates an attractive potential with its maximum at the beam waist ω_0.

When the thermal energy of the trapped atoms is much smaller than the depth of the dipole potential [GWO00], the potential can be approximated by a cylindrically symmetric harmonic oscillator:

$$U_{\mathrm{trap}} \simeq -U_0\Big(1 - 2\frac{r^2}{\omega_0^2} - \frac{z^2}{z_R^2}\Big), \tag{2.109}$$

where the trap depth is given by

$$U_0 = \frac{\alpha_0 P_0}{\epsilon_0 c \pi \omega_0^2}. \tag{2.110}$$

The harmonic approximation is beneficial for the characterization of the dipole trap geometry. The characteristic radial and axial trap frequencies are defined as

$$\omega_r = \sqrt{\frac{4U_0}{m\omega_0^2}}, \tag{2.111}$$

and

$$\omega_z = \sqrt{\frac{4U_0}{mz_R^2}}, \tag{2.112}$$

where m is the mass of ^{87}Rb. By measuring the trap frequency of the dipole trap in the experiment, one can infer the exact trap depth U_0. Furthermore, the ratio between the radial and axial trap frequency characterizes the confinement of the trap. For the present cavity-based dipole trap, with weak axial confinement, this ratio is approximately $\omega_r/\omega_z \approx 300$.

2.4.2 AC Stark Shift of the $5P_{3/2}$ Level

So far, we have discussed the energy shift of the $5S_{1/2}$ ground state induced by an external, far-detuned optical driving field that generates a trapping potential for the atoms polarized in this state. However, the $5P_{3/2}$ excited state also experiences an AC Stark shift, which is important to consider for loading of the atoms into the dipole trap and their subsequent manipulation in the trap. For a simple two-level system, this AC Stark shift [SZ97] of the excited state has the same magnitude but opposite sign compared to the shift experienced by the ground state. As mentioned in Eq. 2.106, the polarizability of the atomic state depends on its coupling to all allowed transitions. In case of the $5P_{3/2}$ excited state, optical transitions

to the $4D_{3/2}$ and $4D_{5/2}$ states at wavelengths of $1527.261\,\mathrm{nm}$ and $1527.363\,\mathrm{nm}$, add major contributions to the polarizability of the state [BCV+08]. For a dipole trap at $1560\,\mathrm{nm}$, these contributions dominate and counteract the shift originating from the coupling to the ground state.

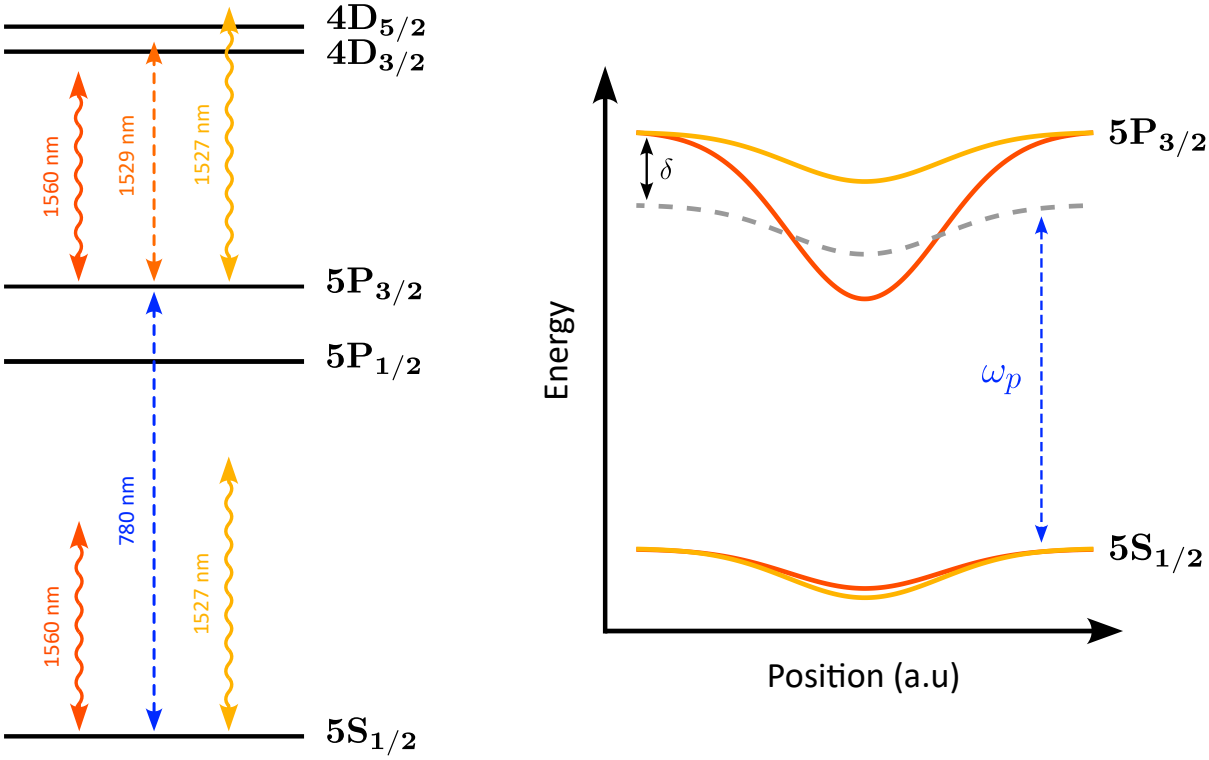

Figure 2.11: *Left:* Levels of ^{87}Rb with relevant contributions to AC Stark shift of the $5S_{1/2}$ ground and $5P_{3/2}$ excited state. Dashed lines indicate atomic transitions (bule, orange). The dark orange waved arrow indicates couplings of the $1560\,\mathrm{nm}$ dipole trap light. The light orange waved arrow indicates the $1527\,\mathrm{nm}$ tone that is applied to compensate for the shift of the $5P_{3/2}$ state. *Right:* Spatial profile of the AC-Stark shift across the cavity mode. Dark orange curves indicate shifts induced by the dipole trap. Light orange profiles corresponds to light shifts in AC-Stark compensated mode. The differential light shift induced by the $1560\,\mathrm{nm}$ trap light leads to inhomogeneous coupling of the atoms to a probe tune with frequency ω_p and detuning δ. In AC Stark shift compensated configuration, the differential light shift is kept constant (dashed gray) across the trap via an auxiliary $1527\,\mathrm{nm}$ potential.

On the left of Fig. 2.11, the level structure relevant for the dipole trap at $1560\,\mathrm{nm}$ (dark orange) is illustrated. The main contributions to the AC Stark shift of the $5P_{3/2}$ excited state originate from its couplings to the $5S_{1/2}$ ground state (dashed blue) and the $4D_{3/2}$ and $4D_{5/2}$ excited states (dashed orange). A schematic illustration of the spatial profile of the dipole potential across the cavity mode is shown on the right of Fig. 2.11. The dark orange curves correspond to the AC Stark shift of the $5S_{1/2}$ and $5P_{3/2}$ states. Contributions of the 4D states dominate the shift of the excited state. The inhomogeneous differential light shift between the ground and excited state results in an inhomogeneous detuning (δ) of light that addressees this transition (ω_p, dashed blue). In the experiment, this differential light shift prevents direct loading of the dipole trap from the MOT. Moreover, it introduces inhomogeneous light shifts across the atomic ensemble, which hinder coherent manipulation of the atomic state.

To evaluate the extent of the differential light shift, we can calculate the scalar polarizability

of the $5P_{3/2}$ using Eq. 2.106 and obtain

$$\alpha_0^{5P_{3/2}} = 3.259 \times 10^{-37} \frac{Jm^2}{W}, \tag{2.113}$$

and the scalar polarizability ratio for the ^{87}Rb D_2 line becomes

$$R_\alpha = \frac{\alpha_0^{5P_{3/2}}}{\alpha_0^{5S_{1/2}}} = 47.9. \tag{2.114}$$

In [BCV+08], tomography of the differential light shift was applied to characterize a free-space cross-dipole trap, whereas the same method was applied for in situ characterization of a cavity-mediated cross-dipole trap in [BBV+10]. Here, fluorescence or absorption imaging with a detuned probe beam is used to map the energy landscape of the trap. The relation between probe detuning δ and the trap potential $\Delta E_{5S_{1/2}}$ is given by

$$\hbar\delta = (R_\alpha - 1)\Delta E_{5S_{1/2}}. \tag{2.115}$$

In the discussion above, we considered the scalar polarizability as the dominant contribution to the AC Stark shift. However, for the $5P_{3/2}$ excited state, the tensor component of the AC polarizability [ASC07] contributes significantly to the total AC Stark shift and leads to splitting of the magnetic sublevels. In the context of this experiment, where the MOT-cooling beams are used for dipole trap tomography, the tensor contribution results in a broadening of the observed transition (Sec. 4.2.2). The dependence of Stark shift tomography on the probe light polarization was studied in [SC13], while in [CPG+17], light shift tomography in a bichromatic dipole trap was applied to measure light shifts in a regime, where the tensor component is significant.

2.4.3 AC Stark Shift Compensation

Fig. 2.11 illustrates the concept of AC Stark shift compensation with an auxiliary dipole trap tone. The second tone, in this experiment at a wavelength of $1527\,\mathrm{nm}$, adds to the trap potential of the $5S_{1/2}$ ground state, but is blue detuned to the $5P_{3/2} \leftrightarrow 4D_{3/2,5/2}$ transitions. Hence, the $5P_{3/2}$ state experiences a light shift opposing the shift induced by the $1560\,\mathrm{nm}$ tone. Tuning of the auxiliary tone intensity enables manipulation of the differential shift between the ground and first excited state and even allows the cancellation of the differential shift.

This AC Stark shift compensation using an auxiliary trap tone was first demonstrated in [PCG+18], where a cancellation tone was introduced to one arm in a free-space cross-dipole trap. As a result, improved loading efficiency into the dipole trap was reported.

In this experiment, the compensation tone is mediated by the optical cavity (Sec. 3.2.6), ensuring near-perfect mode matching with the main $1560\,\mathrm{nm}$ trap. The cavity-laser locking setups (Sec. 3.3.3, 3.19) guarantee stability and precise control of the intra-cavity power levels.

According to Eq. 2.106, the scalar polarizablities for the rubidium ground and first excited state induced by a $1527\,\mathrm{nm}$ optical tone are given by

$$\alpha_{0,1527}^{5S_{1/2}} = 6.906 \times 10^{-39} \frac{Jm^2}{W}, \tag{2.116}$$

$$\alpha_{0,1527}^{5P_{3/2}} = -3.928 \times 10^{-36} \frac{Jm^2}{W}. \tag{2.117}$$

Comparison with the values of Eq. 2.107 and Eq. 2.113, the scalar polarizabilites for a $1560\,\mathrm{nm}$ potential, it becomes evident that the $5P_{3/2}$ experiences an opposite shift with stronger coupling due to the smaller detuning to the $5P_{3/2} \leftrightarrow 4D_{3/2,5/2}$ transitions. In order to archive full cancellation of the differential AC Stark shift, the intensities of the $1527\,\mathrm{nm}$ and $1560\,\mathrm{nm}$ tone have to satisfy the relation:

$$I_{1527} = \frac{1}{12.05} I_{1560}. \tag{2.118}$$

The AC Stark shift profiles of the $5S_{1/2}$ ground state and $5P_{3/2}$ excited state across the cavity mode are schematically illustrated on the right-hand side of Fig. 2.11. The light orange profiles correspond to the configuration of the compensated differential shift. The detuning of the probe tone (dashed gray) is constant across the trap potential, enabling the implementation of cooling and state preparation sequences in the dipole trap.

As we will demonstrate experimentally in Sec. 4.2, with the AC Stark shift compensation deployed, the dipole trap can remain engaged at high power throughout the MOT cooling cycle to pre-trap and cool the atoms, thereby ensuring thermal stability compared to pulsed operation. Furthermore, as will be shown in Sec 4.2.2, the control of differential shift enables the implementation of continuous loading, in-trap molasses cooling, and optical pumping for atomic state preparation.

2.5 Cavity-Mediated Raman-Beam Splitter

In an atom interferometer, the beam splitter and mirror operations are realized through coherent exchange of photon momentum between the atomic sample and a pair of laser pulses. Depending on the atomic level structure, this photon exchange can be mediated through two distinct mechanisms.

The Raman transition is a two-photon transition that couples two ground states via an optical excited state, thus changing the internal state of the atoms [KC92]. Raman transitions are commonly used in experiments with alkali atoms such as Rb or Cs, where the hyperfine splitting of the ground state is in the GHz range. According to the selection rules, the polarization of the beams determines which magnetic sublevels are coupled. Counter-propagating Raman beams lead to a state dependent momentum transfer of $\Delta p = \pm 2\hbar k$, and can, therefore, be used for beam-splitter and mirror operations. Co-propagating Raman beams do not transfer momentum, but can be useful to flip the atomic internal state or to characterize systematic effects of the experiment.

Bragg transitions, on the other hand, enable beam splitter and mirror operations on atomic samples with a simple two-level structure. Here, the frequency detuning of two counter-propagating beams is tuned to match the Doppler shift of the atomic ground state imparted by the momentum transfer. Since the internal state of the atoms is not affected, multi-photon Bragg diffraction is suitable for realizing large momentum transfer [MCL$^+$08].

In context of cavity-mediated atom interferometry, Mach-Zehnder sequences have been demonstrated using both Bragg diffraction [LZK$^+$24, LZC$^+$25] and Raman transitions [JXH$^+$18]. In these experiments, the atoms were trapped in a Fabry-Perot cavity and subsequently released to freely fall along the cavity axis during the interferometer sequence. The free-fall induced Doppler shift lifted the symmetry between the two Raman or Bragg beams coupled to the cavity. Therefore, selective addressing of the two counter-propagating modes enabled implementation of the beam splitter and mirror operations.

The atom interferometer discussed here, which employs a propagating-wave cavity (Sec. 2.3.1), conceptually differs from the approaches above. First, the cavity is oriented horizontally, and a dipole potential with a weak axial component (Sec. 2.4) traps the atoms throughout the interferometer sequence. Second, the propagating-wave nature of the cavity enables the coupling of counter-propagating Raman beams, which map the squeezed internal state of the atoms onto the external degrees of freedom, the interferometer paths.

Although the experimental demonstration of the Raman beam splitter lies beyond the scope of this thesis, its intended implementation guided the conceptual design of the entire experimental apparatus. Therefore, a theoretical introduction into the underlying physics of the Raman beam splitter is given in the following, serving as a framework for its future realization. For a more detailed discussion, we refer to the underlying references of this introduction [MWKC92, Ste12, Dun15, Jaf18, Xu20]

2.5.1 Raman Transitions in ^{87}Rb

^{87}Rb, the atomic species used in our experiment, provides the Λ-level system required for Raman transitions. Fig. 2.12 illustrates the corresponding level scheme and the interaction with the Raman beam pair, denoted by ω_1 and ω_2. The ground states are magnetically insensitive clock states $|\downarrow\rangle = |5\mathrm{S}_{1/2}, F = 1, m_f = 0\rangle$ and $|\uparrow\rangle = |5\mathrm{S}_{1/2}, F = 2, m_f = 0\rangle$, which form the pseudo-spin system discussed in Sec. 2.3.3. The hyperfine splitting between these two

ground states is $\omega_a = 2\pi \times 6.834\,\mathrm{GHz}$ and defines the detuning between the Raman beams ($\omega_{ab} = \omega_2 - \omega_1$). Each of the Raman beams couples one ground state to the optical excited state $|e\rangle = |5P_{3/2}\rangle$ via a virtual state with detuning Δ. A more detailed illustration of the hyperfine structure of the ^{87}Rb D_2-line is shown in Appendix B and [Ste10].

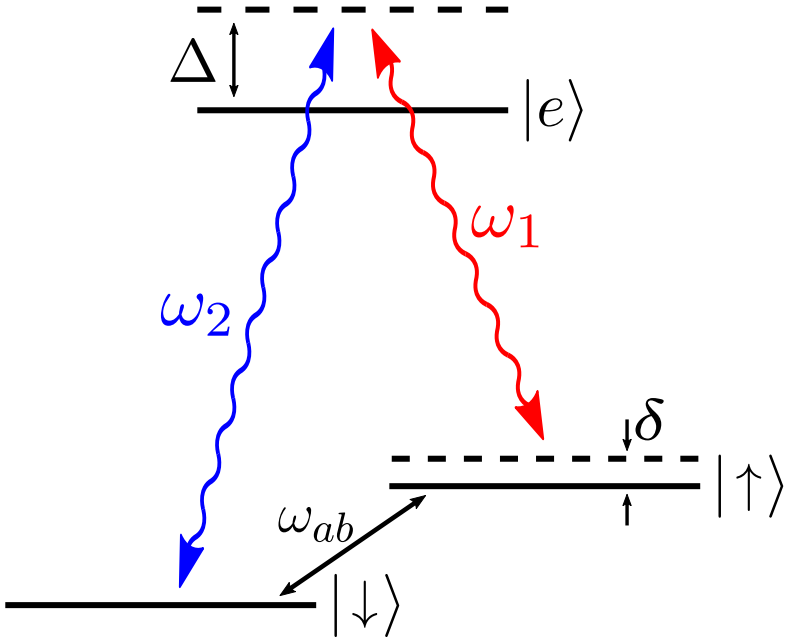

Figure 2.12: Λ-level system interacting with the Raman beam pair. The system depicts the hyperfine structure of ^{87}Rb. Birefringence of the cavity results in a blue-detuned Raman beam pair in reference to the optical transitions.

The requirement for the Raman beams to be blue-detuned from the atomic transitions is a subtle consequence of the birefringent nature of the cavity (Sec. 3.2.1). The cavity length that enables simultaneous coupling of both Raman beams, while fitting in the vacuum chamber geometry, results in a s-polarization mode with a lower resonance frequency relative to the p-polarization mode. The s-polarization mode simultaneously acts as the high-finesse mode that dispersively couples the atoms to enable the squeezing interaction (Sec. 2.3.4). Consequently, $\omega_1 = \omega_{\mathrm{QND}}$ and the Raman beam detuning is fixed to $\Delta = \omega_{\mathrm{ab}}/2$. In the literature, ω_1 typically corresponds to the $|\downarrow\rangle \leftrightarrow |e\rangle$ transition. However, in the following discussion, we stick to the lab convention where Raman beam 1 corresponds to the QND measurement tone and drives the $|\uparrow\rangle \leftrightarrow |e\rangle$ transition. To resume the description of the level scheme, δ is a small detuning of the Raman beams in reference to the hyperfine splitting ω_{ab}.

The tuning of δ enables velocity selective Raman pulses [MWKC92], while sweeping of δ in combination with Raman beam intensity modulation in an adiabatic passage [BF07, JXH+18] can be applied to enhance the fidelity of the Raman mirror or beam splitter sequences. In a cavity-mediated interferometer, the tunability of δ is limited by the cavity linewidth. In order to enable implementation of an adiabatic passage, the mirror coatings were designed to produce a broad p-polarization mode (Sec. 3.2.6), allowing the Raman beam frequency to be swept through this resonance.

2.5.2 Three-Level Atom Interaction with Classical Fields

To find a description for the time dynamics of the Raman transition, we consider the three-level system interacting with two classical light fields. The full Hamiltonian of the system is given

by:

$$\hat{H} = \hat{H}_0 + \hat{H}_I = \sum_{i=\downarrow,\uparrow,e} \left(\frac{\hat{p}^2}{2m} + \hbar\omega_i \left|i\right\rangle \left\langle i\right| \right) - \hat{d} \cdot \vec{E}, \tag{2.119}$$

where $\hat{H}_0$ is the free Hamiltonian of an atom with momentum $\hat{p}$ and mass m. The interaction term, $\hat{H}_I = \hat{d}\vec{E}$, describes the electric dipole interaction of the atom with a total electric field formed by the two Raman beams, defined as

$$\vec{E}(\vec{r},t) = \vec{E}_1 \cos(\vec{k}_1\vec{r} - \omega_1 t + \phi_1) + \vec{E}_2 \cos(\vec{k}_2\vec{r} - \omega_2 t + \phi_2) \tag{2.120}$$

$$= \frac{1}{2}(\vec{E}_1 e^{i(\vec{k}_1\vec{r}-\omega_1 t+\phi_1)} + \vec{E}_1^* e^{-i(\vec{k}_1\vec{r}-\omega_1 t+\phi_1)}) + \frac{1}{2}(\vec{E}_2 e^{i(\vec{k}_2\vec{r}-\omega_2 t+\phi_2)} + \vec{E}_2^* e^{-i(\vec{k}_2\vec{r}-\omega_2 t+\phi_2)}), \tag{2.121}$$

where $\phi_{1,2}$ indicates the phase of the Raman beams. The atomic dipole operator accounts for the coupling of the ground states to the excited state, and can be expressed as

$$\hat{d} = \sum_{j=\downarrow,\uparrow} \Big[\left\langle j\right| e\hat{r} \left|e\right\rangle \left|j\right\rangle \left\langle e\right| + h.c. \Big]. \tag{2.122}$$

Considering only resonant couplings and neglecting cross-couplings, such that each light field drives a single transition, the Rabi frequency associated for each transition can be defined as

$$\Omega_i = -\frac{e}{\hbar} \left\langle i\right| \hat{r} \left|e\right\rangle |E_j| e^{i\phi_j}. \tag{2.123}$$

The Rabi frequency defines the coupling strength of an atomic transition to an external driving field in dependence on the transition matrix element $\left\langle i\right| \hat{r} \left|e\right\rangle$ and the corresponding resonant field amplitude E_j. Assuming a counter-propagating Raman beam pair and applying the rotating wave approximation, $\hat{H}_I$ can be rewritten as

$$\hat{H}_I = \frac{\hbar\Omega_\uparrow}{2} e^{i(-k_1 z+\omega_1 t)} \left|\uparrow\right\rangle \left\langle e\right| + \frac{\hbar\Omega_\downarrow}{2} e^{i(k_2 z+\omega_2 t)} \left|\downarrow\right\rangle \left\langle e\right| + c.c. \tag{2.124}$$

The phase factor of the exponents in Eq. 2.124 contains the photon momenta k_i. This term acts on the momentum space of the atom and its substitution with the relation

$$e^{\pm ikz} = \int dp \ \left|p\right\rangle \left\langle p \mp \hbar k\right|, \tag{2.125}$$

shows that the atom-field interaction induces coupling between momentum states differing by one photon recoil. Hence, photon emission or absorption changes the total momentum of the atom by $\mp\hbar k$. The full Hamiltonian of the system can be given in the matrix form:

$$\hat{H} = \begin{pmatrix} \frac{p^2}{2m} + \hbar\omega_\downarrow & 0 & \frac{\Omega_\downarrow}{2} e^{i\omega_2 t} \\ 0 & \frac{(p+\hbar k_2-\hbar k_1)^2}{2m} + \hbar\omega_\uparrow & \frac{\Omega_\uparrow}{2} e^{i\omega_1 t} \\ \frac{\Omega_\downarrow^*}{2} e^{-i\omega_2 t} & \frac{\Omega^*\uparrow}{2} e^{-i\omega_1 t} & \frac{(p+\hbar k_2)^2}{2m} + \hbar\omega_e \end{pmatrix}. \tag{2.126}$$

In order to derive the time evolution of the system, we solve the Schrödinger equation

$$i\hbar \frac{d}{dt} \left|\psi(t)\right\rangle = \hat{H} \left|\psi(t)\right\rangle, \tag{2.127}$$

for an atomic wave function of the form

$$\left|\psi(t)\right\rangle = c_\downarrow(t) \left|\downarrow\right\rangle + c_\uparrow(t) \left|\uparrow\right\rangle + c_e(t) \left|e\right\rangle. \tag{2.128}$$

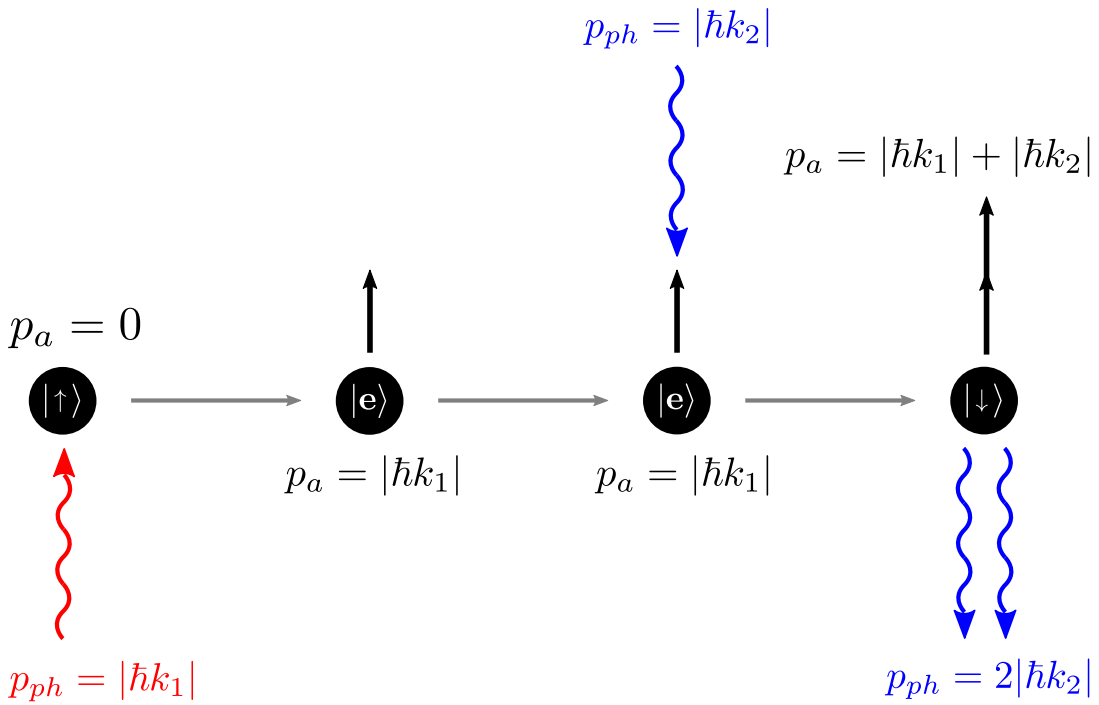

Figure 2.13: Illustration of the momentum transfer governed by the Raman transition. An atom (black sphere) in $|\uparrow\rangle$ absorbs a photon with momentum $\hbar k_1$ (red). The atom is excited and acquires a momentum kick (black arrow). A counter-propagating photon with momentum $\hbar k_2$ (blue) stimulates emission of a photon with equal energy and momentum. The atom is transferred into $|\downarrow\rangle$ and experiences a second photon recoil.

Since the driving fields are far-detuned from the atomic transitions, spontaneous emission can be neglected and the norm of the wave function is conserved $\langle\psi(t)|\psi(t)\rangle = 1$.

The equations of motion for the probability amplitudes are then obtained as

$$\dot{c}_\downarrow = -i\left(\frac{p^2}{2m\hbar} + \omega_\downarrow\right)c_\downarrow + i\frac{\Omega_2}{2}e^{i\omega_2 t}c_e, \tag{2.129}$$

$$\dot{c}_\uparrow = -i\left(\frac{(p+\hbar k_2 - \hbar k_1)^2}{2m} + \omega_\uparrow\right)c_\downarrow + i\frac{\Omega_1}{2}e^{i\omega_1 t}c_e, \tag{2.130}$$

$$\dot{c}_e = i\frac{\Omega_2^*}{2}e^{-i\omega_2 t}c_\downarrow + i\frac{\Omega_1^*}{2}e^{-i\omega_1 t}c_\uparrow - i\left(\frac{(p+\hbar k_2)^2}{2m\hbar} + \omega_e\right)c_e. \tag{2.131}$$

To isolate the slow dynamics of the Raman transitions, it is convenient to transform into the interaction picture, the rotating frame defined by the free evolution of the atomic states. Hence, the wave function is written as

$$|\tilde{\psi}(t)\rangle = \tilde{c}_\downarrow(t)\,|\downarrow\rangle + \tilde{c}_\uparrow(t)\,|\uparrow\rangle + \tilde{c}_e(t)\,|e\rangle\,, \tag{2.132}$$

where the slowly varying probability amplitudes are defined through the transformation

$$\tilde{c}_\downarrow(t) = c_\downarrow(t)e^{i\left(\frac{p^2}{2m\hbar}+\omega_\downarrow\right)t} \tag{2.133}$$

$$\tilde{c}_\uparrow(t) = c_\uparrow(t)e^{i\left(\frac{(p+\hbar k_2-\hbar k_1)^2}{2m\hbar}+\omega_\uparrow\right)t} \tag{2.134}$$

$$\tilde{c}_e(t) = c_e(t)e^{i\left(\frac{(p+\hbar k_2)^2}{2m\hbar}+\omega_\downarrow\right)t} \tag{2.135}$$

Substituting these relations into Eqs. 2.129-2.131 yield the following equations of motion for the three-level system:

$$\dot{\tilde{c}}_{\downarrow} = i\frac{\Omega_2}{2}e^{-i\tilde{\Delta}_2 t}\tilde{c}_e \tag{2.136}$$

$$\dot{\tilde{c}}_{\uparrow} = i\frac{\Omega_1}{2}e^{-i(\tilde{\Delta}_1+\tilde{\delta})t}\tilde{c}_e \tag{2.137}$$

$$\dot{\tilde{c}}_e = i\frac{\Omega_2^*}{2}e^{-i\tilde{\Delta}t}\tilde{c}_{\downarrow} + i\frac{\Omega_1^*}{2}e^{-i(\tilde{\Delta}+\tilde{\delta})t}\tilde{c}_{\uparrow} \tag{2.138}$$

The momentum term in the transformation leads to recoil and Doppler terms in the characteristic detunings $\tilde{\Delta}_{1,2}$ and $\tilde{\delta}$. This deviation from the bare detunings illustrated in Fig. 2.12 can be neglected for the single-photon detunings

$$\tilde{\Delta}_1 = \Delta + k_1 v + \frac{\hbar k_1 k_2}{m} + \frac{\hbar k_1^2}{2m} \approx \Delta, \tag{2.139}$$

$$\tilde{\Delta}_2 = \Delta + k_2 v + \frac{\hbar k_2^2}{2m} \approx \Delta, \tag{2.140}$$

since the Doppler term (kv) with an initial atom velocity v parallel to k and the recoil term ($\frac{\hbar k_{1,2}^2}{2m}$) are small compared to the bare detuning $\Delta = \frac{\omega_a}{2}$. For a ^{87}Rb atom absorbing a photon on its D_2 line, the recoil frequency is $\delta_{\mathsf{rec}} = \frac{\hbar k^2}{2m} = 2\pi \times 3.625\,\mathrm{kHz}$, corresponding to a recoil velocity of $v_r = 5.7754\,\mathrm{mm/s}$

However, these contributions to the two-photon detuning have a comparable magnitude to the bare detuning and have to be considered for the experimental implementation of the Raman transitions. The two-photon detuning is given by

$$\tilde{\delta} = \tilde{\Delta}_2 - \tilde{\Delta}_1 = \delta + k_{\mathsf{eff}} \cdot v + \left(\frac{\hbar k_{\mathsf{eff}}^2}{2m}\right), \tag{2.141}$$

where $k_{\mathsf{eff}} = k_2 - k_1$ corresponds to the effective momentum transfer mediated by the Raman transition. Assuming a counter-propagating beam pair where $k_1 \approx -k_2$, the two-photon recoil frequency becomes $\delta_{\mathsf{rec}}^{2\gamma} = \frac{2\hbar k^2}{m} = 15.086\,\mathrm{kHz}$ and the two-photon Doppler shift becomes $\delta_D^{2\gamma} = 2kv$.

2.5.3 Adiabatic Elimination of the Excited State

Having derived the equations of motion for the slowly varying probability amplitudes, we can adiabatically eliminate the excited state, resulting in an effective two-level system constituted by the ground states. Since the single photon detuning is much larger than the transition linewidth $\Delta \gg \Gamma$, the population of the excited state is nearly negligible, and the ground-state dynamics evolve much slower than those of the excited state $|\Omega_1|, |\Omega_2|, \delta \ll \Gamma$. Therefore, we can assume that $\tilde{c}(0)_e = 0$ and the integration of Eq. 2.138 yields the steady state of the excited state amplitude,

$$\tilde{c}_e = -\frac{\Omega_2^*}{2\Delta}e^{i\Delta t} - \frac{\Omega_1^*}{2\Delta}e^{i(\Delta+\tilde{\delta})t}. \tag{2.142}$$

Substitution of this solution into Eq. 2.136 and Eq. 2.137 gives an effective two-level system between $|\downarrow\rangle$ and $|\uparrow\rangle$ described by the following equations of motion:

$$\dot{\tilde{c}}_{\downarrow} = i\Big(-\frac{\Omega_2^2}{4\Delta}\tilde{c}_{\downarrow} - \frac{\Omega_2^*\Omega_1}{4\Delta}e^{i(\tilde{\delta}t-\phi_L)}\tilde{c}_{\uparrow}\Big), \tag{2.143}$$

$$\dot{\tilde{c}}_{\uparrow} = i\Big(-\frac{\Omega_1^*\Omega_2}{4\Delta}e^{-i(\tilde{\delta}-\phi_L t)}\tilde{c}_{\downarrow} - \frac{\Omega_1^2}{4\Delta}\tilde{c}_{\uparrow}\Big), \tag{2.144}$$

where the relative laser phase $\phi_L = \phi_2 - \phi_1$ originates from the phase term in Eq. 2.123. The coupling between the state amplitudes is characterized by the two-photon Rabi frequency

$$\Omega_{2\gamma} = \frac{\Omega_1^* \Omega_2}{2\Delta}, \tag{2.145}$$

which determines the coupling strength of the Raman transition. The diagonal terms in Eq. 2.143 and Eq. 2.144 correspond to the Raman beam induced AC Stark shift of the two ground states.

2.5.4 Dressed Hamiltonian

In order to transform into the dressed state picture, which is particularly useful to describe the state evolution under Raman transitions, we first apply a uniform common-mode AC Stark shift $\delta_{\mathsf{AC}}^{\mathsf{com}} = \frac{1}{2}(\frac{\Omega_2^2}{4\Delta} + \frac{\Omega_1^2}{4\Delta})$ to the diagonal elements of the previously described two-level system and thus has no influence on the dynamics. The resulting Hamiltonian is given by

$$\hat{H} = -\frac{\hbar}{2}\begin{pmatrix} -\delta_{\mathsf{AC}}^{\mathsf{dif}} & \Omega_{2\gamma} e^{i(\tilde{\delta}t - \phi_L)} \\ \Omega_{2\gamma}^* e^{-i(\tilde{\delta}t - \phi_L)} & \delta_{\mathsf{AC}}^{\mathsf{dif}} \end{pmatrix}, \tag{2.146}$$

with the differential AC Stark shift defined as $\delta_{\mathsf{AC}}^{\mathsf{dif}} = (\frac{\Omega_2^2}{4\Delta} - \frac{\Omega_1^2}{4\Delta})$.

Diagonalizing the Hamiltonian in Eq. 2.146 yields the dressed state basis, the eigenbasis of the effective two-level system. In this basis, the Hamiltonian becomes:

$$\hat{H}_{\mathsf{dres}} = -\frac{\hbar}{2}\begin{pmatrix} -\tilde{\Omega} & 0 \\ 0 & \tilde{\Omega} \end{pmatrix}, \tag{2.147}$$

where the generalized two-photon Rabi frequency is given by

$$\tilde{\Omega} = \sqrt{\Omega_{2\gamma}^2 + (\delta_{\mathsf{AC}}^{\mathsf{dif}})^2}, \tag{2.148}$$

and the dressed eigenstates [Ste12] become

$$\begin{pmatrix} |-\rangle \\ |+\rangle \end{pmatrix} = \begin{pmatrix} \cos(\frac{\theta}{2}) & -\sin(\frac{\theta}{2}) e^{i(\tilde{\delta}t - \phi_L)} \\ \sin(\frac{\theta}{2}) e^{-i(\tilde{\delta}t - \phi_L)} & \cos(\frac{\theta}{2}) \end{pmatrix} \begin{pmatrix} |\downarrow\rangle \\ |\uparrow\rangle \end{pmatrix}, \tag{2.149}$$

with

$$\sin\theta = \frac{\Omega_{2\gamma}}{\tilde{\Omega}}, \tag{2.150}$$

$$\cos\theta = \frac{\delta_{\mathsf{AC}}^{\mathsf{dif}}}{\tilde{\Omega}}, \tag{2.151}$$

and

$$\tan\theta = \frac{\Omega}{\delta_{\mathsf{AC}}^{\mathsf{dif}}}. \tag{2.152}$$

The main motivation of the above derivation is that the dressed states constitute the eigenstates of the Raman-coupled system. Therefore, they provide a suitable framework to describe Raman transitions as rotations on the Bloch sphere [FVH57]. The two ground states, $|\downarrow\rangle, |\uparrow\rangle$ can be mapped onto the south and north poles of the Bloch sphere, respectively. The dressed state can be visualized as a vector $\tilde{\mathbf{\Omega}}$ with orientation defined by Eqs. 2.150-2.150. The time evolution of the initial state under interaction with the Raman light fields then corresponds to a precession of the state vector about the vector $\tilde{\mathbf{\Omega}}$.

2.5.5 Raman-π-Pulses

The Mach-Zehnder interferometer that we aim to realize in this experiment has a momentum separation of $k_{\text{eff}} = 4\hbar k$. Fig. 2.14 illustrates the envisioned experimental sequence. Prior to the MZI sequence, the atoms are prepared in a spin-squeezed state (Sec. 2.2.3), with their mean spin aligned in the equatorial plane of the Bloch sphere and the reduced spin-projection variance oriented along the phase-sensitive quadrature. In Fig. 2.14, the superposition of the input state in the internal state basis is indicated by the dashed red and blue line. A Raman-π-pulse will be applied to this input state to act as a beam splitter, imparting a state-dependent momentum kick of $\pm 2\hbar k$ [JXH+18]. Hence, each path can be associated with a fixed internal state (red/blue, Fig. 2.14), and the effective momentum separation between the two paths of the interferometer becomes $k_{\text{eff}} = 4\hbar k$. The coherent, state-dependent momentum transfer will map the squeezed input state onto the arms of the Mach-Zehnder interferometer, thus realizing a macroscopic entanglement.

The mirror operation that closes the interferometer will be implemented by a composite of two Raman-π-pulses with a microwave π-pulse in between, which flips the internal state of the atoms. The first Raman-π-pulse stops the wave-packet separation, before the second Raman-π-pulse is applied to reverse the wave-packet separation. The internal state flip in between the Raman pulses is required because the current optical setup does not allow reversing the propagation direction of the Raman beams coupled to the cavity. The final Raman-π-pulse is applied to transfer the interferometer phase into the internal state basis, required for cavity-mediated read-out (Sec. 2.3.4).

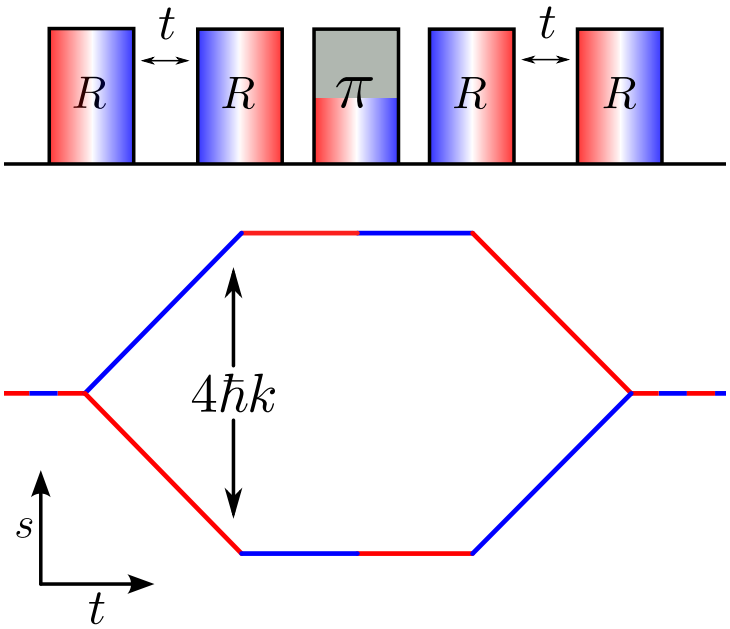

Figure 2.14: *Top:* Schematic representation of the pulse sequence. Raman π pulses (R) are indicated by a red-blue transition, and the center π pulse indicates the internal state flip required for the mirror operation. *Bottom:* Space-time diagram of the MZI trajectory. Blue and red indicate the internal state of the atoms ($|F = 1, m_F = 0\rangle$ and $|F = 2, m_F = 0\rangle$) during the sequence.

Furthermore, laser phase noise between the Raman pulses directly adds to the interferometer phase (Eq. 2.10), thereby degrading the sensitivity and stability of the interferometer. Hence,

switching the optical paths of the Raman beams during the sequence is a potential source for laser phase noise and would be a technically challenging task.

The state evolution during a Raman pulse of duration τ can be written as the time evolution under the unitary operator

$$\hat{U}(t_0, t_0+\tau) = \exp\left(-\frac{i}{\hbar}\int_{t_0}^{t_0+\tau} dt' \hat{H}(t')\right). \tag{2.153}$$

For a π-pulse, the product of the pulse duration with the effective two-photon Rabi frequency must satisfy the condition

$$\tilde{\Omega}\tau = \pi. \tag{2.154}$$

On two-photon resonance, $\delta = 0$, the corresponding unitary operator in the basis of the effective two-level system has the form

$$\hat{U}_\pi = \begin{pmatrix} 0 & ie^{i\phi_L} \\ ie^{-i\phi_L} & 0 \end{pmatrix}, \tag{2.155}$$

where ϕ_L is the relative phase between the Raman beams.

2.5.6 Outlook to an Adiabatic Raman Passage

Atomic state control with resonant driving fields requires precise control of the drive intensity, frequency, and duration. Fluctuations in any of these parameters lead to variations in the Rabi frequency (Eg. 2.123) and consequently fluctuations in the prepared state. In the context of Raman transitions and their application in atom interferometers, the Rabi frequency is further influenced by Doppler shifts of the atoms and by spatial variations in the laser intensity.

An adiabatic passage can be applied to overcome the limitations of resonant driving fields and allows robust and efficient atomic state transfer. In Sec. 2.5.3, we described the Raman transition as a rotation of the state vector about a drive vector $\tilde{\mathbf{\Omega}}$, whose orientation is defined by $\delta_{\mathsf{AC}}^{\mathsf{dif}}$ and $\Omega_{2\gamma}$. During an adiabatic passage, this drive vector is initially aligned with the state vector. By slow tilting of the drive vector, achieved by controlled variation of $\delta_{\mathsf{AC}}^{\mathsf{dif}}$ and $\Omega_{2\gamma}$, the state vector precesses rapidly around the drive vector and, thereby, adiabatically follows its orientation. By gradually rotating the drive vector towards the desired final state, the atomic state can be prepared efficiently, while remaining insensitive to variations in intensity and detuning.

It was shown [BF07] that for a π-pulse of duration τ, the optimum parameters are the following:

$$\Omega_{2\gamma}(t) = \Omega_0 \cos^2\left(\frac{\pi t}{\tau}\right), \tag{2.156}$$

$$\delta_{\mathsf{AC}}^{\mathsf{dif}} = \frac{\pm\Omega_{2\gamma}(t)\Gamma(t)}{\sqrt{1-\Gamma(t)^2}}, \tag{2.157}$$

$$\Gamma(t) = \frac{2t}{\tau} + \frac{1}{\pi}\sin\left(\frac{2\pi t}{\tau}\right)' \tag{2.158}$$

for $-\tau/2 \leq t \leq \tau/2$. [BF07, Jaf18]

Adiabatic Raman pulses in a cavity-mediated Mach-Zehnder interferometer were successfully demonstrated in [JXH+18], and are discussed in detail in [Jaf18]. This work serves as a guideline for the future realization of the Raman transitions in our experiment.

CHAPTER 3

The Experimental Setup

This chapter outlines the key concepts and technical implementations of the experiment's main components. We begin with a description of the vacuum chamber, followed by a detailed discussion of the science cavity design and its optical properties. The optical setup section covers the generation and relationship of all optical tones used in the experiment, with an emphasis on the feedback methods employed for their stabilization. This is followed by a discussion of the imaging system, microwave setup, and homodyne detection setup, all of which are essential for state preparation and diagnostics of the atomic sample. The chapter concludes with an introduction to Quantrol, our experimental control system.

3.1 The Vacuum Chamber

Cold-atom experiments must be run in an ultra-high vacuum environment to prevent scattering processes between the atomic sample and the background gas, which cause decoherence and atom loss. In Fig. 3.1, the rendered model of the vacuum chamber of the experiment is shown. The customized main body (Kimball Physics) consists of a 2.75" spherical cube welded to a 4.50" spherical decagon machined from A4/316 steel. Due to the lower magnetic permeability compared to standard A2/304 steel, we chose A4/316 steel for all metallic components of the chamber. Mounted to the bottom of the main body's spherical cube is the combined NEG- and ion-pump (SAES, NexTorr 100-5) via a 2.75" close coupler (Kimball Physics). This coupler serves as a spacer to prevent the pump's NEG element from blocking the atomic beam generated by the atom source (ColdQuanta, PICAS-1000-Rb).

The atom source consists of two modules, a vapor cell (shown on the left of Fig. 3.1) with two independently drivable ^{87}Rb filaments and a fiber-coupled optical power distribution module. This module distributes and reflects the fiber-coupled, cooling and repump tones across the full length of the vapor cell. In addition, integrated permanent magnets generate a magnetic quadrupole field across the vapor cell. Therefore, atoms are trapped in a 2D-MOT and form a cigar-shaped cloud. The module's fiber-coupled push beam generates an atomic beam towards the location of the optical science cavity by pushing the atom cloud through a pinhole that seals the vapor cell from the rest of the vacuum chamber.

The science cavity is mounted in the main body's spherical decagon. As illustrated in the cut showing the interior of the vacuum chamber in Fig. 3.1 and in Fig. 3.2, the cavity's mode waist is centered in the decagon and aligned with the atom source. Except for the CF-16 SMA

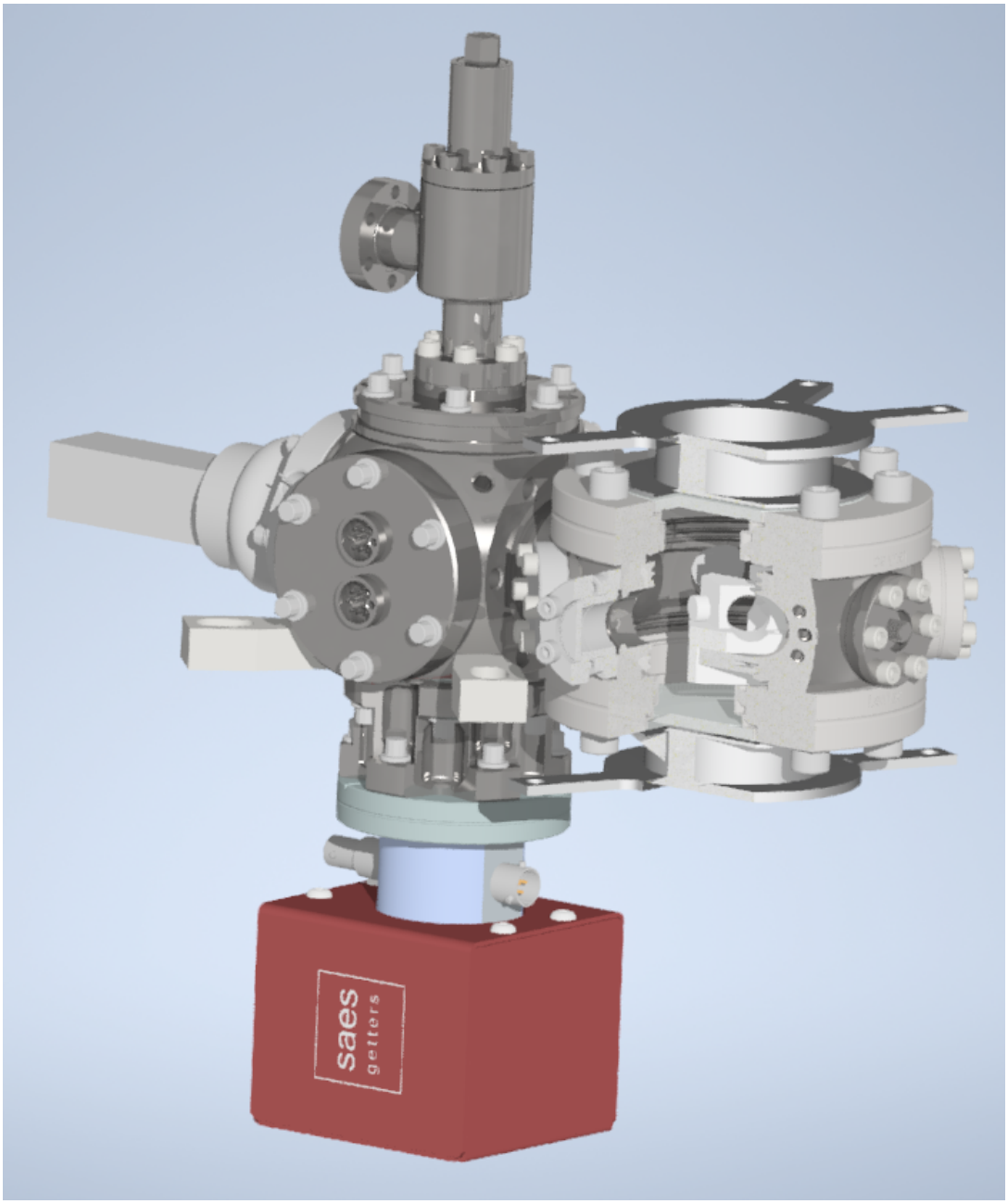

Figure 3.1: 3D-CAD model of the vacuum chamber. The three-quarter section shows the mounted science cavity in the interior of the chamber. On top and bottom of the main body's spherical decagon are the mounts for the MOT-coil pair.

feed-through (MPF Products, custom-made A4 steel) driving the $\lambda/4$ antenna, all CF-16 ports are closed with viewports. Viewports with optical access to the cavity mode are AR-coated for $780\,\mathrm{nm}$, $1527\,\mathrm{nm}$, and $1560\,\mathrm{nm}$ (MPF Products, A21656-1). In addition, the two viewports on the optical paths for cavity coupling are mounted on angled flanges (Kimball Physics,) to suppress parasitic optical étalons. The remaining two CF-16 viewports, along with the CF-63 viewports on the top and bottom of the decagon, provide optical access for the 3D-MOT cooling beams. Problems with the manufacturing quality of the AR-coated viewports, leakages within the glass-metal welds, forced us to replace these four viewports with standard kodial borosilicate glass viewports (LewVac, VP-16CF & VP-63CF).

The cavity's linear stage and ring piezo (Sec. 3.2.3) are driven via a 9-pin C-type feedthrough.

Similarly to our considerations for the pump mount, we use a vertically two-channel feedthrough (LewVac, C9 F/T X2 ON DN40CF) to prevent the connector from blocking the atom beam.

Preparation of Ultra-High Vacuum

To achieve a pressure in the low $10^{-10}\mathrm{mbar}$ range, the chamber must be baked before activating the NEG/ion pump because vapor, absorbed by the inner chamber walls and other components mounted inside the chamber, starts to outgas at such low pressures. During baking, this vapor is desorbed and can be pumped with a turbopump stage that is temporarily connected to the vacuum chamber.

In our experiment, we prepared the vacuum chamber in two phases:

1. **UHV test**: Solely the NEG/ion pump was mounted to the chamber's main body; other ports were sealed with blank flanges. In the UHV test, the chamber was baked at a temperature of $220°$. After the cool-down and activation of the NEG/ion pump, a pressure of $<10^{-10}\mathrm{mbar}$ was reached.

2. **Science upgrade**: The baking and pump activation procedure was repeated for the stepwise installation of the viewports, the atom source, feedthroughs, and the science cavity to check for leaks. Due to recurring leaks in the AR-coated viewports weld joints during baking at higher temperatures, and the glass transition temperature of Torr Seal®at $120°$, we restricted the baking temperature to $100°$. Baking at this reduced temperature is still sufficient to reach a pressure within the $10^{-10}\mathrm{mbar}$ range. The pressure, derived from the ion pump current, stabilizes under operating conditions with an activated atom source at $<5.3 \times 10^{-10}\mathrm{mbar}$. Another indicator of sufficiently low pressure in the chamber is the lifetime of the atoms in the MOT, which is limited by collisions with the background gas. A MOT lifetime of $5.4\,\mathrm{sec}$ is in good agreement with the pressure reading derived from the ion pump current.

3.2 The Science Cavity

The science cavity forms the central element of the experiment, governing all the atom-light interactions required to realize the squeezed-MZI. These interactions include:

- **Dipole trap** - A cavity mode resonant at $1560\,\mathrm{nm}$ generates the dipole trap potential (Sec. 2.4). The potential is shallow along the mode axis due to the mode's propagating wave character. This will enable the atomic sample to be trapped during the complete interferometer sequence.
- **Homodyne measurement** - A high-finesse cavity mode is tuned to dispersively couple the two ^{87}Rb hyperfine ground states to the first optical excited state. This dispersive atom-cavity interaction enables spin-squeezing via OAT and QND measurement (Sec. 2.3.4), and is also used for the interferometer phase measurement at the end of the MZAI-sequence.
- **Raman-beam splitter** - The requirement for Raman transition-driven momentum transfer is a set of two counter-propagating beams with perpendicular polarization (Sec. 2.5.1). The propagating-wave character of the cavity conserves the propagation direction of the light. The cavity is designed to have two resonant modes with perpendicular polarization, and a detuning of $6.834\,\mathrm{GHz}$, the ^{87}Rb ground-state hyperfine splitting.
- **AC-Stark shift compensation** - The $1560\,\mathrm{nm}$/dipole trap mode generates an AC-Stark shift of the optical excited, $5P_{3/2}$-state due to its coupling to the $4D_{3/2}$, and $4D_{5/2}$ states. Their transition energies correspond to a wavelength of approximately $1529\,\mathrm{nm}$. To compensate for this shift, a weak blue-detuned $1527\,\mathrm{nm}$-tone will be coupled into the cavity (Sec. 4.2.2). This AC Stark shift compensation will allow for cooling and optically pumping the atomic ensemble while it is kept trapped.

3.2.1 Cavity Length Calculation

A key requirement for the science cavity is that both Raman tones must be simultaneously resonant to mediate the Raman beam splitter operation. The power build-up of the resonant tones enhances the Raman coupling (Eq. 2.5.1) and, therefore, the efficiency of the stimulated Raman transition. A further requirement for the Raman beam splitter is that the polarization of the Raman beams has to be orthogonal. Therefore, the cavity length must be designed so that a pair of resonant s/vertical- and p/horizontal-polarized cavity modes are detuned by $\delta\omega = 2\pi\times 6.834\,\mathrm{GHz}$, the hyperfine splitting of the ^{87}Rb ground states.

Since we chose an equilateral triangular geometry for the cavity, the angle of incidence (AOI) of the light reflected by the cavity mirrors is 30°. For this AOI, the birefringence of the dielectric mirror coating causes a polarization-dependent phase shift upon reflection that is slightly off π. Another relative phase shift of π between the polarizations originates from the handedness flip caused by reflection and the odd number of reflections [PM15]. The polarization-dependent resonance conditions for a triangular cavity are given by Eq. 3.1 and Eq. 3.2.

$$k_s L + 3\varphi_s^m = 2\pi q_s \tag{3.1}$$

$$k_p L + 3\varphi_p^m + \pi = 2\pi q_p \tag{3.2}$$

Here, $k_{s,p}$ is the magnitude of the resonant mode's wave vector, L the length of the cavity, $\varphi_{s,p}^m$ is the polarization dependent phase shift upon reflection by the three mirrors of the cavity,

and $q_{s,p}$ is the longitudinal mode number with integer value. The subscripts s and p indicate the polarization of the mode.

To calculate the cavity length, we subtract Eq. 3.1 from Eq. 3.2, use the wave vector-angular frequency relation, $k_{s,p} = \omega_{s,p}/c$, substitute with the frequency relation of the Raman tones, $\omega_p = \omega_s \pm \delta\omega$, and get Eq. 3.3. We solve for the cavity length, L, and get the final expression Eq. 3.4, where Δq is the spectral displacement of the two polarization modes used to couple the Raman tones.

$$\pm\frac{\delta\omega}{c}L + 3(\varphi_p - \varphi_s) + \pi = 2\pi(q_p - q_s) \tag{3.3}$$

$$L = \left[2\pi\left(\Delta q - \frac{1}{2}\right) - 3(\varphi_p - \varphi_s)\right]\left(\pm\frac{c}{\delta\omega}\right) \tag{3.4}$$

Note that the birefringent phase shift sets the sign of the detuning between the Raman beam polarizations for a given cavity length solution. Without it, the problem would be symmetric and the resonant s- and p-polarized modes would be separated by $1/2$ FSR.

In the experiment, we use mirrors that are custom coated by LAYERTEC for the science cavity (specification in Appendix C). The birefringent phase shifts, for AOI $= 30°$, are specified as $\varphi_s^m = 171° \times \frac{\pi}{180°}$, and $\varphi_p^m = 140° \times \frac{\pi}{180°}$. The geometry of the vacuum chamber (Sec3.1) constrains the range of cavity lengths applicable due to the limited access to the cavity reflections required for the cavity lock and homodyne detection. We chose a cavity length of $L = 9.83\,\mathrm{cm}$, resulting in a free spectral range of FSR $\approx 3\,\mathrm{GHz}$, and the Raman modes are separated by $\sim 2.25 \times$ FSR, where the s-polarized mode is red-detuned to the p-polarized mode. The mirror coatings were designed to have high reflectance, and accordingly low transmittance for the s-polarization ($T \approx 13\,\mathrm{ppm}$). Therefore, the s-polarized cavity mode will have high finesse and will be utilized for homodyne detection of the atomic population. For homodyne detection, the cavity resonance is tuned to couple the $5P_{3/2}$-optical excited state to a virtual state in between the two hyperfine ground states to achieve homogeneous dispersive coupling of the ground states to the cavity. This requirement for homodyne detection and the chosen cavity length will result in the Raman tones having to be blue-detuned to the ^{87}Rb D_2-line. Furthermore, the mirror coating was purposely designed to have lower reflection for the p-polarization ($T \approx 1000\,\mathrm{ppm}$). These reflectivity properties will lead to a broad linewidth of the p-polarized mode. That, in turn, will allow us to sweep the Raman laser through the p-polarized mode to apply an adiabatic Raman passage.

3.2.2 Stability and Mode Waists

The geometrical properties of the science cavity (Sec. 2.3.1) are determined by its mirror configuration. It consists of two plane mirrors and one convex mirror, forming a cavity mode with a single waist centered between the plane mirrors. The convex mirror has a radius of curvature $R = 100\,\mathrm{mm}$. Table 3.1 lists the stability parameters (Eq. 2.38), the Rayleigh lengths and the mode waists (Eqn. 2.32) for the sagittal and tangential planes of the cavity mode at the wavelengths of $1560\,\mathrm{nm}$, $1527\,\mathrm{nm}$ and $780\,\mathrm{nm}$.

Note that the stability criterion would allow for a larger curved mirror radius, leading to larger beam waists. However, a larger mode waist increases the mode volume and, therefore, decreases the coupling of the atoms to the cavity (Eq. 2.61). Second, the cavity locking scheme, squash-lock, is based on the interference of reflected second-order modes with the resonant 00-mode. A relative phase of $\approx \pi/2$, originating from a Gouy phase shift between

	$\lvert A+D\rvert$	z_R (cm)	ω_0^{1560} (µm)	ω_0^{1527} (µm)	ω_0^{780} (µm)
sagittal	0.285	5.71	168.45	166.66	119.11
tangential	0.286	4.286	145.88	144.33	103.15
	⊘	4.998	157.17	155.50	111.13

Table 3.1: Geometrical properties of the cavity

the sagittal and tangential optical planes, is crucial for the method. A larger beam waist would lead to slower acquisition of the Gouy phase and further separation between the cavity and its coupling optics (see Sec.3.2.4) For more details on squash-lock, see Sec. 3.3.3.

3.2.3 Science Cavity Assembly

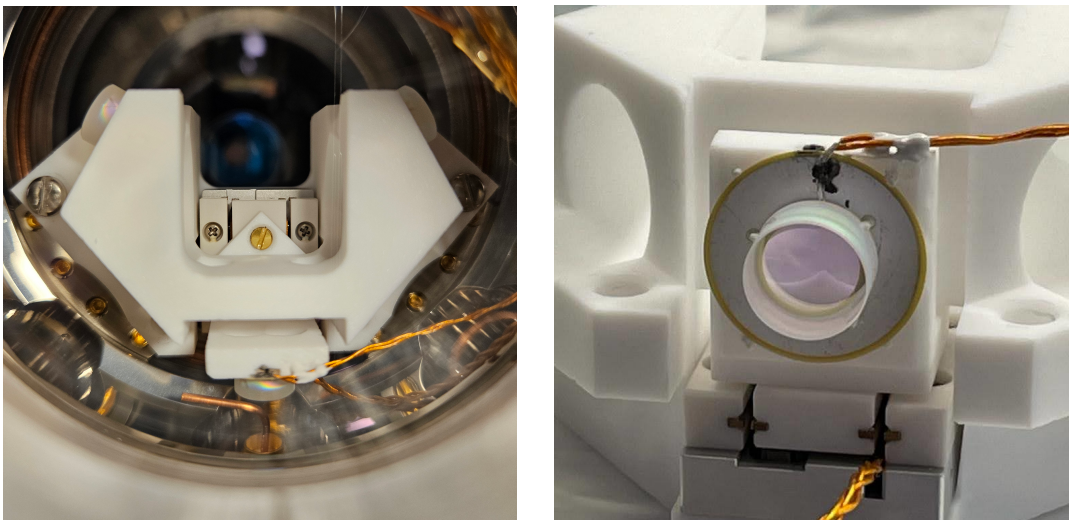

Figure 3.2: *Left:* Image of the science cavity mounted in the vacuum chamber. Next to the bottom cavity mirror, one can see the mounted *microwave*-antenna. *Right:* Image of the mirror holder assembly. The holes in the cavity body, left and right of the mirror holder assembly, are required for the MOT beam pairs.

The science cavity has an equilateral triangular geometry. The $1/2$-inch mirrors (LAYERTEC) are in a plane, plane, plano-convex configuration such that the cavity mode has a single waist in between the two plane mirrors. The image on the left of Fig. 3.2 shows the top view of the science cavity mounted in the vacuum chamber. The cavity waist, and, therefore, the location of the trapped atomic ensemble, is between the two plane mirrors, the mirrors' top-left and top-right in the image. Since the MOT, required for pre-trapping and cooling of the atoms, is superposed with the dipole trap in the center of the vacuum chamber, the cavity body has to enable optical access for the three counter-propagating MOT beam pairs. Furthermore, the cavity body is designed to block the atomic beam, originating from the atom source, from coating the plano-convex mirror. As a material, we chose MACOR®, a glass ceramic. Its low thermal expansion coefficient ($\alpha = 9.0 \times 10^{-6} K^{-1}$) outperforms those of metallic materials, and its mechanical properties allow machining of complex shapes such as the cavity.

The mirror mount for the plano-convex mirror is mounted on a UHV-compatible, ceramic linear stage (Smaract, SLC-1720-UHV -NM), which in turn is mounted on the cavity body. The linear stage enables fine-tuning of the cavity length over a wide range and is used for

active cavity-length stabilization. The mirror itself is attached to the MARCOR® mount via a piezo-ring (PI Ceramic). With the ring piezo, we are capable of adding another faster piezo layer for cavity length stabilization. An image of the mirror mount assembly is shown to the right of Fig. 3.2. The mirrors and the ring-piezo are glued via four joints each of Torr Seal®, a UHV-compatible adhesive. For the electrical bonding of the ring-piezo, UHV-compatible Ni paste (PELCO®, 16059) was used, and the connecting wires were glued to the mount to ensure the stability of the bond.

3.2.4 The Optical Cavity Coupling Setup

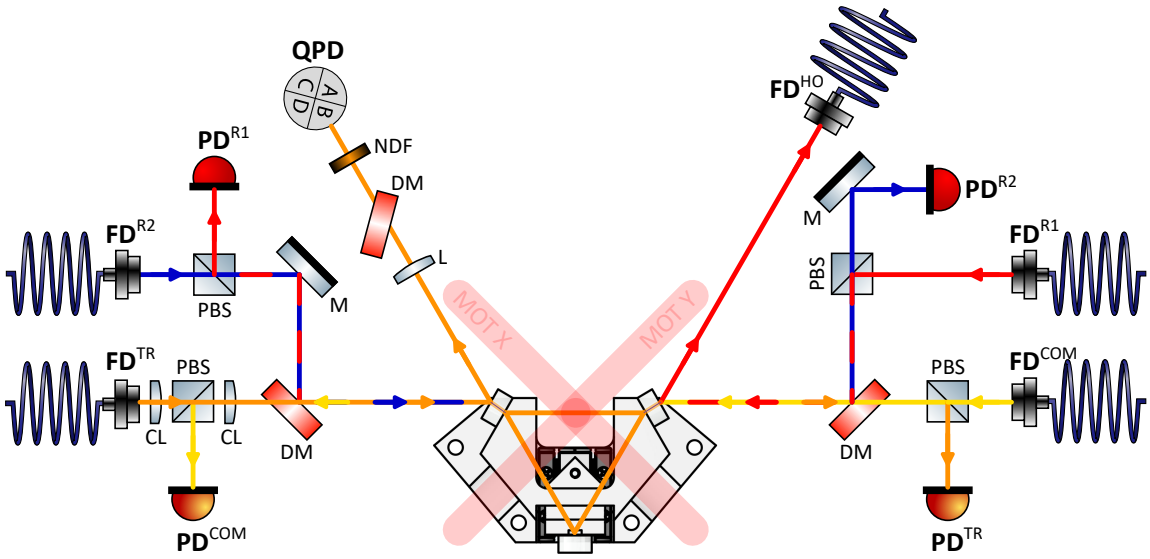

Figure 3.3: Schematic diagram of the optical setup coupling to the science cavity. Colored arrows indicate the propagation direction of the coupled tones. *Orange:* dipole trap (TR); *Yellow:* AC Stark shift compensation (COM); *Red:* Raman 1 (R1); *Blue:* Raman 2 (R2). The cavity reflection of R1 is coupled to the homodyne detection setup (HO). Abbreviations: FD, fiber dock; PD, photo diode; QPD, quadrant photo detector; PBS, polarizing beam splitter; CL, cylindrical lens; L, lens; M, mirror; DM, dichroic mirror; NDF, neutral-density filter. The figure was created using components from [Fra].

During an experimental sequence, up to four tones of light are simultaneously coupled to the cavity. Figure 3.3 illustrates the optical setup required to couple these beams. All optics except the cavity are mounted outside the vacuum chamber. For illustrative purposes, the distances between elements and the cavity are scaled out of proportion, and the vacuum chamber is not depicted. The colored arrows indicate the propagation direction of the input, reflection, and transmission of each beam, the trap (TR, $1560\,\mathrm{nm}$, orange), compensation (COM, $1527\,\mathrm{nm}$, yellow), first Raman/QND (R1, $780\,\mathrm{nm}$, red), and second Raman (R2, $780\,\mathrm{nm}$, blue).

For efficient coupling into the cavity, the location and size of the beam waist of the incident beam must be matched to the cavity mode. This mode matching is achieved using a fiber dock (FD), an adjustable fiber collimator (Thorlabs, CFC-8-A/B) mounted on a five-axis stage (Newport, 9031-M), and guided by beam propagation simulations. The distance between the fiber dock and the cavity mode waist is calculated, the collimator is tuned to focus the beam at this position, and the alignment is adjusted with the five-axis stage.

The collimators of the $780\,\mathrm{nm}$ fiber docks ($\mathrm{FD}^{\mathrm{R1}}$, $\mathrm{FD}^{\mathrm{R2}}$) were selected to provide longer distances to the cavity compared to those used for the trap ($\mathrm{FD}^{\mathrm{TR}}$) and the compensation

(FD^{COM}) beams. This configuration enabled coupling of all tones into the cavity along the same optical axis using dichroic mirrors (DM). Furthermore, the reflection of beam R1 is coupled into fiber dock FD^{HD} and delivered by polarization-maintaining fibers to the homodyne detection setup for the QND measurement. Since the two Raman tones have perpendicular polarization, polarizing beam splitters (PBS) are used to separate the transmitted beams from the incident beams, directing them onto photo diodes for power monitoring and stabilization.

The optical path for the trap beam contains the optics required for squash-lock, the applied laser-cavity stabilization method. The cylindrical lens pair (CL) displaces the beam focus in the sagittal and tangential planes to excite second-order Hermite-Gaussian modes. After reflection, the resulting elliptical beam is focused by a collector lens (L) onto a quadrant photo detector (QPD). The neutral-density filter (NDF) in front of the QPD prevents its saturation by attenuating the incident optical power. Furthermore, a dichroic mirror filters the reflected R2-beam from the trap beam. In Sec. 3.3.3, we discuss the optical alignment applied for squash lock and the laser-cavity stabilization in more detail. The dipole trap power is stabilized by monitoring the transmitted power (PD^{TR}) and feeding back to the incident power.

To avoid interference with the laser-cavity and trap power feedback systems, the compensation tone is coupled to the p-polarization mode, which is orthogonal to the polarization of the trap. For stabilization of the compensation laser to the cavity, we apply a side-of-the-fringe lock (Sec. 3.3.4), where the error signal is derived from the cavity transmission (PD^{COM}).

3.2.5 Cavity Length Adjustment

As discussed in Sec. 3.2.1, the cavity is designed to be simultaneously resonant with the two Raman tones. For fine-tuning the cavity length, the linear stage position is iteratively adjusted in vacuum while monitoring the transmission of both tones. Since both Raman tones are generated from the same source, the $1560\,\mathrm{nm}$-trap laser (Sec. 3.3), they can be swept simultaneously through the cavity resonance by modulating the laser with a triangular ramp signal, while maintaining the fixed frequency offset of $\Delta = 6.834\,\mathrm{GHz}$.

Figure 3.4 shows the transmission of both Raman tones over the frequency offset for the final cavity length configuration. It confirms that two of the main design requirements are met. First, the Raman tones are simultaneously resonant with the correct frequency offset, and second, the birefringence of the mirrors gives rise to two polarization modes with clearly distinct linewidths.

3.2.6 Linewidth Measurements

To measure the linewidth of the cavity mode, the frequency of the incident laser was swept across resonance over a well-defined range, and the resulting cavity transmission or reflection was recorded. For an accurate linewidth measurement, the cavity has to be driven in steady-state conditions, meaning that the sweep of the probe laser frequency is slow compared to the cavity linewidth. If the sweep is too fast, the intra-cavity field can not build up sufficiently, resulting in asymmetric transmission profiles with oscillatory decay features [RESKB02, LWH+99]. Consequently, measuring high-finesse modes becomes challenging due to the acoustic and mechanical noise present in the experiment. An example of an asymmetric transmission profile is the s-pol. mode shown in Fig. 3.4.

To suppress the noise, we first stabilized the cavity to the trap laser (Sec. 3.3.3) and probed the cavity with tones generated from the same laser (Sec. 3.3). The cavity resonance was then

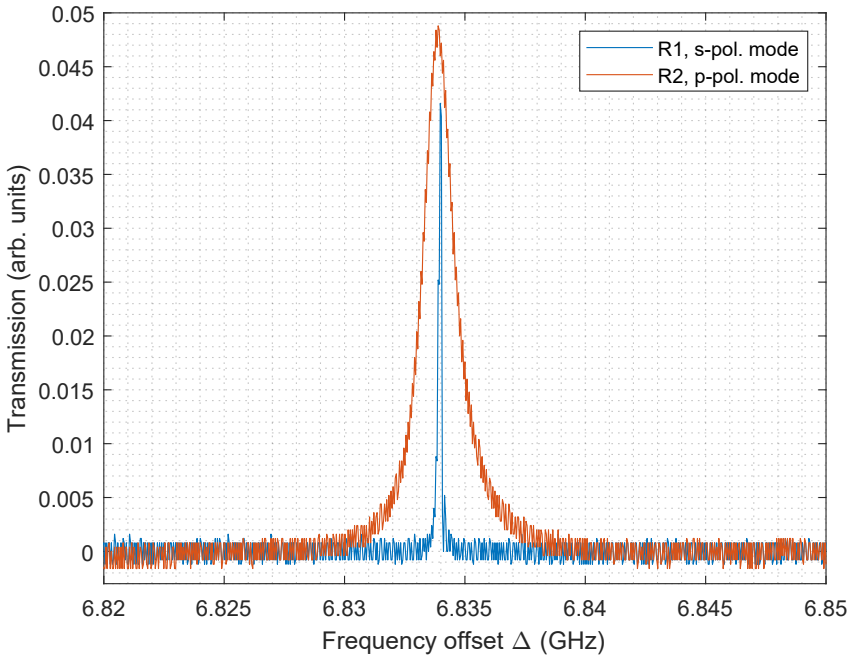

Figure 3.4: Cavity transmission of Raman tones after length adjustment. Two cavity modes with orthogonal polarization are simultaneously resonant with a frequency offset of $\Delta = 6.834\,\mathrm{GHz}$. The birefringence of the mirrors creates distinct linewidths of the modes.

scanned by modulating the probe beam frequency using an acousto-optic modulator (AOM).

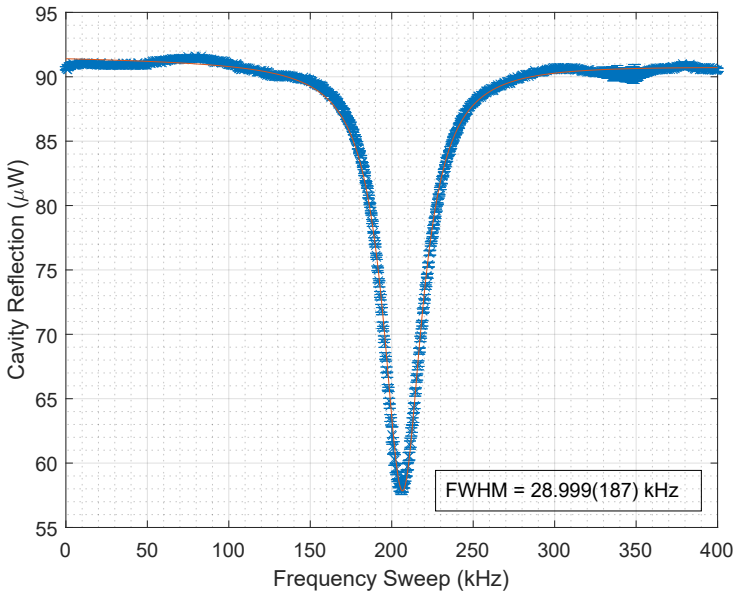

Figure 3.5: Linewidth measurement of the s-polarization mode at $1560\,\mathrm{nm}$. The data indicate the average of nine consecutive reflection profile measurements. The data were fitted with an absorptive Lorentzian profile (red) with FWHM $= 28.999(187)\,\mathrm{kHz}$.

Figure 3.5 shows the linewidth measurement data of the s-polarization mode at $\lambda = 1560\,\mathrm{nm}$. To avoid interference with the laser-cavity lock, we measured the reflection of a counter-propagating probe. The results indicate that the mode has a full width half maximum (FWHM) of $\kappa = 2\pi \times 28.999(187)\mathrm{kHz}$.

In addition, the FSR (Eq. 2.46) of the cavity was measured using an electro-optic I/Q modulator operated in carrier-suppressed sideband mode (Sec. 3.3.5). The sidebands become simultaneously resonant with the cavity if the modulation frequency matches the FSR. The measured value, FSR $= 3.006\,\mathrm{GHz}$, is in good agreement with the theoretical prediction derived in Sec. 3.2.1.

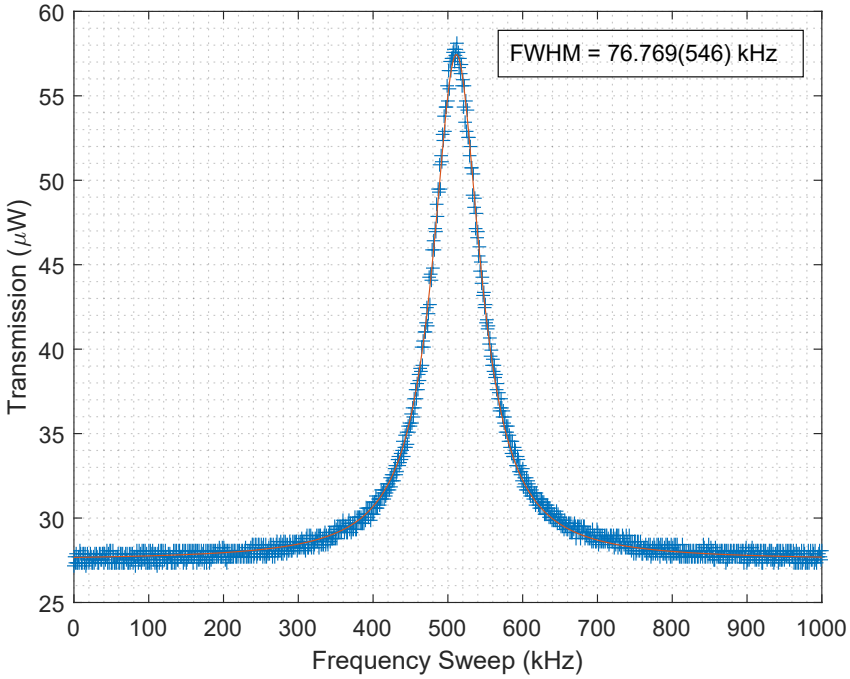

Figure 3.6: Linewidth measurement of the s-polarization mode at $780\,\mathrm{nm}$. The data show a transmission profile measurement and the Lorentzian fit (red) for analysis. The average fit result over six transmission measurements is FWHM $= 76.769(546)\,\mathrm{kHz}$.

Figure 3.6 presents the transmission measurement of the s-polarized mode at $\lambda = 780\,\mathrm{nm}$, which will be used for the homodyne measurement (Sec. 3.6). The results indicate that the mode has a FWHM of $\kappa = 2\pi \times 76.769(546)\mathrm{kHz}$.

To measure the broad linewidth of the p-polarized mode at $\lambda = 780\,\mathrm{nm}$, the measurement method was adapted to account for the non-linear response of the AOM during wide frequency sweeps. Since the linewidth is sufficiently broad to allow rapid resonance scans, the laser frequency was directly modulated to sweep through the unlocked cavity resonance. As a frequency reference, sidebands generated by the probe-controlling AOM were used. Figure 3.7 shows the reflection measurement, indicating a FWHM of $\kappa = 2\pi \times 1.394(58)\mathrm{MHz}$.

Finally, we characterize the p-polarized mode at $\lambda = 1527\,\mathrm{nm}$, which is used for AC-Stark shift compensation. This is the only cavity probe not derived from the $1560\,\mathrm{nm}$ trap laser. For the measurement, the cavity length was stabilized while the laser frequency was swept through the resonance. As in the measurement of the $780\,\mathrm{nm}$ p-polarization mode, sidebands generated by the probe-controlling AOM were served as a frequency reference. In Fig. 3.8, a transmission measurement is shown that yields a FWHM of $\kappa = 2\pi \times 99.810(592)\mathrm{kHz}$.

Table 3.2 summarizes the cavity linewidth measurements and the corresponding finesse values for the various modes. The cavity supports two high finesse modes at $\lambda = 1560\,\mathrm{nm}$ and $\lambda = 1527\,\mathrm{nm}$, which are used to generate the dipole trap and to compensate the trap-induced AC Stark shift, respectively. At $\lambda = 780\,\mathrm{nm}$, the birefringent properties of the mirror coatings give rise to a high finesse mode (s-polarized) suitable for homodyne detection of the atom

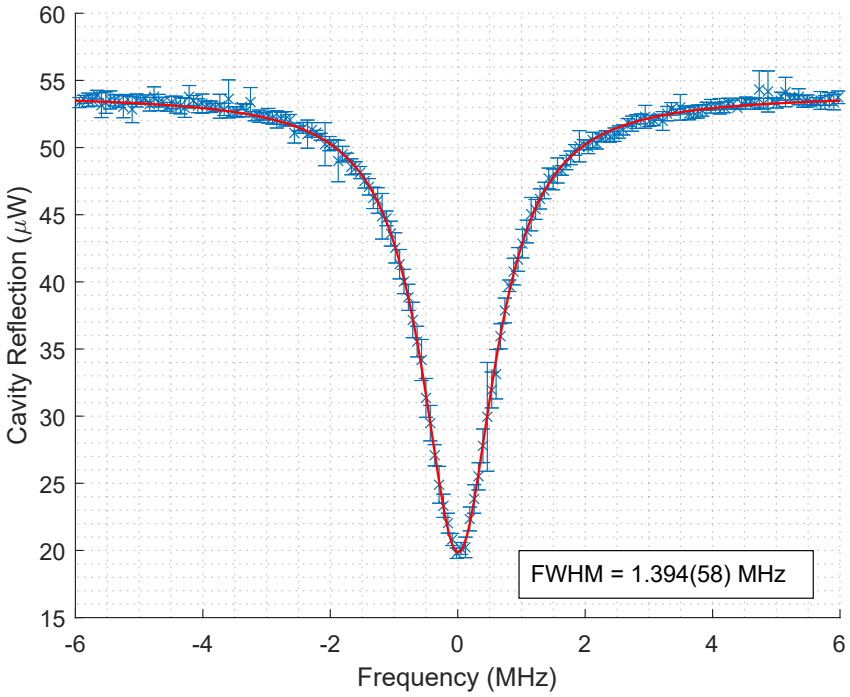

Figure 3.7: Linewidth measurement of the p-polarization mode at $780\,\mathrm{nm}$.

population, and the low-finesse p-polarization mode that enables adiabatic Raman pulse sweeps.

	$1560\,\mathrm{nm}$, s-pol.	$1527\,\mathrm{nm}$, p-pol.	$780\,\mathrm{nm}$, s-pol.	$780\,\mathrm{nm}$, p-pol.
FWHM (kHz)	28.999(187)	99.810(592)	76.769(546)	1394.000
F	103600	30100	39100	2156

Table 3.2: Linewidth and Finesse values

3.2.7 Atom-Cavity Coupling Parameters

Knowing the geometric and spectral properties of the cavity together with the spectral properties of the ^{87}Rb D_2 line allows us to evaluate the effective single-photon Rabi frequency and the single-atom cooperativity for our experimental setup. For spin squeezing and homodyne measurements, the cavity probe addresses π transitions. To calculate the effective single-photon Rabi frequency (g_0), we calculate the couplings of all allowed transitions [Ste10], using Eq. 2.61, and take the square of their sums. Thus, the approximate effective single-photon Rabi frequency becomes

$$g_0 = 2\pi \times 85.442 \text{ kHz}, \tag{3.5}$$

and the resulting single-atom cooperativity (Eq. 2.63) is

$$C = 0.062. \tag{3.6}$$

3.2.8 Back-Scatter Characterization

So far, the geometric and spectral properties of the cavity have been studied. However, the propagating wave nature of the cavity remains to be characterized. Any mirror imperfections or

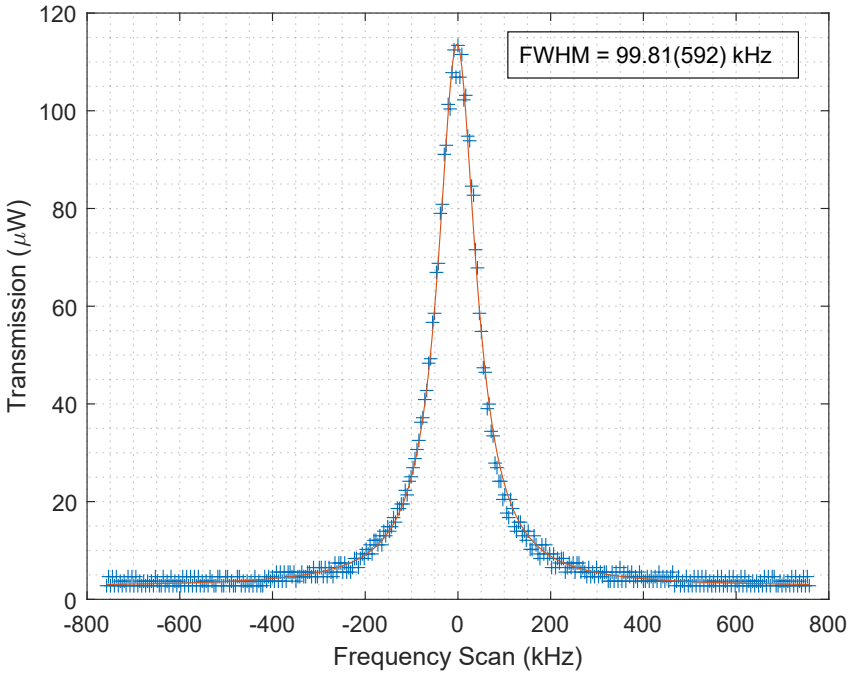

Figure 3.8: Linewidth measurement of the p-polarization mode at $1527\,\mathrm{nm}$. The data show a transmission profile measurement and the Lorentzian fit (red) for analysis. The average fit result over four transmission measurements is FWHM $= 99.810(592)\,\mathrm{kHz}$.

surface contamination can cause photon scattering and the buildup of a counter-propagating mode with amplitude E_{sc}. This counter-propagating mode interferes with the primary mode field E_0, resulting in spatial modulation of the intra-cavity intensity, given by

$$I_{\mathrm{cav}}(r) \propto |E_0|^2 + 2E_0E_{\mathrm{sc}}\cos(kr) + |E_{\mathrm{sc}}|^2. \tag{3.7}$$

Effectively, back-scattering generates a standing wave modulation on top of the propagating Gaussian mode.

To quantify this effect, the transmitted power is measured at a port that would remain dark in an ideal configuration (Fig. 3.3, FD^{HO}), and is compared with the transmission along the main propagation direction (Fig. 3.3, PD^{TR}). A back-scattered fraction of $|E_{\mathrm{sc}}|^2 \approx 0.005 \times |E_0|^2$ is observed. According to Eq. 3.7, this corresponds to a standing-wave modulation of approximately 14% relative to the intra-cavity intensity $|E_0|^2$.

The effect on the intended Mach-Zehnder sequence has to be evaluated at the time. For operation at shallow trap depths, this modulation might be negligible. However, a phase-locked counter-propagating beam can be coupled to the cavity to cancel the effect. Such a configuration would allow to explore alternative trapping schemes, such as a full standing-wave trap to prepare or maintain atomic samples spatially separated, or a conveyor-belt trap to create time-dependent light shifts.

3.3 Optical Setup

Cold-atom experiments require precise control of the timing, frequency, and phase of the light interacting with the atoms. In the following, we will provide an overview of the grand optical setup used to generate the light for the experiment, and we will discuss the methods developed in the lab to stabilize the optical systems and reference them to each other.

Figure 3.9 depicts the grand light generation setup and the relation between its subunits. Note that the complete light generation setup is built on a single optical table. The light is delivered via polarization-maintaining fibers to the cavity, which is mounted in the vacuum chamber, which in turn is installed on a neighboring optical table. All shown AOMs are controlled with Quantrol, our experimental control software (Sec.3.7), and are required for fast switching and power control of the light delivered to the experiment.

The source for the dipole trap and the Raman tones is a laser (OEwaves, Hi-Q OE4030) on the top left in Fig. 3.9. It has a center wavelength of $\lambda = 1560.48\,\mathrm{nm}$, twice the wavelength of the ^{87}Rb D_2 line, and a linewidth of $\gamma = 2.57\,\mathrm{Hz}$. If we horizontally follow the output of the laser, we show the generation scheme of the second Raman tone. An electro-optic I/Q modulator (SSB1, exail, MXIQER-LN-30) in carrier-suppressed single-sideband mode (CS-SSB) is used to shift the laser frequency by $\Delta = 3.417\,\mathrm{GHz}$, half of the ^{87}Rb hyperfine ground state splitting. The modulation frequency is generated by mixing a local $3.6\,\mathrm{GHz}$ oscillator with an offset frequency controlled by Quantrol. A small portion of the modulator's output is fed to a scanning Fabry-Perot interferometer (FPI) for set-point adjustment and to a fast photodetector (Thorlabs, PDA20CS2) for bias voltage stabilization. Feedback for the modulators' bias voltages is based on modulation with an auxiliary tone and will be discussed in Sec.3.3.5 [WDH23]. To compensate for losses induced by the modulator and the low inefficiency of subsequent frequency doublers (2xf, NTT electronics, WH-0780), the light is amplified to $20\,\mathrm{mW}$ with an erbium-doped fiber amplifier (EDFA, Thorlabs, EDFA100P). After frequency doubling, the generated light has a wavelength of $\lambda = 780\,\mathrm{nm}$ and will later in the experiment address the ^{87}Rb $|F = 1\rangle \leftrightarrow |e\rangle$ transition.

Subsequently, the light is injected into a distributed feedback (DFB) laser (Eagleyard, DFB-0780) with a center wavelength around $\lambda = 780.24\,\mathrm{nm}$. If the seed tone possesses superior spectral properties, the injection-locked laser copies these characteristics while amplifying the optical power [BGSB00]. For stabilization of the injection lock, a small portion of the laser output is reflected onto a QPD to detect its beam ellipticity. Fundamentally, one can understand the beam ellipticity as a measure of the mismatch between the natively astigmatic DFB laser mode and the circular mode profile of the seed laser. Under injection conditions, the mode-matched portion of the seed will couple into the internal laser cavity and acquire a cavity-related phase, whereas the unmatched portion will be reflected from the laser facet. We demonstrated in [MLW$^+$23] that the inference between these two components results in a varying beam ellipticity, and its monitoring can be used to feed back on the DFB laser current, extending its injection range.

If we follow the vertical output of the $1560\,\mathrm{nm}$ laser, Fig. 3.9 illustrates the scheme to generate the Raman1/QND/OAT tone and to reference the laser to a ^{85}Rb hyperfine transition. After an initial amplification with an EDFA (Thorlabs, EDFA100P), approximately $8\,\mathrm{mW}$ of light is coupled to the frequency doubler. The generated light will be utilized in the experiment as Raman beam addressing the ^{87}Rb $|F = 2\rangle \leftrightarrow |e\rangle$ transition and as homodyne probe for the atomic population measurement (QND). Similar to described above, injection lock of a second DFB laser (Eagleyard, DFB-0780) amplifies the frequency-doubled tone, and the laser

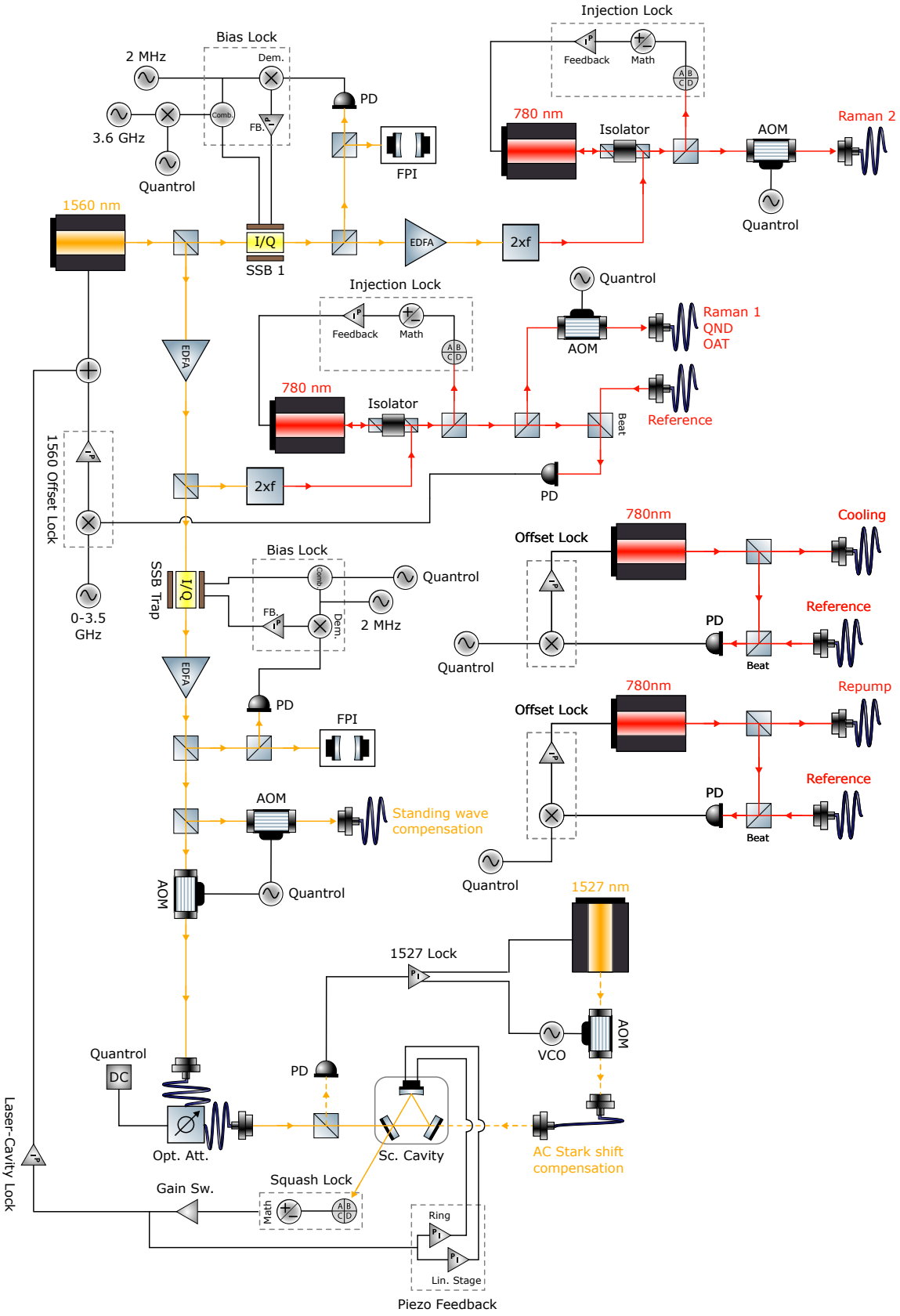

Figure 3.9: Schematic diagram of the grand optical setup. The beam splitters indicate either free-space $\lambda/2$-PBS pairs or fiber-coupled PBS' required for optical power distribution. The figure was created using components from [Fra].

current is stabilized via ellipticity monitoring.

The main portion of the resulting light is coupled to a polarization-maintaining fiber, transferring the light to the homodyne detection setup (Sec.3.6). Note that after frequency doubling, the Raman beams have the intended frequency offset of $\Delta = 6.834\,\mathrm{GHz}$, the ^{87}Rb hyperfine ground state splitting. The residual light interferes with the reference laser (Sacher Lasertechnik, VBG-780-1120) that is locked to the ^{85}Rb $|F = 3\rangle \leftrightarrow |F' = 4\rangle$ transition using modulation transfer spectroscopy (Sec. 3.3.1). The resulting beat is detected with a fast photodetector and the $1560\,\mathrm{laser}$ stabilized to a defined beat frequency by the 1560 offset lock (Sec. 3.3.2).

The lower half of Fig. 3.9 illustrates the locking scheme for the science cavity. Although the Raman1/QND-tone is generated from the trap laser via frequency doubling, the effective cavity length differs between the two wavelengths due to wavelength- and polarization-dependent phase shifts upon reflection, as well as wavelength-dependent penetration depths into the mirror coatings. In order to compensate for this, a second electro-optic I/Q modulator (SSB Trap), operated in carrier-suppressed single-sideband (CS-SSB) mode, is used to shift the frequency of the trap laser, ensuring simultaneous resonance of both the trap and Raman1/QND light with the cavity. The subsequent EDFA (Amonics, AEDFA-PM-C-33) compensates for the modulator-induced optical losses and provides sufficient power for the dipole trap.

The error signal required for laser-cavity locking is generated via squash lock (Sec. 3.3.3). A gain switch circuit (Gain Sw.) attenuates this error signal, enabling continuous cavity locking for the dipole trap in both high- and low-power configurations. The gain switch is controlled by the dipole trap power feedback circuit, which stabilizes the transmitted trap power by regulating the input power via an optical attenuator (Thorlabs V1550PA) or, alternatively, an AOM. The laser-cavity lock itself consists of the following three separate feedback channels:

Cavity length stabilization - Feedback to the linear stage locks the cavity length to the trap laser frequency. The limited bandwidth of the stage allows to correct only slow drifts, such as those caused by thermal fluctuations.

Structural resonance damping - A filter circuit provides feedback to the ring piezo to suppress a structural resonance of the cavity body at $3.5\,\mathrm{kHz}$.

Laser frequency stabilization - Vibrations and acoustic noise in a range up to tens of kHz cannot be compensated by mechanical systems due to their limited modulation bandwidth. Therefore, fast feedback directly to the laser frequency is required.

To conceptually summarize the laser-cavity locking setup, Fig. 3.9 shows that a low-bandwidth feedback loop locks the trap laser frequency to the ^{85}Rb $|F = 3\rangle \leftrightarrow |F' = 4\rangle$ transition. Consequently, the cavity length is stabilized to the same reference via low-bandwidth feedback to the linear stage. However, to compensate for vibrations and acoustic noise affecting the cavity, an additional fast feedback loop is applied to the laser frequency. A detailed description of the laser-cavity lock channels will follow in Sec. 3.3.3.

To compensate for the dipole trap-induced AC-Stark shift, a $1527\,\mathrm{nm}$ laser (NP Photonics, The Rock module) is coupled to the cavity. The laser frequency is locked to the cavity using the side-of-the-fringe locking method (Sec.3.3.4). The feedback system consists of two channels, a low-bandwidth loop that modulates the laser directly, and a high-bandwidth loop that controls the driving voltage of the AOM via a voltage-controlled oscillator (VCO).

The generation scheme for the cooling and repump tones, required for pre-trapping and cooling atoms in the magneto-optical trap (MOT), is illustrated in the center-right of Fig. 3.9. The beat frequency between both lasers (Sacher, VBG-780-1120) and the reference laser is detected using a fast photodetector (Thorlabs, DX12CF) and stabilized to a frequency offset set by Qauntrol. The offset locking method, based on beat frequency discrimination using a hybrid LC filter, was developed specifically for this experiment [LDH22]. It provides tight locking behavior while offering a broad locking range.

3.3.1 Modulation Transfer Spectroscopy

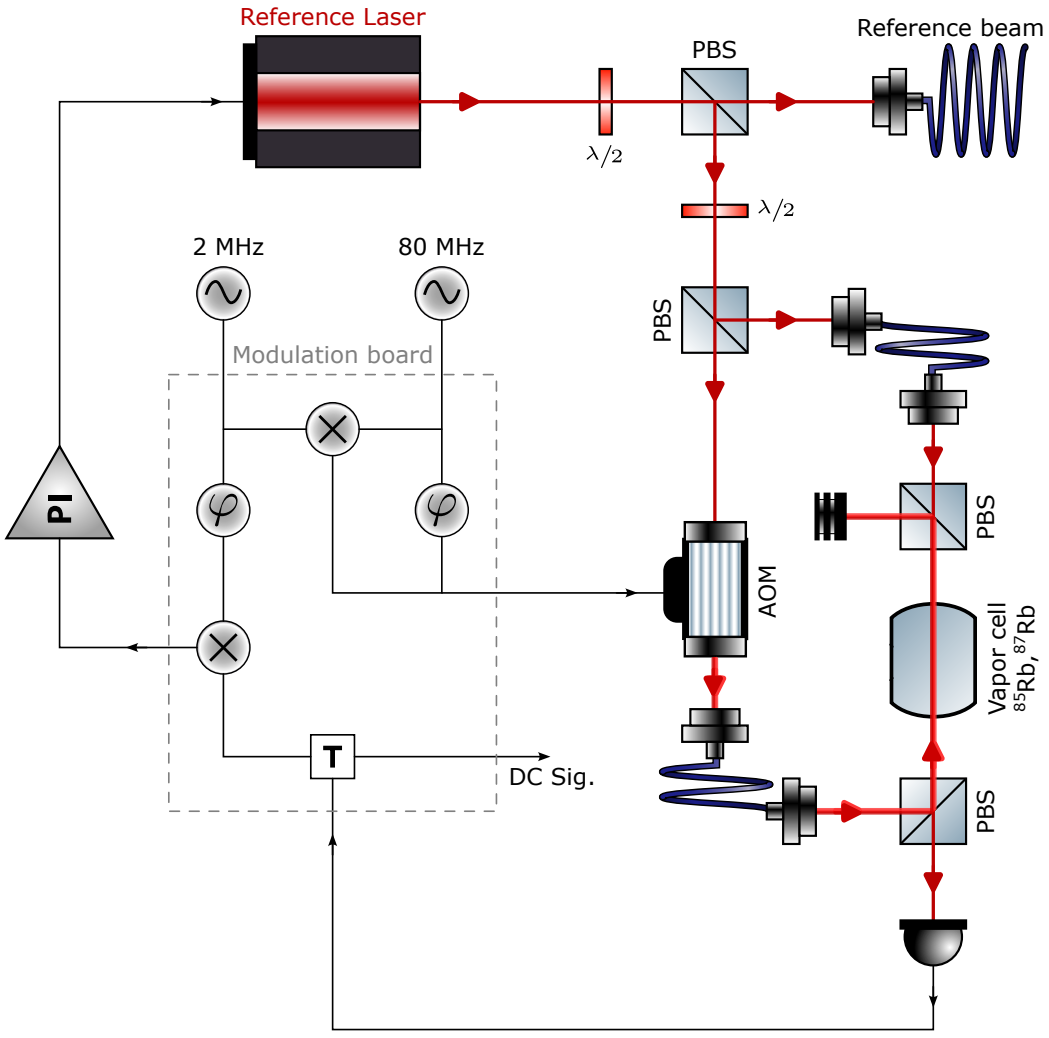

Figure 3.10: Optical and electronic configuration of the MTS setup. The figure was created using components from [Fra].

An external-cavity diode laser (ECDL, Sacher Lasertechnik, VBG-780-1120), locked to the $|F = 3\rangle \leftrightarrow |F' = 4\rangle$ hyperfine transition of the ^{85}Rb D_2 line, serves as the frequency reference for all optical tones addressing the atoms. At room temperature, Doppler broadening ($\approx 500\,\mathrm{MHz}$) covers the hyperfine features of the D_2 line. To achieve sub-Doppler resolution, we employ modulation transfer spectroscopy (MTS) [Shi82], a variant of saturation spectroscopy. MTS is based on four-wave mixing [RBS+80, DB82], in which the nonlinearity of the atomic medium mediates the interaction between two frequency components of the modulated

saturation beam and the counter-propagating probe beam, resulting in the generation of sidebands on the probe. The effect is most pronounced for closed transitions, such as the $|F = 3\rangle \leftrightarrow |F' = 4\rangle$ transition, due to the reduced population loss into other ground states. Demodulation of the beat of the transferred sidebands with the probe produces dispersive signals that are well-suited for laser frequency stabilization [ZWXP03, MKC08]. A key advantage of modulation transfer spectroscopy is that the zero-crossing of the dispersive signal consistently aligns with the center of the atomic resonance, intrinsically insensitive to variations in laser intensity, polarization, and temperature.

Figure 3.10 depicts the optical and electronic configuration of the MTS setup. The optical sidebands in the saturation arm are generated via the AOM operated in single-pass configuration, and driven by a multi-tone RF-signal comprising an $80\,\mathrm{MHz}$ carrier and two sidebands at $78\,\mathrm{MHz}$ and $82\,\mathrm{MHz}$. The RF-signal is synthesized on the modulation board by mixing (Mini-circuits, SRA-3+) a local oscillator ($80\,\mathrm{MHz}$) with a $\omega_m = 2\pi\times 2\,\mathrm{MHz}$ modulation tone to generate sidebands and combining these with the original $80\,\mathrm{MHz}$. A variable phase shifter (φ, Mini-circuits, PS-927) in the unmodulated arm allows fine adjustment of the relative phase between the carrier and the sidebands, enabling optimization of the MTS signal. To maintain spatial overlap among the three frequency components of the saturation beam, the modulated light is coupled into a polarization-maintaining fiber, which enforces common spatial mode propagation. Precise alignment is required to ensure balanced and homogeneous coupling of the sidebands. Collimation optics mounted on a fiber bench are used to overlap the saturation and probe beams within the room temperature Rb vapor cell.

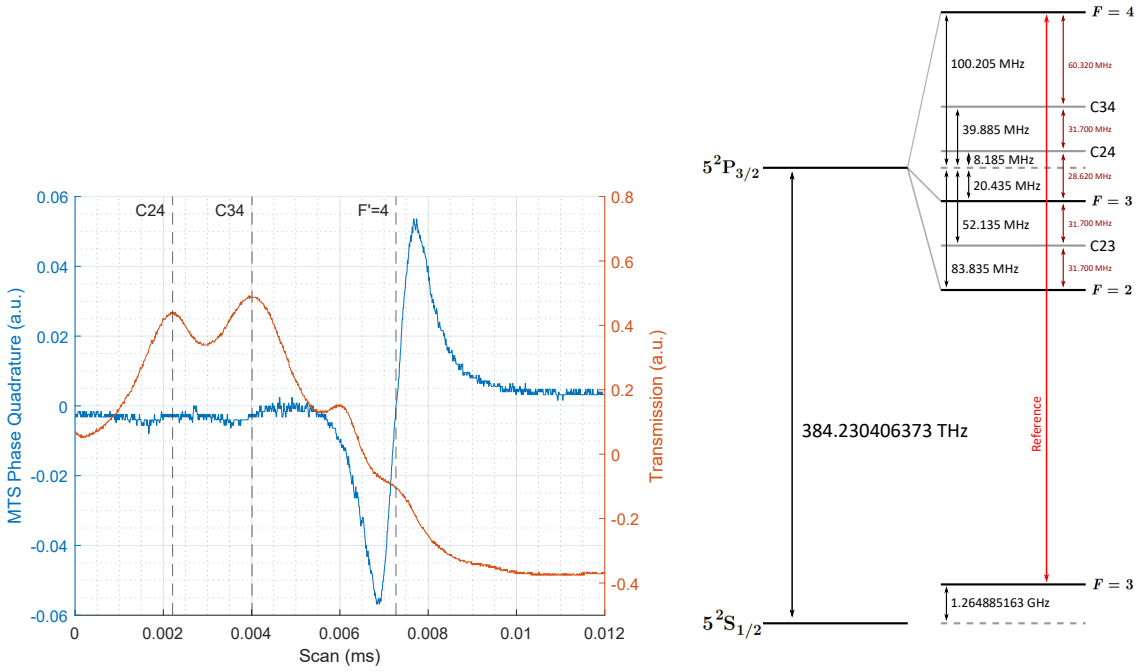

Figure 3.11: *Left:* Laser frequency scan through the ^{85}Rb $|F = 3\rangle \leftrightarrow |F'\rangle$ transitions. The phase quadrature (blue) and the saturation spectroscopy data (orange) are shown. Dashed lines indicate the $|F = 3\rangle \leftrightarrow |F'\rangle$ transition and the cross-over peaks C24 and C34. *Right:* Level scheme and frequency offset of the ^{85}Rb $|F = 3\rangle \leftrightarrow |F'\rangle$ transitions. Gray levels indicate the location of cross-over dips.

After modulation transfer during propagation through the vapor cell, the probe beam is

detected via a fast photodetector (Thorlabs, PDA10A2). The MTS signal is extracted via demodulation (Mini-circuits, RPD-1-1+) of the photodetector signal with the same $2\,\mathrm{MHz}$ tone as used for sideband generation. By tuning the demodulation tone's phase (φ, Mini-circuits, JCPHS-2.5+), the quadrature of the MTS signal can be chosen. The plot left in Fig. 3.11 shows the phase quadrature of the MTS signal (blue) over a laser frequency scan through the ^{85}Rb $|F=3\rangle \leftrightarrow |F'\rangle$ transitions. The obtained signal has the previously discussed dispersive character and its zero-crossing indicates the closed $|F=3\rangle \leftrightarrow |F'=4\rangle$ transition. For frequency calibration, we determine the atomic resonance frequency ω_a from the known hyperfine level splittings [Ste08], as illustrated in the schematic diagram on the right of Fig. 3.11 The frequency offset of $\Delta = 80\,\mathrm{MHz}$ between probe and saturation beam must be taken into account in this calibration. The resonance conditions for four-wave mixing are satisfied only for atoms with a Doppler shift $|kv| = \Delta/2$. As a result, the observed resonance occurs at a frequency

$$\omega = \omega_a - \frac{\Delta}{2}. \tag{3.8}$$

The orange trace in the spectroscopy plot represents the DC component of the detected signal, corresponding to the conventional saturation spectroscopy signal. The dashed lines mark the $|F'=4\rangle$ - transition and cross-over resonances, which arise as artifacts due to the finite linewidths and overlap of hyperfine transitions. The cross-over dips emerge at their mid-point frequency between hyperfine transitions [Foo05]. Note that power broadening almost hides the $|F'=4\rangle$ peak in the saturation signal but does not affect the MTS signal. The fourth resonance emerges between peaks C34 and $F'=4$ at high probe intensity. This feature originates from parasitic backscatter of the probe beam, leading to a self-induced saturation absorption. The dip is a copy of the C34 cross-over resonance shifted by a frequency of $\Delta/2$.

For laser frequency stabilization, the MTS signal is used as input for a home-built analog feedback circuit (PI), which in turn modulates the laser current. The feedback circuit was developed for frequency-offset locking. Details about the electronic configuration of the circuit can be found in [LDH22].

3.3.2 Offset Lock for $1560\,\mathrm{nm}$-Laser

A key requirement for the QND measurement in this experiment is homogeneous dispersive coupling of the two ^{87}Rb hyperfine ground states to the cavity mode (Sec.2.3.4). To achieve this, the cavity length is stabilized to the dipole-trap laser, which is itself offset-locked to a reference laser (Sec.3.3.1). The $780\,\mathrm{nm}$ tone used for dispersive coupling is derived from frequency doubling of this dipole-trap laser. Hence, the chosen offset defines the exact frequency of this $780\,\mathrm{nm}$ light.

In Fig. 3.9, the optical configuration of the offset lock is shown. The beat note between the reference laser and the frequency-doubled dipole trap laser is detected using a fast photodetector (Thorlabs, DX12DF). After amplification (Mini-Circuits, ZX60-83LN-S+), the beat signal is mixed (Mini-Circuits, ZX05-C24-S+) with a local oscillator (LO, Rigol, DSG836), which defines the frequency offset between the QND tone and the reference. The error signal, with a zero crossing at a beat frequency of $22.6\,\mathrm{MHz}$, is generated by frequency discrimination using the hybrid LC filter described in [LDH22]. The analog integrating circuit shown in Fig. 3.12 provides feedback to the laser's modulation port for frequency stabilization. The unity-gain bandwidth of the integrating operational amplifier (op-amp, OP27) is set to approximately $80\,\mathrm{Hz}$, which is deliberately kept low for two key reasons. First, it prevents interference with

the laser–cavity locking loop (Sec.3.3.3), which becomes dominant at frequencies above a few hundred Hz. Second, it suppresses frequency noise transfer from the reference laser with a linewidth of $\gamma < 3\,\mathrm{kHz}$ to the narrow linewidth dipole trap laser. To eliminate ground loops, the differential amplifiers LT1167 and AMP03 are used to isolate the ground of the feedback circuit from those of the frequency discriminator and the laser. In addition, the AMP03s at the circuit's output add an offset voltage (V^{off}) for tuning the laser frequency and a modulation signal (V^{MOD}) to the feedback signal. The modulation input port will later be connected to the laser-cavity feedback circuit. The resistor and the Zener diodes at the output ensure impedance matching and protect the laser's modulation port from voltage transients.

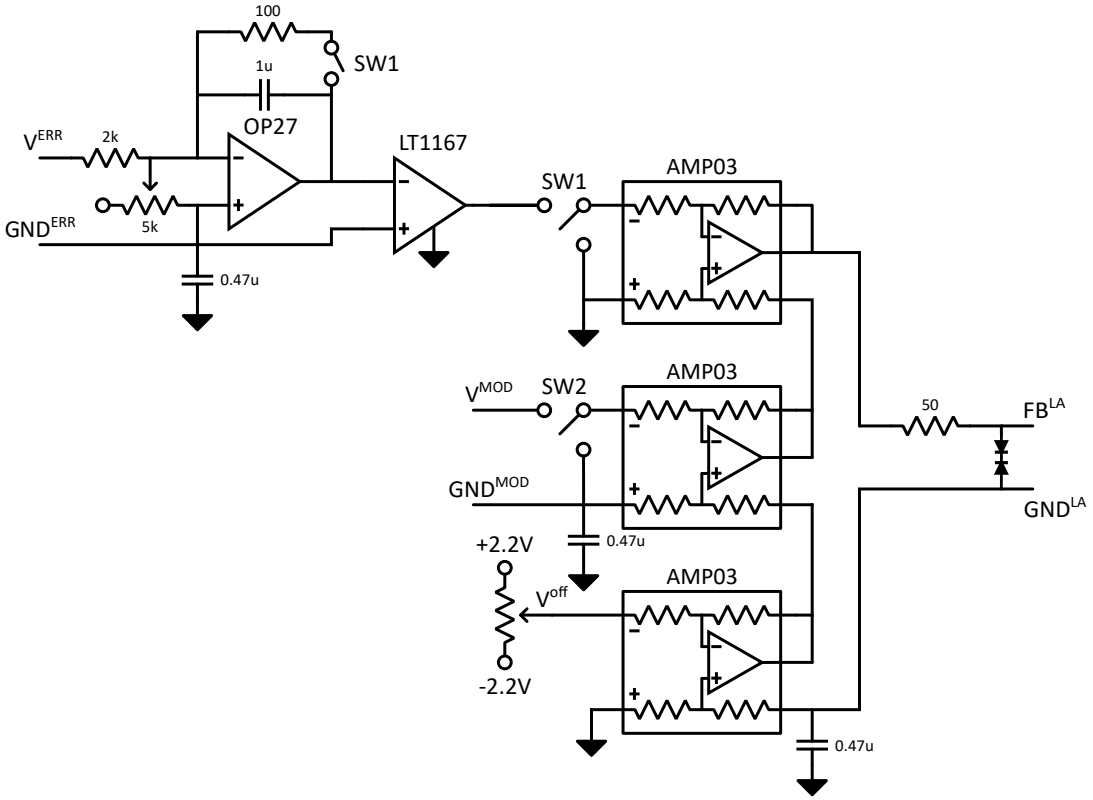

Figure 3.12: Offset lock feedback circuit for the $1560\,\mathrm{nm}$ laser

To determine the theoretical frequency offset, the dispersive shifts of the relevant hyperfine transitions are calculated using Eq. 2.71 with transition strength and frequency data taken from [Ste10]. The cavity resonance condition is then solved under the assumption of balanced dispersive shifts for the two ground states (Eq. 2.71). Accounting for the reference frequency (Eq.3.8) and the $22.6\,\mathrm{MHz}$ from locking, the resulting offset of the cavity resonance, and thus the QND tone, is $\Delta_{\mathrm{off}} \approx 2.062\,\mathrm{GHz}$.

3.3.3 Squash-Lock of Science Cavity

The frequency stability between the dipole trap laser and the science cavity is a crucial parameter for the experiment. Since the QND-measurement probe beam is derived from the dipole trap laser, any noise originating from the dipole laser-cavity lock will be transferred onto the QND measurement and will limit its performance. We aim for a lock stability that enables resolving single spin flips, which correspond to a frequency shift of $\frac{2g_0^2}{\Delta} = 4.3\,\mathrm{Hz}$.

We chose the squash lock method, developed in our lab [DZH24], to generate the error signal required for feedback. Compared to standard laser-cavity locking techniques, such as the PDH

[DHK+83] method, squash lock offers the advantage that it is a purely passive scheme that requires neither light modulation nor electronic demodulation.

As discussed in Sec. 2.3.1, the cavity has a non-degenerate Hermite-Gaussian mode spectrum. Squash lock exploits this non-degeneracy by detecting spatial mode interference of the reflected input light. The incident beam is prepared with a slightly elliptical profile, composed of the fundamental Hermite-Gaussian H_{00} mode and a small admixture of the '+' mode, which is an equal superposition of the second-order modes, H_{20} and H_{02}, with a relative phase shift of π. The relative phase between the fundamental and the '+' mode is encoded in the ellipticity of the beam.

On cavity resonance, the '+' component is reflected, while the buildup of the H_{00} mode in the cavity induces a relative phase shift between the modes. Consequently, monitoring the beam ellipticity provides a measure for frequency discrimination. To do so, we detect the reflected light with a quadrant photo diode (QPD) at the position where the modes are matched in beam diameters. The difference between the sums of the QPD's diagonal segments yields a signal proportional to the beam ellipticity, resulting in a dispersive error signal. Frequency shifts on opposite sides of the cavity resonance result in opposite ellipticities of the reflected beam. Figure 3.13 illustrates the beam ellipticity detection with a QPD and the resulting dispersive signal used for feedback.

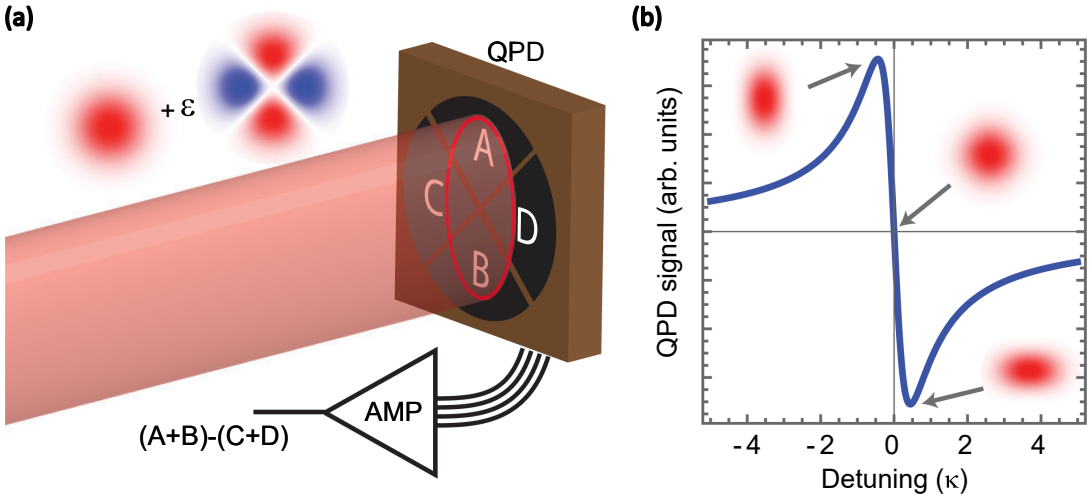

Figure 3.13: (a) Ellipticity detection with a QPD, and mode composition of a slightly elliptic beam, where ϵ is a small complex number. (b) Laser frequency dependent QPD signal near the fundamental cavity mode with linewidth κ. Figures taken from [DZH24].

Beam shaping and propagation

The optical squash lock setup was shown in Fig. 3.3. We use an adjustable aspherical fiber collimator (CFC8A-C, Thorlabs) mounted on a five-axis stage to align and mode match the incident beam with the cavity mode. The beam ellipticity is introduced by two plano-convex cylindrical lenses (LJ1277L1-C,Thorlabs) that are mounted on the same base as the collimator. The distance between the cylindrical lenses is matched to the average Rayleigh length of the cavity mode $z_R = 5\,\mathrm{cm}$ (Table 3.1) to induce a π phase shift between the sagittal and tangential planes around the cavity mode waist, which is required to excite the '+' mode.

Fig. 3.14 shows the beam propagation simulation for mode matching and squash lock alignement. The dashed red line indicates the cavity mode, while the blue and orange lines

represent the incident beam diameter in the sagittal and tangential planes, respectively. The focal length of the collimator lens defines the distance to the cavity, and the cylindrical lenses displace the beam waists of the optical planes. The collimator is adjusted so that the incident beam matches the cavity mode waist in both optical planes, but with a position symmetrically displaced around the cavity waist position.

This intentional mode mismatch between the incident beam and the cavity mode leads to excitation of the H_{20} and H_{02} modes, while the waist displacement introduces the π phase shift necessary to form the '$+$' mode. In our setup, the coupling strength of both the H_{20} and H_{02} modes is approximately 5% relative to the fundamental mode.

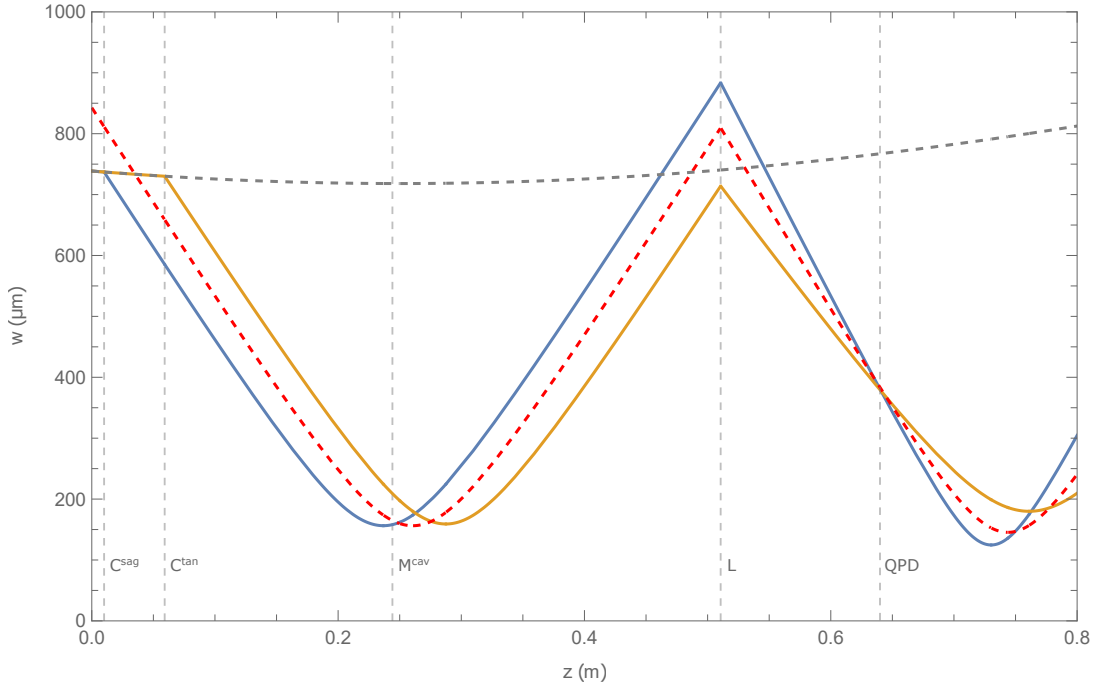

Figure 3.14: Mode matching simulation for squash lock. Blue and orange lines represent the propagated beam diameter of the incident beam in the sagittal and tangential planes. The dashed red line indicates the average cavity mode. Vertical dashed grey lines indicate the position of the optical elements: Cylindrical lenses (C^{sag}, C^{tan}), reflecting cavity mirror (M^{cav}), collector lens (L), and QPD. The dashed dark grey beam corresponds to the freely propagating output from the collimator.

Vertical dashed gray lines indicate the position of optical elements in Fig. 3.14. From the position of the cavity mirror (M^{cav}), the propagated beams indicate the incident reflected beam and the out-coupled cavity mode. As described before, the measurement of the beam ellipticity gives a dispersive signal when the QPD is positioned where the beam diameters of the cavity mode and the reflected beam are matched. To do so, a collector lens (L, LA1986-C, Throlabs) is integrated into the optical path to focus the diverging beams. Restricted by the available space, the focal length of the collector lens and its position were chosen to match the beam diameter with the cross-section of the QPD (G6849, Hamamatsu).

All quadrants of the QPD are individually amplified with a home-built transimpedance amplifier circuit, which has a transimpedance gain of $10\,\mathrm{k\Omega}$ and a $1.59\,\mathrm{MHz}$ bandwidth. A separate operational amplifier circuit performs the arithmetic operations that give simultaneous access to the diagonal, left-right, up-down, and sum channels, all required to align and center the QPD on the cavity reflection. Small mismatches in the QPDs' alignment to the incident wavefront and

residual ellipticity can be compensated with adjustable weights of the diagonal sums. During a typical QPD alignment procedure, we first simultaneously zero the left-right and up-down channels before compensating a potential offset of the diagonal channels' zero-crossing with the weights of the diagonal sums.

In typical experiments, the maximum input beam intensity ranges from $3 - 4.5\mathrm{mW}$. In order to avoid saturation of the QPD transimpedance circuit, an absorptive neutral density filter (NENIR506B-C) is used to attenuate the optical input. To give a figure of merit, a typical peak-to-peak amplitude of the error signal is in the range of $V_{pp} = 0.5 - 1\mathrm{V}$, when the cavity length is slowly modulated through resonance.

Except for having the experimental setup mounted on a floatable optical table, vibration isolation or thermal isolation was not considered in the experimental design. Therefore, acoustics and thermal fluctuations are transmitted to the cavity body and are sources of cavity length fluctuations. To mitigate these fluctuations, we implemented three feedback layers that address separate noise frequency bands to stabilize the cavity length and laser frequency. In the following, we will discuss all three feedback layers and the configuration of their analog feedback circuits.

Cavity Length Stabilization

The cavity length is controlled with a linear slip-stick stage (Smaract, SLC-1720-UHV), which adjusts the position of the curved cavity mirror. A slip-stick stage operates based on a piezoelectric cantilever that drives a slider. In typical operation, the cantilever is actuated with a sawtooth signal. During the ramp, the slider sticks to the cantilever and is pushed forward, while the inertia of the slider prevents it from following the sharp movement of the cantilever caused by the rapid voltage drop, resulting in a stepwise displacement of the slider. Such stages offer a wide movement range, ideal for the cavity length adjustment discussed in Sec. 3.2.5.

However, for cavity length stabilization, the position increment of $1\,\mu\mathrm{m}$ in slip-stick mode, corresponding to a resonance shift of $6.5\,\mathrm{GHz}$, is far too coarse. To achieve precise control of the stage position, we developed an analog control circuit, with its circuit diagram shown in Fig. 3.15. The circuit operates the stage solely in stick mode around an adjustable offset. A battery-powered $90\,\mathrm{V}$ source provides a low-noise control voltage, while two trimpots enable coarse and fine tuning of the cavity length. Since the opamps can only output signals within $\pm 11\mathrm{V}$, the battery-powered output is connected to the positive, high-voltage input of the linear stage, whereas the feedback signal is applied to the floating ground of the stage. The feedback part of the circuit consists of a single operational amplifier (OPA277) in an integrating circuit configuration with a cut-off frequency of $8\,\mathrm{Hz}$. The mechanical inertia of the linear stage prevents a large feedback bandwidth, and in the presented configuration, the stage should mainly compensate for slow thermal and seismic drifts. In addition, the circuit enables modulation of the cavity length with a ground-separated source, which eases tuning of the cavity length into resonance with the laser.

Laser Frequency Stabilization

In the context of laser stabilization to a cavity, we have to introduce the concept of feedback and stability, with a more detailed discussion in Appendix A. We aim to stabilize a system to a set point, a certain output condition, like the frequency of a laser to match a cavity resonance. Intrinsic drifts or external effects cause the system to deviate from this set point. A feedback

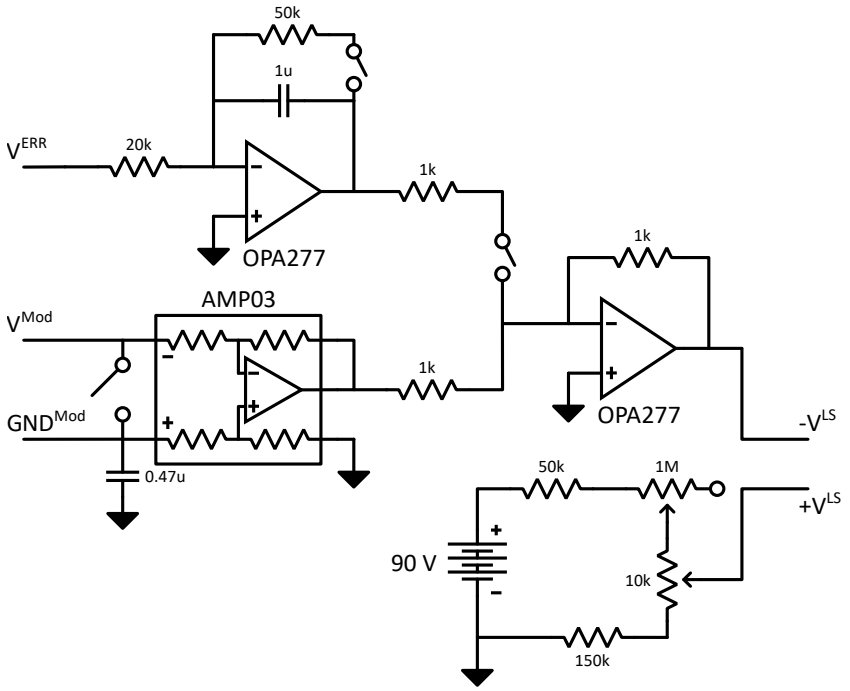

Figure 3.15: Control circuit for the linear stage. The linear stage is operated in stick-modes around a positive DC offset applied to the positive stage input ($+V^{LS}$) from a battery source. The feedback part consists of a single integrating opamp circuit with a cut-off frequency of $8\,\mathrm{Hz}$. The opamp adder circuit driving the floating linear stage ground ($-V^{LS}$) combines the feedback signal with a modulation signal from a ground-separated source.

loop discriminates this deviation and applies arithmetic operations to this discriminator to generate a control signal for the system to suppress the deviation. The closed-loop gain of the feedback loop becomes the suppression factor of the deviation that we aim to maximize. At this point, the frequency response of the entire feedback network becomes relevant. If the feedback signal component at the loop unity-gain frequency reaches or surpasses a phase shift of π , the feedback circuit will amplify the error. The feedback circuit becomes unstable, and we observe ringing at this frequency, which also defines the bandwidth of the feedback circuit. The 'art' in feedback circuit design is to optimize the frequency response of the circuit to achieve the largest possible loop gain and bandwidth [FOH03].

For the discussed laser feedback, we primarily account for the frequency responses of the laser and the cavity. The detector, with a bandwidth of $1.59\,\mathrm{MHz}$, is sufficiently fast and will not limit the circuit performance. Laser and cavity represent both low passes. The $1560\,\mathrm{nm}$ dipole trap laser (Oewaves, OE4030) is an external cavity diode laser based on a whispering gallery mode resonator. The laser is modulated via piezoelectric strain on the resonator, which limits the modulation bandwidth to approx. $50\,\mathrm{kHz}$. The low-pass behavior of the cavity originates from the cavity linewidth ($\kappa = 29\,\mathrm{kHz}$), where the intra-cavity photon lifetime limits the response to a fast external modulation.

Fig. 3.16 shows the schematic diagram of the analog feedback circuit that we developed to lock the $1560\,\mathrm{nm}$-laser to the science cavity. The circuit applies operational amplifiers (OP27) in a double-integrator configuration. Operational amplifiers are electronic linear devices that offer high open-loop gain with a frequency response that can be precisely adjusted by the input and feedback impedance of the op-amp network. An excellent introduction to op-amps and their application for analog feedback is given in [CM17]

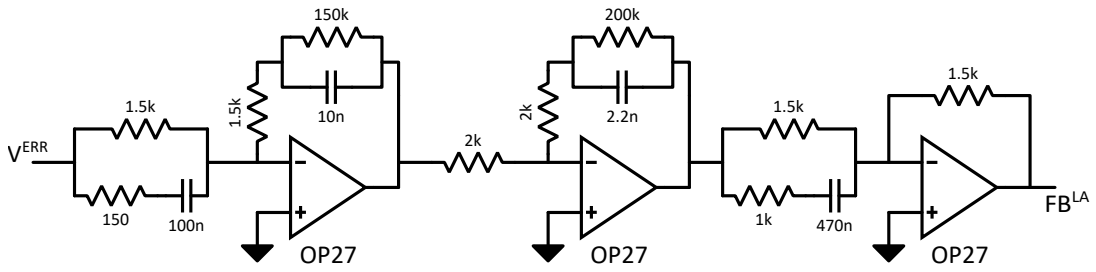

Figure 3.16: Schematic diagram of the $1560\,\mathrm{nm}$-laser feedback circuit.

Conceptually, each integrator addresses a specific system within the feedback network, where the feedback impedance in the high-pass configuration compensates for the low-pass characteristic of the subsystem. During circuit development, the corner frequency of the feedback impedance is first matched with the expected low-pass cut-off frequency and then adjusted to optimize the feedback performance. The optimum performance of the presented circuit was achieved with the corner frequencies $10.6\,\mathrm{kHz}$ and $36.2\,\mathrm{kHz}$, respectively. Not shown in the diagram is the buffered voltage divider at the circuit's input, which is used to fine-tune the overall gain close to instability. By observing the ringing frequency and adding filter elements at the integrator input impedance, we can further push the bandwidth and gain of the feedback circuit. The bandwidth of the shown laser-feedback circuit is $\mathrm{BW}_{1560} \approx 110\,\mathrm{kHz}$, likely limited by the second harmonic of the laser's internal piezo.

As discussed in Sec. 3.3.2, the dipole trap laser is offset locked to the ^{85}Rb $|F=3\rangle \leftrightarrow |F'=4\rangle$ transition with a low bandwidth of approximately $80\,\mathrm{Hz}$. The laser must follow the frequency reference in the low-frequency band, but be locked to the cavity at higher frequencies to suppress acoustically induced noise. To avoid interference with the offset lock, the integrators of the feedback circuit have finite DC gain, and a $340\,\mathrm{Hz}$ high-pass at the circuit's output suppresses low-frequency components.

Structural Resonance Damping

In the current feedback configuration, the dominant noise source is a structural resonance of the cavity's mirror holder at $3.5\,\mathrm{kHz}$. Mechanical analysis of the L-shaped holder performed in COMSOL revealed a mode within this frequency range that couples directly to the cavity length.

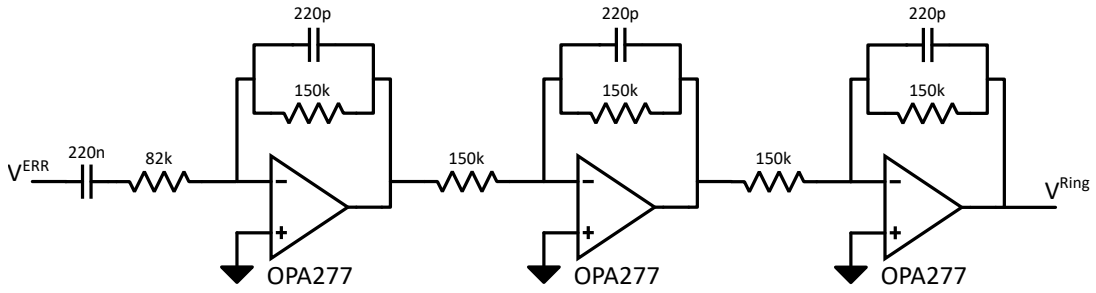

Figure 3.17: Circuit diagram of the third-order filter for ring piezo feedback.

In order to address this resonance, a third-order filter was implemented to apply feedback to the ring piezo, on which the cavity mirror is mounted. The schematic circuit diagram of the filter is shown in Fig. 3.17 The filter bandwidth is $4.8\,\mathrm{kHz}$, with the $9\,\mathrm{Hz}$ high-pass at the input preventing cross-coupling to the linear stage. A suppression of the structural resonance by a factor of four was observed. Depending on the residual laser-cavity noise observed with

homodyne detection, further optimization of the filter circuit to achieve a larger suppression might be required.

3.3.4 Side-of-the-Fringe Lock of the $1527\,\mathrm{nm}$-Laser

For compensation of the dipole trap-induced AC-Stark of the $5P_{3/2}$ state, a $1527\,\mathrm{nm}$ tone is coupled to the cavity (Fig. 3.3). To avoid interference of the $1527\,\mathrm{nm}$ tone with the $1560\,\mathrm{nm}$ squash lock detection, the tone is coupled to the perpendicular p-polarization mode from the counter-propagating direction. The perpendicular polarization of the transmitted light allows, as shown in Fig. 3.3, separation from the dipole trap light with a PBS and detection of the transmitted power (PD: Thorlabs, FDG05; amplifier: Koheron, TIA100). To simultaneously stabilize the transmitted power and the laser frequency, we applied the side-of-the-fringe (SOF) locking method.

In SOF-locking, the frequency discriminator is obtained by subtracting the cavity transmission signal from a defined offset, typically set to the half-maximum of the cavity transmission. If it is intended to stabilize the laser to the exact cavity resonance, SOF locking is disadvantageous because the lock becomes unstable at the cavity resonance frequency. Another disadvantage of SOF-locking is that it maps laser intensity noise into frequency noise.

However, for AC-Stark shift compensation, where the stability of the intra-cavity power is essential, SOF-locking offers an advantage. The laser input power can be kept constant, while the set point, defined by the experimental control software, determines the frequency detuning from the cavity resonance frequency, and thus the transmitted power.

Following the procedure described for the dipole trap laser stabilization (Sec. 3.3.3), the feedback design must take the properties of the laser and the cavity into account. The $1527\,\mathrm{nm}$ fiber laser (NP Photonics, the Rock module) has a modulation bandwidth of $14\,\mathrm{kHz}$, with mechanical resonances at $50\,\mathrm{kHz}$ and $100\,\mathrm{kHz}$, while the p-polarized cavity mode at $1527\,\mathrm{nm}$ has a linewidth of $99.8\,\mathrm{kHz}$ (Tab. 3.2). A challenge in SOF-lock optimization is the narrow locking range between the chosen set point and the cavity resonance. Any noise source or overcorrection by the feedback loop that drives the laser frequency across the cavity resonance leads to loss of the lock. To improve stability and simplify gain adjustment of the laser feedback loop, a second feedback branch was added to address high-frequency noise.

As illustrated in Fig. 3.9, feedback is applied to a voltage-controlled oscillator (VCQ, Mini-Circuits, ZOS-150+), which drives an AOM and thereby controls the optical input for the cavity. Consequently, VCO-driven AOMs enable fast and precise tuning of the frequency of the light. In the presented setup, the modulation bandwidth of the AOM is limited by the VCO, with a bandwidth of $100\,\mathrm{kHz}$.

Fig. 3.18 shows the diagram of the VCO feedback circuit. Not shown are the buffered voltage dividers to adjust the input amplitude of the error signal (V^{ERR}) and the differential amplifier circuit following the output to combine the feedback signal with an offset voltage, defining the center frequency of the VCO output ($80\,\mathrm{MHz}$). Similar to the feedback circuit for the dipole trap laser (Sec. 3.3.3), the circuit consists of two integrating op-amps with limited DC-gain. The high-passes in the feedback impedance with corner frequencies of $100\,\mathrm{kHz}$ and $80\,\mathrm{kHz}$ compensate for the low-pass characteristics of the cavity and the VCO. A further $800\,\mathrm{Hz}$ high-pass between the op-amps serves to decouple the VCO feedback from the laser feedback loop. The input impedance configurations of the op-amps were adjusted to optimize the feedback bandwidth, yielding $230\,\mathrm{kHz}$.

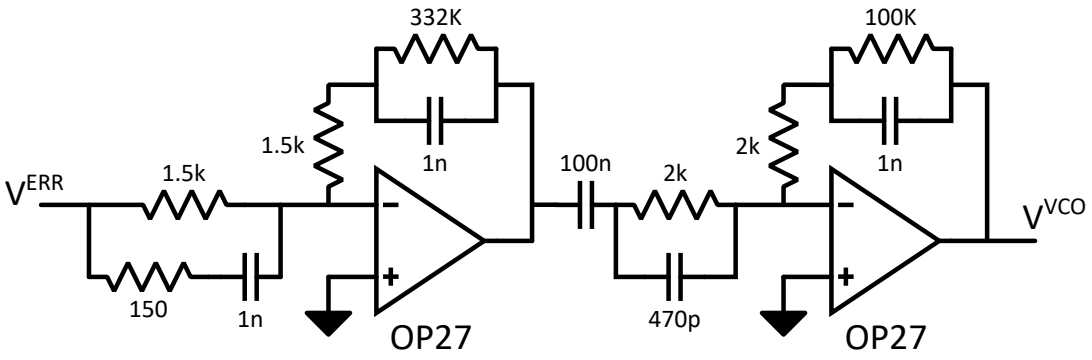

Figure 3.18: Diagram of the VCO feedback circuit

The introduction of the VCO feedback reduced the requirements for the $1527\,\mathrm{nm}$ laser feedback to only compensate for slow drifts of the laser frequency. Fig. 3.19 shows the simple PI-configuration of the laser feedback circuit. The first op-amp amplifies the error signal proportionally by a factor 4, while the second, integrating op-amp has a unity gain at $100\,\mathrm{Hz}$. Not shown in the diagram is a buffered voltage divider at the circuit's input for overall gain adjustment. Also not shown are a voltage offset and a modulation channel, which are both summed to the feedback signal. The offset enables tuning the laser frequency, and the modulation allows scanning through the resonance.

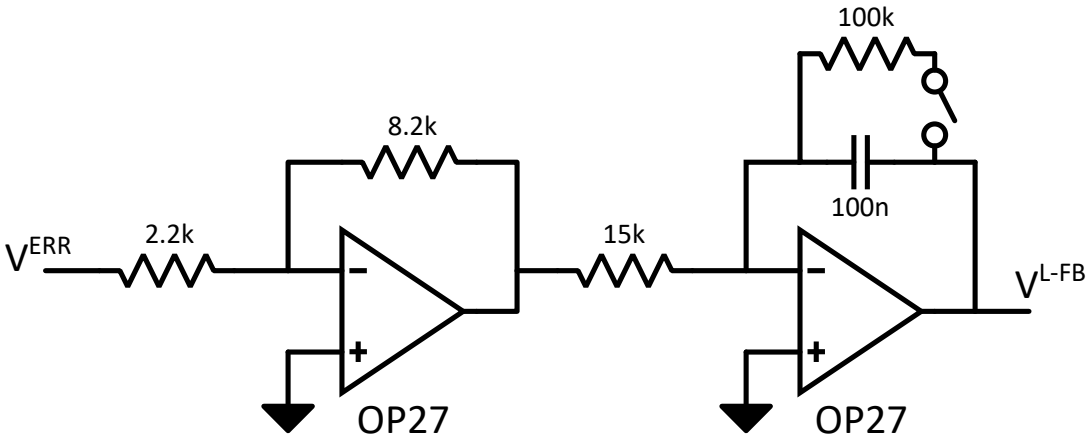

Figure 3.19: Diagram for the $1527\,\mathrm{nm}$ laser feedback circuit

3.3.5 Bias-Feedback for Electro-Optic I/Q Modulators

In the following subsection, we will describe the function of electro-optic I/Q modulators and a bias voltage feedback method that we developed to stabilize the modulator in carrier-suppressed single-sideband mode. The subsection is based on the paper [WDH23] that we prepared during this study.

Electro-optic modulators (EOMs) are key elements for modern telecommunication technologies [WKYY+00]. In atomic, molecular, and optical physics, they are widely used to lock lasers to optical cavities [DHK+83], to frequency offset lock lasers [JHKwC10, GLWT22] and to shift the frequency of a single laser [ZLH+18, THC+21].

Waveguide-based EOMs integrating nonlinear crystals, such as lithium niobate, enable broadband electronic phase modulation of the transmitted light up to tens of GHz [BBC62]. More complex waveguide structures allow further applications. A single Mach-Zehnder interferometer (MZI) structure enables amplitude modulation and a dual-parallel MZI structure gives simultaneous access to the phase and amplitude of the transmitted light (I/Q modulator) [ISS81, CSS+04]. The phase bias between the internal MZI arms defines the operating mode of the modulator. For example, an I/Q modulator can be operated in either single-sideband (SSB) or carrier-suppressed single-sideband mode (CS-SSB).

Internal charge and external environmental fluctuations can induce drifts of these phase biases, which in turn, reduce the effectiveness of amplitude and I/Q modulators [Šv10]. Especially for high-precision experiments, these drifts can induce phase and amplitude noise. Hence, active stabilization of the phase biases is required. Prior and commercially available stabilization schemes rely on weak modulation of the phase bias voltage, adding dither tones in the kHz range with an amplitude of several tens or hundreds of mV to the bias voltage. This modulation is transferred to the optical carrier and an error signal can be extracted from the monitored optical signal. In [FOSE13], bias voltages were modulated with different dither frequencies and stabilized with lock-in amplifiers. Other commercially available feedback modules (Thorlabs, MX10A; iXBlue, MBC-IQ-LAB) modulate the phase biases with a single frequency dither and obtain the error signals by digital analysis of the optical spectrum [BNLR+11]. For amplitude modulators, ditherless bias control is possible. Thereby, the bias voltage is stabilized to a set value or the ratio between the modulator's optical input and output is stabilized by continuous adjustment of the phase bias. Such schemes are not applicable for electro-optic I/Q modulators because bias voltage stabilization cannot compensate modulator drifts and ratio stabilization is not able to adjust drifts, since access to individual internal interferometer outputs is not available.

Here, we make use of a small auxiliary modulation to realize a stabilization method for electro-optic amplitude and I/Q modulators instead of dithering the phases of the device's interferometers. In particular, using a telecom band electro-optic I/Q modulator, we apply an auxiliary $2\,\mathrm{MHz}$-modulation to generate a set of sidebands (SB) in addition to the primary modulation sidebands of interest that lie in the GHz range. The beat signals between these sidebands and the optical carrier allow us to generate the phase bias error signals using standard RF-mixers. A home-built, all-analog feedback circuit receives the error signals and stabilizes the corresponding phase biases. The single auxiliary tone allows us to efficiently stabilize all three interferometers of the modulator in comparison to other methods, and in principle permits smaller modulations due to bypassing technical noise problems at kHz frequencies.

Below, we first review the use of an I/Q modulator as a CS-SSB generator, and describe our method of obtaining error signals for all three phase biases. Then we discuss the experimental

setup and the developed circuitry including the home-built demodulation and feedback circuits. Finally, we show experimental results for the generated error signals and demonstrate the stability of the locked modulator in CS-SSB mode.

Electro-Optic I/Q Modulator

The dual-parallel Mach-Zehnder structure of a fiber-coupled, electro-optic I/Q modulator is illustrated in Fig. 3.20. Each sub-MZI ($MZI_{A,B}$) can be individually modulated via separate RF-ports. The three DC-ports ($V^{DC}_{A,B,P}$) allow tuning of the relative phase between the MZI arms ($\Phi_{A.B}$) and between the sub-MZIs (Φ_P). By applying an RF-tone with frequency Ω, both arms of a single sub-MZI are phase modulated. For CS-SSB generation, the applied RF-modulation has a $\pi/2$-phase between the two RF-ports. This shifts the phase of the generated sidebands by 90 degrees between the two sub-MZIs as depicted in Fig. 3.20. The generated sidebands within each sub-MZI have a relative phase of π between the upper and lower arms. This allows the optical carrier with frequency ω_0 to destructively interfere at the outputs of the sub-MZIs while the sidebands interfere constructively when the phase bias between the arms is tuned to $\Phi_{A,B} = \pi$. With the adjustment of the phase bias between the arms of the outer-MZI to $\Phi_P = \pi/2$ or $\Phi_P = -\pi/2$, the upper or lower sideband destructively interferes and the output of the modulator is a CS-SSB with the frequency $\omega_0 + \Omega$ or $\omega_0 - \Omega$, respectively.

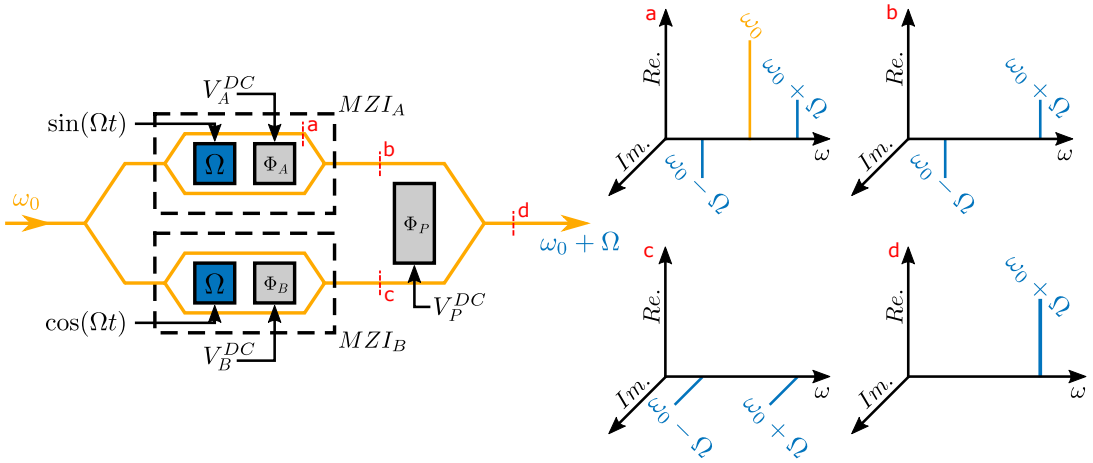

Figure 3.20: Left: Schematic of an electro-optic I/Q modulator. The dual-parallel MZI structure enables simultaneous amplitude and phase modulation. For CS-SSB generation, the sub-MZIs ($MZI_{A,B}$) are modulated with frequency Ω and a relative phase of $\pi/2$. By tuning the control voltages $V^{DC}_{A,B,P}$, the corresponding phase biases are adjusted to $\Phi_{A,B} = \pi$ and $\Phi_P = \pi/2$. The optical carrier (ω_0) and one sideband ($\omega_0 - \Omega$) are suppressed. Right: Optical frequency spectra at the marked locations in the schematic. (a) Phase modulation of the carrier. (b,c) Output of $MZI_{A,B}$. The phase bias $\Phi_{A,B} = \pi$ between their arms leads to destructive interference of the carrier. (d) The combination of the sub-MZI with a phase bias $\Phi_P = \pi/2$ generates a single-sideband.

Error Signal Generation

Inadvertent drifts in the phase biases require their continuous adjustment over the course of hours. To sense and correct for these drifts we apply a weak auxiliary modulation at a relatively low frequency ($\Omega_{LF} = 2\pi \times 2\,\mathrm{MHz}$) that generates sidebands, which beat with each other and the carrier. In order to describe this beat signal, we assume a single tone optical carrier at

the I/Q modulator input, represented by the electric field amplitude $E_{in} = E_0 \exp(-i\omega_0 t)$. We evaluate the output for a single MZI, where the phase shifts for the upper and lower arms are $\pm\Phi/2$, where $\Phi = \phi + \pi + \delta$. Here, ϕ is the phase modulation, π is the target phase bias between the MZI-arms and δ is a small perturbation of the phase bias. The output field of such a MZI is given by

$$E_{out}^{MZI} = \frac{E_{in}}{2}\Big[\exp(-i\Phi/2) + \exp(i\Phi/2)\Big]. \tag{3.9}$$

In case of small ϕ and δ, Eq. 3.9 can be simplified using the linear terms of its Taylor expansion. The output fields of the two sub-MZIs of our I/Q modulator can then be expressed as:

$$\begin{aligned} E_{out}^{MZI_A} &= -\frac{E_0}{4}\Big[2\beta\exp(-i\omega_0 t)\sin(\Omega_{LF}t) + \delta_A\exp(-i\omega_0 t)\Big] \\ E_{out}^{MZI_B} &= -\frac{E_0}{4}\Big[2\beta\exp(-i\omega_0 t)\cos(\Omega_{LF}t) + \delta_B\exp(-i\omega_0 t)\Big] \end{aligned} \tag{3.10}$$

Here, δ_A is the phase bias error of MZI_A, δ_B is the phase bias error of MZI_B, β is the modulation depth, Ω_{LF} is the modulation frequency and $\sin(\Omega_{LF}t)$, $\cos(\Omega_{LF}t)$, respectively originates from the phase of the modulation signal. As seen from the last terms of Eqs. 3.10, the residual optical carrier at the sub-MZI outputs are directly proportional to the phase bias errors. The bias errors do not affect the sidebands (the first terms of Eqs. 3.10) at this order of approximation. Next, we calculate the output field of the complete I/Q modulator. Similar to Eq. 3.9, we take the phase bias for the outer MZI, $\Phi_P = \pi/2 + \delta_P$, into account to derive the following expression:

$$E_{out}^{tot} = E_{out}^{MZI_A}\exp(i\Phi_P/2) + E_{out}^{MZI_B}\exp(-i\Phi_P/2). \tag{3.11}$$

After applying the first-order approximation for the small phase bias error δ_P and only considering first-order phase errors, we get the following expression for the output field:

$$\begin{aligned} E_{out}^{tot} = -\frac{E_0}{4}\exp[-i(\omega_0 t)]\Big\{&\Big[(2\beta + i\beta\delta_P)\sin(\Omega_{LF}t) + \delta_A\Big]\exp(i\pi/4) \\ &+ \Big[(2\beta - i\beta\delta_P)\cos(\Omega_{LF}t) + \delta_B\Big]\exp(-i\pi/4)\Big\} \end{aligned} \tag{3.12}$$

By taking the Euler identity and the exponential identity of the trigonometric functions into account we can simplify Eq. 3.12 to:

$$E_{out}^{tot} = -\frac{E_0}{4}\exp[-i(\omega_0 t + \pi/4)]\Big[2\beta\exp(i\Omega_{LF}t) - i\beta\delta_P\exp(-i\Omega_{LF}t) + i\delta_A + \delta_B\Big] \tag{3.13}$$

The power which is detected with a photodiode is proportional to $|E_{out}^{tot}|^2$. Retaining only first-order terms in the phase errors, we get:

$$|E_{out}^{tot}|^2 = \frac{E_0^2}{4}\Big[\beta^2 + \delta_A\beta\sin(\Omega_{LF}t) + \delta_B\beta\cos(\Omega_{LF}t) - \delta_P\beta^2\sin(2\Omega_{LF}t)\Big] \tag{3.14}$$

Eq. 3.14 shows that the sine and cosine quadratures of the beatnote observed at the photodiode at frequency Ω_{LF} give access to the phase bias errors δ_A, δ_B, and that the beatnote tone at frequency $2 \times \Omega_{LF}$ gives access to the phase bias error δ_P. Each of these bias errors can be extracted independently by demodulating three copies of the beatnote signal.

In principle, it is possible to use the primary modulation for error signal generation. However, the primary modulation often gets tuned or switched on and off during an experimental sequence. Thus, an additional weak auxiliary modulation can be applied to continuously generate an error signal for the phase biases. We choose the frequency of this modulation to be $2\,\mathrm{MHz}$, where it can be conveniently processed with standard RF-components.

The schematic frequency spectrum in presence of both the auxiliary (Ω_{LF}) and the primary (high frequency, Ω_{HF}) modulations is shown in Fig. 3.21a. The modulations are depicted in a configuration where the lower sidebands are transmitted, with the dashed lines indicating suppressed frequency components. Drifts of the phase biases cause reappearance of the suppressed components as dictated by Eq. 3.14. However, utilization of the generated error signals in a feedback loop that controls the phase biases acts to keep these components suppressed – by keeping the condition $\delta_{A,B,P} = 0$. Importantly, due to the broadband nature of the modulator, the sidebands at Ω_{LF} and Ω_{HF} are always correlated: suppressing a sideband at Ω_{LF} also suppresses the corresponding sideband at Ω_{HF}. Furthermore, potential deviations from this ideal behavior can easily be corrected by fine-tuning the locking points of the phase biases.

Experimental Setup

The schematics of the experimental setup is shown in Fig. 3.22. A $1560\,\mathrm{nm}$ laser (OEwaves, Hi-Q OE4030) is fiber coupled to an electro-optic I/Q modulator (Thorlabs, LN86S-FC). The RF-inputs for the modulator are generated by a circuit that combines primary and auxiliary modulation tones. The primary tone with frequency $\Omega_{HF} = 2\pi \times 3.6\,\mathrm{GHz}$ (chosen for future experimental considerations discussed below) and the auxiliary tone with frequency $\Omega_{LF} = 2\pi \times 2\,\mathrm{MHz}$ are split separately with $90°$-hybrid splitters. Then, the primary and the auxiliary tones are combined into two channels, where one channel has an additional phase of $\pi/2$ for both tones. The input power at the RF-ports for the Ω_{HF}-modulation is $23\,\mathrm{dBm}$ corresponding to a modulation depth of $\beta_{HF} \approx 2.23$ – defined as $\beta = \pi(V_{mod}/V_\pi)$, where V_π is the modulator's half-wave voltage ($V_\pi = 4.5\,\mathrm{V}$). For the auxiliary modulation, the power is $-6\,\mathrm{dBm}$ corresponding to a modulation depth of $\beta_{LF} \approx 0.08$, making the weak modulation analysis (Eq. 3.10 and Eq. 3.14) applicable. The bandwidths of the hybrid splitter for the HF-tone (Mini-circuits QCN-45D+) was chosen to match the requirements of our intended application. Its replacement with a splitter with larger bandwidth can enable the application of the presented locking scheme at higher primary modulation frequencies.

Fig. 3.21b-c shows the spectrum of the output of the I/Q modulator in CS-SSB mode. For this measurement, the laser frequency was ramped through manipulation of the laser current and the transmission through a home-built $63\,\mathrm{kHz}$-linewidth cavity was detected. The optical carrier and the upper Ω_{HF}-SB are suppressed by $-29.3\,\mathrm{dB}$ and $-30.7\,\mathrm{dB}$ respectively, relative to the maximized lower Ω_{HF}-SB. The auxiliary modulation generates a weak CS-SSB with a $-25.5\,\mathrm{dB}$ peak relative to the maximized Ω_{HF}-SB.

In order to detect the beat signal, $100\,\mu\mathrm{W}$ of the modulator's output (out of $0.9\,\mathrm{mW}$) is split-off with a beam splitter and detected on a photodiode (Thorlabs, PDA20CS2, $11\,\mathrm{MHz}$ bandwidth). The photodiode signal is fed to the demodulation circuit (Fig. 3.22), where the three phase bias error signals are obtained by mixing down the input with the appropriate beat frequencies. The phase bias errors δ_A and δ_B are derived from the $2\,\mathrm{MHz}$ quadratures. Shifting the phase θ_2 of the global $2\,\mathrm{MHz}$ demodulation tone and a following $90°$-power splitting gives access to the quadratures and enables decoupling of the error signals. Similarly, the $4\,\mathrm{MHz}$ demodulation tone is generated by frequency doubling and appropriately shifting the phase θ_1.

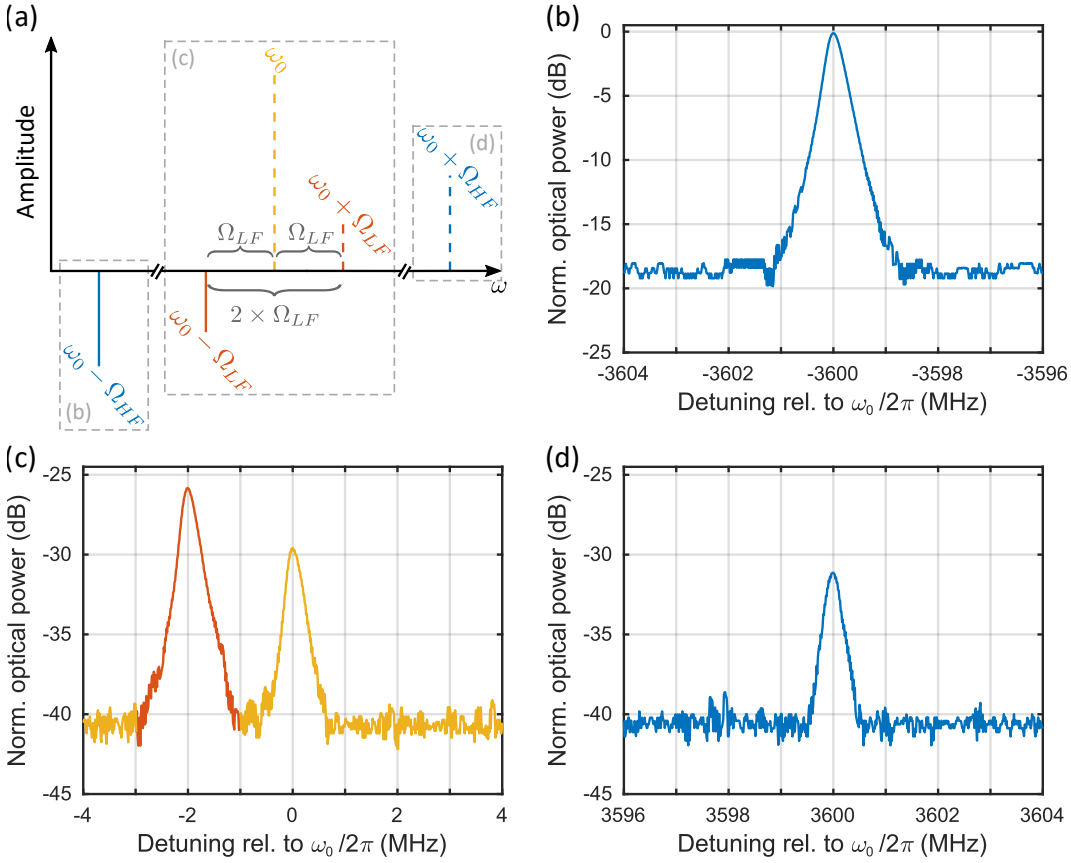

Figure 3.21: (a) Schematic frequency spectrum with frequencies Ω_{HF} (blue) and Ω_{LF} (red). Dashed lines indicate suppressed frequency components. The upper and lower auxiliary SBs beat with the carrier (yellow) at frequency Ω_{LF}. Choosing the correct demodulation phase gives access to the phase bias errors δ_A and δ_B. The beat between the two auxiliary SBs at frequency $2\Omega_{LF}$ is proportional to the phase bias error δ_P. (b) Optical spectrum for the maximized lower primary sideband (Ω_{HF}-SB) in the CS-SSB configuration. (c) Optical spectrum of the carrier including the auxiliary SBs. The carrier is suppressed by $-29.3\,\mathrm{dB}$ relative to the maximized SB. Optimization of the lower Ω_{HF}-SB maximizes the lower auxiliary Ω_{LF}-SB (red) as well. The upper auxiliary SB is suppressed below the noise floor in this measurement. (d) Optical spectrum showing $-30.7\,\mathrm{dB}$ suppression of the upper Ω_{HF}-SB. The different noise floors in (b-d) originate from varying the signal resolution of the oscilloscope used for measurement. The resolution required to measure (c-d) can not measure the full amplitude in (b). All spectra are normalized to the power of the Ω_{HF}-SB.

Not shown in the schematics are the attenuators and amplifiers (Mini-circuits, MAN-1LN), which are required to ensure the correct input power levels for the shown components.

Fig. 3.23 shows measurements of the phase bias error signals. The phase biases were sequentially modulated around their set points for the CS-SSB operation and the error signals ($V^{err}_{A,B,P}$) generated by the demodulation circuit were recorded with an oscilloscope. The plots show that changes in each individual phase bias mainly affect only one of the three error signals. The optimization of the demodulation phases $\theta_{1,2}$ is facilitated through such measurements. A minor cross talk between the two $2\,\mathrm{MHz}$ quadratures can be observed. It originates from the fixed imperfect phase between the demodulation tones given by the $90°$-power splitter (Fig. 3.22, demodulation circuit). Nevertheless this does not cause a problem in phase bias locking, since every signal has its own dominant channel.

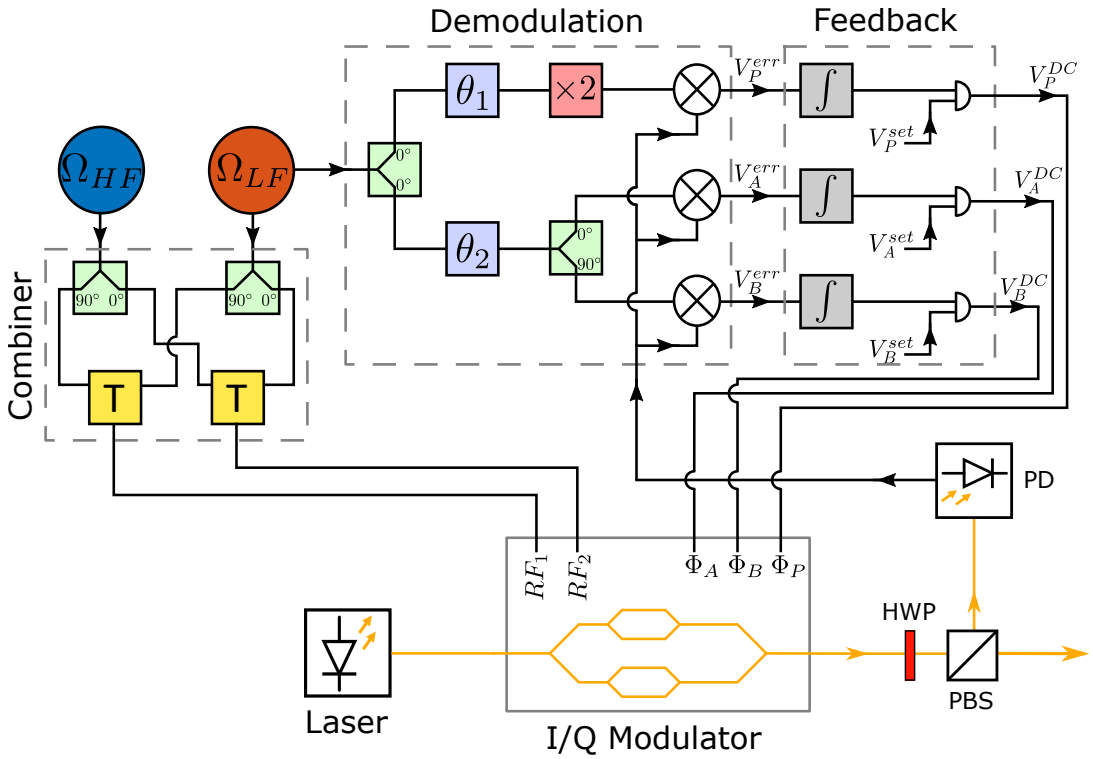

Figure 3.22: Schematic experimental setup for CS-SSB stabilization. The I/Q modulator receives both the auxiliary (Ω_{LF}) and the primary (Ω_{HF}) modulations. The optical beat signals of the Ω_{LF} sidebands are detected with a photodiode (PD). The phase bias error signals ($V^{err}_{A,B,P}$) are generated with a demodulation circuit that generates the demodulation tones with adjustable phases (θ_1, θ_2) for cross talk suppression. The feedback circuit adjusts the phase bias control voltages ($V^{DC}_{A,B,P}$) and stabilizes the CS-SSB operation. HWP, half-wave plate; PBS, polarizing beam splitter. Part list – Ω_{LF}-Splitters: Mini-circuits PSC-2-2+, PSCQ-2-8+ and PSC-3-2+; Phase shifters: Mini-circuits JCPHS-2.5+; Frequency doubler: Mini-circuits RK-3+; Mixers: Mini-circuits RPD-1+; Ω_{HF}-Splitter:, Mini-circuits QCN-45D+; Bias tee (T): Mini-circuits TCBT-14+; Opamps in feedback circuit: Texas Instruments OPA277; PD: Thorlabs PDA20CS2; Laser: OEwaves HI-Q OE4030; I/Q modulator: Thorlabs LN86S-FC.

A home-built, 3-channel, analog feedback circuit simultaneously controls the phase bias voltages ($V^{DC}_{A,B,P}$). Since the expected drifts are slow, the bandwidth of the feedback circuit was designed to be around $100\,\mathrm{Hz}$. In order to lock the modulator, the phase bias set points ($V^{set}_{A,B,P}$) are adjusted manually. By engaging the lock, the circuit adds the feedback signals to the corresponding set point voltages.

The error signals in Fig. 3.23 have small offsets. In order to compensate those offsets, the zero-crossing of the error signals are adjustable by adding offsets to the error signals prior to the integrating part of the circuit. For all mathematical operations to perform feedback we use OPA277 operational amplifiers (see supplemental document Fig. S2), and avoid ground loops between connected instruments by using differential amplifiers (AMP03) for all inputs and outputs.

Feedback Stability

We evaluate the stability of the presented locking method by tracking the powers of the suppressed optical carrier and SB over the course of $9\,\mathrm{h}$. The optical powers are measured with

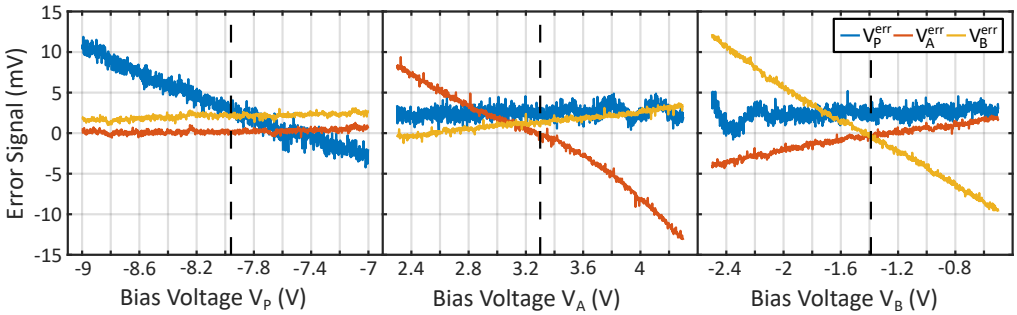

Figure 3.23: Error signals over phase bias voltage scan. For evaluation of the error signals $V^{err}_{A,B,P}$, the phase bias voltages ($V^{DC}_{A,B,P}$) were scanned through their set points (dashed black lines) and the signals that were generated by the demodulation circuit were measured. Left: $V^{err}_{A,B}$ are decoupled from changes in V^{DC}_{P}, indicated by absence of a gradient. Offsets can be compensated by adjusting the set points ($V^{set}_{A,B,P}$) with the feedback circuit. Center and right: Scans of V^{DC}_{A} and V^{DC}_{B} show a minor cross talk between V^{err}_{A} and V^{err}_{B}, which originates from the fixed imperfect phase ($\sim 90°$) between the LO signals used for demodulation.

a scanning Fabry-Perot interferometer (Thorlabs, SA200-12B). Fig. 3.24a shows an example for the unlocked modulator in SC-SSB mode. The carrier power drifts from $-27.4\,\mathrm{dB}$ to $-11.6\,\mathrm{dB}$ while the upper Ω_{HF}-sideband drifts drifts between $-29.3\,\mathrm{dB}$ and $-19.4\,\mathrm{dB}$. Fig. 3.24b shows the measurement of the suppressed optical frequency components for the locked modulator. The feedback keeps the suppression of the carrier and upper SB below $-27\,\mathrm{dB}$. The locked modulator was running in laboratory conditions for several weeks without losing the set point. Note that the linewidth ($7.5\,\mathrm{MHz}$) of the Fabry-Perot interferometer used for these particular measurements was too large to distinguish the auxiliary SBs from the carrier. Therefore, the bare measurements indicate the sum of the powers in the auxiliary SBs and the carrier. However, the weak auxiliary modulation with a maximum intensity of $-25.5\,\mathrm{dB}$ with respect to the unsuppressed Ω_{HF}-sideband (Fig. 3.21c) allows us to calculate the power in the carrier alone. In principle, the auxiliary sidebands can be made much smaller, however, this was not pursued since the residual sideband levels are sufficient for our intended applications. The beat signal between the auxiliary sideband and the unsuppressed Ω_{HF}-sideband at $3.598\,\mathrm{GHz}$ is too fast to affect the intended application. As a separate note, we observed that the drifts in the suppression levels do not originate directly from temperature drifts, since deliberate temperature changes larger than ambient fluctuations did not cause similar effects.

3.4 Imaging System

Resonance fluorescence imaging is employed for aligning the magneto-optical trap (MOT) and diagnosing the atomic ensemble. In this technique, atoms absorb resonant cooling laser photons and re-emit them isotropically via spontaneous emission. The resulting fluorescence is detected to enable *in situ* characterization of the atomic cloud, including its position, spatial distribution, atom number, temperature, and internal state.

A picture of the optical imaging setup is shown in Fig. 3.25. The partially transparent red lines indicate the optical paths of the fluorescence photons to the two cameras (FLIR, Blackfly BFS-U3-32S4M), enabling imaging of the atomic cloud along three spatial directions. Dashed bold red lines mark the positions of lenses (L) and a mirror (M) used to project an inverted real image of the atoms onto the camera's internal CMOS chip (Sony, IMX252). Each optical path includes an objective lens with focal length f_o and an ocular lens with focal length f_i.

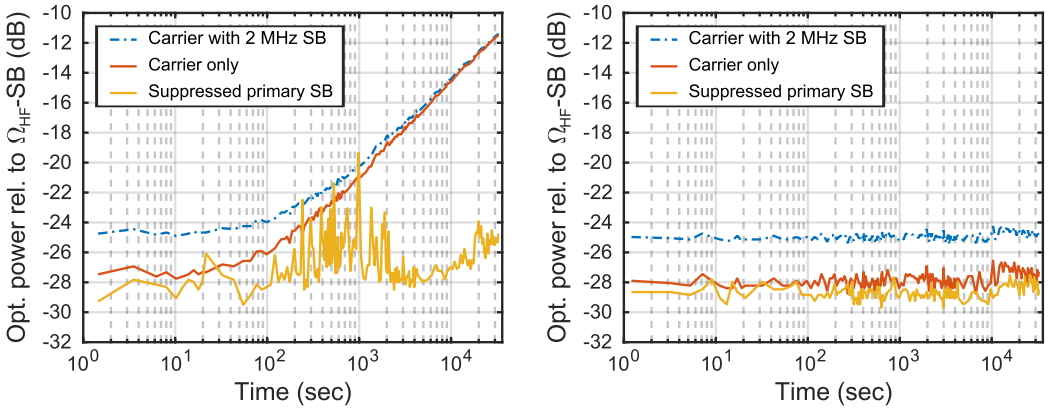

Figure 3.24: CS-SSB modulation stability over time ($\sim 9\,\mathrm{h}$). The logarithmic time scale demonstrates the short term and long-term behaviours of the suppressed primary SB (yellow), the suppressed carrier including the $2\,\mathrm{MHz}$-SB (dashed blue), and the inferred carrier only (red). Left: Example trace for the unlocked modulator. The carrier drifts from $-27.4\,\mathrm{dB}$ to $-11.6\,\mathrm{dB}$ relative to the unsuppressed Ω_{HF}-SB power and the suppressed SB fluctuates between $-29.3\,\mathrm{dB}$ and $-19.4\,\mathrm{dB}$. Right: Trace of the locked modulator. Suppressed carrier and SB are stabilized below $-27\,\mathrm{dB}$ relative to the unsuppressed Ω_{HF}-SB power.

The lenses are chosen such that $f_o = f_i$ and are separated by a distance $2 \times f_o$, resulting in a magnification of $M = -f_o/f_i = -1$.

For efficient imaging of the atoms in the horizontal plane (CAM Z), the object lens (L_Z^o, $f_o = 60\,\mathrm{mm}$) is mounted as close as possible to the atom position, maximizing the solid angle for fluorescence collection. This top-view configuration is used for *in situ* observation of the MOT and enables measurements of atom number, temperature, and internal state.

Imaging in the two vertical planes is constrained by limited optical access, permitting observation only along the MOT beam propagation axes (MOT X and MOT Y). Polarizing beam splitters separate the fluorescence imaging paths from the MOT beam paths and combine both imaging directions onto a single camera (CAM X/Y). In Fig. 3.25, L_x and L_y indicate the object lenses ($f_o = 100\,\mathrm{mm}$) for the respective imaging plane. Since both paths share the same camera, only one ocular lens (L_{XY}, $f_i = 100\,\mathrm{mm}$) is required.

Fig.3.26 shows example images of an atom cloud released from the dipole trap. On the left side, the top view of the atom cloud is shown. The camera (CAM Z) is aligned with the longitudinal axis (y) of the dipole trap, generated by the cavity. The right side of the figure displays the side views of the atom cloud, imaged simultaneously along the horizontal MOT beam axes. As the longitudinal cavity mode axis forms a $45°$ with the MOT beams, the horizontal axes in these side-view images differ from those in the top-view image and are labeled x' and y' accordingly.

In order to take an image, the fluorescence is recorded over a typical exposure time of $t_e = 300\,\mu\mathrm{s}$, defined by the pulse duration of the cooling and repump beams. Fluctuations in camera shutter latency can lead to intensity noise in the recorded fluorescence. To mitigate this, the shutter time exceeds the duration of the imaging pulse, and a fixed delay ($\delta = 30\,\mu\mathrm{s}$) is implemented between the shutter trigger and the start of the imaging pulse to ensure a consistent exposure time.

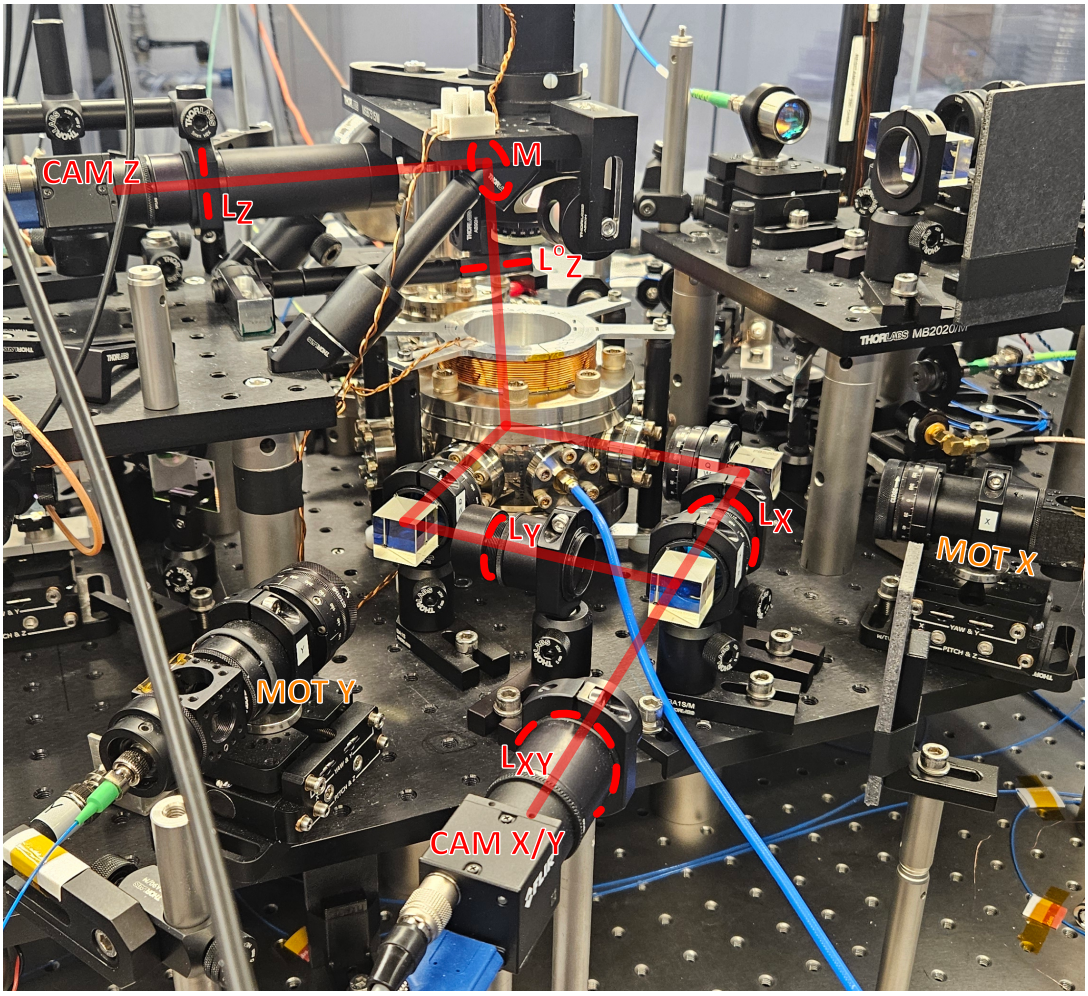

Figure 3.25: Picture of the fluorescence imaging setup. Partially transparent red lines indicate the path of the fluorescence photons to the cameras. Dashed red lines indicate the position of lenses and mirrors along the imaging paths.

3.4.1 Atom Number Measurements

Following the derivation in [Ste10], we can infer an estimate for the atom number N_a from the total intensity of the detected fluorescence image. The relationship between the number of atoms in a MOT and the integrated number of camera counts N_c is given by

$$N_a = \frac{8\pi[1 + 4(\Delta/\Gamma)^2 + 6I_0/I_{\text{sat}}]}{6I_0/I_{\text{sat}}\Gamma t_e \eta_c d\Omega} N_c, \tag{3.15}$$

where $\eta_c = 0.35$ is the camera efficiency, Δ is the detuning of the cooling beam frequency from the $F = 2 \rightarrow F' = 3$ cycling transition, Γ is the linewidth of the ^{87}Rb D_2 line, I_0 is the intensity of a single MOT beam, and $I_{\text{sat}} = 1.669\,\text{mW/cm}^2$ is the saturation intensity of the $F = 2 \rightarrow F' = 3$ transition. For the top-view imaging path, which we use to measure the number of atoms, the solid angle of the light collected by the imaging system is $d\Omega \approx \frac{3}{16}\pi$.

3.4.2 Temperature Measurement

To measure the temperature of the atom cloud, we observe its free ballistic expansion following release from the trapping potential in a time-of-flight (TOF) sequence. For an isotropic thermal gas, the velocity distribution is governed by the Maxwell–Boltzmann distribution,

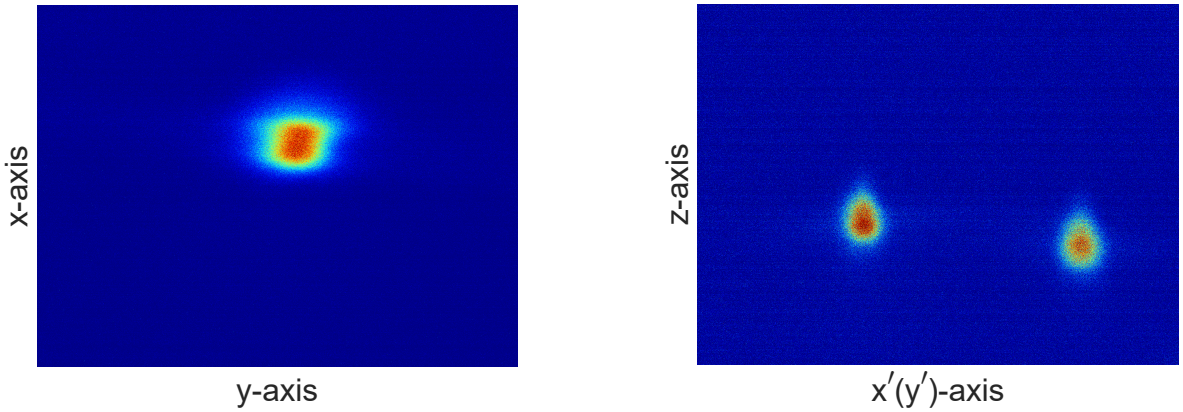

Figure 3.26: *Left:* Example for a top-view fluorescence image of an atomic ensemble released from the dipole trap. *Right:* Example for a side view fluorescence image. The side views along both horizontal MOT beam axes are projected onto the same image.

resulting in a root-mean-square velocity of $v_{rms} = \frac{k_B T}{m}$. Therefore, the spatial width $\sigma(t)$ of the atom cloud expands over time t after release from the trap according to

$$\sigma(t) = \sqrt{\sigma^2(0) + v_{\text{rms}} t^2} = \sqrt{\sigma^2(0) + \frac{k_B T}{m} t^2}, \tag{3.16}$$

where $\sigma(0)$ is the initial spatial width, m is the atomic mass, k_B the Boltzmann constant, and T the temperature.

For an actual temperature measurement, the experimental sequence is repeated, and the imaging time after the atom release is scanned. The spatial width is derived from a Gaussian fit of the fluorescence image's integrated intensity profile. The resulting set of time-dependent spatial widths is fitted with Eq. 3.16 to evaluate the temperature.

3.5 Microwave Setup

The hyperfine splitting between the ^{87}Rb $|F = 1\rangle$ and $|F = 2\rangle$ ground states is $\omega_a = 6.834\,\text{GHz}$. This transition can be coherently driven via magnetic dipole coupling, enabling control of the atomic internal state. In addition to coherent manipulation, we employ microwave spectroscopy to characterize the local magnetic environment experienced by the atoms, as the hyperfine sublevels are sensitive to Zeeman shifts.

To overcome the limited optical access from outside the vacuum chamber, the microwave antenna was mounted inside the chamber. We use a simple $\lambda/4$ monopole design, with the steel chamber wall acting as the ground plane. For adjustment of the emission frequency, the length of the antenna, which is directly attached to the SMA feedthrough, was adjusted in the chamber with a clipper while observing the emission spectrum. Figure 3.2 shows an image of the optical cavity mounted inside the vacuum chamber, where the SMA feedthrough and attached antenna are visible.

The OAT interaction requires a π-polarized cavity mode, meaning that the cavity field's polarization must be aligned with the atomic quantization axis. To drive the magnetically insensitive ^{87}Rb clock transition, $|F = 1, m_f = 0\rangle \longleftrightarrow |F = 2, m_f = 0\rangle$, with the microwave in this configuration, the antenna is aligned horizontally, such that the magnetic component of the emitted transverse electromagnetic wave is parallel to the quantization axis (z-axis).

Note that in the Raman sequence, the quantization axis must instead be aligned along the cavity mode axis to ensure $\Delta m_f = 0$. Consequently, reorienting the quantization axis between Raman and microwave pulses will be necessary.

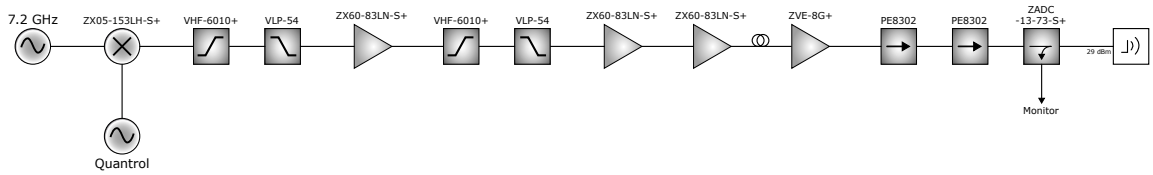

Figure 3.27: Circuit diagram of the microwave generation chain

The circuit diagram of the microwave chain is shown in Figure 3.27. The microwave frequency is generated by mixing a $7.2\,\mathrm{GHz}$ local oscillator (Wenzel, GMXO-PLD) with a $365.32\,\mathrm{MHz}$ tone generated by a Direct Digital Synthesiser (DDS) channel controlled via Quantrol. The DDS allows precise phase control, enabling the definition of relative phases between consecutive microwave pulses. This control over the pulse phase allows for arbitrary rotations on the Bloch sphere and the implementation of composite pulse sequences through controlled shifts of the rotation axis.

The additional components in the microwave chain serve to condition the signal. The low- and high-pass filters (Mini-Circuits, VHF-6010+, VLP-54) remove the undesired sideband and the residual carrier and modulation tone, while low-noise amplifiers (Mini-Circuits, ZX60-83LN-S+) boost the signal. To achieve strong driving fields and correspondingly large Rabi frequencies, a high-power amplifier (Mini-Circuits, ZVE-8G+) delivers $30\,\mathrm{dBm}$ of output power. Two isolators (RF-Lambda, PE8302) protect the amplifier from the reflected power, and a directional coupler (Mini-Circuits, ZADC-13-73-S+) taps a portion of the reflected signal from the antenna for emission spectrum diagnostics.

The emission spectrum of the $\lambda/4$ antenna is measured with a spectrum analyzer (Rigol, DSA875) in tracking generator (TG) mode. In this configuration, the analyzer sweeps the frequency of its internal microwave source, which is connected to the antenna, while simultaneously measuring the amplitude of the reflected signal. Figure 3.28 shows the resulting frequency response of the antenna, compared to the response measured with the antenna disconnected. To align the antenna's resonance with the atomic transition frequency (indicated by the grey dashed line), the antenna was initially trimmed while mounted in the empty vacuum chamber. However, once the cavity and MOT coils were installed, their presence caused a shift in the resonance frequency. Despite this, the measurement indicates that the antenna emits a signal with a return loss of $7.3\,\mathrm{dB}$ at ω_a. Assuming the input drive of $28.3\,\mathrm{dBm}$, the antenna emission corresponds to a radiated power of approximately $550\,\mathrm{mW}$, which is sufficient to efficiently drive Rabi oscillations. A measurement of the Rabi oscillation driven by the microwave field is discussed in Sec.4.3.2.

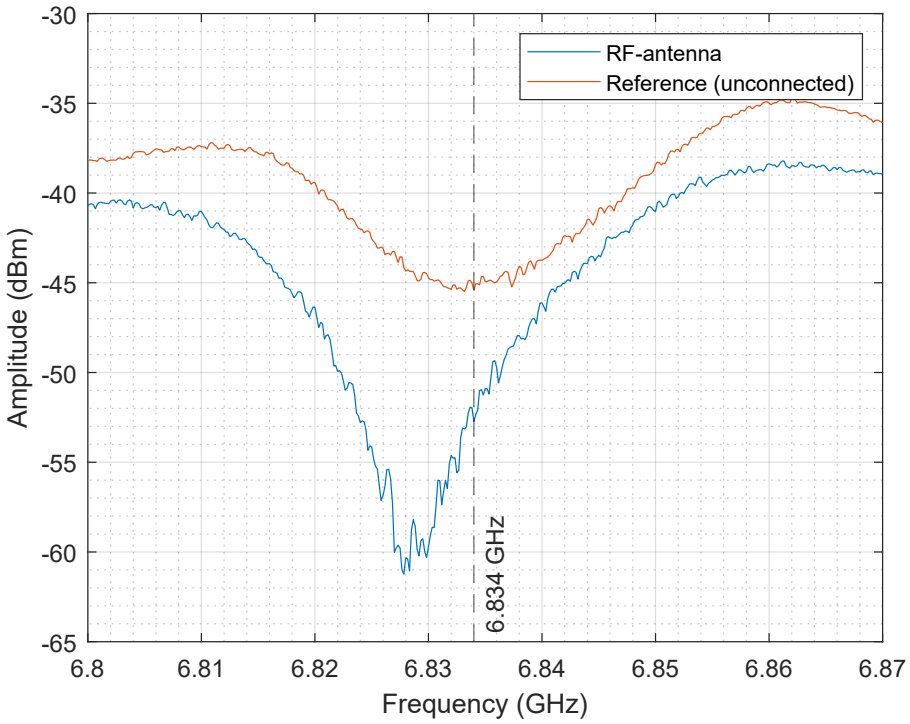

Figure 3.28: Frequency response plot of the $\lambda/4$ antenna

3.6 Homodyne Detection Setup

In Sec 2.3.4, we discussed that the atomic state-induced frequency shift can be detected through a phase measurement of the cavity transmission or reflection, and that such a QND measurement generates a spin-squeezed state. In the experiment, this measurement is implemented using a homodyne detection scheme.

A homodyne measurement is a form of balanced detection [Fox06] that removes classical $1/f$-noise, and allows shot-noise limited measurements of the amplitude or phase of an optical signal. In its most principal form, a homodyne detector consists of a beam splitter and a balanced detector, two photodiodes connected to subtract their photo currents. The beam splitter interferes a weak complex signal field, $\mathcal{E}_s = \mathcal{E}_s^a + i\mathcal{E}_s^\varphi$, with a local oscillator of field amplitude $\mathcal{E}_{LO}$ and phase ϕ_{LO}, and each of the photodiodes detects one of the beam splitters output arms. The resulting measurement signal is

$$V_{HO} \propto 2\mathcal{E}_{LO}\Big(\mathcal{E}_s^a \cos(\phi_{LO}) + \mathcal{E}_s^\varphi \sin(\phi_{LO})\Big), \tag{3.17}$$

showing the two key aspects of the detection method. First, the measurement is sensitive to the local oscillator phase, which allows tuning the detector to be sensitive for the amplitude ($\mathcal{E}_s^a$) or phase quadrature ($\mathcal{E}_s^\varphi$) of the measured signal. Second, the measurement is proportional to the amplitude of the local oscillator ($\mathcal{E}_{LO}$), thus amplifying the signal.

A schematic diagram of the homodyne detection setup developed for this experiment is shown in Fig. 3.29. The detection part of the setup is illustrated in the bottom left quadrant of the figure. The optical paths of the local oscillator and probe beam are mode-matched and focused with a collector lens (L, Thorlabs, LA1131-780) onto the balanced detector, ensuring optimum contrast and signal-to-noise ratio. The balanced detector consists of two photo diodes (Thorlabs, FDS010) in a balanced configuration connected to a low-noise, high-bandwidth transimpedance amplifier (Femto, HCA-4M-500K-C).

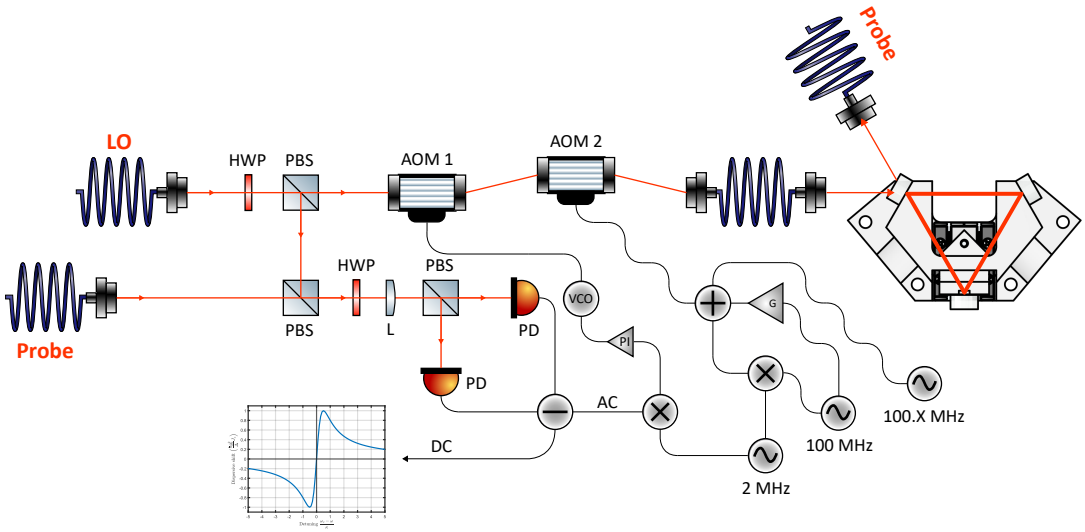

Figure 3.29: Schematic diagram of the homodyne detection setup. The input light (LO) is split into the probe and reference arms. A pair of AOMs on the probe arm enables optical path length stabilization. AOM 2 generates $2\,\mathrm{MHz}$ sidebands that serve as phase reference in a heterodyne detection. The resulting error signal is applied to feed back to a VCO that drives AOM 1, thus correcting for optical path length deviations. The dispersive homodyne signal indicates the atom-induced resonance shift of the cavity. $100\,\mathrm{MHz}$ is the reference for the sidebands, QND, and Raman tones, whereas a $100.X\mathrm{MHz}$ source is required to generate the offset of the OAT-pulse (X indicates this offset). The figure was created using components from [Fra].

The bandwidth of the transimpedance amplifier is required for the optical path stabilization based on heterodyne detection. Any path length fluctuations along the probe arm are transferred into noise on the homodyne phase measurement. To suppress these fluctuations, two AOMs were implemented in the probe arm. Two sidebands ($\omega_{SB} = 2\pi\times 2\,\mathrm{MHz}$), with a power of $P_{SB} \approx 10\,\mathrm{nW}$, are generated on the probe by AOM 2 and used as a path length reference. These sidebands are reflected by the cavity and beat with the LO ($P_{LO} \approx 200\,\mu\mathrm{W}$) on the balanced detector. The resulting heterodyne signal is given by:

$$V_{err}^{het} \propto \mathcal{E}_{LO}\mathcal{E}_{SB}\cos(\phi_{err})\cos(\omega_{SB}t), \tag{3.18}$$

where $\mathcal{E}_{SB}$ is the sideband amplitude and ϕ_{err} is the phase error. Any path length fluctuations, for example, induced by thermal drifts of the optical fibers, result in the accumulation of a relative phase of the probe relative to the LO. The beat of the LO with the probe sidebands, which do not interact with the cavity, gives access to this relative phase.

As shown in Fig. 3.29, the AC component of the detected signal is mixed with the sideband modulation tone to generate a DC error signal. This error signal is subsequently used to stabilize the optical path. The correction is applied via AOM 1, which is driven by a voltage-controlled oscillator (VCO, Mini-Circuits, ZOS-150+). Small variations in the VCO drive frequency result in corresponding changes of the AOM's deflection angle, thereby enabling precise adjustment of the optical path length.

Fig. 3.30 shows the diagram of the feedback circuit applied for path length stabilization. The buffered voltage divider to adjust the error signal amplitude (V_{err}) and the differential amplifier circuit for combining the feedback signal with an adjustable offset are not shown. The offset voltage is set such that the VCO output is $100\,\mathrm{MHz}$, ensuring full cancellation of the frequency

shift of the probe beam after passing both AOMs. The circuit layout follows the design of the circuit previously developed for the stabilization of the $1527\,\mathrm{nm}$ laser (Fig. 3.18). In the current configuration, the feedback has a bandwidth of $140\,\mathrm{kHz}$ and tracks adjustments of the center modulation frequency of AOM 2 over a range of $\pm 4\,\mathrm{MHz}$.

Special care has to be taken for the design of the microwave setup driving AOM2 that generates the probe beam. The amplitude of the probe beam ranges from a few pW for QND measurement up to a few hundred nW for the Raman pulse, and probe-cavity detuning has to be tunable by a few κ to realize OAT. The architecture for accomplishing this broad range of real-time power tuning is currently in development.

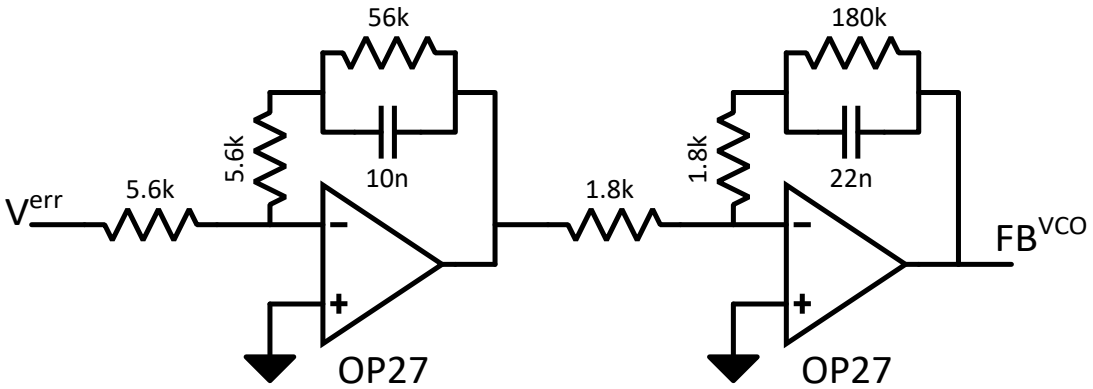

Figure 3.30: Schematic diagram for the path length stabilization circuit

3.7 Quantrol - Experimental Control System

For timing and control of the experiment, we use ARTIQ (Advanced Real-Time Infrastructure for Quantum physics) [BJZ+16]. ARTIQ is a Python-based framework for controlling FPGA hardware with nanosecond timing resolution and sub-microsecond latency, allowing the description and execution of complex experimental sequences.

However, directly coding experimental sequences in ARTIQ can be time-consuming and error-prone. To address this, our group developed Quantrol, an intuitive graphical user interface (GUI) that compiles the experimental sequence in ARTIQ. A detailed description of its design and functionality is provided in the thesis of my colleague Vyacheslav Li[Li24]. Additionally, Quantrol has been published as an open-source project on GitHub [LPG25], making it accessible to the broader scientific community.

In the following, I focus on the configuration of our experimental control system and highlight some key features of Quantrol. The hardware is built entirely within the Sinara open-source ecosystem and consists of the following components:

- FPGA control unit (M-Labs, Kasli), serving as the central timing and logic controller.
- 12 DDS outputs (M-Labbs, Urukul-AD9910), used for defining frequency offsets and driving AOMs.
- 16 analog I/O channels (M-Labs, IDC_BNC), for controlling the MOT-coil current, magnetic field offsets, and cavity transmission powers.
- 16 TTL I/O channels (M-Labs, DIO_BNC), used to trigger cameras, RF-switches, and mechanical shutters.

- 8 ADC channels (M-Labs, Sampler), for analog signal readout.

In Quantrol, the timing of an experimental sequence is defined in the front *Sequence* tab through *edges*. Each edge marks a specific time within the sequence at which an action by the control system is required. The timing of an edge can be specified either as an absolute time relative to the start of the sequence or as a delay relative to a previously defined edge. Based on these timing specifications, Quantrol automatically sorts the edges and ensures a correct and coherent visualization of the entire sequence.

Figure 3.31 shows the *Sequence* tab of an example sequence, including the implementation of the *Scan* and *Ramp* functions into the GUI. In a scan, a sequence is repeated multiple times while a specified parameter is varied linearly between repetitions. The *Scan* table allows users to define the parameter to be scanned along with its minimum and maximum values. The *Number of steps* field sets the number of repetitions, thereby determining the resolution of the parameter scan. A typical application of such scans is the time-of-flight measurement used for determining the temperature of the atomic cloud.

The *Ramp* function enables the variation of a parameter between two consecutive edges within a sequence. A ramp is defined by specifying the ramp variable, the IDs of the start and end edges, the ramp function, and the number of steps *i*. To prevent compilation errors, Quantrol provides a visual check by highlighting the IDs of ramp edges in the *Timing Sequence* table. Green indicates a correctly defined ramp with no intermediate edges in between, and red indicates invalid intermediate edges. Special emphasis was placed on the ramp function itself, which accepts arbitrary real-valued expressions. This flexibility allows for the implementation of complex pulse shapes, such as Gaussian or adiabatic ramps.

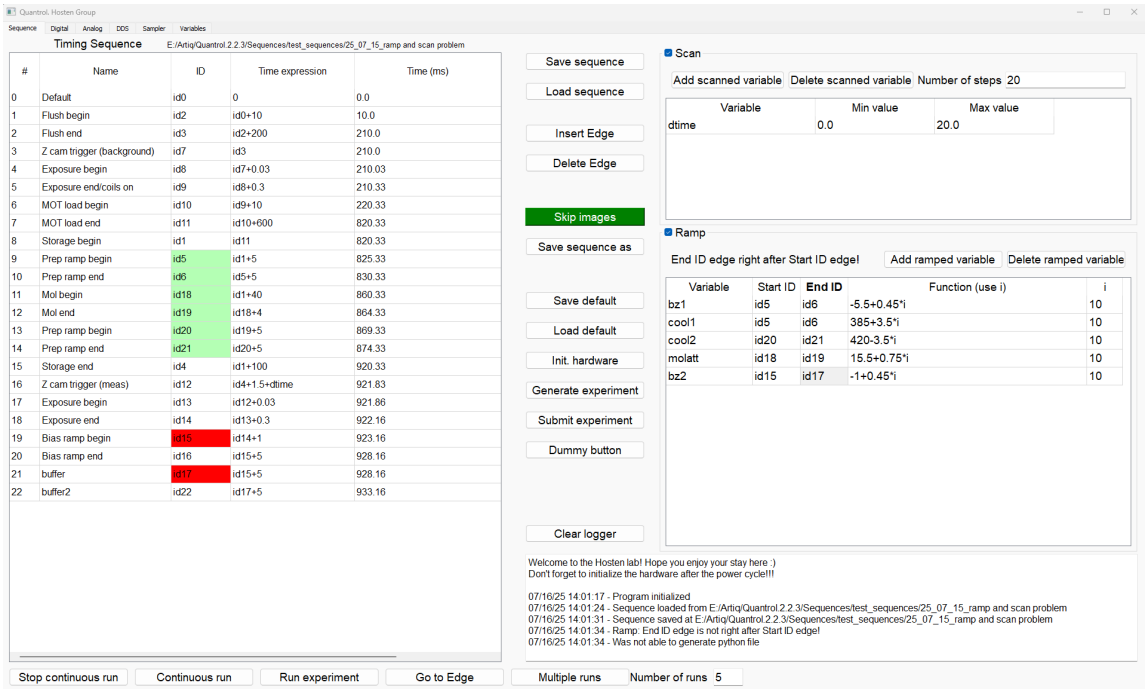

Figure 3.31: Screenshot of the Quantrol - *Sequence* tab

The actual output values for the analog, digital, and DDS output channels are defined in their respective tabs. All three tabs follow the same input structure, illustrated in Fig. 3.32, which shows an example from the *DDS* tab. Each row of the table corresponds to a time edge, with

its number, name, and timing displayed in the first three columns on the left. Each additional column represents an output channel, and the values in a given row define the output assigned to each channel at that specific edge.

Changes in output parameters are visually highlighted. Green indicates a change in value, and red denotes that a channel has been turned off. A single DDS channel is defined by output frequency, amplitude, attenuation, phase, and I/O state. In contrast, analog and digital channels are defined by a single output parameter, the signal amplitude, and the TTL signal state, respectively.

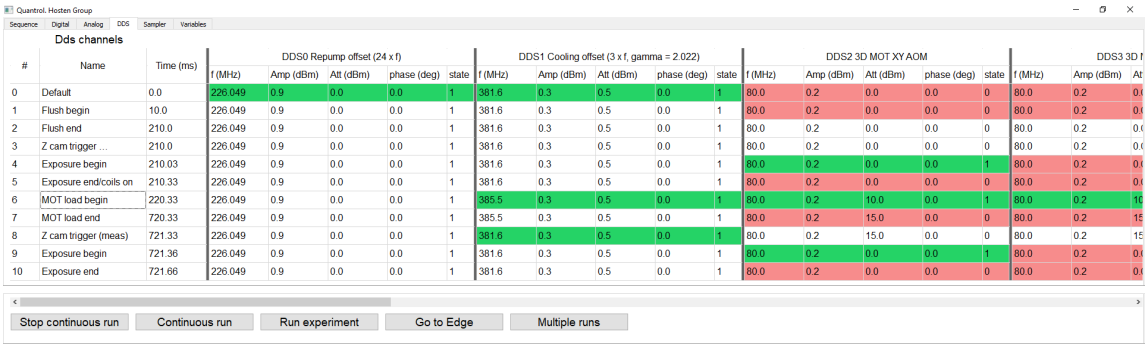

#	Name	Time (ms)	DDS0 Repump offset (24 x f)					DDS1 Cooling offset (3 x f, gamma = 2.022)					DDS2 3D MOT XY AOM					DDS3 3D M
			f (MHz)	Amp (dBm)	Att (dBm)	phase (deg)	state	f (MHz)	Amp (dBm)	Att (dBm)	phase (deg)	state	f (MHz)	Amp (dBm)	Att (dBm)	phase (deg)	state	f (MHz)	Amp (dBm)	At
0	Default	0.0	226.049	0.9	0.0	0.0	1	381.6	0.3	0.5	0.0	1	80.0	0.2	0.0	0.0	0	80.0	0.2	0.0
1	Flush begin	10.0	226.049	0.9	0.0	0.0	1	381.6	0.3	0.5	0.0	1	80.0	0.2	0.0	0.0	0	80.0	0.2	0.0
2	Flush end	210.0	226.049	0.9	0.0	0.0	1	381.6	0.3	0.5	0.0	1	80.0	0.2	0.0	0.0	0	80.0	0.2	0.0
3	Z cam trigger ...	210.0	226.049	0.9	0.0	0.0	1	381.6	0.3	0.5	0.0	1	80.0	0.2	0.0	0.0	0	80.0	0.2	0.0
4	Exposure begin	210.03	226.049	0.9	0.0	0.0	1	381.6	0.3	0.5	0.0	1	80.0	0.2	0.0	0.0	1	80.0	0.2	0.0
5	Exposure end/coils on	210.33	226.049	0.9	0.0	0.0	1	381.6	0.3	0.5	0.0	1	80.0	0.2	0.0	0.0	0	80.0	0.2	0.0
6	MOT load begin	220.33	226.049	0.9	0.0	0.0	1	385.5	0.3	0.5	0.0	1	80.0	0.2	10.0	0.0	1	80.0	0.2	10
7	MOT load end	720.33	226.049	0.9	0.0	0.0	1	385.5	0.3	0.5	0.0	1	80.0	0.2	15.0	0.0	0	80.0	0.2	15
8	Z cam trigger (meas)	721.33	226.049	0.9	0.0	0.0	1	381.6	0.3	0.5	0.0	1	80.0	0.2	15.0	0.0	0	80.0	0.2	15
9	Exposure begin	721.36	226.049	0.9	0.0	0.0	1	381.6	0.3	0.5	0.0	1	80.0	0.2	0.0	0.0	1	80.0	0.2	0.0
10	Exposure end	721.66	226.049	0.9	0.0	0.0	1	381.6	0.3	0.5	0.0	1	80.0	0.2	0.0	0.0	0	80.0	0.2	0.0

Figure 3.32: Screenshot of the Quantrol - *DDS* tab

Another main feature of ARTIQ is its capability to sample input signals and derive output values from these samples in real-time within the same experimental sequence. To make use of this functionality in Quantrol, we introduced three dedicated variable types. First, *Sampled variables* are defined in the *Sampler* tab, where the user specifies the sampling edge and input channel. The *Sampler* tab follows the same tabular structure as the output control tabs discussed above. Second, *Derived variables* allow mathematical expressions to be defined using the sampled variable as an argument. In addition to specifying an initial derived variable value, this variable type can be passed over between consecutive experimental sequences, enabling, for example, adjustment of frequency offsets based on previous measurements. Third, the sampled variable can be used to assign a value to a *Lookup variable* from a predefined list.

CHAPTER 4

Experimental Results

Before any squeezing or MZI sequence can be realized in the experiment, the atomic sample must be reliably cooled, trapped, and prepared in a well-defined internal state. The scope of this chapter is to provide a reference of characteristic experimental parameters relevant for ongoing and future development of the setup, aiming to demonstrate entanglement-enhanced Mach-Zehnder-type atom interferometry.

The experimental sequence begins with the capture and cooling of ^{87}Rb atoms from an atom beam, generated by the atom source, in a standard magneto-optical trap (MOT). The MOT is optimized for a maximum atom loading, after which a subsequent far-detuned MOT (FD-MOT) cools the atoms to sub-Doppler temperatures. In Sec. 4.1, a summary of the main experimental parameters and characteristic temperatures of the atomic sample in both MOT configurations are presented, and results obtained for optical molasses in free space are discussed. An AC-Stark shift-compensated, two-tone dipole trap (Sec. 2.4) allows MOT-loading in the presence of the dipole trap, and thus enables continuous loading of the trap from the MOT. Sec. 4.2 presents experimental results for this continuous loading into the dipole trap, *in-trap* molasses cooling, and trap depth characterization. Furthermore, an alternative loading scheme is presented that leads to a more efficient and robust transfer of atoms into the trap. AC Stark shift compensation is also applied to realize *in-trap* optical pumping to polarize the atoms in the magnetically insensitive ^{87}Rb clock state manifold. Experimental results for this pumping scheme and coherent state control are discussed in Sec. 4.3. The chapter concludes with the characterization of atom-cavity coupling via measurements of the atomic state-induced dispersive shift of the cavity resonance (Sec. 4.4).

4.1 MOT & Molasses Cooling

For efficient loading of atoms into an optical dipole trap, the kinetic energy of the atoms is typically an order of magnitude lower than the trap depth, which is on the order of a few hundred $\mu\mathrm{K}$. Therefore, pre-cooling and trapping methods are required to cool the atoms from their initial thermal distribution at the source temperature and to confine the atoms at the position of the dipole trap.

The vacuum chamber (Sec. 3.1) and the optical cavity mediating the dipole trap (Sec. 3.2.3) are configured to accommodate the three pairs of counter-propagating cooling laser beams of a magneto-optical trap (MOT), such that the MOT overlaps with the dipole trap (Fig. 3.3).

For loading the MOT, an atom source (ColdQuanta, PICAS-1000-Rb) positioned opposite the cavity (Sec. 3.1) generates an atomic beam that is directed towards the trap region.

Before discussing the experimental configuration and parameters of the pre-cooling sequence, we first provide a brief introduction to the underlying physics of magneto-optical traps and sub-Doppler cooling [MvdS99]. The trapping mechanism of a MOT relies on optical pumping of moving atoms in a spatially inhomogeneous magnetic field with a linear gradient. Due to the magnetic field, the degeneracy of the atomic hyperfine levels is lifted, and the magnetic sub-levels experience a Zeeman shift [Ste10]:

$$\Delta E_{|F,m_F\rangle} = \mu_B g_F m_F B_z, \tag{4.1}$$

where μ_B is the Bohr magneton, g_F is the hyperfine Landé factor, m_F is the magnetic quantum number of the atomic state, and B_z is the magnetic field along the quantization axis. The restoring force required to generate an attractive potential originates from this spatially inhomogeneous Zeeman shift, the opposite σ^+ and σ^- polarizations of the counter-propagating cooling laser beams, and the detuning of the cooling laser frequency, δ.

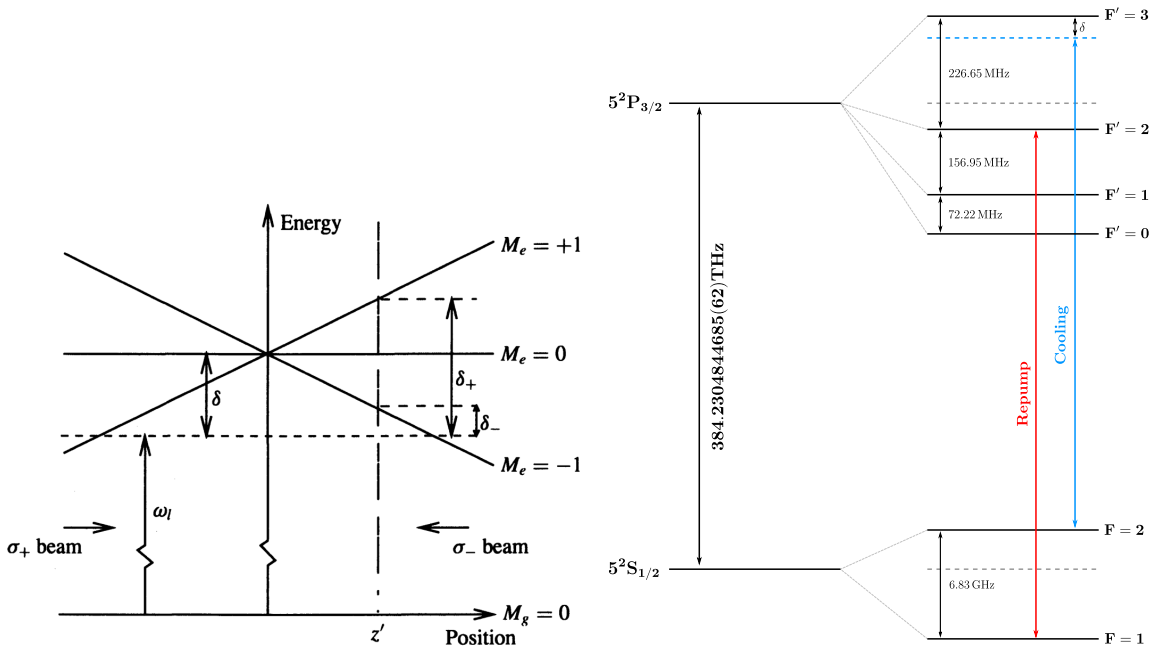

(a) (b)

Figure 4.1: (a) Schematic diagram of a MOT in 1D. Figure taken from [MvdS99] (b) Hyperfine structure of the ^{87}Rb D_2 line.

Fig. 4.1a (from [MvdS99]) illustrates the concept of a MOT in 1D based on a $|F = 0\rangle \leftrightarrow |F = 1\rangle$ transition. The magnetic sublevels of the excited state experience a state- and position-dependent Zeeman shift, which modulates the detuning of the atomic transitions relative to the cooling laser frequency. According to the selection rules, the polarization of the cooling light determines which transition between the magnetic sublevels is driven ($\sigma^\pm \rightarrow \Delta m = \pm 1$).

At position z', the $(m_F = -1)$-sublevel is tuned towards the resonance with the cooling laser, whereas the $(m_F = +1)$-sublevel is tuned out of resonance. Each of the cooling beams exerts

a radiative force on the atoms given by

$$\vec{F}_{\pm} = \pm\frac{\hbar\vec{k}\Gamma}{2}\frac{I/I_0}{1 + I/I_0 + (\delta_{\pm}(z)/\Gamma)^2}, \tag{4.2}$$

where $\hbar\vec{k}$ is the photon momentum, Γ is the natural linewidth of the atomic transition, and I/I_0 is the saturation parameter defined with respect to the saturation intensity I_0. The position-dependent detuning for each beam is

$$\delta_{\pm}(z) = \delta \pm \omega_D \pm \omega_Z(z), \tag{4.3}$$

where the Doppler shift due to the atomic velocity $\vec{v}$ is $\omega_D = \vec{k}\cdot\vec{v}$, and the relative Zeeman shift between the ground and excited sublevels is $\omega_Z = \mu_B(g_{F'}m_{F'} - g_F m_F)B(z)/\hbar$. Considering the polarization-dependent detuning of the cooling beams, the resulting total radiative force drives the atoms towards $B = 0$ at the center of the MOT.

Extending this concept to three dimensions, the 3D-MOT is formed by three orthogonal pairs of counter-propagating cooling laser beams in a σ^+-σ^- polarization configuration. A magnetic quadrupole field, generated by a pair of coils in anti-Helmholtz configuration, provides a linear magnetic field gradient along the propagation axis of the cooling laser pairs. The typical field gradient applied in this setup is $\frac{\partial B_z}{\partial z} = 10\,\mathrm{G/cm}$. Information on the MOT-coil current control and magnetic bias field control developed for this experiment can be found in [Li24].

Fig. 4.1b illustrates the hyperfine structure of the ^{87}Rb D_2 line, along with the corresponding cooling and repump transitions required for a ^{87}Rb MOT. The $|F = 2\rangle \leftrightarrow |F' = 3\rangle$ is a closed transition that is suitable for laser cooling.

However, there is a finite probability for the cooling light to excite $|F' = 2\rangle$, leading to the population of the $|F = 1\rangle$ ground state. Therefore, the repump laser is tuned on resonance with the $|F = 1\rangle \leftrightarrow |F' = 2\rangle$ transition to optically pump the atoms back into the cooling transition. The frequency offset locking method developed to control the repump and cooling laser frequencies is described in [LDH22].

There are two characteristic temperatures associated with laser cooling methods, the Doppler temperature T_D and the recoil temperature T_r. The first is associated with the natural linewidth of the cooling transition and describes the lowest achievable temperature for the pure two-level system. For the ^{87}Rb D_2 line with a natural linewidth of $\Gamma = 2\pi \times 6.065\mathrm{MHz}$, the Doppler temperature is

$$T_D = \frac{\hbar\Gamma}{2k_B} = 146\,\mu K. \tag{4.4}$$

However, atoms with a hyperfine structure and a ground state with $F \neq 0$ experience optical molasses, a sub-Doppler cooling effect. The second characteristic temperature describes the absolute limit for laser cooling and corresponds to the temperature associated with a single photon recoil of $\hbar k_L$, which is for the ^{87}Rb D_2 line:

$$T_r = \frac{\hbar^2 k_L^2}{m k_B} = 361.96\,nK. \tag{4.5}$$

In this setup, optical molasses cooling is applied via the MOT beams. The superposition of the counter-propagating MOT beams with σ^+-σ^- polarization creates an optical lattice with linear polarization that rotates along the beam axis. This results in an AC Stark shift that lifts the

degeneracy of the magnetic manifold of the ground state due to the varying coupling strength of the magnetic sublevels to the excited state. For an atom moving along the beam axis, the AC Stark shift leads to a perturbation, and the dressed states become an addmixture of the unperturbed states, with coefficients depending on the velocity of the atom. In this dressed state basis, the populations of the states with negative or positive magnetic quantum numbers become unequal, resulting in an imbalance between optical pumping rates. Consequently, the probability of absorbing a counter-propagating photon exceeds the probability of absorbing a co-propagating photon, giving rise to a velocity-dependent, friction-like cooling force [DCT89].

In the experiment, sub-Doppler cooling is implemented in two stages. Following the initial MOT, a far-detuned MOT (FD-MOT) phase is applied, during which the detuning of the cooling light is increased and the MOT beam power is reduced. This sequence compresses the atomic cloud and cools the atoms to temperatures of a few tens of $\mu\mathrm{K}$. Subsequently, pure molasses can be applied by switching the magnetic field completely off, enabling the atoms to reach temperatures below $10\,\mu\mathrm{K}$.

In the following, we discuss the main parameters for the MOT, FD-MOT, and molasses stages implemented in the experiment and refer the reader to [DCT89] for a more detailed theoretical description of the molasses cooling mechanism.

4.1.1 3D-MOT Cooling

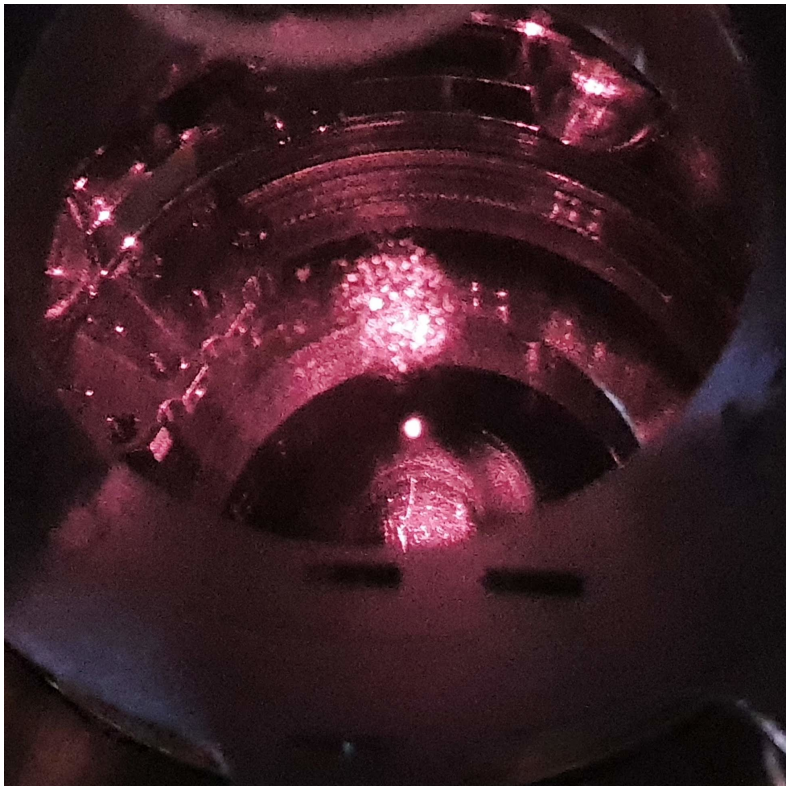

Figure 4.2: Image of the ^{87}Rb MOT prior to installation of the science cavity in the vacuum chamber.

Each experimental cycle begins with the preparation of a new atomic sample. The MOT is loaded from an atomic flux generated in a source region, spatially separated from the main science chamber (see Sec. 3.1). This atom source (ColdQuanta, PICAS-1000-Rb) consists of two components: A vapor cell containing a heatable ^{87}Rb filament, which is connected to the

main chamber via a pinhole, and an external optical power distribution module that delivers and retro-reflects the cooling and repump light along the vapor cell to form a cigar-shaped 2D MOT aligned with the pinhole axis.

Typical optical powers coupled to the distribution module are $P_{\text{cool}} = 15\text{-}20\,\text{mW}$ for the cooling tone and $P_{\text{rep}} = 1\text{-}3\,\text{mW}$ for the repump tone. A push beam, typically consisting of $P_{\text{cool}} = 4\text{-}7\,\text{mW}$ and $P_{\text{rep}} = 1\,\text{mW}$, directs the pre-cooled atoms through the pinhole toward the MOT region. We did not observe significant fluctuations in the MOT loading rate as long as the coupled cooling-beam power remained well above the saturation intensity of the D_2 line for σ^+-σ^- polarized light ($I_0 = 1.669\,\text{mW/cm}^2$) across the vapor cell. The main parameter to adjust the brightness of the atom source is the filament driving current, which is typically set to $I_{\text{source}} = 2.65\,\text{A}$.

The atomic flux generated by the source enables efficient loading of the 3D-MOT in the main chamber. The 3D-MOT overlaps spatially with the dipole trap, whose position is defined by the optical cavity. To optimize the loading process, the MOT beam alignment was first adjusted for maximum atom capture. This configuration then served as the starting point for iterative optimization of the magnetic field biases and beam alignment to maximize the loading efficiency from the 3D MOT into the dipole trap.

	Intensity (mW/cm^2)	δ (Γ)	Offset frequency (MHz)
Cooling	10	-2.67	386.6
Repump	5	0	226.0

Table 4.1: MOT: Cooling and repump tone parameters. The offset frequency denotes the respective control frequency defined in Quantrol. Note that the offset frequencies are system specific and do not represent any absolute numbers.

Table 4.1 summarizes the optimum parameters for the cooling and repump tones during 3D-MOT operation. The listed intensities correspond to the average optical power per beam normalized to the beam waist area ($\pi \times 0.398^2\,\text{cm}^2$) at the MOT position. The detunings δ are given relative to the cooling and repump transitions shown in Fig. 4.1b, expressed in units of the Γ. The offset frequencies denote the respective control frequencies defined in Quantrol for the offset lock of the cooling and repump lasers.

Fig. 4.3 shows a typical measurement of the MOT loading dynamics, where the atom number as a function of the loading time was measured via fluorescence imaging (Sec, 3.4.1). To evaluate the loading rate R and the MOT lifetime τ during loading, we fit the data with

$$N(t) = R\tau(1 - e^{-t/\tau}), \tag{4.6}$$

yielding $R = 78 \times 10^6\ \text{atoms/s}$ and $\tau = 1.7\,\text{s}$. During loading, the MOT life time is typically shorter than the decay lifetime measured in the absence of the atomic flux, as loading introduces additional loss channels. The observed decay lifetime is highly sensitive to the alignment of the MOT beams and typically ranges from $3\text{-}6\,\text{s}$ when the MOT is optimized for dipole trap loading. For alignments optimized solely for 3D-MOT performance, we observed lifetimes $\tau > 10\,\text{s}$. Under standard operation conditions, the atomic ensemble reaches temperatures of $\approx 300\,\mu\text{K}$. Measurements of the atom-cavity coupling and the state-dependent dispersive shift (Sec. 4.4) indicate that fluorescence imaging underestimates the atom number by a factor of two. The origin of this underestimation is an imperfect alignment of the imaging system (Sec. 3.4.1, CAM Z). A future revision of the imaging setup, with the imaging lenses

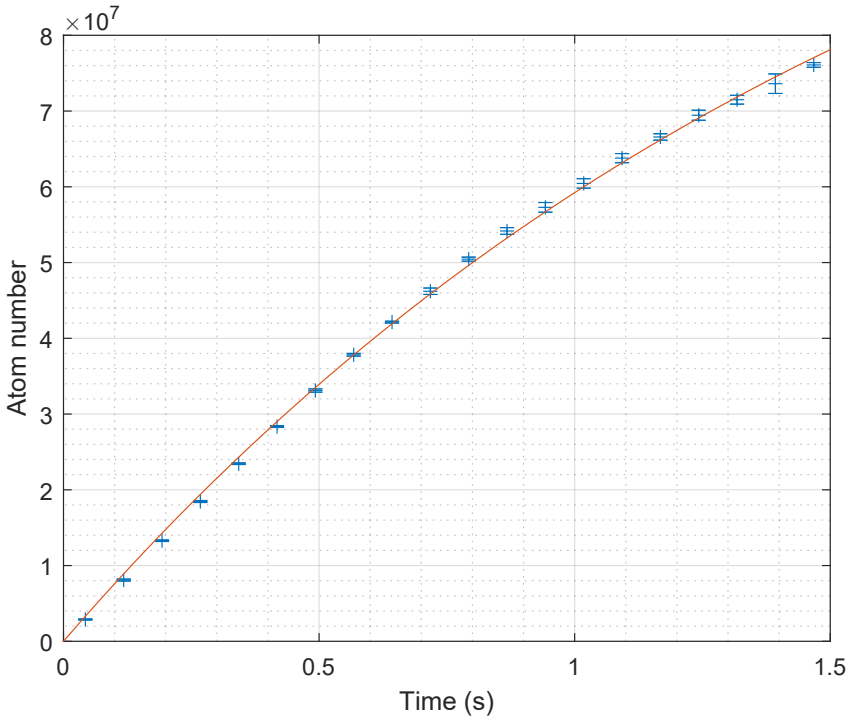

Figure 4.3: Atom number (blue plus signs) over MOT loading time. The red line shows a fit to the loading curve, yielding a loading rate $R = 78 \times 10^6$ atoms/s and a MOT lifetime $\tau = 1.7\,\mathrm{s}$.

aligned along one optical axis without a mirror in between, might be considered. Taking this underestimation into account, the MOT loading rate is $R = 1.56 \times 10^8$ atoms/s.

4.1.2 FD-MOT Sequence

To realize sub-Doppler cooling, a far-detuned MOT sequence was developed, in which the detuning of the cooling light is gradually increased while its intensity is simultaneously reduced. In this configuration, the optical molasses becomes the dominant cooling mechanism, while the MOT magnetic field continues to provide confinement. The variable-ramp function of the experimental control system (Sec: 3.7) enables continuous ramping of the cooling tone parameters. This smooth and continuous adjustment minimizes atom loss that would occur from more abrupt parameter changes, ensuring stable compression and efficient cooling of the atomic cloud, with $\approx 80\%$ of the atoms in the initial 3D-MOT retained in the FD-MOT.

Time (ms)	Intensity ($\mathrm{mW/cm^2}$)	I/I_0	δ (Γ)	Offset frequency (MHz)
t_{FD}	10	6	-2.67	386.6
t_{FD}+17.7	1.6	≈ 1	-9.3	400

Table 4.2: FD-MOT: Cooling ramp parameters.

In Tab. 4.2, the key parameters for the FD-MOT sequence are given. The time t_{FD} indicates the starting time of the within the experimental cycle. Within $17.7\,\mathrm{ms}$, the intensity of the cooling beams is linearly reduced from the initial MOT beam intensity to approximately the saturation intensity I_0, while the frequency detuning to the cooling transition is linearly tuned to $-9.3\,\Gamma$.

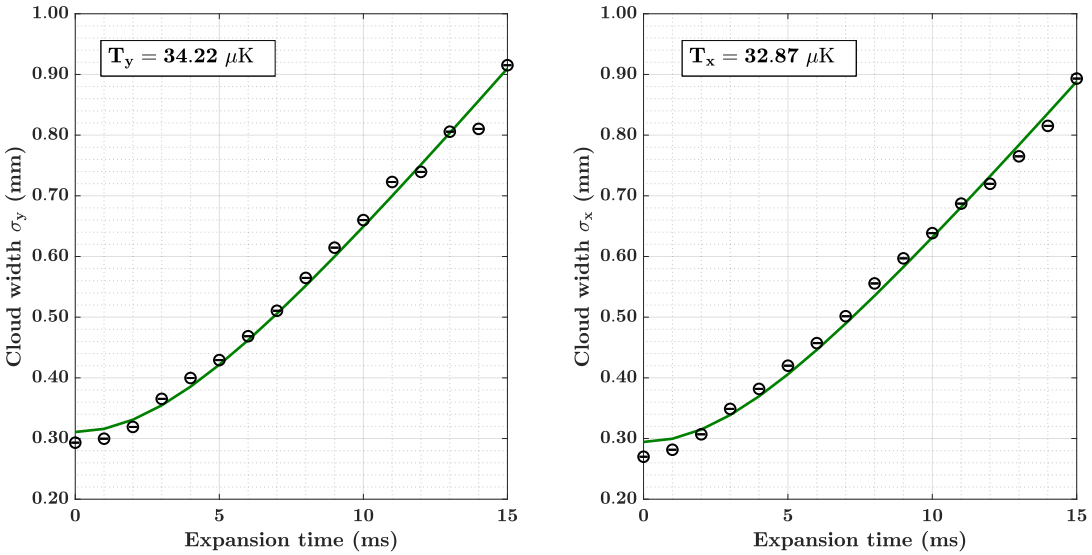

Figure 4.4: TOF measurement of the atomic temperature after the FD-MOT sequence. The projections of the fluorescence images along the camera axes are fitted with Gaussian profiles to determine the cloud diameter at each expansion time. Homogeneous temperatures indicate good MOT beam alignment, and after a typical FD-MOT sequence, the temperature of the atomic ensemble reaches below $35\,\mu\mathrm{K}$.

Fig. 4.4 shows a typical TOF measurement (Sec.3.4.2) to determine the temperature of an atomic ensemble. Following the FD-MOT sequence, the atomic ensemble reaches a typical temperature below $35\,\mu\mathrm{K}$. The homogeneity of the temperatures observed in both cloud projections indicates good alignment of the MOT beams.

4.1.3 Molasses Sequence

After the FD-MOT sequence, pure optical molasses is applied as the final cooling stage. As described in the introduction to this section, molasses cooling relies on the AC Stark shift-induced mixing of the magnetic sublevels, which enhances the probability of absorbing counter-propagating light. Therefore, any residual magnetic field must be compensated, as it lifts the degeneracy of the magnetic sublevels and compromises molasses cooling. To characterize and minimize these residual fields at the position of the atomic cloud, microwave spectroscopy on the ground-state hyperfine transition is performed.

At the end of the FD-MOT sequence, the atoms are accumulated in the magnetic manifold of the $|F = 2\rangle$ ground state, as the continuous repump tone transfers any population from $|F = 1\rangle$ back into the cooling transition. During microwave (MW) spectroscopy, a microwave pulse (Sec. 3.5) is applied to drive the hyperfine transition $|F = 2\rangle \rightarrow |F = 1\rangle$. After the MW pulse, a resonant push beam tuned to the $|F = 2\rangle \leftrightarrow |F' = 3\rangle$ transition removes any remaining atoms in $|F = 2\rangle$ from the imaging region. Subsequent fluorescence imaging of the remaining atoms provides a direct measure of the population transferred to $|F = 1\rangle$. For maximum signal contrast, the duration of the MW pulse is chosen to correspond to a π-pulse.

In the presence of a residual magnetic field, the degeneracy of the hyperfine magnetic sublevels is lifted via the Zeeman effect (Eq. 4.1). Therefore, the MW transitions between these sublevels of the $|F = 1\rangle$ and $|F = 2\rangle$ ground states experience a shift in frequency. Since the Landé factor g_F for the two hyperfine ground states has opposite signs, the sublevels with $m_F < 0$ experience a shift towards each other, while the states with $m_F > 0$ are shifted apart.

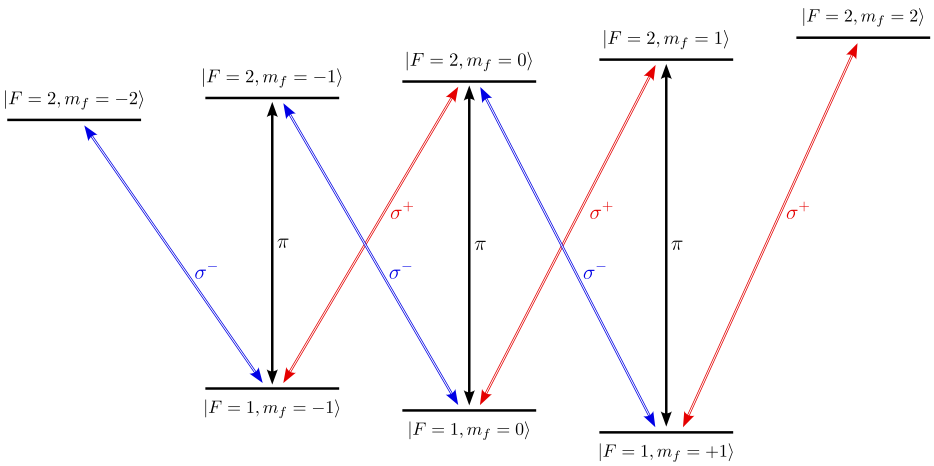

Figure 4.5: Schematic diagram of the Zeeman splitting of the magnetic sublevels in the ^{87}Rb hyperfine ground states. Colored arrows indicate MW transition and the corresponding MW polarization to drive the transition.

Fig. 4.5 illustrates this Zeeman shift induced by an ambient magnetic field and indicates the allowed MW transitions for the different MW polarizations. By measuring the Zeeman shift of the seven non-degenerate MW transitions, MW spectroscopy is a precise method to determine the local magnetic field at the position of the atoms. Fig. 4.6 shows an example of a MW spectroscopy measurement with an applied bias field. As a figure of merit, the expected differential Zeeman shift derived from Eq. 4.1 of a MW transition is $\frac{\partial\omega}{\partial B} \approx 2\pi \times 700\,\mathrm{Hz/mG}$.

For molasses cooling, the bias magnetic fields are adjusted until any residual Zeeman splitting observed in MW spectroscopy is eliminated. Because local magnetic fields vary over the course of an experimental cycle, MW spectroscopy must be performed at the specific time of any experimental sequence that is sensitive to stray magnetic fields.

Time (ms)	Intensity ($\mathrm{mW/cm^2}$)	I/I_0	δ (Γ)	Offset frequency (MHz)
t_{mol}	0.44	1/4	-9.27	400
t_{mol}+10	0.44	1/4	-18.5	420

Table 4.3: Molasses: Ramp parameters for cooling beam. During the $10\,\mathrm{ms}$ molasses sequence, the cooling beam intensity is kept constant below the saturation intensity, while the detuning is linearly further tuned to higher red detunings with respect to the cooling transition.

The parameters for a typical molasses sequence are given in Tab. 4.3. Over a duration of $10\,\mathrm{ms}$, the cooling beam intensity is reduced to one quarter of the saturation intensity, while its frequency detuning is linearly ramped to $-18.5\,\Gamma$ relative to the cooling transition. The detuning and offset values in parentheses indicate the initial parameters used when molasses is applied in the dipole trap during a continuous loading sequence. Fig. 4.7 shows a representative TOF measurement of the temperature, where molasses was applied directly after the FD-MOT sequence and the atoms were not loaded into the dipole trap. In this configuration, typical temperatures achieved with molasses cooling are in the range $T = 5 - 10$ µK.

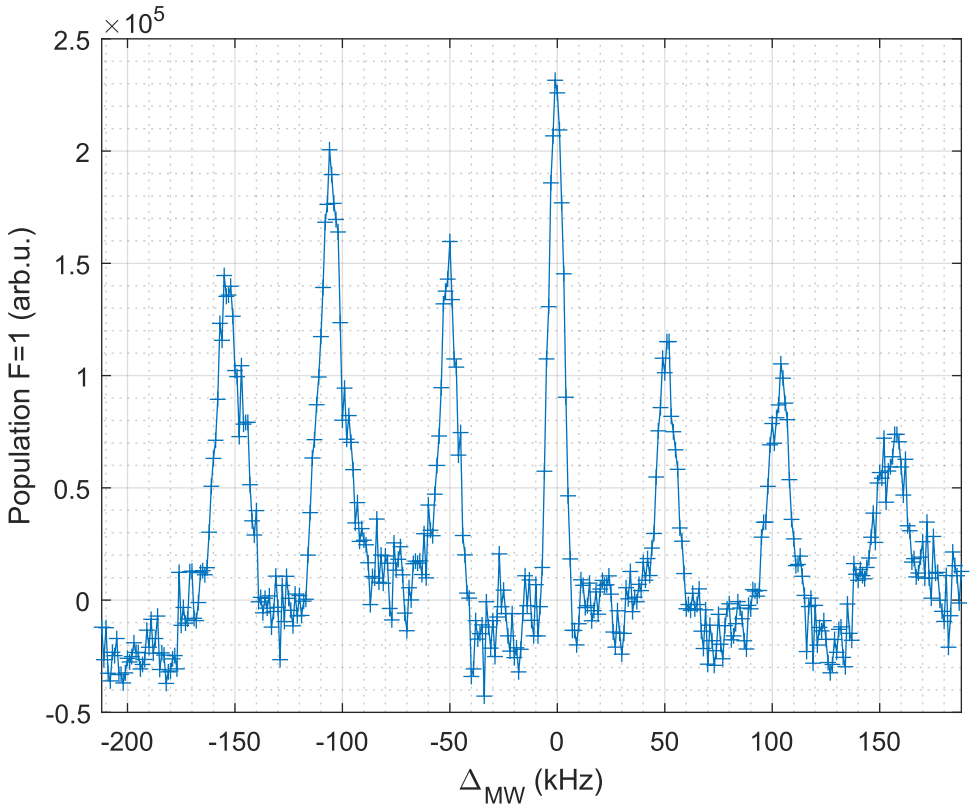

Figure 4.6: MW spectroscopy of the ^{87}Rb ground state hyperfine transitions in presence of a $71\,\mathrm{mG}$ bias field. The spectrum shows the Zeeman splitting of the $|F=1\rangle \leftrightarrow |F=2\rangle$ transition into seven non-degenerate MW transitions. The frequency spacing between adjacent peaks provides a measure of the local magnetic field strength. The x-axis indicates the detuning Δ_{MW} of the microwave drive to the atomic microwave transition $\omega_a = 2\pi\times 6.834\,\mathrm{GHz}$.

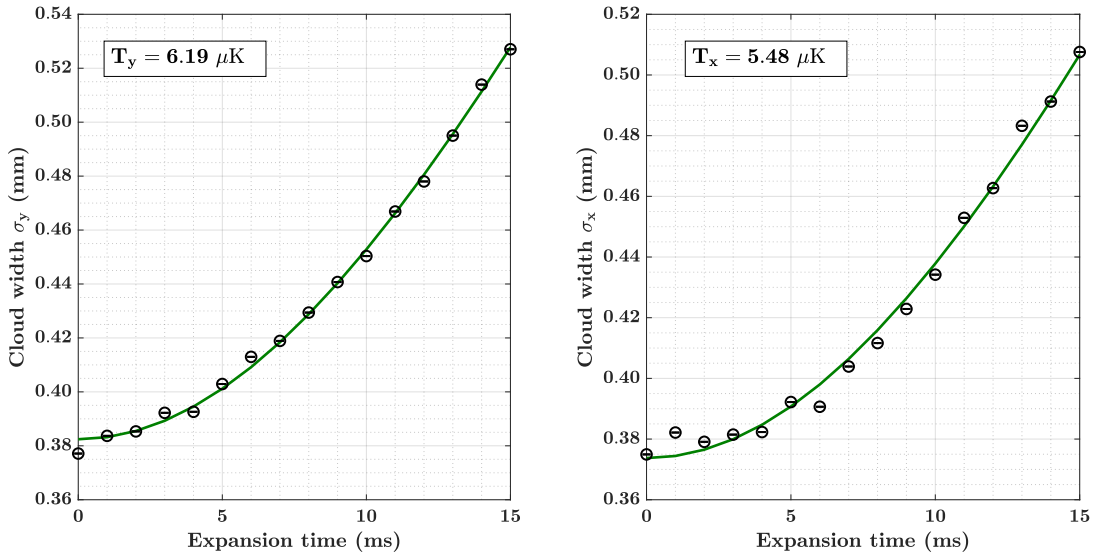

Figure 4.7: TOF measurement of the atomic temperature following the molasses sequence. The atomic ensemble is typically cooled to temperatures $T < 10\,\mu\mathrm{K}$.

4.2 Dipole Trap Experiments

In the following section, we discuss the experimental implementation of loading and molasses cooling of an atomic ensemble in the cavity-mediated dipole trap. As detailed in Sec. 2.4, the optical dipole trap operates at a wavelength of $1560\,\mathrm{nm}$. This wavelength is chosen because the laser-cavity lock (Sec 3.3.3) automatically stabilizes the $780\,\mathrm{nm}$ tones that are derived from the same laser to the cavity.

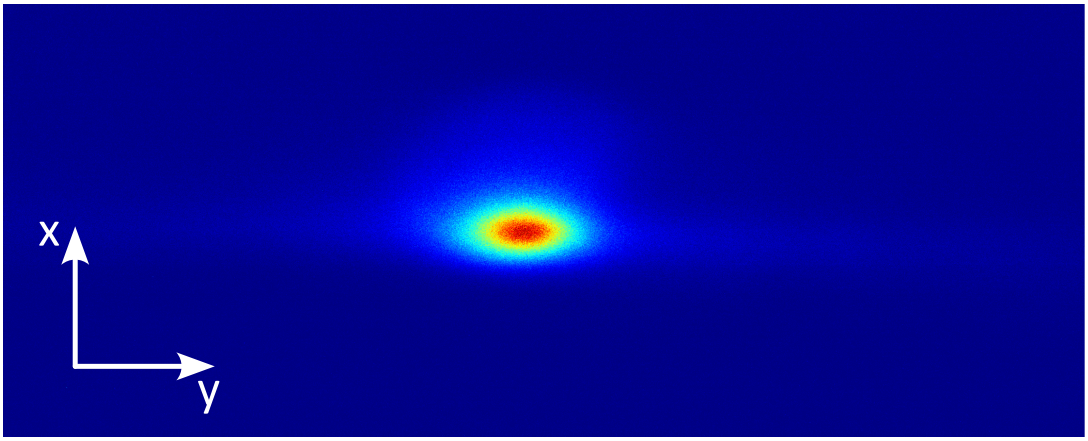

Figure 4.8: Fluorescence image of an atomic ensemble in the dipole trap

A disadvantage of this scheme is the significant AC Stark shift of the first optically excited $5P_{3/2}$ state of ^{87}Rb, which shifts the MOT and molasses cooling transitions towards (an past) resonance within the trapping region, which complicates direct and efficient transfer of atoms into the dipole trap. Previous experiments realized dipole trap loading with sequential cooling schemes, in which the cavity-mediated dipole trap was gradually ramped up during a final molasses [HEKK16] or dark-Mot [NKP$^+$18, NEIC$^+$20] phase. Alternatively, partial compensation of the light-induced Stark shift has been demonstrated by introducing an auxiliary trapping potential in a free-space crossed dipole trap configuration [PCG$^+$18].

In the present setup, a compensation tone at $1527\,\mathrm{nm}$ is coupled into the cavity to counteract the AC Stark shift across the full trapping volume. Since both wavelengths are resonant with the fundamental cavity mode, the cavity intrinsically ensures near-perfect spatial mode matching between the $1560\,\mathrm{nm}$ and $1527\,\mathrm{nm}$ trapping potentials, resulting in a tunable homogeneous differential shift of the $5S_{1/2} \leftrightarrow 5P_{3/2}$ transition (Sec. 2.4.3).

4.2.1 Trap Activation Induced Parasitic Cavity Mode

Initial dipole trap loading experiments were performed using a sequential cooling sequence, in which the atoms were first prepared in a dark MOT before the dipole trap potential was ramped up. In this configuration, the dark-MOT [KCM$^+$00] refers to optical pumping of the atoms into the $F = 1$ ground state by switching off the repump laser during the final $1\,\mathrm{ms}$ of the FD-MOT sequence. However, these measurements revealed inconsistent loading behavior, which was traced back to the excitation of a high-order cavity mode that emerged during trap activation, when the intra-cavity power was switched from $2\,\mathrm{W}$ to $35\,\mathrm{W}$.

We attribute this effect to local heating and deformation of the cavity mirrors during the power ramp, which temporarily alters the cavity geometry and leads to scattering of light into the parasitic higher-order mode before the mirrors reach thermal equilibrium. Fig. 4.9 shows the recorded transmission and reflection signals of the cavity during this process. Scattering into

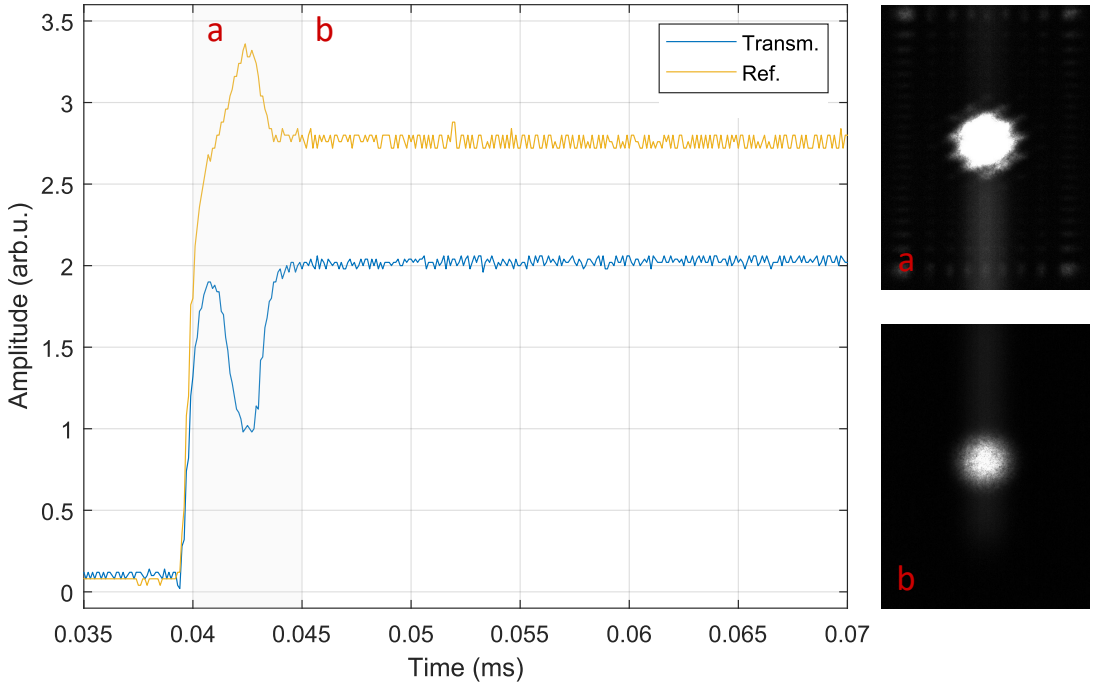

Figure 4.9: Cavity transmission and reflection traces during the dipole trap activation. The sharp rise in intra-cavity power induces geometric effects on the mirror, which lead to scattering in a parasitic high-order mode. The mode mismatch with the coupling beam, which is induced by this process, results in a dip in transmitted power and a spike in the observed reflection. The right panels display the intensity profiles of the high-order and fundamental modes, with the red markers (a, b) indicating their occurrence in the transmission and reflection traces.

the high-order mode reduces the cavity coupling efficiency to the fundamental mode, resulting in a dip in the transmitted power accompanied by a corresponding spike in reflection. To visualize this effect, the cavity transmission was monitored with a camera, enabling the direct observation of the spatial mode structure. The right panels of Fig. 4.9 display the intensity profiles of the high-order and fundamental modes, with the red markers (a, b) indicating their occurrence in the transmission and reflection traces.

During dipole trap loading, the appearance of a parasitic cavity mode leads to a decay of the intra-cavity power, resulting in atom loss and inconsistent loading behavior. Besides its potential applications for steady-state loading, in-trap molasses cooling, and state preparation, the prospect of operating the cavity at stable intra-cavity powers under thermal equilibrium provides a strong motivation for developing an AC Stark shift compensation scheme.

4.2.2 Steady-State Accumulation of Atoms in an Optical Cavity

An original result of this thesis is the demonstration of steady-state accumulation of atoms in an optical cavity, achieved through the implementation of a mode-matched auxiliary dipole trap potential that enables tuning of the differential AC Stark shift of the $5S_{1/2} \leftrightarrow 5P_{3/2}$ transition.

A theoretical framework for this AC Stark shift compensation, utilizing an auxiliary trapping potential blue-detuned relative to the $5P_{3/2} \leftrightarrow 4D$ transitions, was presented in Sec. 2.4.3 In addition, Sec. 3.3.4 described the side-of-fringe locking scheme developed to stabilize the $1527\,\mathrm{nm}$ compensation laser to the cavity resonance. This locking method provides precise

and dynamic control over the strength of the compensation potential, enabling adjustment of the differential AC Stark shift during operation.

The experimental results presented in this section form the basis of our current preprint [GWPH25] (expected by the time of the final submission of this thesis).

As the AC Stark shift scales linearly with the trap light intensity (Eq. 2.105), a calibration of the compensation tone intensity relative to the intensity of the primary dipole trap tone is essential. We will return to the trap loading procedure, but once loaded, the $5S_{1/2}$ ground and $5P_{3/2}$ excited state experience a differential light shift, δ_ν (Eq. 2.115). This differential light shift can be experimentally characterized with an *in-situ* dipole trap tomography measurement [BCV+08, SC13, CPG+17], in which fluorescence imaging of the trapped atomic ensemble is performed while the frequency of the excitation beam is scanned with respect to the unperturbed $F = 2 \leftrightarrow F' = 3$ cooling transition. Each measurement consists of $30\,\mu s$ exposure with four $10\,\mathrm{mW/cm^2}$ cooling (excitation) beams and a $5\,\mathrm{mW/cm^2}$ repump beam in a zero magnetic field. Note that for each differential shift measurement, the repump beam frequency is resonantly tuned to the $F = 1 \leftrightarrow F' = 2$ transition.

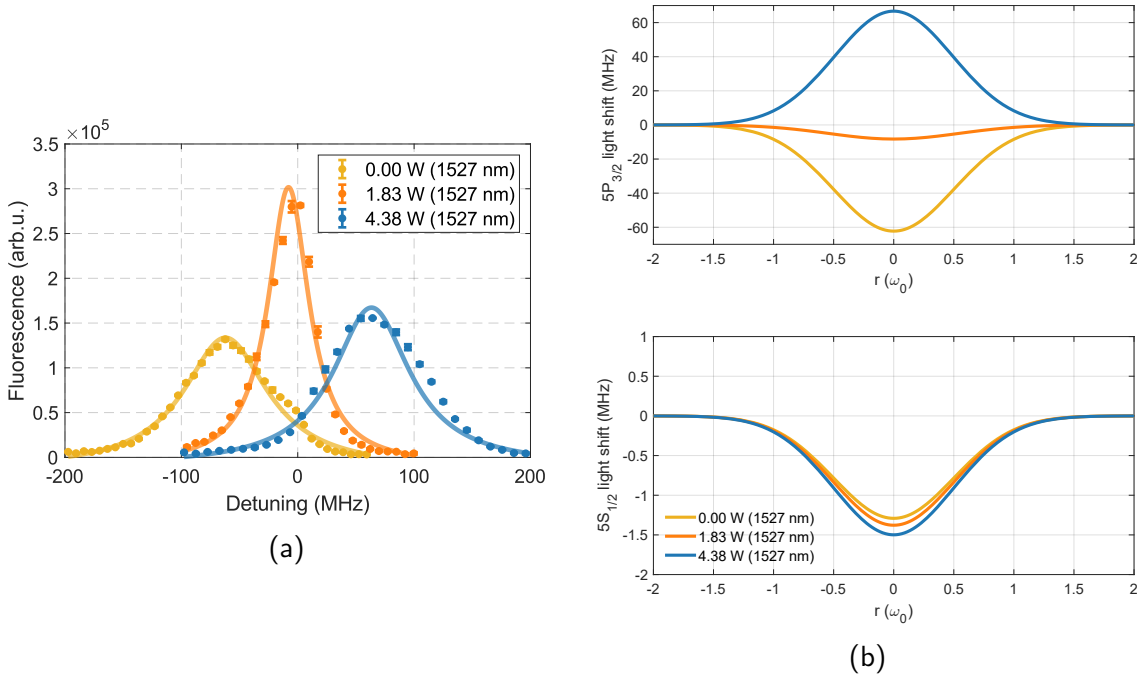

(a) (b)

Figure 4.10: (a) *In-situ* dipole potential tomography for three different $1527\,\mathrm{nm}$ intracavity powers. The $1560\,\mathrm{nm}$ intra-cavity power is fixed at $26\,\mathrm{W}$ for all measurements. The repump detuning is adjusted for each measurement: $\delta\nu = -50\,\mathrm{MHz}$, $0\,\mathrm{MHz}$, and $67\,\mathrm{MHz}$ for yellow, orange, and blue, respectively. (b) Illustration of the total light-induced shift of the $5S_{1/2}$ ground state and $5P_{3/2}$ excited state for the three intra-cavity $1527\,\mathrm{nm}$ compensation tone powers from (a). The calculation assumes a beam waist of $\omega_0 = 157\,\mu\mathrm{m}$, and a intra-cavity power of $26\,\mathrm{W}$ for the $1560\,\mathrm{nm}$ tone.

Fig. 4.10 (a) shows trap tomography measurements for a constant primary $1560\,\mathrm{nm}$ dipole trap tone of $26\,\mathrm{W}$ intra-cavity power and three different $1527\,\mathrm{nm}$ compensation tone powers (P_{1527}). Fig. 4.10 (b) illustrates the corresponding total light-induced shift of the $5S_{1/2}$ ground state and the $5P_{3/2}$ excited state across the waist of the dipole trap. In the absence of the compensation tone $P_{1527} = 0\,\mathrm{W}$ (yellow), the $F = 2 \leftrightarrow F' = 3$ transition of trapped atoms experiences a negative differential light shift, which tunes the atoms in resonance and

even further towards blue-detunings relative to the MOT cooling beam frequency, thereby hindering simultaneous MOT and dipole trap operation. The orange data indicate the fully compensated configuration, where the relative shift is fully canceled. In the over-compensated configuration (blue), trapped atoms experience a positive differential light shift that tunes the atomic transition apart from the MOT cooling beam frequency. This configuration enables a steady-state loading scheme, where a 3D-MOT is operated in spatial overlap with the over-compensated dipole trap. The MOT captures and pre-cools the atoms in the vicinity of the dipole trap, while at the center of the dipole trap, the MOT cooling and repump beams are tuned towards the red of the corresponding atomic transitions. Consequently, atoms captured by the dipole trap experience a far-detuned dark MOT that further loads and cools the atoms into the trap. The fluorescence spectra in Fig. 4.10 (a) are fitted with a Gaussian to evaluate the center frequency of the differential shift (δ_ν). Observed spectra in over- and under-compensated configurations exhibit a broadening effect arising likely from the atomic tensor polarizability, leading dispersion in the magnetic manifolds [SC13].

Fig. 4.11 shows the number of loaded atoms into the dipole trap as a function of the intra-cavity power of the $1527\,\mathrm{nm}$ compensation tone. For reference, the three power values corresponding to the light shifts studied in Fig. 4.10 are indicated. In the under-compensated regime, the light shift induced by the $1560\,\mathrm{nm}$ dipole trap is too large, preventing the loading of atoms into the 3D-MOT. Near full compensation, around $\mathrm{P}_{1527} = 1.83\,\mathrm{W}$, the MOT begins to capture atoms. However, the cooling process is insufficient for dipole trap loading, as the temperature of the atoms remains too high compared to the dipole trap depth ($63\,\mu\mathrm{K}$). With increasing $1527\,\mathrm{nm}$ power, the system enters the over-compensated regime, where the differential light shift becomes positive, and atoms start to accumulate steadily in the dipole trap.

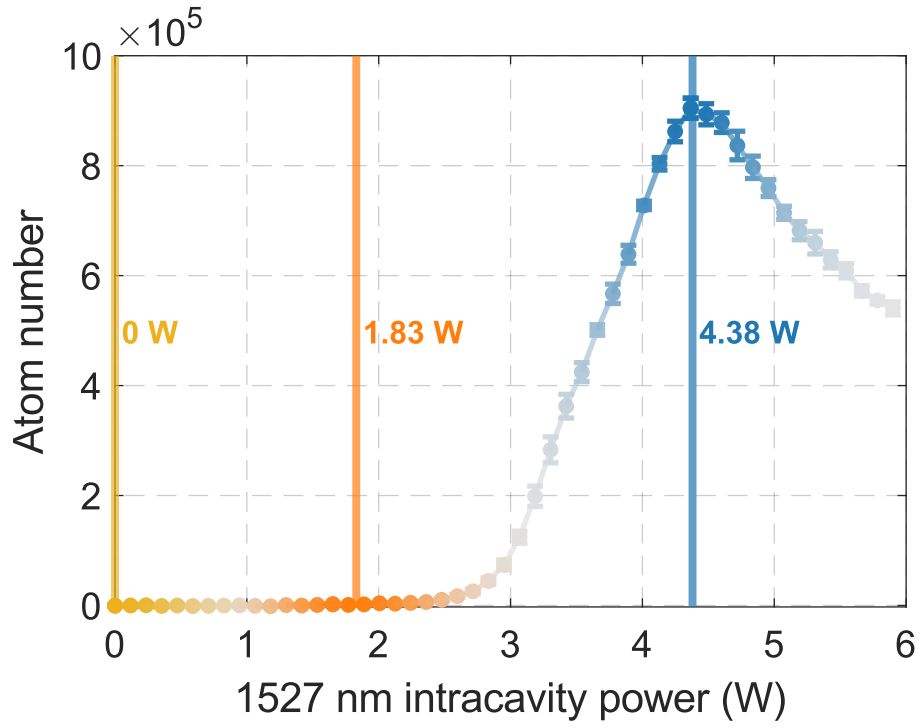

Figure 4.11: Number of accumulated atoms in the dipole trap as a function of compensation tone power. Three specific levels associated with under-, full- and over-compensated regions are highlighted.

For all data points shown, the loading sequence begins with the simultaneous engagement of the MOT coils, the cooling and the repump beams for the atom source and the MOT, as well as the dipole trap tones, with variable value for the $1527\,\mathrm{nm}$ tone. The optimum beam powers for the 3D-MOT were found to be $5\,\mathrm{W/cm^2}$ for the cooling beams and $180\,\mu\mathrm{W}$ for the repump beam. This loading phase lasts for $550\,\mathrm{ms}$, after which the coils, source, and MOT beams are turned off. The atoms are then held by another $100\,\mathrm{ms}$ in the dipole trap before being released for resonant fluorescence imaging.

The maximum number of trapped atoms is observed for an intra-cavity compensation tone power of $\mathrm{P}_{1527} = 4.38\,\mathrm{W}$ ($\mathrm{P}_{1560} = 26\,\mathrm{W}$), corresponding to a blue detuned differential shift of $\delta_\nu = 11\,\Gamma$ ($+67\,\mathrm{MHz}$) at the deepest point of the dipole trap potential. During loading, the 3D-MOT beams remain red detuned by $-2.5\,\Gamma$ from resonance. Hence, atoms in the vicinity of the dipole potential are initially captured by the 3D-MOT. As they move towards the trap center, they experience increasingly red detuning of the cooling and repump tones, reaching effectively $-13.5\,\Gamma$ and $-11\,\Gamma$, respectively, at the dipole trap depth.

Atomic state detection via fluorescence imaging reveals that 85% of the trapped atoms reside in the $F = 1$ manifold. Atoms captured in the dipole trap undergo a few cooling cycles within the F = 2 manifold, before the repump beam becomes off-resonant near the trap center, optically pumping the atoms into $F = 1$. In this state, the atoms are dark to the cooling light and remain confined in the dipole potential. This process represents a spatial analog of sequential loading of a dipole trap in a standard far-detuned MOT to dipole trap loading sequence [AR97]. Under these conditions, nearly 1×10^6 atoms are loaded into the cavity-mediated dipole trap, corresponding to approximately 5% of the number captured in an optimized 3D-MOT (see Fig. 4.3) for an equal loading duration. The most relevant parameters of the steady-state accumulation sequence are summarized in Tab. 4.4.

Loading time (ms)	I_{cool} $(\mathrm{mW/cm^2})$	δ_{cool} (Γ)	I_{rep} $(\mathrm{mW/cm^2})$	δ_{rep} (Γ)	δ_ν (Γ)
550	5	-2.5	0.18	0	+11

Table 4.4: Parameters of the continuous loading sequence. All detunings are referred to the corresponding unperturbed atomic transitions.

4.2.3 Molasses Cooling in Light Shift Compensated Dipole Trap

In free expansion, after release from the dipole trap, the atoms retain a fingerprint of the cooling process that is related to the asymmetry of the dipole trap potential. Due to the Gaussian spatial profile of the cavity mode that mediates the dipole trap, the trap frequencies are inherently anisotropic (Eqs. 2.111, 2.112). For a trap depth of $63\,\mu\mathrm{K}$, the corresponding radial and axial trap frequencies are $\omega_x = 160\,\mathrm{Hz}$ and $\omega_y = 0.35\,\mathrm{Hz}$, respectively. Note that weak sinusoidal modulation of the trap frequency and a subsequent measurement of the atom number can be applied to measure the radial trap frequency. If the modulation frequency matches twice the trap frequency, the atomic motion is resonantly excited, leading to heating and, eventually, atom loss [Vog19]. Such trap frequency measurements were performed to calibrate the trap depth and intra-cavity power.

During the continuous loading sequence, the asymmetry of the dipole trap affects the cooling dynamics. Trapped atoms undergo several oscillations along the radial direction, while their motion in the axial direction remains largely unaffected due to the much weaker confinement. Thus, the differential light shift of a trapped atom is modulated at the trap frequency, which

leads to reduced cooling efficiency along the radial axis. The blue data points in Fig. 4.12 show a representative time-of-flight (TOF) measurement of the atomic ensemble after a continuous loading sequence. The results reveal an anisotropic temperature distribution. The axial temperature of the atoms is as low as $T_y = 13.61\,\mu\mathrm{K}$, while the radial temperature is $T_x = 39.76\,\mu\mathrm{K}$, proximately three times larger.

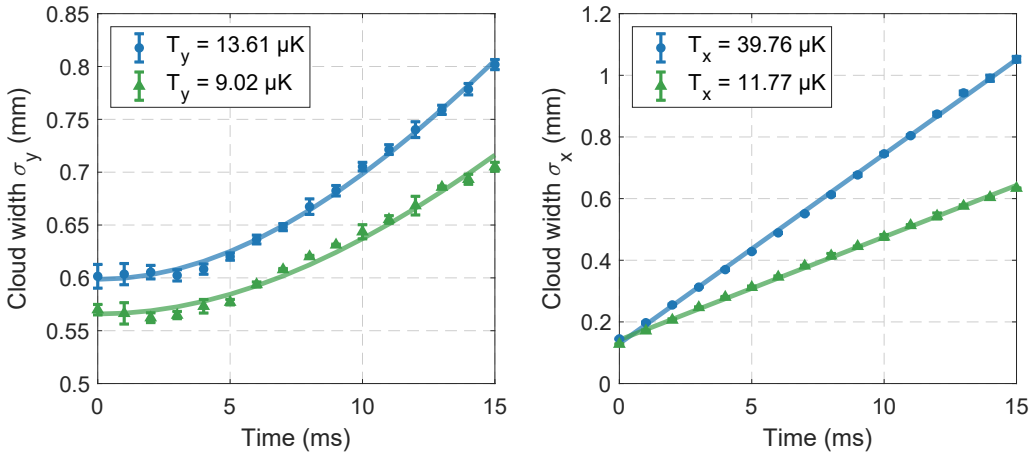

Figure 4.12: Temperature measurements of the atoms in the axial 'y' and radial 'x' directions, characterized by TOF. Blue circles: Measurements after continuous accumulation. The differential light shift is set to $\delta_\nu = 11\,\Gamma$ throughout accumulation and storage. Green triangles: After accumulation, the differential light shift is set to $\delta_\nu = 0\,\Gamma$, and optical molasses is applied for 10 ms.

To eliminate the temperature anisotropy and achieve further cooling of the trapped atoms, optical molasses is applied directly within the dipole trap under the conditions of full AC Stark shift compensation ($\delta_\nu = 0\,\Gamma$). Following the initial $550\,\mathrm{ms}$ accumulation period, the $1527\,\mathrm{nm}$ intra-cavity power is adjusted to $I_{\mathrm{rep}} = 1.83\,\mathrm{W}$, and a $10\,\mathrm{ms}$ molasses sequence is performed. The intensities and detunings of the cooling and repump beams applied during this *in trap* molasses sequence can be found in Tab. 4.5. The green triangles in Fig. 4.12 show the TOF measurement to determine the temperature after *in trap* molasses cooling. The results demonstrate a homogeneous temperature of around or below $10\,\mu\mathrm{K}$ in both the radial and axial trap directions, confirming molasses cooling in the compensated dipole trap.

Time in Molasses (ms)	I_{cool} $(\mathrm{mW/cm^2})$	δ_{cool} (Γ)	I_{rep} $(\mathrm{mW/cm^2})$	δ_{rep} (Γ)	δ_ν (Γ)
10	0.8	-20	0.18	0	0

Table 4.5: Parameters of the *in trap* molasses sequence. All detunings are referred to the corresponding unperturbed atomic transitions.

4.2.4 An Alternative Loading Scheme

We briefly discuss an alternative AC Stark-compensated trap loading scheme that resulted in a twofold increase in loading efficiency and highlights potential for future optimization of the dipole trap loading sequence. In this approach, the compensation tone is initially set to $P_{1527} = 1.83\,\mathrm{W}$, corresponding to full cancellation of the differential AC Stark shift ($\delta_\nu = 0\,\Gamma$). The 3D-MOT is operated under optimized free-space loading conditions (see Tab. 4.1), where atoms are first accumulated for 500 ms. Subsequently, the cooling beam intensity is reduced

to $P_{cool} = 0.5\,\mathrm{W/cm^2}$ and the repump beam is switched off, while the compensation tone power is linearly ramped up to $P_{1527} = 4.38\,\mathrm{W}$, the optimum value in the continuous loading configuration.

The final 40 ms of this sequence effectively form a weak, continuously detuned FD-MOT phase, during which the linear ramp of the compensation tone power gradually shifts the MOT beam detuning in the center of the trap from $\delta_{\mathrm{cool}} = -2.5\,\Gamma$ to $\delta_{cool} = -20\,\Gamma$. The intensities and detunings of the MOT-beams, as well as the *in trap* light shift ramp parameters for this loading sequence, can be found in Tab. 4.6. This procedure yields approximately 2×10^6 atoms loaded into the dipole trap, corresponding to 12% of the total 3D-MOT population, which is twice of the efficiency achieved in the continuous loading sequence. To the best of our knowledge, this represents the highest reported MOT-to-$1560\,\mathrm{nm}$ dipole trap transfer efficiency to date. Although this sequence technically breaks the steady-state condition, it reduces the overall duty cycle by half, while the change in intra-cavity power ($\Delta P_{1527} = 2.5\,\mathrm{W}$) remains small enough to avoid significant photothermal effects. Furthermore, we observed reduced fluctuation in the number of trapped atoms compared to the continuous loading sequence. These results suggest that the investigation of more sophisticated loading schemes, combining elements of steady-state operation with dynamic modulation of the light shift compensation and MOT cooling parameters, could further enhance the atom loading and cooling efficiencies and should be considered for future development.

Time (ms)	I_{cool} ($\mathrm{mW/cm^2}$)	δ_{cool} (Γ)	I_{rep} ($\mathrm{mW/cm^2}$)	δ_{rep} (Γ)	δ_{ν} (Γ)
0	10	-2.5	5	0	0
500	0.5	-2.5	0	0	0
540	0.5	-2.5 (-13.5)	0	(-11)	+11

Table 4.6: Parameters of an alternative AC Stark-compensated trap loading scheme. Detunings are referred to the corresponding unperturbed atomic transitions. Detunings in parentheses correspond to the effective detuning at the center of the trap.

4.3 Atomic-State Preparation

4.3.1 Optical Pumping

Above, we demonstrated the experimental capability for efficient loading and cooling of atoms into the optical dipole trap. For the implementation of future squeezing sequences (Sec. 2.3.4) and Raman transitions (Sec. 2.5), it is necessary to polarize the atomic ensemble into the magnetically insensitive $|F = 1, m_F = 0\rangle$ hyperfine ground state. During molasses cooling (Sec. 4.2.3), however, the atoms are optically pumped into the magnetic manifold of the $|F = 2\rangle$ ground state. In order to polarize the atoms into the clock state manifold ($m_F = 0$) of the two hyperfine ground states, we apply an optical pumping sequence[AGC$^+$87, DWX$^+$17], while the atoms are kept in a dipole trap in a fully compensated differential light shift configuration.

Optical pumping relies on the selective population transfer between magnetic sublevels until the atoms accumulate in a state that is dark to the pump light. Fig. 4.13, the diagram of the applied optical pumping scheme is shown. The initial population in the $|F = 2\rangle$ ground state is transferred via the $|F = 2\rangle \leftrightarrow |F' = 2\rangle$ transition, which is off-resonantly driven by the σ^+-σ^- polarized MOT cooling light. Atoms excited to $|F' = 2\rangle$ decay spontaneously

($\Gamma = 2\pi \times 6.065\,\mathrm{MHz}$) with a 60% probability into the magnetic manifold of the $|F = 1\rangle$ ground state [Ste10]. Repeated absorption and spontaneous emission cycles deplete the $|F = 2\rangle$ population and accumulate atoms in the $|F = 1\rangle$ manifold.

From there, the π polarized repump light, resonant with the $|F = 1\rangle \leftrightarrow |F' = 1\rangle$ transition, drives $\Delta m_F = 0$ transitions between the magnetic sublevels. Since the $|F = 1, m_F = 0\rangle \leftrightarrow |F' = 1, m_{F'} = 0\rangle$ transition is dipole forbidden, the $m_F = 0$ sublevel remains dark for the pump light. After several optical pumping cycles, the atomic ensemble is efficiently prepared by spontaneous decay into the targeted $|F = 1, m_F = 0\rangle$ state.

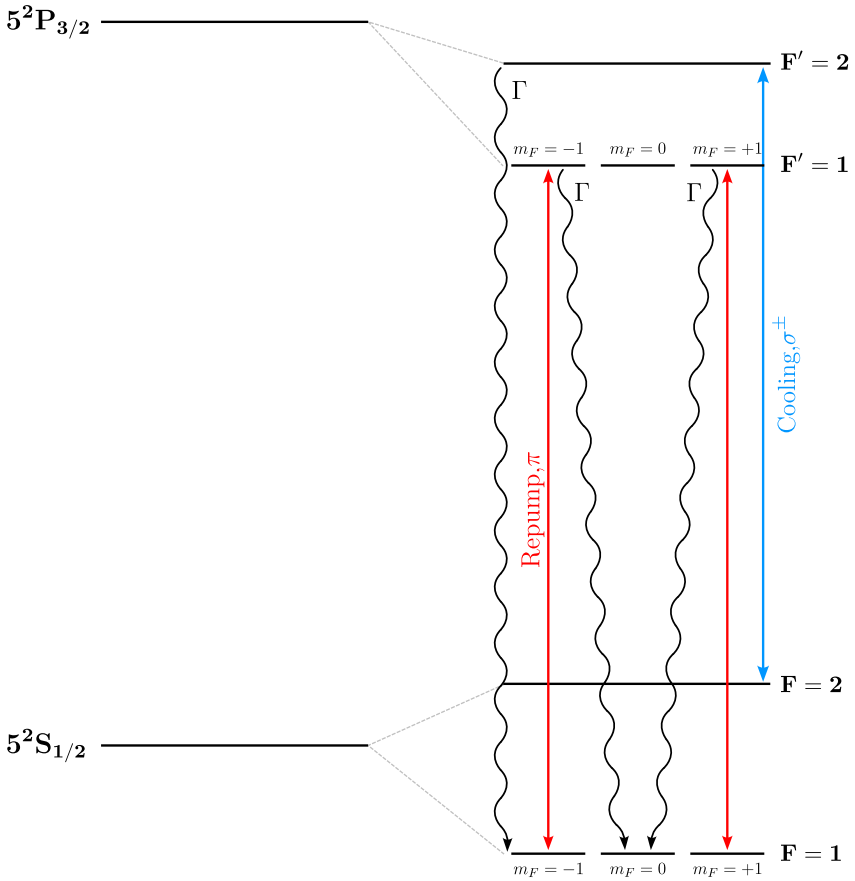

Figure 4.13: Diagram of the optical pumping scheme in ^{87}Rb.

Prior to the experimental realization of optical pumping, the correct quantization axis must be set.The incident repump beam has polarization parallel to the cavity mode axis. In order to enable π transitions, the quantization axis must be aligned with the light polarization, and, therefore, with the cavity mode axis. Furthermore, the ramp function of the control system (Sec. 3.7) is used to tune the repump and cooling light frequencies. The repump light is tuned into resonance with the $|F = 1\rangle \leftrightarrow |F' = 1\rangle$ transition, corresponding to a detuning $\delta_{\mathrm{rep}} = -25.88\,\Gamma$ from its reference $|F = 1\rangle \leftrightarrow |F' = 2\rangle$ transition. Similarly, the cooling beam is tuned into resonance $|F = 2\rangle \leftrightarrow |F' = 2\rangle$, corresponding to $\delta_{rep} = -44\,\Gamma$ from its reference $|F = 2\rangle \leftrightarrow |F' = 3\rangle$ transition.

The optical powers for both beams are chosen well below the saturation intensity (I_{sat}) to prevent heating and avoid saturation of the pump transitions. The pump sequence lasts for $0.1\,\mathrm{ms}$, corresponding to several thousand pump cycles (excited-state lifetime $\tau \approx 26\,\mathrm{ns}$). The duration was found experimentally by monitoring the pump efficiency. With this sequence, approximately 87% of the initially trapped atoms are pumped into the $|F = 1, m_F = 0\rangle$ state.

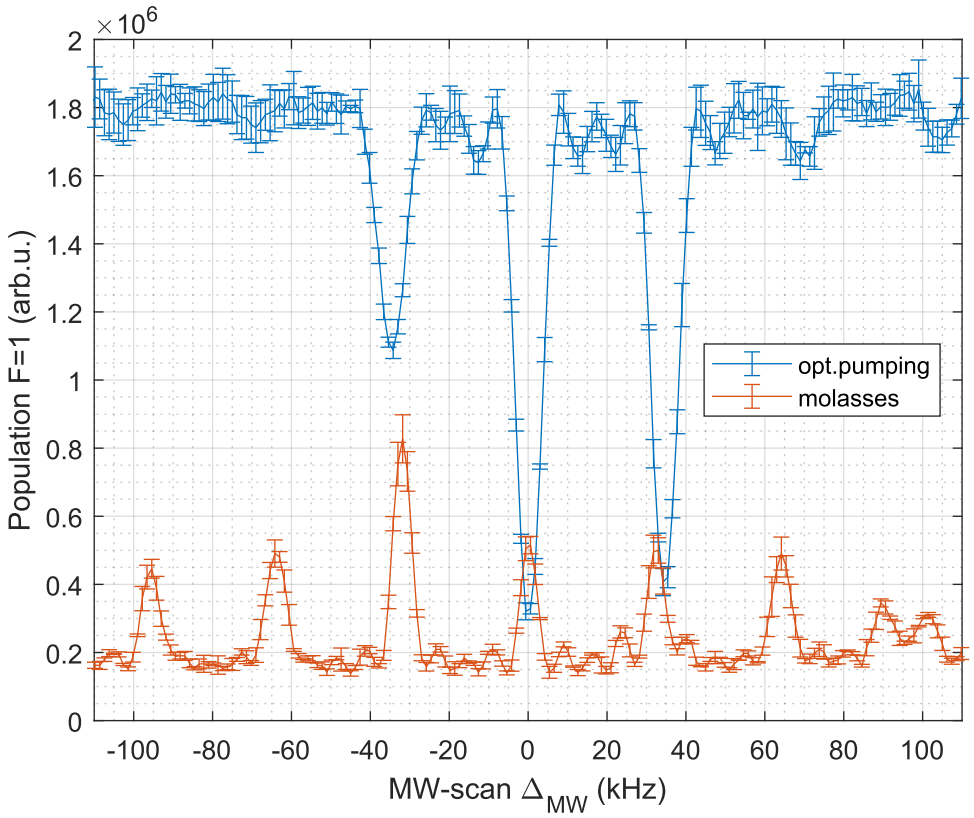

Figure 4.14: MW spectroscopy of the atomic ensemble before and after optical pumping. The observation of three resonances and the absence of additional lines demonstrates successful optical pumping of the atomic ensemble in the $|F = 1, m_F = 0\rangle$ state.

For state preparation, the residual population in the $|F = 2\rangle$ state is removed from the trap with a push beam. For a compact overview, Tab. 4.7 summarizes the main parameters of the optical pumping sequence.

Pump duration (ms)	I_{cool} (mW/cm^2)	δ_{cool} (Γ)	I_{rep} (mW/cm^2)	δ_{rep} (Γ)
0.1	0.8	-44	0.18	-25.88

Table 4.7: Parameters of the optical pumping sequence. The cooling light is tuned in resonance with the $|F = 2\rangle \leftrightarrow |F' = 2\rangle$ transition, and the repump light is tuned in resonance with the $|F = 1\rangle \leftrightarrow |F' = 1\rangle$ transition.

To confirm that the atomic ensemble is polarized in the $|F = 1, m_F = 0\rangle$ state, we can perform MW spectroscopy and compare the spectra for a measurement before and after the optical pumping sequence. Recalling the magnetic sublevel structure and the corresponding MW transitions in Fig. 4.5, only three transitions should be observable, if the atoms are populated in $m_f = 0$. For MW spectroscopy, the atomic ensemble is kept trapped in the dipole trap, and the quantization axis is aligned with the z-axis in the laboratory frame. After a π_{MW} pulse, a $30\,\mu\text{s}$ push beam is applied to remove the $F = 2$ population from the trap. The residual population in $F = 1$ is held in the trap for another $20\,\text{ms}$ before the ensemble is released from the trap for a standard fluorescence detection (resonant, $0.3\,\mu\text{s}$ exposure time).

Fig. 4.14 compares MW spectra recorded after the molasses sequence (orange) and after the optical pumping sequence (blue). Following the molasses stage, the atomic population is

distributed across the magnetic manifold of the $F = 2$ state. The applied π_{MW} pulse transfers resonant atoms to $F = 1$, enabling their observation after the clean-out sequence. Seven distinct transitions, separated by approximately $35\,\mathrm{kHz}$, are observed, consistent with the the $50\,\mathrm{mG}$ bias field that defines the quantization axis. The presence of these seven transitions early indicates population across the magnetic manifold.

In contrast, the spectrum recorded after the optical pumping sequence exhibits only three resonances, corresponding to the $m_F = 0 \rightarrow m_F = 0, \pm 1$ transitions. The absence of additional lines demonstrates successful preparation of the atomic ensemble in the $|F = 1, m_F = 0\rangle$ state. The reversed polarity of the spectroscopy signal arises from the atoms being pumped into $F = 1$. In this case, the π_{MW} pulse drives resonant atoms to $F = 2$, where they are subsequently removed by the push beam. The slight displacement of the off-center peaks between the two spectra is attributed to fluctuations in the bias magnetic field.

4.3.2 Microwave-Driven Rabi Oscillation

After demonstrating that the trapped atoms can be prepared in the$|F = 1, m_F = 0\rangle$ state, we proceed to demonstrate full control over the atomic state preparation. To this end, we apply a resonant microwave tone ($\omega_{MW} = 2\pi\times\ 6.834\,\mathrm{GHz}$) to directly drive Rabi oscillations in the magnetic insensitive ^{87}Rb clock state manifold.

Before discussing the experimental results, we briefly recall the physical fundamentals of Rabi oscillations [SZ97]. We consider a two-level atomic system interacting via the electric dipole interaction with an external oscillating field of frequency ω. Transforming into the rotating frame and applying the rotating-wave approximation, the Hamiltonian of the interacting system takes the form

$$\hat{H}_{int} = -\frac{\hbar}{2}\begin{pmatrix} -\Delta & \Omega \\ \Omega^* & \Delta \end{pmatrix}, \tag{4.7}$$

where $\Delta = \omega - \omega_a$ is the detuning of the driving field from the atomic transition and Ω is the Rabi frequency, defined in Eq. 2.123.

The corresponding Schrödinger equations for the slowly varying probability amplitudes of the ground ($\tilde{c}_g$) and excited ($\tilde{c}_g$) states are

$$\dot{\tilde{c}}_g(t) = i\frac{\Omega}{2}e^{i\Delta t}\tilde{c}_e(t), \tag{4.8}$$

$$\dot{\tilde{c}}_e(t) = i\frac{\Omega^*}{2}e^{i\Delta t}\tilde{c}_g(t). \tag{4.9}$$

For an atom initially in the ground state $\tilde{c}_g(0) = 1$, the analytical solutions are

$$\tilde{c}_g(t) = \left(\cos\left(\frac{|\Omega'|}{2}t\right) - i\frac{\Delta}{|\Omega'|}\sin\left(\frac{|\Omega'|}{2}t\right)\right)e^{i\Delta/2t}, \tag{4.10}$$

$$\tilde{c}_e(t) = i\frac{\Omega}{|\Omega'|}\sin\left(\frac{|\Omega'|}{2}t\right)e^{-i\Delta/2t}, \tag{4.11}$$

where the detuned Rabi frequency is given by $|\Omega'| = \sqrt{|\Omega|^2 + \Delta^2}$. One resonance ($\Delta = 0$), the time-dependent populations of the ground and excited states simplify to

$$P_g(t) = |\tilde{c}_g(t)|^2 = \sin^2\left(\frac{\Omega}{2}t\right), \tag{4.12}$$

$$P_e(t) = |\tilde{c}_e(t)|^2 = \cos^2\left(\frac{\Omega}{2}t\right), \tag{4.13}$$

with the population inversion defined as

$$W(t) = P_g(t) - P_e(t) = \cos(\Omega t). \tag{4.14}$$

To observe Rabi oscillations and determine the Rabi frequency, we employ the state preparation protocol described above. Following preparation, a resonant microwave pulse of variable duration is applied, coherently coupling the $|F = 1, m_F = 0\rangle$ and $|F = 2, m_F = 0\rangle$ states and generating a controllable superposition of these two clock states. For state detection, the atoms are released from the dipole trap, and a push beam is applied to separate the hyperfine states spatially. After an appropriate separation time, fluorescence imaging is performed to extract the fluorescence intensities associated with each state.

Fig. 4.15 shows a representative measurement of the Rabi oscillations. The population inversion is obtained from the measured fluorescence intensities of the $F = 1$ and $F = 2$ states. A fit (red curve) to the data using Eq. 4.14 yields a Rabi frequency of $\Omega = 2\pi \times 3.832\,\mathrm{kHz}$. The background is an artifact of the performed fluorescence imaging and has two contributions.

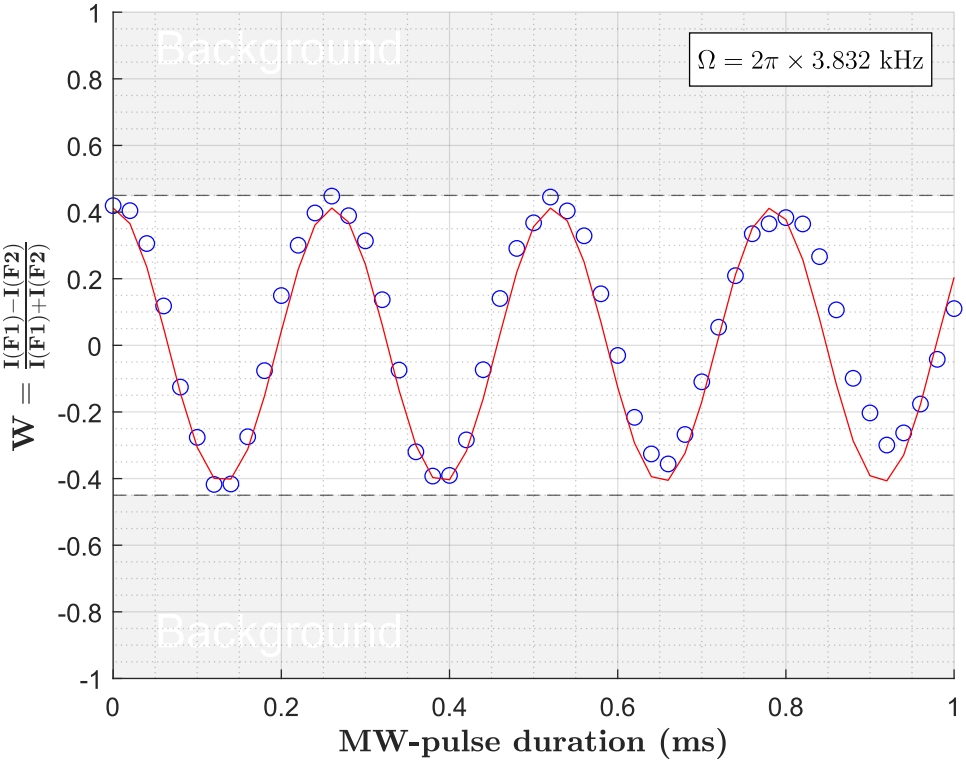

Figure 4.15: Rabi oscillation measurement. The population inversion is calculated with the observed fluorescence intensities of the $F = 1$ and $F = 2$ states (blue circles). A fit (red) of the observed oscillations with Eq. 4.14 resulted in a Rabi frequency $\Omega = 2\pi \times 3.832\,\mathrm{kHz}$. The Background is an artifact of the imperfect fluorescence detection that does not allow sufficient separation times.

The observed limited contrast originates from artifacts in the fluorescence imaging process and has two main contributions. First, the push beam used for state preparation displaces the atoms from the imaging plane, thereby reducing detection efficiency and cloud separability. Second, residual fluorescence from the background gas adds a constant offset. These data were recorded prior to implementing the continuous loading and in-trap optical pumping sequences, resulting in reduced loading efficiency and hence lower signal contrast.

To evaluate the contrast of the Rabi oscillations, and thus the fidelity of the atomic state preparation, we repeated the experiment with atoms confined in an AC Stark shift-compensated trap. This configuration allows the application of the push beam directly to the trapped atomic ensemble for state separation. The additional hold time ensures that the expelled $F = 2$ population from the trap, the remaining atoms in $F = 1$ are held for $23.5\,\mathrm{ms}$ before being released for fluorescence imaging. The additional hold time ensures that the removed $F = 2$ atoms experience sufficient free-fall to be completely removed from the fluorescence image, thereby eliminating residual background contributions. The corresponding measurement of the Rabi oscillation contrast is shown in Fig. 4.16. In this measurement, the MW pulse duration was varied up to the π pulse duration, covering the range primarily used in the experiment. A contrast of 95% is observed, demonstrating precise control over the microwave-driven system.

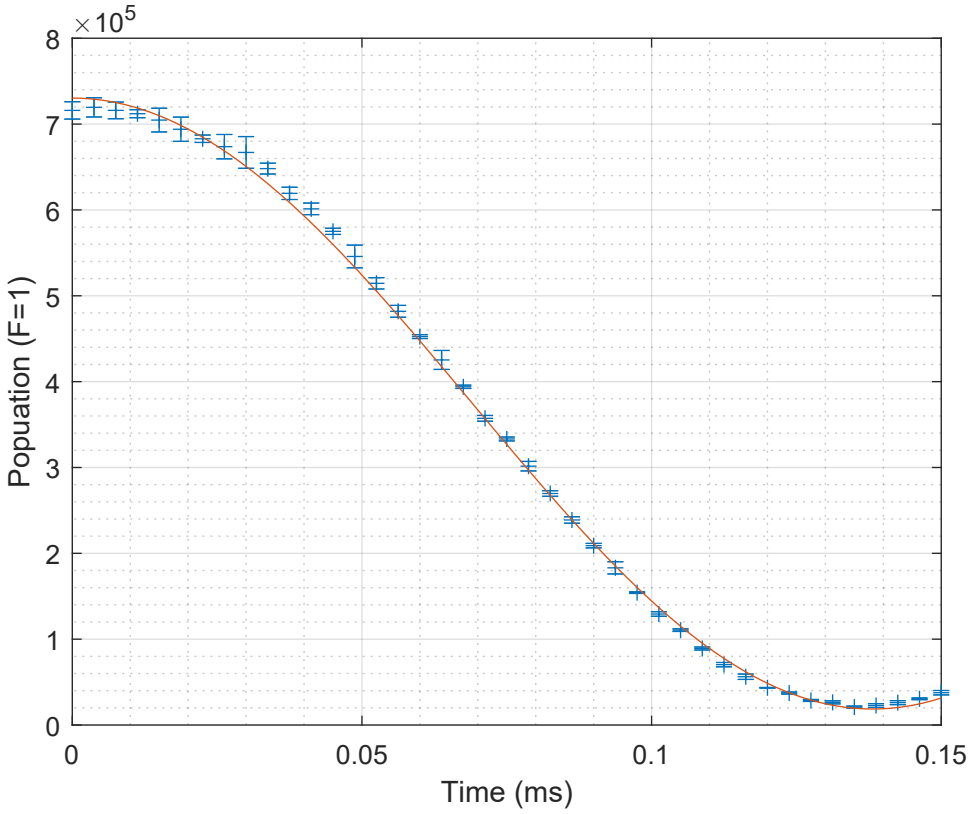

Figure 4.16: Rabi oscillation contrast measurement. The contrast of the MW driven Rabi oscillations is evaluated from measurements of the trapped $F = 1$ population. The extended hold time after state separation effectively eliminates background contributions, enabling an accurate determination of the oscillation contrast. A contrast of 95% is observed

4.4 Atom-Cavity Coupling

In this section, we characterize the dispersive coupling (Sec. 2.3.3) between the trapped atomic ensemble with the high-finesse $780\,\mathrm{nm}$ cavity mode (Sec. 3.2.6). Demonstrating this coupling is a key step toward the preparation of spin-squeezed states. As described in Sec. 2.3.4 and Sec. 2.3.4, dispersive coupling is the fundamental interaction underlying one-axis twisting dynamics and enables detection of the collective atomic state via a measurement of the dispersive shift of the cavity resonance, $\Delta_{\mathrm{disp}} = \frac{2g_0^2}{\Delta}\hat{J}_z$. In the following, we demonstrate this measurement experimentally.

Before the atom-cavity coupling can be measured, the frequency of the $780\,\mathrm{nm}$ cavity (s-pol.) must be adjusted so that both hyperfine ground states experience a symmetric dispersive shift. This is achieved by comparison of the empty cavity resonance with the resonance of the cavity loaded with an atomic ensemble prepared in a $50:50$ superposition. When the cavity is tuned such that both ground states couple dispersively to the optical excited state with equal strength, the resonance of the coupled system coincides with that of the empty cavity. Since the frequency of the $780\,\mathrm{nm}$ probe beam is derived from the dipole trap laser, it can be adjusted via the offset lock frequency of the dipole trap laser (see Sec. 3.3.2).

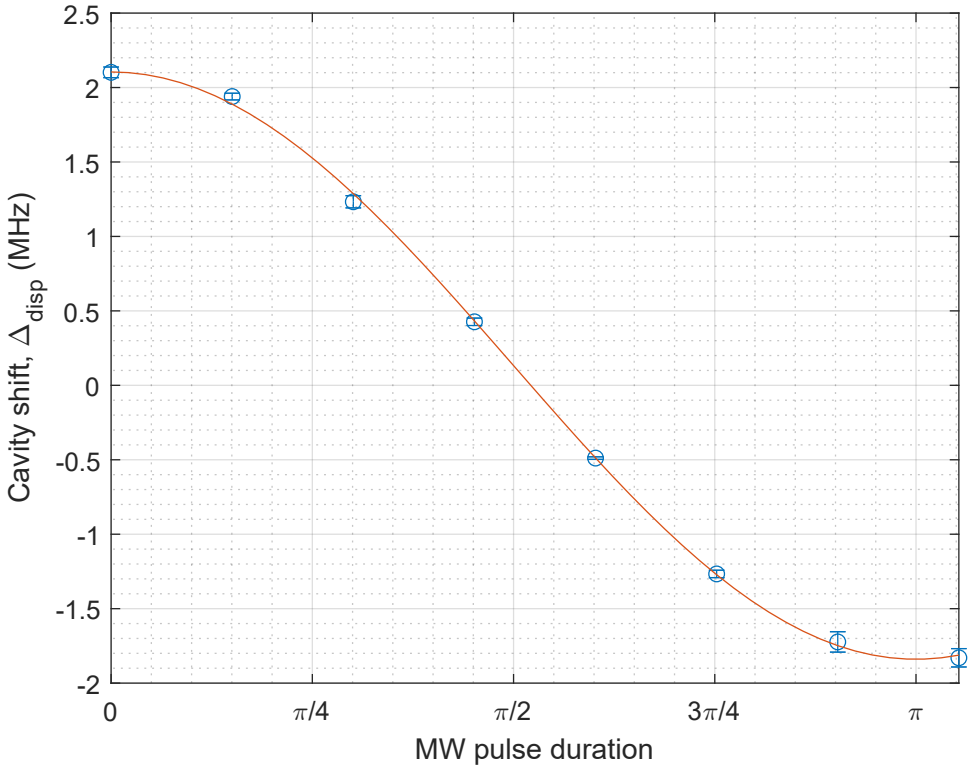

Figure 4.17: Dispersive shift of the cavity resonance during a Rabi-$\pi/2$ cycle. The total shift of $3.936\,\mathrm{MHz}$ matches precisely the expected dispersive shift derived from Eqs. 2.71 & 3.5. The fit of the experimental data using Eq. 4.15 yields the atom number $N = 9.2 \times 10^5$.

The dispersive shift is measured by preparing the trapped atomic ensemble in a superposition state defined by the duration of the applied MW pulse. For a given state, the frequency offset between the dipole trap laser and the $780\,\mathrm{nm}$ probe tone is adjusted to bring the probe into resonance with the coupled atom–cavity system. The dispersive shift is then determined as the difference between this newly set frequency offset and the offset corresponding to the empty cavity configuration. Figure 4.17 shows the results of the conducted dispersive shift measurements. The atomic ensemble contained approximately 4.5×10^5, and the cavity was probed with a power of $P_{780} = 80\,\mu\mathrm{W}$. A total dispersive shift of $\Delta_{\mathrm{total}} = 3.936\,\mathrm{MHz}$ is observed. The experimental data are fitted using

$$\Delta_{\mathrm{disp}}(t_{\mathrm{mw}}) = \frac{2g_0^2}{\Delta}\frac{N}{2}\cos(\Omega t_{\mathrm{mw}}), \tag{4.15}$$

where t_{mw} denotes the duration of the applied MW pulse, g_0 is the single-photon Rabi frequency, Δ is the atom-cavity detuning, and Ω he Rabi frequency. The fit allows for a calibration of the atom number obtained from fluorescence imaging with the dispersive shift measurement. Assuming the single-photon Rabi frequency derived from the geometric cavity properties

($g_0 = 2\pi \times 85.442\,\mathrm{kHz}$), the inferred atom number is 9.2×10^5, which is twice the atom number derived from fluorescence imaging. The mismatch originates from the imperfect alignment of the imaging system caused by separation of the telescope lenses and the mirror in between (Sec. 3.4.1, top view). An update to an imaging system that allows on-axis imaging might be considered in the future. The observed $130\,\mathrm{kHz}$ offset of the measurement curve originates from a slight inaccuracy in the initial offset frequency alignment. The future application of homodyne detection will enable more precise and stable measurements.

CHAPTER 5

Conclusion & Future Prospects

5.1 Conclusion

During the course of this thesis, an atom interferometer experiment aimed at realizing cavity-mediated, squeezed Mach-Zehnder-type interferometry was designed and set up from scratch. At the heart of the experiment is a triangular, propagating-wave cavity, engineered to mediate all relevant atom-light interactions:

1. The fundamental mode at $1560\,\mathrm{nm}$ generates a dipole potential for an ensemble of ^{87}Rb atoms with weak axial confinement, enabling an in-trap Mach–Zehnder sequence.

2. An auxiliary tone at $1527\,\mathrm{nm}$ coupled to the cavity is applied to tune the relative light shift of the ^{87}Rb D_2 line. This facilitates continuous trap loading, in-trap molasses cooling, and optical pumping.

3. A high finesse cavity mode at $780\,\mathrm{nm}$ dispersively couples the two ^{87}Rb hyperfine ground states to the first optical excited state. In this regime, spin-squeezing sequences based on OAT interaction and QND measurements can be realized.

4. The cavity also supports a low-finesse mode at $780\,\mathrm{nm}$, polarized perpendicular to the high-finesse mode and detuned by $6.834\,\mathrm{GHz}$, matching the hyperfine splitting of the ^{87}Rb ground states. This detuning, combined with the propagating-wave nature of the cavity, enables Raman transitions for the beam-splitter and mirror pulses of the interferometer.

Chapter 2 provided the theoretical framework for all these atom-light interactions and motivated the cavity design. The experimental realization of the cavity was presented in Chapter 3. In addition, the full experimental setup was discussed in detail, including the optical light-generation scheme and all laser-locking methods in their current configuration. It is worth noting that during the development of the optical setup, there was an emphasized focus on the development of new optical stabilization techniques. The resulting publications include squash lock for laser-cavity frequency stabilization [DZH24], laser offset locking [LDH22], stabilization of electro-optic I/Q modulators [WDH23] and laser current stabilization for injection-locked DFB lasers [MLW+23].

The experimental results presented in Chapter 4 gave a summary of the found optimum parameters for all involved cooling stages. The chapter emphasized the demonstration of continuous loading from the 3D-MOT into the dipole trap via the AC Stark shift compensation. Using this method, up to 4×10^6 atoms were loaded into the dipole trap within $500\,\mathrm{ms}$, enabling short repetition cycles and efficient data collection. Furthermore, AC Stark shift compensation allowed *in-trap* molasses cooling and optical pumping, thereby preserving the atom number during state preparation following the initial trapping. After the final cooling sequence, the typical atomic temperature was around $10\,\mu\mathrm{K}$, and optical pumping was achieved with an efficiency of 87%. In the final part of the chapter, coherent control of the trapped atoms was demonstrated through the measurement of microwave-driven Rabi oscillations. This state-preparation capability was subsequently applied to characterize the atom-cavity coupling.

5.2 Short Term Prospects

The next natural step in the development of the experiment is the demonstration of Raman transitions. To this end, current efforts focus on realizing Raman lasing [VHL$^+$11]. The implemented AC-Stark shift compensation enables continuous loading of atoms into the dipole trap while one of the Raman beams drives the cavity. In this configuration, when two cavity modes fulfill the two-photon Raman resonance condition, continuous Raman lasing should be observable. Future investigations could explore the preferred emission direction of the lasing light as well as possible bistable behavior. Furthermore, the setup allows driving Raman transitions with $lin \perp lin$ polarization in both co- and counter-propagating configurations, which will facilitate the initial observation of Raman transitions since co-propagating beams address a broader velocity distribution of the atoms. Once Raman transitions with counter-propagating beams are achieved, adiabatic pulse ramps will be implemented to increase their fidelity.

A second short-term goal is the completion of the homodyne detection setup, which will enable the implementation of spin-squeezing sequences and QND state detection following the procedure described in [HEKK16]. To achieve this, the microwave setup used to generate the probe beam must be capable of driving the tone in three distinct power configurations: high power for the Raman beam, intermediate power to drive the OAT dynamics, and low power for the QND cavity probe. Once this capability is established, we can begin developing and characterizing squeezing protocols.

5.3 Long Term Prospect

The long term prospect of the experiment is still the realization of the entangled Mach-Zehnder type interferometer. Figure 5.1 illustrates the envisioned experimental sequence. The initial state-preparation protocol (gray area), which polarizes the atoms into one of the ^{87}Rb hyperfine ground states, was developed during the work presented in this thesis. This is followed by the generation of a spin-squeezed collective state in the internal basis (red area). A microwave-$\pi/2$ pulse first aligns the initial coherent spin state along the equatorial plane. An initial probe pulse then generates one-axis twisting interaction, followed by a microwave-α pulse that compensates the shearing angle and aligns the squeezed spin variance along J_z. At this point, a QND measurement is performed to project the state into the further squeezed variance, thereby enhancing the effective squeezing strength.

Before the start of the Mach–Zehnder interferometer sequence (green area), a microwave-$\pi/2$ rotates the state such that the squeezed variance aligns with the phase quadrature. A first momentum kick, applied via a Raman π pulse, imparts a state-dependent momentum of $p = \pm 2\hbar k$, creating a delocalized entangled state. The relative momentum separation between the two interferometer arms is thus $\Delta p = 4\hbar k$. After a pulse separation time t, a composite mirror pulse sequence stops and reverses the spatial separation. The composite nature of this pulse arises because the propagation direction of the Raman beams cannot be reversed during the sequence. Therefore, an internal state flip must be applied after the Raman π pulse that halts the wavepacket separation. The nature of this state-flip pulse remains to be defined, possible implementations are a microwave-π pulse or a co-propagating Raman π pulse. Finally, the last Raman pulse of the Mach–Zehnder sequence recombines the interferometer paths, mapping the accumulated phase onto the internal atomic states. This phase is subsequently transferred onto the atomic population by a final microwave-$\pi/2$ pulse, which can be read out via a QND measurement of the dispersive cavity shift.

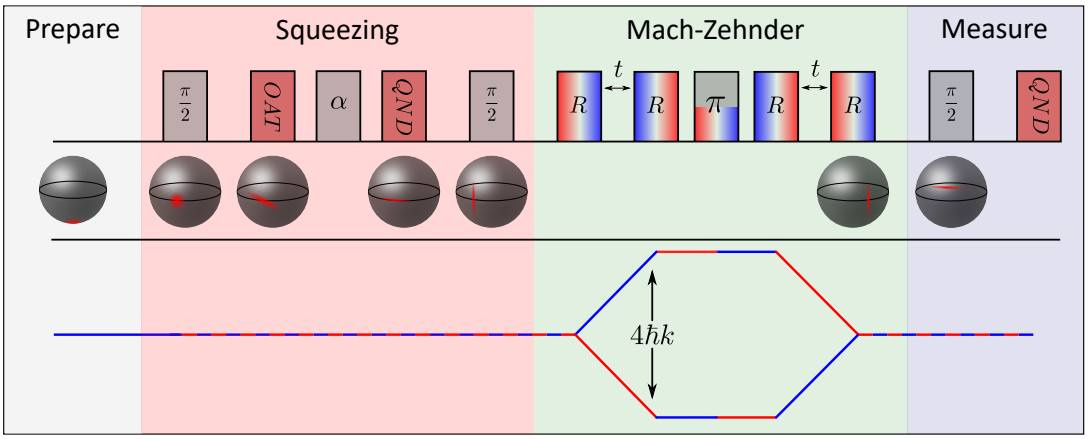

Figure 5.1: Experimental sequence of squeezed Mach-Zehnder atom interferometer. Top part: Schematic representation of the pulse sequence. microwave pulses have gray filling, squeezing sequences have red filling, and Raman pulse pairs are indicated by a red-blue transition, which also indicates the direction of the momentum transfer. Center part: State evolution in Bloch sphere representation. Lower part: Evolution of the interferometer trajectories. Blue and red colors represent the internal state of the atoms ($|F = 1, m_F = 0\rangle$ and $|F = 2, m_F = 0\rangle$, respectively). Dashed lines represent a superposition state.

Bibliography

[ACGT72] F. T. Arecchi, Eric Courtens, Robert Gilmore, and Harry Thomas. Atomic coherent states in quantum optics. *Physical Review A*, 6:2211, 12 1972.

[AEM+95] M. H. Anderson, J. R. Ensher, M. R. Matthews, C. E. Wieman, and E. A. Cornell. Observation of bose-einstein condensation in a dilute atomic vapor. *Science*, 269:198–201, 1995.

[AGC+87] G. Avila, V. Giordano, V. Candelier, E. De Clercq, G. Theobald, and P. Cerez. State selection in a cesium beam by laser-diode optical pumping. *Physical Review A*, 36:3719, 10 1987.

[AKW+24] Alexander Aeppli, Kyungtae Kim, William Warfield, Marianna S. Safronova, and Jun Ye. Clock with 8×10^{-19} systematic uncertainty. *Physical Review Letters*, 133:023401, 7 2024.

[AMW88] P. Alsing, G. J. Milburn, and D. F. Walls. Quantum nondemolition measurements in optical cavities. *Physical Review A*, 37:2970, 4 1988.

[AR97] C. S. Adams and E. Riis. Laser cooling and trapping of neutral atoms. *Progress in Quantum Electronics*, 21:1–79, 1997.

[AS68] J.R.P. Angel and P.G.H Sandars. The hyperfine structure stark effect i. theory. *Proceedings of the Royal Society of London. Series A. Mathematical and Physical Sciences*, 305:125–138, 5 1968.

[ASC07] Bindiya Arora, M. S. Safronova, and Charles W. Clark. Magic wavelengths for the np-ns transitions in alkali-metal atoms. *Physical Review A*, 76:052509, 11 2007.

[BBB+21] Kyle Beloy, Martha I. Bodine, Tobias Bothwell, Samuel M. Brewer, Sarah L. Bromley, Jwo Sy Chen, Jean Daniel Deschênes, Scott A. Diddams, Robert J. Fasano, Tara M. Fortier, Youssef S. Hassan, David B. Hume, Dhruv Kedar, Colin J. Kennedy, Isaac Khader, Amanda Koepke, David R. Leibrandt, Holly Leopardi, Andrew D. Ludlow, William F. McGrew, William R. Milner, Nathan R. Newbury, Daniele Nicolodi, Eric Oelker, Thomas E. Parker, John M. Robinson, Stefania Romisch, Stefan A. Schäffer, Jeffrey A. Sherman, Laura C. Sinclair, Lindsay Sonderhouse, William C. Swann, Jian Yao, Jun Ye, and Xiaogang Zhang. Frequency ratio measurements at 18-digit accuracy using an optical clock network. *Nature*, 591:564–569, 3 2021.

[BBC62] C F Buhrer, D Baird, and E M Conwell. Oprical frequency shifting by electro-optic effect. *Applied Physics Letters*, 1:46–49, 1962.

[BBV+10] A. Bertoldi, S. Bernon, T. Vanderbruggen, A. Landragin, and P. Bouyer. In situ characterization of an optical cavity using atomic light shift. *Optics Letters*, 35:3769–3771, 11 2010.

[BCN+14] J. G. Bohnet, K. C. Cox, M. A. Norcia, J. M. Weiner, Z. Chen, and J. K. Thompson. Reduced spin measurement back-action for a phase sensitivity ten times beyond the standard quantum limit. *Nature Photonics*, 8:731–736, 2014.

[BCV+08] J. P. Brantut, J. F. Clément, M. Robert De Saint Vincent, G. Varoquaux, R. A. Nyman, A. Aspect, T. Bourdel, and P. Bouyer. Light-shift tomography in an optical-dipole trap for neutral atoms. *Physical Review A*, 78:031401, 9 2008.

[Ber11] Simon Bernon. *Trapping and nondemolition measurement of cold atoms in a high-finesse ring cavity*. PhD thesis, Laboratoire Charles Fabry de l'Institut d'Optique / Optique atomique, 4 2011.

[BF07] James Bateman and Tim Freegarde. Fractional adiabatic passage in two-level systems: Mirrors and beam splitters for atomic interferometry. *Physical Review A*, 76:013416, 7 2007.

[BGSB00] M. Bondiou, R. Gabet, G. M. Stéphan, and P. Besnard. Linewidth of an optically injected semiconductor laser. *Journal of Optics B: Quantum and Semiclassical Optics*, 2:41, 2 2000.

[BJZ+16] Sébastien Bourdeauducq, Robert Jördens, Peter Zotov, Joe Britton, Daniel Slichter, David Leibrandt, David Allcock, Aaron Hankin, Florent Kermarrec, Yann Sionneau, Raghavendra Srinivas, Ting Rei Tan, and Justin Bohnet. Artiq 1.0. *Zenodo*, 2016.

[BKA+22] Tobias Bothwell, Colin J. Kennedy, Alexander Aeppli, Dhruv Kedar, John M. Robinson, Eric Oelker, Alexander Staron, and Jun Ye. Resolving the gravitational redshift across a millimetre-scale atomic sample. *Nature*, 602:420–424, 2 2022.

[BKPP+19] Boris Braverman, Akio Kawasaki, Edwin Pedrozo-Peñafiel, Simone Colombo, Chi Shu, Zeyang Li, Enrique Mendez, Megan Yamoah, Leonardo Salvi, Daisuke Akamatsu, Yanhong Xiao, and Vladan Vuletić. Near-unitary spin squeezing in yb171. *Physical Review Letters*, 122:223203, 6 2019.

[BNLR+11] Dang Thanh Bui, Chi Thanh Nguyen, Isabelle Ledoux-Rak, Joseph Zyss, and Bernard Journet. Instrumentation system for determination and compensation of electro-optic modulator transfer function drift. *Measurement Science and Technology*, 22:125105–125117, 2011.

[Bro25] Louis De Broglie. Recherches sur la théorie des quanta. *Annales de Physique*, 10:22–128, 1925.

[BVT80] Vladimir B. Braginsky, Yuri I. Vorontsov, and Kip S. Thorne. Quantum nondemolition measurements. *Science*, 209:547–557, 8 1980.

[CBAC86] Steven Chu, J. E. Bjorkholm, A. Ashkin, and A. Cable. Experimental observation of optically trapped atoms. *Physical Review Letters*, 57:314, 1986.

[CBW+14] Zilong Chen, Justin G. Bohnet, Joshua M. Weiner, Kevin C. Cox, and James K. Thompson. Cavity-aided nondemolition measurements for atom counting and spin squeezing. *Physical Review A*, 89:043837, 4 2014.

[CGL+22] Sebastian C. Carrasco, Michael H. Goerz, Zeyang Li, Simone Colombo, Vladan Vuletić, and Vladimir S. Malinovsky. Extreme spin squeezing via optimized one-axis twisting and rotations. *Physical Review Applied*, 17:064050, 6 2022.

[CLM+16] R. Culver, A. Lampis, B. Megyeri, K. Pahwa, L. Mudarikwa, M. Holynski, Ph W. Courteille, and J. Goldwin. Collective strong coupling of cold potassium atoms in a ring cavity. *New Journal of Physics*, 18:113043, 11 2016.

[CM17] Bruce Carter and Ron Mancini. *Op Amps for Everyone: Fifth Edition*. Elsevier Inc., 7 2017.

[CMHRK25] Christophe Cassens, Bernd Meyer-Hoppe, Ernst Rasel, and Carsten Klempt. Entanglement-enhanced atomic gravimeter. *Physical Review X*, 15:011029, 2 2025.

[CPG+17] Simon Coop, Silvana Palacios, Pau Gomez, Y Natali, Martinez De Escobar, Thomas Vanderbruggen, and Morgan W Mitchell. Floquet theory for atomic light-shift engineering with near-resonant polychromatic fields. *Optics Express*, 25:32550–32559, 12 2017.

[CPPA+22] Simone Colombo, Edwin Pedrozo-Peñafiel, Albert F. Adiyatullin, Zeyang Li, Enrique Mendez, Chi Shu, and Vladan Vuletić. Time-reversal-based quantum metrology with many-body entangled states. *Nature Physics*, 18:925–930, 8 2022.

[CSP09] Alexander D. Cronin, Jörg Schmiedmayer, and David E. Pritchard. Optics and interferometry with atoms and molecules. *Reviews of Modern Physics*, 81:1051, 7 2009.

[CSS+04] Benedict J Cusack, Benjamin S Sheard, Daniel A Shaddock, Malcolm B Gray, Ping Koy Lam, and Stan E Whitcomb. Electro-optic modulator capable of generating simultaneous amplitude and phase modulations. *Applied Optics*, 43:5079–5091, 2004.

[DB82] M. Ducloy and D. Bloch. Theory of degenerate four-wave mixing in resonant doppler-broadened media. - ii. doppler-free heterodyne spectroscopy via collinear four-wave mixing in two- and three-level systems. *Journal de Physique*, 43:57–65, 1 1982.

[DCT89] J. Dalibard and C. Cohen-Tannoudji. Laser cooling below the doppler limit by polarization gradients: simple theoretical models. *JOSA B*, 6:2023–2045, 11 1989.

[ddCCA+24] Quentin d'Armagnac de Castanet, Cyrille Des Cognets, Romain Arguel, Simon Templier, Vincent Jarlaud, Vincent Ménoret, Bruno Desruelle, Philippe Bouyer, and Baptiste Battelier. Atom interferometry at arbitrary orientations and rotation rates. *Nature Communications*, 15:1–9, 7 2024.

[DG27] C. Davisson and L. H. Germer. Diffraction of electrons by a crystal of nickel. *Physical Review*, 30:705, 1927.

[DHK+83] R. W.P. Drever, J. L. Hall, F. V. Kowalski, J. Hough, G. M. Ford, A. J. Munley, and H. Ward. Laser phase and frequency stabilization using an optical resonator. *Applied Physics B*, 31:97–105, 1983.

[DMA+95] K. B. Davis, M. O. Mewes, M. R. Andrews, N. J. Van Druten, D. S. Durfee, D. M. Kurn, and W. Ketterle. Bose-einstein condensation in a gas of sodium atoms. *Physical Review Letters*, 75:3969, 1995.

[DPA54] R H Dicke, Palmer Physical, and I Aboratory. Coherence in spontaneous radiation processes. *Physical Review*, 93:99, 1 1954.

[DSK06] D. S. Durfee, Y. K. Shaham, and M. A. Kasevich. Long-term stability of an area-reversible atom-interferometer sagnac gyroscope. *Physical Review Letters*, 97:240801, 2006.

[Dun15] Alexander J. Dunning. *Coherent Atomic Manipulation and Cooling*. PhD thesis, University of Southampton, 2015.

[DWX+17] Yu-Xiong Duan, Bin Wang, Jing-Feng Xiang, Qian Liu, Qiu-Zhi Qu, De-Sheng Lü, and Liang Liu. State preparation in a cold atom clock by optical pumping. *Chinese Physics Letters*, 34:073201, 7 2017.

[DZH24] Fritz Diorico, Artem Zhutov, and Onur Hosten. Laser-cavity locking utilizing beam ellipticity: accessing the 10^{-7} instability scale relative to cavity linewidth. *Optica*, 11, 2024.

[Eng16] Nils Johan Engelsen. *Quantum metrology using large ensembles of entangled atoms*. PhD thesis, Stanford University, 2016.

[FGZ+19] Yaakov Y. Fein, Philipp Geyer, Patrick Zwick, Filip Kiałka, Sebastian Pedalino, Marcel Mayor, Stefan Gerlich, and Markus Arndt. Quantum superposition of molecules beyond 25 kda. *Nature Physics*, 15:1242–1245, 2019.

[FOH03] Richard W. Fox, Chris W. Oates, and Leo W. Hollberg. 1. stabilizing diode lasers to high-finesse cavities. *Experimental Methods in the Physical Sciences*, 40:1–46, 1 2003.

[Foo05] Christopher J. Foot. *Atomic Physics*. Oxford University Press, 2005.

[FOSE13] S. J. Fabbri, C. O'Riordan, S. Sygletos, and A. D. Ellis. Active stabilisation of single drive dual-parallel mach-zehnder modulator for single sideband signal generation. *Electronics Letters*, 49:135–136, 1 2013.

[Fox06] Anthony Mark Fox. *Quantum Optics: An Introduction*, volume 15. Oxford University Press, 2006.

[Fra] Alexander Franzen. Componentlibrary: a free vector graphics library for optics.

[FVH57] Richard P. Feynman, Frank L. Vernon, and Robert W. Hellwarth. Geometrical representation of the schrödinger equation for solving maser problems. *Journal of Applied Physics*, 28:49–52, 1 1957.

[GC85] C. W. Gardiner and M. J. Collett. Input and output in damped quantum systems: Quantum stochastic differential equations and the master equation. *Physical Review A*, 31:3761, 6 1985.

[GLWT22] Graham P. Greve, Chengyi Luo, Baochen Wu, and James K. Thompson. Entanglement-enhanced matter-wave interferometry in a high-finesse cavity. *Nature*, 610:472–477, 10 2022.

[GWO00] Rudolf Grimm, Matthias Weidemüller, and Yurii B. Ovchinnikov. Optical dipole traps for neutral atoms. *Advances in Atomic, Molecular and Optical Physics*, 42:95–170, 1 2000.

[GWPH25] Edward Gheorghita, Sebastian Wald, Andrea Pupic, and Onur Hosten. Continuous accumulation of cold rubidium atoms in an optical cavity. *arXiv:TBD*, 2025.

[HEKK16] Onur Hosten, Nils J. Engelsen, Rajiv Krishnakumar, and Mark A. Kasevich. Measurement noise 100 times lower than the quantum-projection limit using entangled atoms. *Nature*, 529:505–508, 2016.

[HKEK16] O. Hosten, R. Krishnakumar, N. J. Engelsen, and M. A. Kasevich. Quantum phase magnification. *Science*, 352:1552–1555, 6 2016.

[HMY+24] Ross B. Hutson, William R. Milner, Lingfeng Yan, Jun Ye, and Christian Sanner. Observation of millihertz-level cooperative lamb shifts in an optical atomic clock. *Science*, 383:2025, 1 2024.

[HSA+13] Jan Harms, Bram J.J. Slagmolen, Rana X. Adhikari, M. Coleman Miller, Matthew Evans, Yanbei Chen, Holger Müller, and Masaki Ando. Low-frequency terrestrial gravitational-wave detectors. *Physical Review D*, 88:122003, 2013.

[ISS81] Masayuki Izutsu, Tadasi Sueta, and Shinsuke Shikama. Integrated optical ssb modulator/frequency shifter. *IEEE Journal of Quantum Electronics*, 17:2225–2227, 1981.

[Jaf18] Matthew Jaffe. *Atom interferometry in an optical cavity*. PhD thesis, UC Berkeley, 2018.

[JC63] E. T. Jaynes and F. W. Cummings. Comparison of quantum and semiclassical radiation theories with application to the beam maser. *Proceedings of the IEEE*, 51:89–109, 1963.

[JHKwC10] D. M. S. Johnson, J. M. Hogan, M. A. Kasevich, and S. w. Chiow. Broadband optical serrodyne frequency shifting. *Optics Letters*, 35:745–747, 3 2010.

[JXH+18] Matt Jaffe, Victoria Xu, Philipp Haslinger, Holger Müller, and Paul Hamilton. Efficient adiabatic spin-dependent kicks in an atom interferometer. *Physical Review Letters*, 121:040402, 2018.

[KC92] M. Kasevich and S. Chu. Measurement of the gravitational acceleration of an atom with a light-pulse atom interferometer. *Applied Physics B Photophysics and Laser Chemistry*, 54:321–332, 5 1992.

[KCM+00] S. J.M. Kuppens, K. L. Corwin, K. W. Miller, T. E. Chupp, and C. E. Wieman. Loading an optical dipole trap. *Physical Review A*, 62:013406, 6 2000.

[KU93] Masahiro Kitagawa and Masahito Ueda. Squeezed spin states. *Physical Review A*, 47:5138, 6 1993.

[LCS+23] Zeyang Li, Simone Colombo, Chi Shu, Gustavo Velez, Saúl Pilatowsky-Came, Roman Schmied, Soonwon Choi, Mikhail Lukin, Edwin Pedrozo-Peñafie, and Vladan Vuletic. Improving metrology with quantum scrambling. *Science*, 380:1381–1384, 6 2023.

[LDH22] Vyacheslav Li, Fritz Diorico, and Onur Hosten. Laser frequency-offset locking at 10-hz-level instability using hybrid electronic filters. *Physical Review Applied*, 17:054031, 5 2022.

[Li24] Vyacheslav Li. Towards a quantum entanglement enhanced atom interferomter, 2024.

[LPG25] Vyacheslav Li, Andrea Pupic, and Alexei Gurchenko. Github - whichislovely/hosten-group-quantrol-control-system: A gui that allows running experiments using artiq system without coding., 2025. Accessed: 2025-11-27.

[LSSV10] Ian D. Leroux, Monika H. Schleier-Smith, and Vladan Vuletić. Implementation of cavity squeezing of a collective atomic spin. *Physical Review Letters*, 104:073602, 2010.

[LWH+99] M. J. Lawrence, B. Willke, M. E. Husman, E. K. Gustafson, and R. L. Byer. Dynamic response of a fabry–perot interferometer. *JOSA B*, 16:523–532, 4 1999.

[LZC+25] Chengyi Luo, Haoqing Zhang, Anjun Chu, Chitose Maruko, Ana Maria Rey, and James K. Thompson. Hamiltonian engineering of collective xyz spin models in an optical cavity. *Nature Physics*, 21:916–923, 6 2025.

[LZK+24] Chengyi Luo, Haoqing Zhang, Vanessa P.W. Koh, John D. Wilson, Anjun Chu, Murray J. Holland, Ana Maria Rey, and James K. Thompson. Momentum-exchange interactions in a bragg atom interferometer suppress doppler dephasing. *Science*, 384:551–556, 5 2024.

[MAMFF+02] J. M. M. A. McGuirk, G. T. Foster, J. B. Fixler, M. J. Snadden, and Kasevich. Sensitive absolute-gravity gradiometry using atom interferometry. *Physical Review A*, 65:33608, 2002.

[MCAD+25] Mason C. Marshall, Daniel A. Rodriguez Castillo, Willa J. Arthur-Dworschack, Alexander Aeppli, Kyungtae Kim, Dahyeon Lee, William Warfield, Joost Hinrichs, Nicholas V. Nardelli, Tara M. Fortier, Jun Ye, David R. Leibrandt, and David B. Hume. High-stability single-ion clock with 5.5×10^{-19} systematic uncertainty. *Physical Review Letters*, 135:033201, 7 2025.

[MCL+08] Holger Müller, Sheng Wey Chiow, Quan Long, Sven Herrmann, and Steven Chu. Atom interferometry with up to 24-photon-momentum-transfer beam splitters. *Physical Review Letters*, 100:180405, 5 2008.

[MKC08] D. J. McCarron, S. A. King, and S. L. Cornish. Modulation transfer spectroscopy in atomic rubidium. *Measurement Science and Technology*, 19:1–14, 2008.

[MLW+23] Umang Mishra, Vyacheslav Li, Sebastian Wald, Sofia Agafonova, Fritz Diorico, and Onur Hosten. Monitoring and active stabilization of laser injection locking using beam ellipticity. *Optics Letters*, 48:3973–3976, 8 2023.

[MM87] A. A. Michelson and E. W. Morley. On the relative motion of the earth and the luminiferous ether. *American Journal of Science*, 34:333–345, 1887.

[MvdS99] Harold J. Metcalf and Peter van der Straten. *Laser Cooling and Trapping*. Springer New York, 3rd edition, 1999.

[MWKC92] Kathryn Moler, David S. Weiss, Mark Kasevich, and Steven Chu. Theoretical analysis of velocity-selective raman transitions. *Physical Review A*, 45:342, 1 1992.

[MWMRK22] Benjamin K. Malia, Yunfan Wu, Julián Martínez-Rincón, and Mark A. Kasevich. Distributed quantum sensing with mode-entangled spin-squeezed atomic states. *Nature*, 612:661–665, 11 2022.

[Nag14] Warren Nagourney. *Quantum Electronics for Atomic Physics and Telecommunication*. Oxford Univerity Press, second edition, 2014.

[NEIC+20] D. S. Naik, H. Eneriz-Imaz, M. Carey, T. Freegarde, F. Minardi, B. Battelier, P. Bouyer, and A. Bertoldi. Loading and cooling in an optical trap via hyperfine dark states. *Physical Review Research*, 2:013212, 2 2020.

[NKP+18] D. S. Naik, G. Kuyumjyan, D. Pandey, P. Bouyer, and A. Bertoldi. Bose–einstein condensate array in a malleable optical trap formed in a traveling wave cavity. *Quantum Science and Technology*, 3:045009, 8 2018.

[OAC+22] Chris Overstreet, Peter Asenbaum, Joseph Curti, Minjeong Kim, and Mark A. Kasevich. Observation of a gravitational aharonov-bohm effect. *Science*, 375:226–229, 1 2022.

[PCC01] A Peters, K Y Chung, and S Chu. High-precision gravity measurements using atom interferometry. *Metrologia*, 38:25, 2 2001.

[PCG+18] Silvana Palacios, Simon Coop, Pau Gomez, Thomas Vanderbruggen, Y. Natali Martinez De Escobar, Martijn Jasperse, and Morgan W. Mitchell. Multi-second magnetic coherence in a single domain spinor bose–einstein condensate. *New Journal of Physics*, 20:053008, 5 2018.

[PM15] Justin Peatross and Ware Michael. *Physics of Light and Optics*. Brigham Young University, Department of Physics, 2015.

[PPM85] William D. Phillips, John V. Prodan, and Harold J. Metcalf. Laser cooling and electromagnetic trapping of neutral atoms. *Journal of the Optical Society of America B*, 2:1751–1767, 1985.

[PS09] Luca Pezzé and Augusto Smerzi. Entanglement, nonlinear dynamics, and the heisenberg limit. *Physical Review Letters*, 102:100401, 3 2009.

[PSO+18] Luca Pezzè, Augusto Smerzi, Markus K. Oberthaler, Roman Schmied, and Philipp Treutlein. Quantum metrology with nonclassical states of atomic ensembles. *Reviews of Modern Physics*, 90:035005, 9 2018.

[RBS+80] R. K. Raj, D. Bloch, J. J. Snyder, G. Camy, and M. Ducloy. High-frequency optically heterodyned saturation spectroscopy via resonant degenerate four-wave mixing. *Physical Review Letters*, 44:1251, 5 1980.

[RESKB02] H. Rohde, J. Eschner, F. Schmidt-Kaler, and R. Blatt. Optical decay from a fabry–perot cavity faster than the decay time. *Journal of the Optical Society of America B*, 19, 2002.

[RSC+14] G. Rosi, F. Sorrentino, L. Cacciapuoti, M. Prevedelli, and G. M. Tino. Precision measurement of the newtonian gravitational constant using cold atoms. *Nature*, 510:518–521, 2014.

[RTB74] H. Rauch, W. Treimer, and U. Bonse. Test of a single crystal neutron interferometer. *Physics Letters A*, 47:369–371, 1974.

[SC13] Chung Yu Shih and Michael S. Chapman. Nondestructive light-shift measurements of single atoms in optical dipole traps. *Physical Review A*, 87:063408, 6 2013.

[Sch72] Robert W. Schmieder. Matrix elements of the quadratic stark effect on atoms with hyperfine structure. *American Journal of Physics*, 40:297–311, 2 1972.

[SCT94] Pippa Storey and Claude Cohen-Tannoudji. The feynman path integral approach to atomic interferometry. a tutorial. *Journal de Physique II*, 4:1999–2027, 1994.

[SGOAD96] Pascal Szriftgiser, David Guéry-Odelin, Markus Arndt, and Jean Dalibard. Atomic wave diffraction and interference using temporal slits. *Physical Review Letters*, 77:4–7, 1996.

[SHH21] Stuart S. Szigeti, Onur Hosten, and Simon A. Haine. Improving cold-atom sensors with quantum entanglement: Prospects and challenges. *Applied Physics Letters*, 118:140501, 4 2021.

[Shi82] Jon H. Shirley. Modulation transfer processes in optical heterodyne saturation spectroscopy. *Optics Letters*, 7:537–539, 11 1982.

[SS11a] M. S. Safronova and U. I. Safronova. Critically evaluated theoretical energies, lifetimes, hyperfine constants, and multipole polarizabilities in ^{87}rb. *Physical Review A*, 83:052508, 2011.

[SS11b] Monika Helene Schleier-Smith. *Cavity-enabled spin squeezing for a quantum-enhanced atomic clock*. PhD thesis, Massachusetts Institute of Technology, 2011.

[SSLV10a] Monika H. Schleier-Smith, Ian D. Leroux, and Vladan Vuletić. Squeezing the collective spin of a dilute atomic ensemble by cavity feedback. *Physical Review A*, 81:021804, 2 2010.

[SSLV10b] Monika H. Schleier-Smith, Ian D. Leroux, and Vladan Vuletić. States of an ensemble of two-level atoms with reduced quantum uncertainty. *Physical Review Letters*, 104:073604, 2 2010.

[SSLV11] Monika H. Schleier-Smith, Ian D. Leroux, and Vladan Vuletić. Erratum: Squeezing the collective spin of a dilute atomic ensemble by cavity feedback [phys. rev. a 81, 021804(r) (2010)]. *Physical Review A*, 83:039907, 3 2011.

[ST91] Bahaa E. A. Saleh and Malvin Carl Teich. *Fundamentals of Photonics*. Wiley, second edition, 1991.

[Ste08] Daniel Adam Steck. Rubidium 85 d line data, 2008. Accessed: 2025-11-27.

[Ste10] Daniel Adam Steck. Rubidium 87 d line data, 2010. Accessed: 2025-11-27.

[Ste12] Daniel A. Steck. Quantum and atom optics, 5 2012. Accessed: 2025-11-27.

[SZ97] Marlan O. Scully and M. Suhail Zubairy. *Quantum Optics*. Cambridge University Press, 6 edition, 9 1997.

[TC68] Michael Tavis and Frederick W. Cummings. Exact solution for an n-molecule-radiation-field hamiltonian. *Physical Review*, 170:379–384, 1968.

[TC69] Michael Tavis and Frederick W. Cummings. Approximate solutions for an n-molecule-radiation-field hamiltonian. *Physical Review*, 188:692, 12 1969.

[THC+21] S. Templier, J. Hauden, P. Cheiney, F. Napolitano, H. Porte, P. Bouyer, B. Barrett, and B. Battelier. Carrier-suppressed multiple single-sideband laser source for atom cooling and interferometry. *Physical Review A*, 16, 7 2021.

[TMP+14] M. G. Tarallo, T. Mazzoni, N. Poli, D. V. Sutyrin, X. Zhang, and G. M. Tino. Test of einstein equivalence principle for 0-spin and half-integer-spin atoms: Search for spin-gravity coupling effects. *Physical Review Letters*, 113:023005, 2014.

[VHL+11] Geert Vrijsen, Onur Hosten, Jongmin Lee, Simon Bernon, and Mark A. Kasevich. Raman lasing with a cold atom gain medium in a high-finesse optical cavity. *Physical Review Letters*, 107:063904, 8 2011.

[Vog19] Christian Vogt. *An Optical DipoleTrap in Microgravity*. PhD thesis, Universität Bremen, 2019.

[WBIH94] D. J. Wineland, J. J. Bollinger, W. M. Itano, and D. J. Heinzen. Squeezed atomic states and projection noise in spectroscopy. *Physical Review A*, 50:67, 7 1994.

[WDH23] Sebastian Wald, Fritz Diorico, and Onur Hosten. Analog stabilization of an electro-optic i/q modulator with an auxiliary modulation tone. *Applied Optics*, 62:1–7, 1 2023.

[WKYY+00] Ed L. Wooten, Karl M. Kissa, Alfredo Yi-Yan, Edmond J. Murphy, Donald A. Lafaw, Peter F. Hallemeier, David Maack, Daniel V. Attanasio, Daniel J. Fritz, Gregory J. McBrien, and Donald E. Bossi. Review of lithium niobate modulators for fiber-optic communications systems. *IEEE Journal on Selected Topics in Quantum Electronics*, 6:69–82, 2000.

[WM25] D. F. Walls and Gerard J. Milburn. *Quantum Optics*. Springer Nature Switzerland, 3rd edition, 2025.

[XJP+19] Victoria Xu, Matt Jaffe, Cristian D. Panda, Sofus L. Kristensen, Logan W. Clark, and Holger Müller. Probing gravity by holding atoms for 20 seconds. *Science*, 366:745–749, 11 2019.

[Xu20] Victoria Ann Xu. *Lattice atom interferometry in an optical cavity*. PhD thesis, UC Berkeley, 2020.

[ZLH+18] Lingxiao Zhu, Yu Hung Lien, Andrew Hinton, Alexander Niggebaum, Clemens Rammeloo, Kai Bongs, and Michael Holynski. Application of optical single-sideband laser in raman atom interferometry. *Optics Express*, 26:6542–6553, 2018.

[ZWXP03] Jing Zhang, Dong Wei, Changde Xie, and Kunchi Peng. Characteristics of absorption and dispersion for rubidium d2 lines with the modulation transfer spectrum. *Optics Express*, 11:1338–1344, 6 2003.

[Šv10] J Švarný. Analysis of quadrature bias-point drift of mach-zehnder electro-optic modulator. In *BEC 2010 - 2010 12th Biennial Baltic Electronics Conference, Proceedings of the 12th Biennial Baltic Electronics Conference*, pages 231–234, 2010.

APPENDIX A

Feedback Theory

Since the design of electronic feedback circuits has been a fundamental part of this thesis, a brief introduction into feedback theory is given. For a more detailed discussion, we refer to [CM17, Nag14], which also form the basis for the following description.

Any electronic system can be represented as a block diagram illustrating the functional relationships between its elements. This representation allows the reduction of any complex feedback loop to its most general form, illustrated in Fig. A.1. The center block symbolizes the system with transfer function A, whose output (V_{out}), we aim to stabilize. This system is controlled by an error signal E, which is defined as the difference (negative feedback system) of the input signal V_{in} and the feedback signal, defined by the transfer function β.

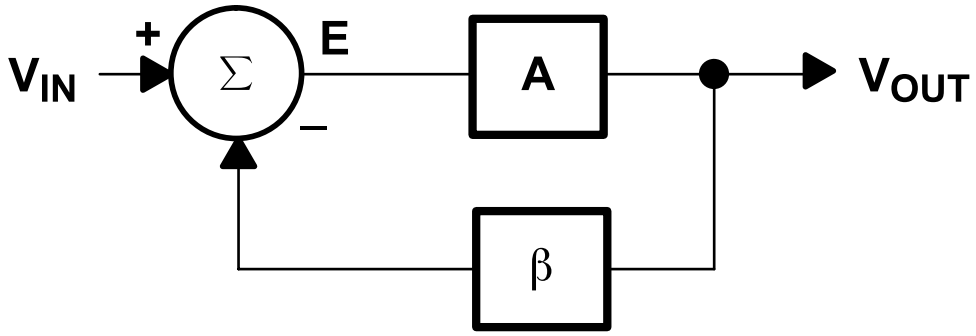

Figure A.1: Block diagram of a generalized electronic feedback circuit. Figure taken from [CM17]

To evaluate the response of the system, we can write the characteristic output and error equations, given by

$$V_{out} = E\,A, \tag{A.1}$$

$$E = V_{in} - \beta V_{out}, \tag{A.2}$$

which combined yield the system error equation

$$E = \frac{V_{in}}{1 + A\beta}. \tag{A.3}$$

The quantity $A\beta$, known as loop gain, defines the behavior of the system. If the loop gain is large, the system error is suppressed, resulting in a stable output. Therefore, the feedback circuit design generally aims to maximize this loop gain.

However, the transient functions A and β are frequency dependent and can induce a phase shift. If the phase shift of the loop gain reaches π and the loop gain approaches unity, $(1 - A\beta) \to 0$, the system error is amplified and approaches infinity. Under these conditions, the feedback becomes unstable and exhibits oscillating behavior. The frequency of the ringing signal indicates the bandwidth of the feedback system, the frequency at which the loop transitions from stable to unstable operation.

In practical feedback circuit design, the complex transfer function β is engineered such that the unity gain frequency is as high as possible, while the phase shift lies well below π (phase margin). Knowledge of the frequency response of the system, e.g. cavity resonance induced low-pass behavior, allows engineering of feedback circuits that compensate for this behavior, thereby increasing the unity gain bandwidth while keeping sufficient phase margin.

APPENDIX B

Hyperfine structure of the ^{87}Rb D_1 and D_2 lines

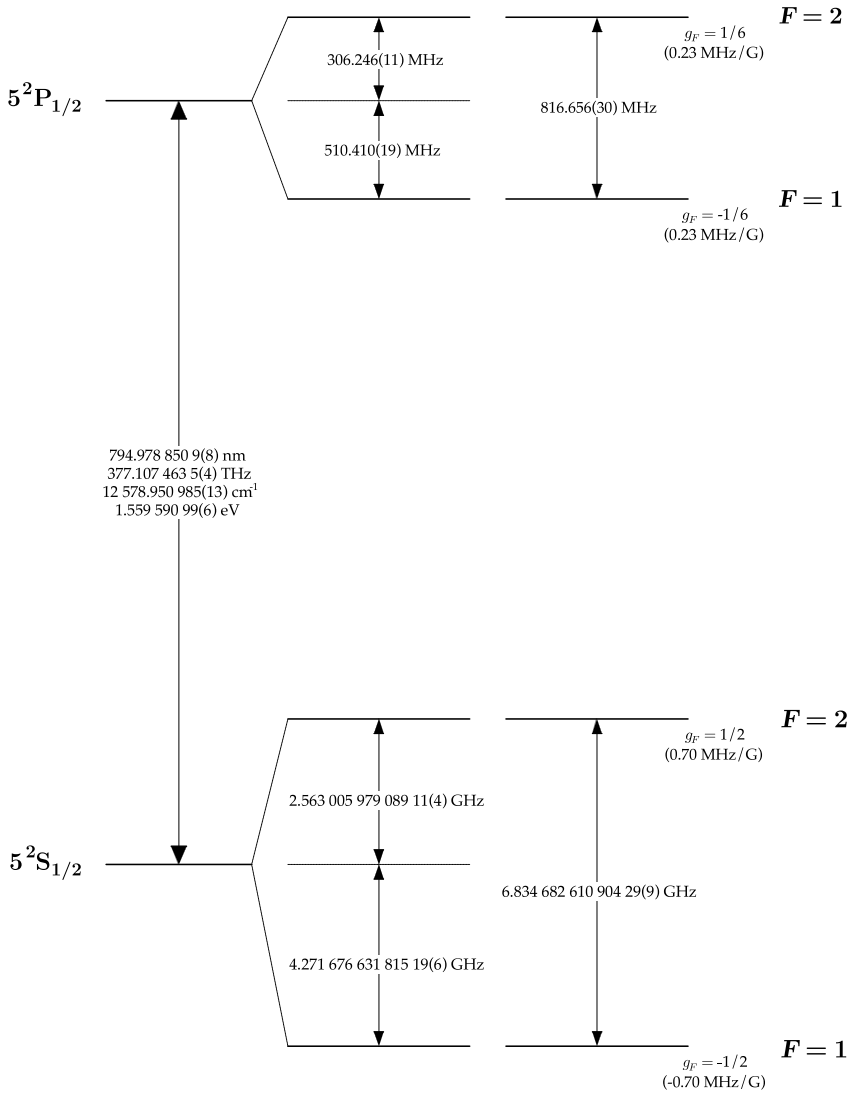

Figure B.1: Hyperfine structure of the ^{87}Rb D_1 line. Figure taken from [Ste10]

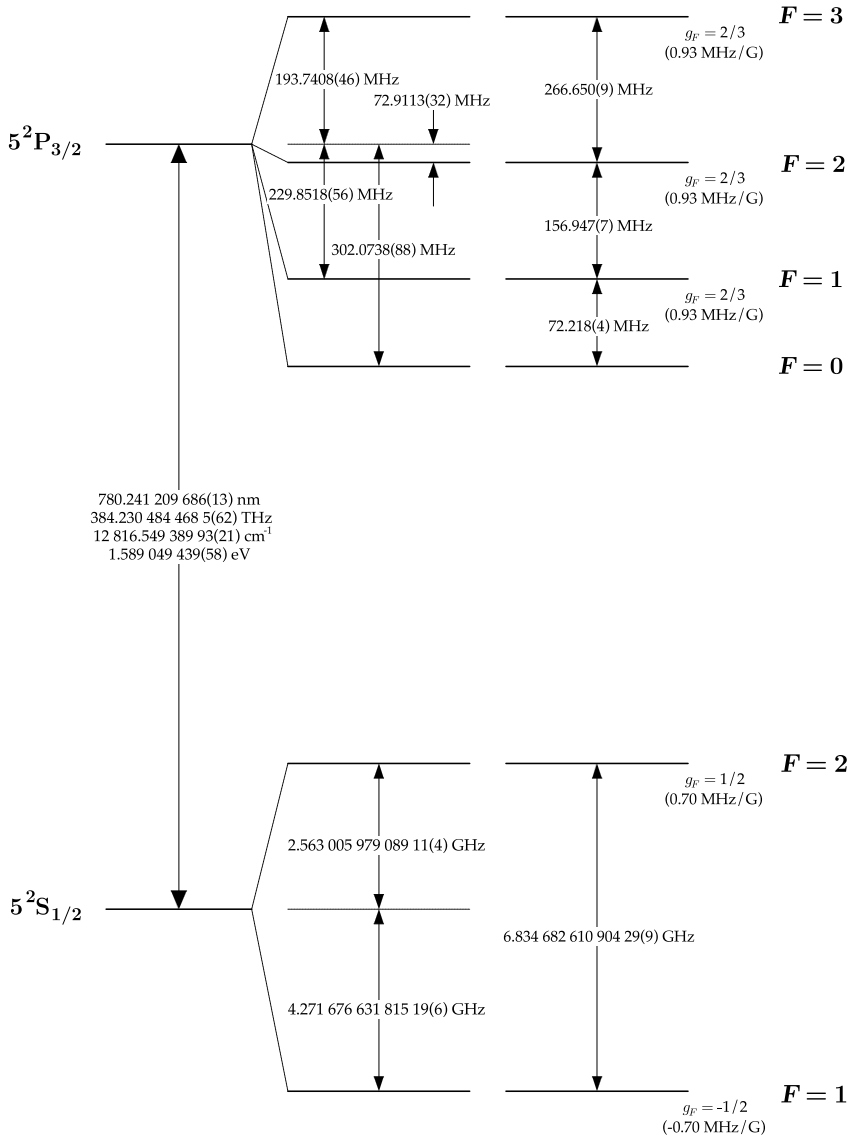

Figure B.2: Hyperfine structure of the ^{87}Rb D_2 line. Figure taken from [Ste10]

APPENDIX C

Specification of Birefringent Mirror Coating

Low loss partial reflector – exemplary data

fig. 1 calculated reflectance (AOI=30°)

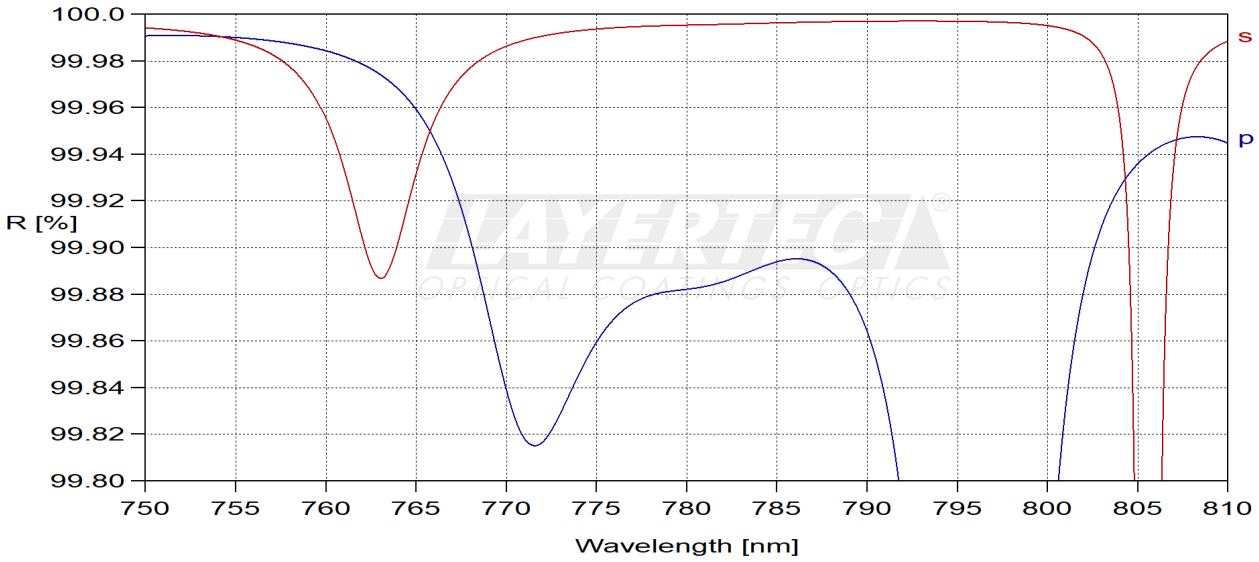

fig. 2 calculated transmittance (AOI=30°)

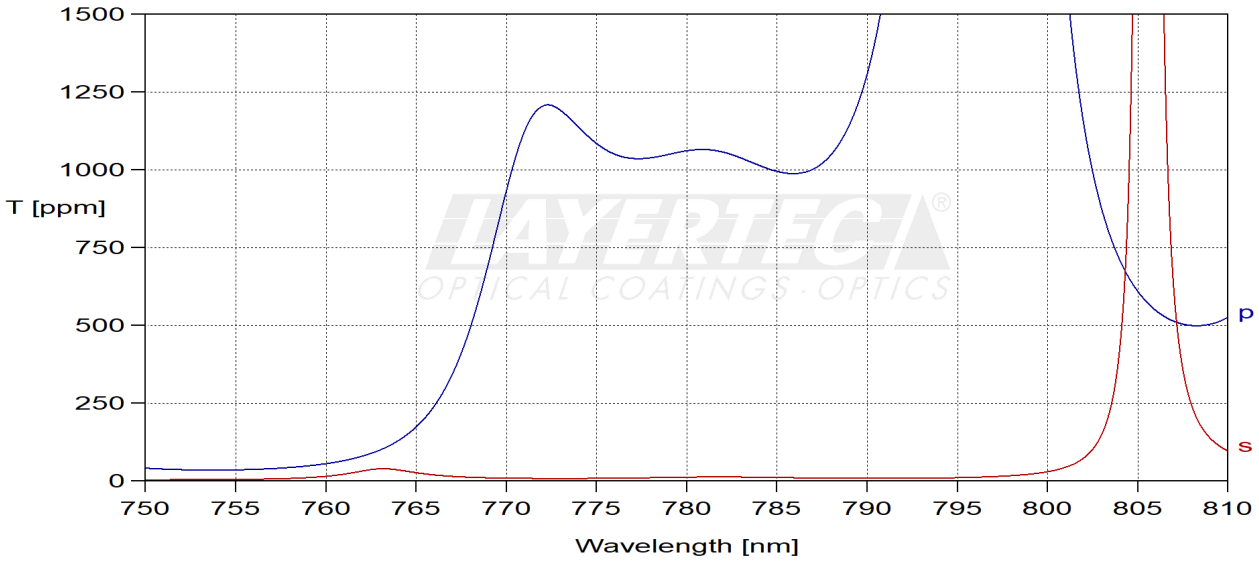

non binding principle curve

fig. 3 calculated transmittance (AOI=30°, s-pol.)

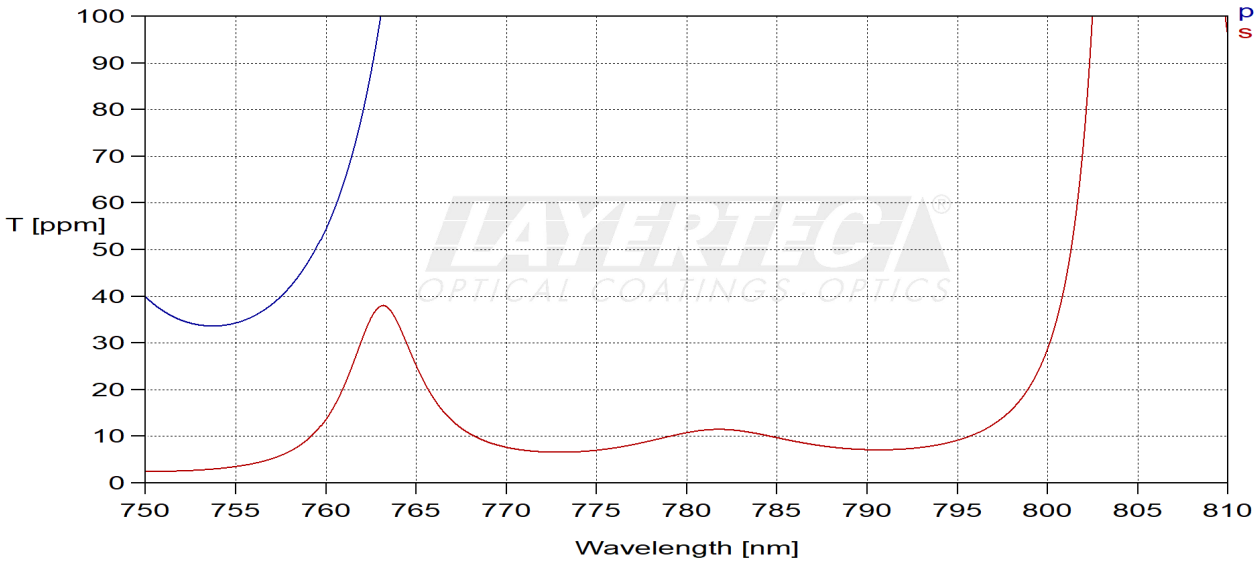

fig. 4 calculated reflected phase (AOI=30°)

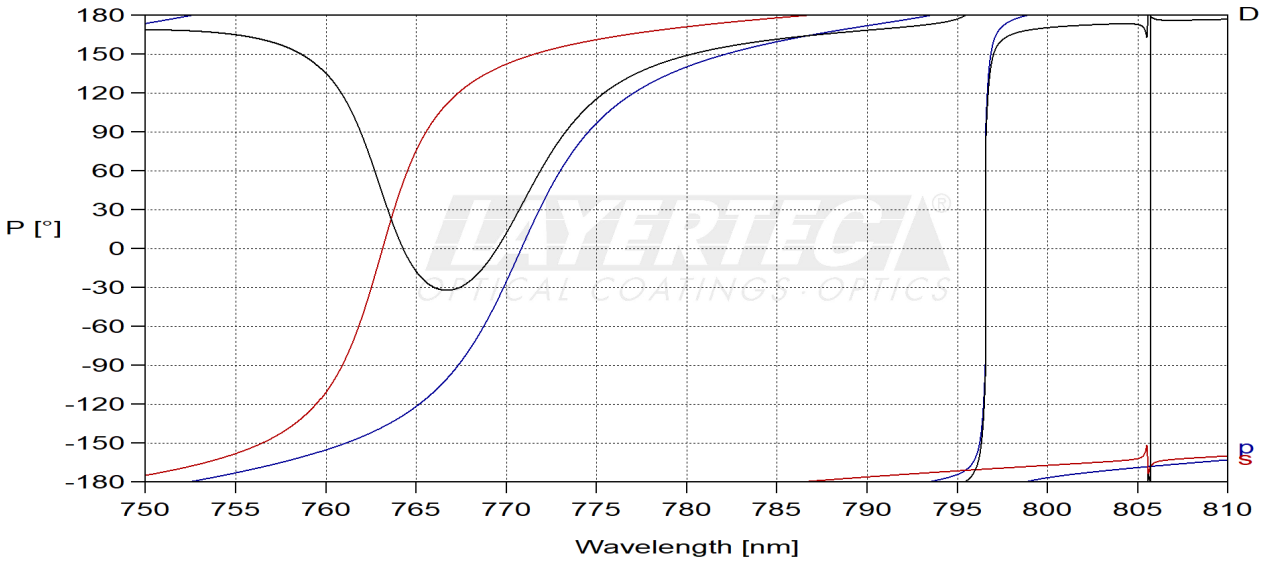

Please note that D = 180° - Phase-Rs + Phase-Rp.

fig. 5 calculated reflectance (AOI=30°, s-pol.)

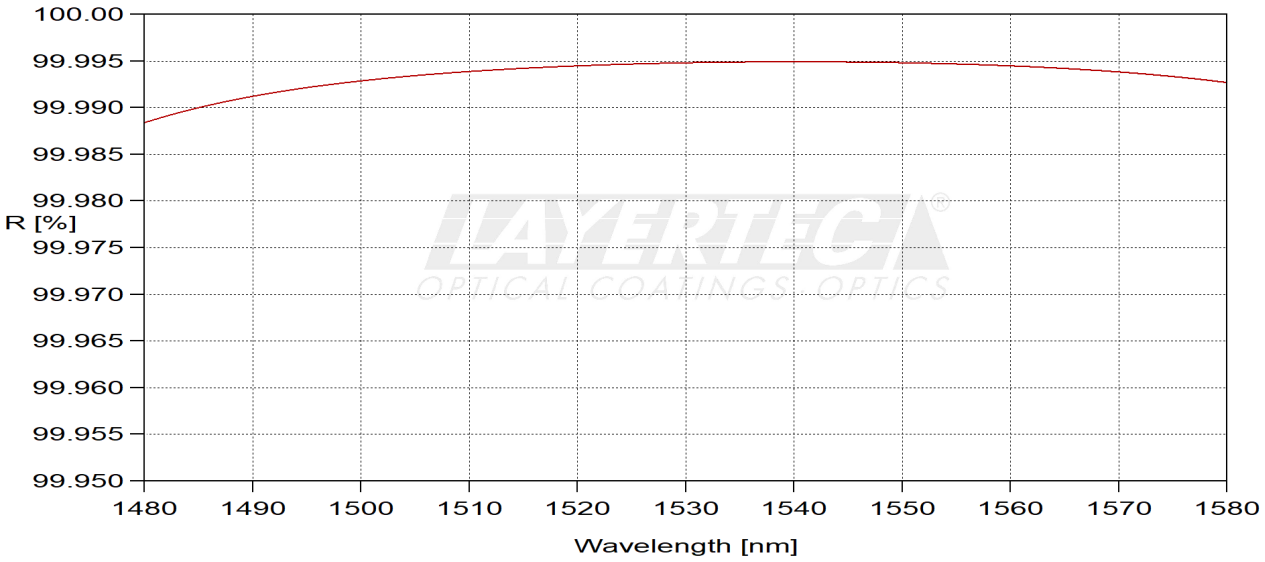

fig. 6 calculated transmittance (AOI=30°, s-pol.)

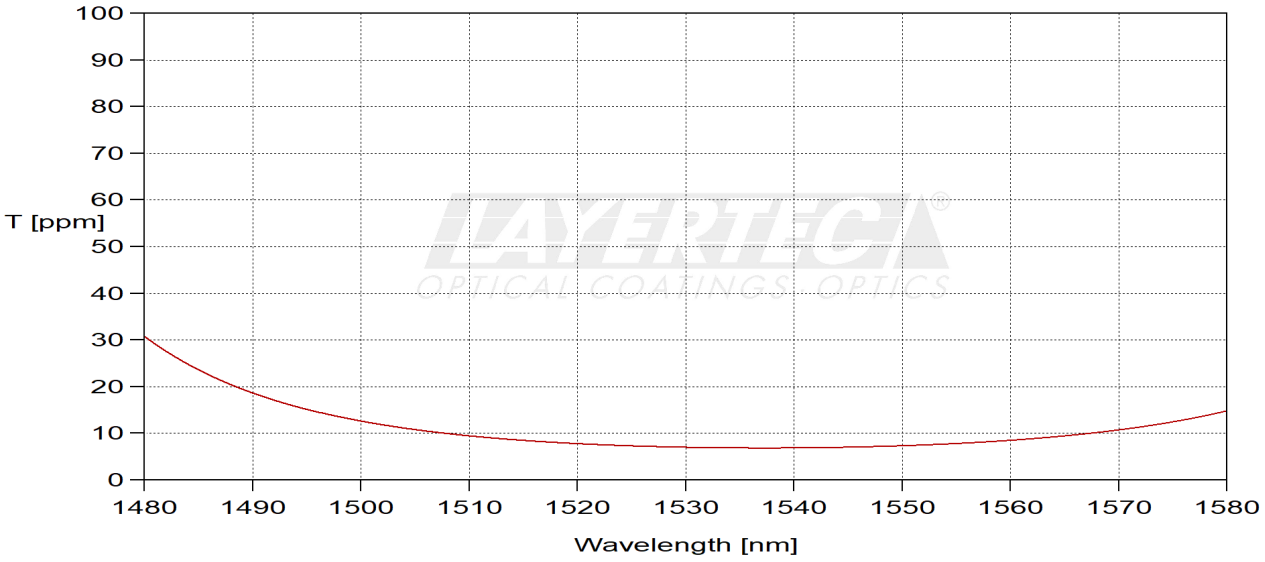

APPENDIX D

MOT Optical Power Distribution Setup

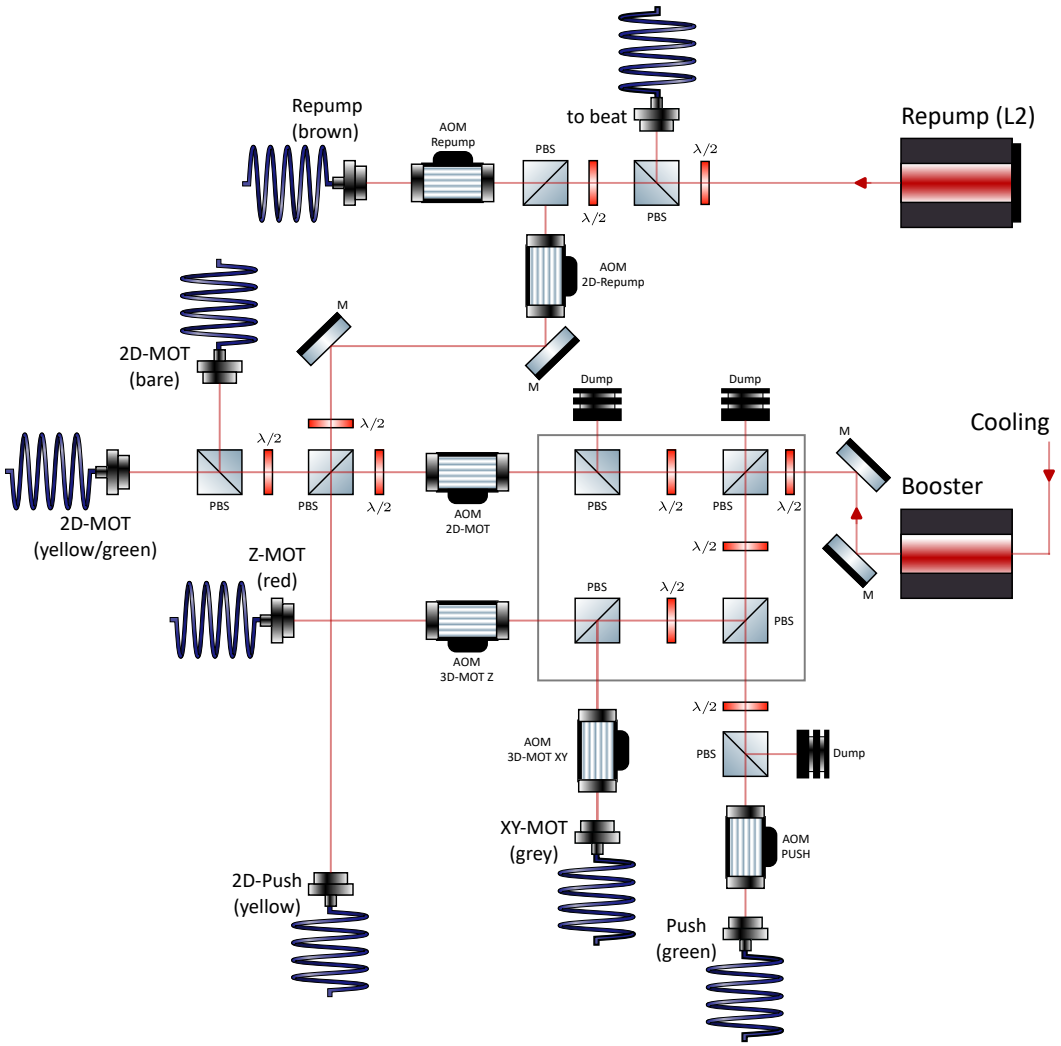

Figure D.1: Optical power distribution for cooling, repump and push beams. The colors in parentheses indicate marks of the fiber heads for simplified identification. AOMs are all controlled by the experimental control software. The figure was created using components from [Fra]